Dynamics and stability of a Bose-Fermi mixture : counterflow of superfluids and inelastic decay in a strongly interacting gas

Sébastien Laurent

To cite this version:

Sébastien Laurent. Dynamics and stability of a Bose-Fermi mixture : counterflow of superfluids and inelastic decay in a strongly interacting gas. Quantum Gases [cond-mat.quant-gas]. Université Paris sciences et lettres, 2017. English. NNT : 2017PSLEE023 . tel-01805141

HAL Id: tel-01805141

https://theses.hal.science/tel-01805141

Submitted on 1 Jun 2018

THÈSE DE DOCTORAT

de l'Université de recherche Paris Sciences et Lettres
PSL Research University

préparée à l'École normale supérieure

Dynamics and stability of a Bose-Fermi mixture: counterflow of superfluids and inelastic decay in a strongly interacting gas

Dynamique et stabilité d'un mélange de Bose-Fermi: contre-courant de superfluides et pertes inélastiques dans un gaz fortement corrélé

Ecole doctorale n°564
Spécialité: Physique

Composition du jury:

Mme. Amandine Aftalion
CNRS
Présidente du jury

M. Vincent Josse
Laboratoire Charles Fabry
Rapporteur

M. Nikolaos Proukakis
Newcastle University
Rapporteur

M. Eric Cornell
Boulder University
Examinateur

M. Ionut Danaila
Université de Rouen
Membre invité

M. Christophe Salomon
École normale supérieure
Directeur de thèse

M. Frédéric Chevy
École normale supérieure
Co-directeur de thèse

Soutenue par **Sébastien LAURENT**
le 9 Octobre 2017

dirigée par **Christophe Salomon**
& **Frédéric Chevy**

ENS
ÉCOLE NORMALE SUPÉRIEURE

PSL
RESEARCH UNIVERSITY PARIS

Contents

Introduction

The discovery of the superconducting behavior of mercury at low temperature in 1911 by Kamerlingh Onnes [1] forerunned the rise of a new field of research in physics aiming at understanding the emerging properties of quantum many-body systems. It was among the first of a continuously growing list of materials to exhibit unexpected and puzzling properties at low temperature due to strong quantum correlations between the constituent particles. Other paradigmatic examples include the superfluid phase of liquid ^{4}He discovered in 1938 [2, 3] and the fractional quantum Hall effect first observed in 1982 [4, 5]. The deep understanding of these systems is generally strongly hindered by the absence of generic theoretical or numerical methods to solve the associated quantum many-body problems and hence requires considerable inputs from the experimental side. Indeed, it took almost 50 years to figure out what was the underlying mechanism allowing for superconductivity and provide a model that could explain quantitatively its features. However, this so-called "conventional" theory proposed by Bardeen, Cooper, and Schrieffer (BCS) in 1957 [6] was later proved unable to explain the properties of a new class of superconductors discovered in 1985 [7] that exhibited anomalous high critical temperatures, a mystery that remains to this day.

In parallel with these discoveries in condensed matter, progress were made in the study of light-matter interaction and the development of laser technologies, following the path of the seminal works of Kastler and Brossel on optical pumping in the 1950's [8]. It then became possible in the 1980s to cool and trap atomic vapors down to low temperatures using the radiation pressure of laser beams and designed magnetic fields [9]. This eventually led to the experimental breakthroughs of the production of Bose-Einstein condensates (BEC) with alkali atoms in 1995 [10, 11] followed by degenerate Fermi gases in 1999 [12]. Since then, ultracold gases have emerged as a versatile platform for studying quantum phases of matter [13]. Indeed, such systems offer an unprecedented degree of control of various parameters essential for their study. Among them, a first important feature is the possibility to create trapping potentials of various shapes for the atoms: harmonic, box-like, periodic or disordered potentials. Second, the interatomic interactions are short-ranged and can be characterized by a single parameter at low temperature, the s-wave scattering length which is almost freely tunable by means of the Feshbach resonances. Finally, the atoms can be coupled to artificial gauge fields that can mimic the effect of a magnetic field on electrons. With these tools, one can realize a quantum system that has all the essential ingredients to be strongly correlated and exhibits the emergent properties observed in condensed matter, predicted for some exotic systems such as neutrons stars [14, 15] and quark-gluon plasmas [16, 17], or yet to be discovered.

Many-body physics with cold atoms

Up to now, several classes of many-body systems have been realized and investigated using cold atoms. One major trend is the study of atoms in periodic potentials mimicking the ion-crystal lattice structure of solid materials experienced by electrons. This allows in particular for the exploration of the rich physics of the so-called Hubbard model [18]. One important feature is the existence of the Mott insulating phase when the on-site repulsive interactions are sufficiently strong [19]. This was observed for both fermionic and bosonic species [20, 21, 22]. For the latter case, a quantum phase transition to a superfluid state when varying the interaction strength was also demonstrated [20]. Many recent experiments have now access to the single atom resolution and can explore further the phase diagram of such systems [23, 24, 25, 26, 27, 28]. Important goals are the observation of antiferromagnetic phase and the elusive d-wave superfluid phase that should be present in the phase diagram of the repulsive 2D Fermi Hubbard model [29] or the realization of topological superfluids by implementing spin-orbit coupling or artificial gauge-fields [30, 31, 32, 33].

Another direction, is the investigation of the bulk properties of homogeneous strongly correlated gases. Here, interactions between atoms are tuned by the means of Feshbach resonances. For an ultracold two-component Fermi gas, one can explore the so-called BEC-BCS crossover [34], where by changing the interactions from weakly to strongly attractive, the system smoothly interpolates between a superfluid of Cooper pairs to a Bose-Einstein condensate of tightly-bound molecules. In between, for infinite scattering lengths, the gas enters the unitary regime, which is a paradigmatic example of strongly correlated system with fascinating properties such as scale invariance and a high critical temperature for superfluidity. The strongly interacting Bose gas is also of high interest as it could bridge the gap between ultracold vapors and superfluid liquid ^{4}He. However, the lifetime of the gas is strongly reduced due the enhancement of inelastic losses close to resonance [35, 36, 37]. It results from few-body exotic physics, namely the Efimov effect, which states the existence of a infinite log-periodic set of three-body bound states [38]. Hence the open question of the stability and the nature of the degenerate unitary Bose gas. The recent realization of homogeneous Bose [39] and Fermi gases [40] has opened up new routes to study these correlated gases and might enable the observation of exotic phases such as the long predicted FFLO phase [41, 42].

In 2014, during my first year of PhD, our group demonstrated the first realization of a mixture of Bose and Fermi superfluids using ultracold vapors of ^{7}Li and ^{6}Li. In the following years, we have investigated various aspects of the mixture focusing mainly on its superfluid properties and its stability with respect to inelastic decay. Before going to the outline of this thesis, I give a short overview of those two compelling topics that illustrates the richness of quantum few-body and many-body physics.

Probing superfluidity with cold atoms

One of the remarkable properties a quantum many-body system can exhibit at low temperature is superfluidity. Abstractly speaking, it arises for interacting systems for which the associated density matrix operator exhibits off-diagonal long range or quasi long-range order, meaning that the system possesses a phase coherence over macroscopic distances. This is the case for Bose-Einstein condensates, as it was revealed by matter-wave interference experiments [43, 44, 45], but also for two-dimensional (2D) systems, where as initially predicted by Beresinkii, Kosterlitz, and Thouless (BKT) [46, 47], a transition to a superfluid phase with quasi long-range order exists despite the impossibility of condensation at finite temperature in 2D. The BKT transition was indeed demonstrated for both interacting 2D Bose and Fermi gases [48, 49]. The phase coherence (and hence the superfluidity) can be mitigated by a deep optical lattice or a disordered potential leading respectively to a Mott insulator [20] and Anderson localization [50, 51].

Superfluidity manifests through a collection of spectacular effects mainly related to flow properties of the system. Probably the most defining one is the existence of a superfluid fraction (equal to the fluid density at zero temperature) that is not put into motion by shearing force using a moving external potential. Indeed, in the spirit of the Hess and Fairbank experiment performed with superfluid liquid helium [52], a strongly interacting Fermi gas was shown to remain at rest in a slowly rotating container [53]. Moreover, quantization of the circulation in the superfluid implies that for increasing rotation frequencies, angular momentum will only be transferred to the system by the nucleation of quantized vortices, which will form a regular hexagonal Abrikosov lattice due to their mutual repulsion [54]. Vortex lattices were observed for Bose gases [55, 56, 57] and two-component Fermi gases in the BEC-BCS crossover [58, 59], demonstrating unambiguously the superfluidity of the strongly interacting Fermi gas at low temperature.

The absence of shear viscosity also allows for persistent currents. Experiments done with a rotating BEC in a ring trap indeed showed that metastable currents could last for more than one minute only limited by the lifetime of the sample [60, 61]. As shown by Landau [62], the frictionless nature of the flow stems from the existence of a critical velocity below which a moving impurity cannot deposit energy in the superfluid. The observation of such a critical velocity was reported for Bose gases both in 3D [63, 64] and 2D [65] and for the interacting Fermi gas in the BEC-BCS crossover [66, 67].

Finally, another hallmark of superfluidity is the existence of a second sound, an entropy wave in which the superfluid and the non-superfluid components oscillate with opposite phases. The second sound was directly observed in a unitary Fermi gas [68]. The measurement of its speed allowed for the extraction of the superfluid fraction as a function of temperature providing another benchmark for many-body theories.

Cold atom setups offer the unique possibility to prepare ultracold mixtures of different atomic species or atoms in different internal states that can exhibit simultaneous superfluidity. An interesting prospect is then to investigate how the features mentioned above generalize to such superfluid mixtures and what kind of dynamics are possible. First investigations on the dynamics of Bose-Bose superfluid mixtures showed strong non-linear and dissipative effects such as the generation of dark-bright train solitons due to a weak miscibility of the two components [69, 70]. The dynamics is expected to be even richer for spinor condensates which exhibit a vectorial order parameter [71, 72, 61].

Inelastic losses in cold atoms

A very specific feature of cold atom systems is that they are actually metastable and are subject to inelastic losses that can strongly limit their lifetime. This originates from the formation of deeply-bound molecules during the collisions of three bodies or more. As such, a natural approach to estimate the inelastic loss rate is to solve the associated quantum few-body problem. For three identical bosons, the existence of an Efimov scattering channel, leads to enhanced inelastic losses when going toward resonant s-wave interactions as mentioned before. This property was actually used to reveal the existence of the

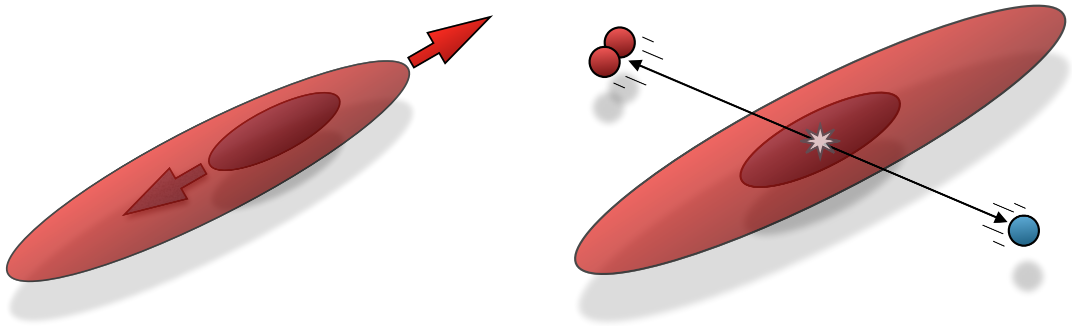

Figure 1: Sketch of the two experiments performed using our mixture of Bose and Fermi superfluids (shown as a small and large ellipsoid respectively) and presented in this thesis. Left figure: Counterflow experiment, where an oscillatory relative motion is created by exciting the dipole modes of both clouds. Right figure: Measurement of the three-body recombination in a strongly correlated system. Each inelastic collision leads to the loss of three particles due to the large released binding energy.

elusive Efimov trimers by the observation of resonant loss peaks associated to their merging with the three-body scattering continuum [73, 74, 75, 76]. In contrast, equal-mass two component Fermi gas were shown to be extremely stable close to resonance due to Pauli repulsion [77, 78, 79, 80]. For mixture of different atomic species, the few-body problem exhibits even more richer features, in particular the Efimov effect is also predicted to occur for fermionic systems in presence of light impurities [81, 82, 83].

However, in a many-body ensemble, inelastic collisions are affected by correlations with surrounding particles and hence cannot be conveniently described using a few-body framework. A striking example is the reduction of the inelastic losses at the condensation threshold for a Bose gas as predicted in [84]. When the gas is fully condensed the reduction amount to a factor 3! due to a complete indiscernability of the colliding bosons as demonstrated in [44]. In a strongly interacting gas, the correlations between atoms become highly non trivial and understanding the behavior of inelastic losses is a compelling problem connected to many-body physics. Indeed, recent experiments done on the unitary Bose gas have observed unusual fractionnal scalings in density for the inelastic loss rate [37, 85].

Outline of the thesis

In this thesis, I will present some of the results we obtained with our ^{6}Li-^{7}Li mixture as well as studies done in parallel to these works that enrich our understanding and give perspective to the phenomena investigated experimentally. In a first part (chapter 3 and 4), I address mainly the topics of energy exchange and mechanisms of dissipation in a counterflow of superfluids. In a second part, I consider the problem of inelastic losses in a strongly correlated gas (chapter 6, 7 and 8).

- The first chapter is dedicated to a presentation of the basic notions and properties of interacting cold gases. We start by discussing the two body problem, to introduce the scattering length, the zero-range model and the Feshbach resonances. We then review the three-body problem and the Efimov physics, which will be useful for chapter 5 and 6. Finally, we presents some known results on the thermodynamics of interacting Bose and Fermi gases, which will be used multiple times throughout this work.

- The second chapter presents the experimental setup that we use to produce our dual Bose-Fermi superfluid. We describe the different steps to achieve double degeneracy using the two lithium isotopes ^{7}Li and ^{6}Li. The final trap consists in a harmonic cigar-shaped trap where the small BEC of ^{7}Li is immersed in the Fermi superfluid of ^{6}Li, see Fig. 1. An adjustable bias magnetic field allows us to tune the interactions between the fermions and to explore the BEC-BCS crossover.

- The third chapter describes a superfluid counterflow experiment. The dynamics is initiated by exciting the dipole modes of the two clouds and letting the system evolve, as depicted in the left panel of Fig. 1. In a first part, we describe the dynamics at low relative speed, where the motion is long-lived and shows at most weak dissipation. We observe a coherent energy exchange between the two superfluids that can be captured theoretically using a sum rule approach and interpreted in terms of coupled oscillators. In a second part, we investigate the dynamics for faster relative motion and identify a threshold for dissipation. We measure the associated critical velocity in the BEC-BCS crossover. The extracted values are surprisingly high and close to theoretical predictions derived for ideal systems [86].

- The fourth chapter presents the results of a numerical simulation of two counterflowing BECs that we have performed to get a better understanding of the counterflow experiment results. We investigate the dynamics for various relative velocities and coupling between the condensates. For low relative velocity , the motion of the clouds is accurately described by the same sum rule model used for the experimental data. For larger relative velocity, we identify two mechanisms of dissipation. One of them corresponds to the simultaneous generation of elementary excitations and exhibits a well defined activation threshold despite the oscillatory motion.

- Chapter 5 is a short review on universal contact relations that relates various observables of a many-body system to two key quantities, the two-body contact parameter (also known as Tan's contact) and three-body contact parameter that describe short-range correlations in the system.

- Chapter 6 introduces the physics of three-body recombination and provides a theoretical framework to predict the loss rate in various regime and in particular for strong interactions. We show that the loss rate can be expressed in terms of the contact parameters that can themselves be computed using the equation of state of the gas.

- Chapter 7 describes two studies of the inelastic losses in the dilute unitary Bose gas. In a first part, we present a model taking into account both three-body recombination and evaporation to describe the atom losses and temperature dynamics in a dilute unitary Bose gas. It allows us to do a quantitative measurement of the three-body loss rate and the method is applied to results obtained by our team (with ^{7}Li) and Chen Chin's group at Chicago (with ^{133}Cs). It demonstrates the universal behavior of the dynamics and confirm the $1/T^2$ scaling of the loss rate measured in [36], where T is the sample temperature. In a second part, we study theoretically the effect of three-body losses and interactions on the momentum distribution of a homogeneous unitary Bose gas in the dilute limit. We compare it to the results at JILA on a gas of ^{85}Rb [37].

- Chapter 8 presents present a study of three-body recombination in our ultracold Bose-Fermi mixture, see right panel of Fig. 1. Using the framework introduced in chapter 6, we expect the decay rate to be proportional to the Tan's contact of the Fermi gas. We probe the recombination rate in both the thermal and dual superfluid regimes. When the interactions between fermions become resonant, we show that the loss rate is proportional to $n_f^{4/3}$, where n_f is the fermionic density. This unusual exponent signals non trivial two-body correlations in the system.

Chapter 1

From few to many

The versatility of ultracold atomic ensembles to study quantum many-body physics mainly lies in the simplicity and large tunability of the interactions between atoms. In this chapter, we review central concepts used to describe interactions and correlations in cold atomic systems. First, we start with the cornerstone of any interacting model, the two body-problem. Then we describe the rich physics that emerges when a third particle is added. Finally, we provide known results on the thermodynamical properties of interacting Bose and Fermi gas. These different properties and theoretical tools will prove useful to understand the physics of inelastic losses in strongly correlated systems or the dynamics of counterflowing superfluids that will interest us in the following chapters.

1.1 Two-body problem

The starting point for any interacting many-body theory is the modeling of interactions between the particles. In this section, we will describe the dominant interaction mechanisms for lithium atoms. They can be simplified to a more practical interacting "potential", the pseudo-potential which is parametrized by a single parameter, the scattering length. Finally, we will see, that this scattering length can be tuned to any arbitrary value by the means of Feshbach resonances.

1.1.1 Interacting potential

As for others alkali atoms, two lithium atoms will mainly interact via an isotropic van der Waals interaction coming from their induced dipole. This gives the well-known $-C_6/r^6$ attraction law at long distances. The range of this interaction is given by the van der Waals length

$$l_{\mathrm{vdw}} = \frac{1}{2}\left(\frac{mC_6}{\hbar^2}\right)^{1/4}, \tag{1.1}$$

which is of the order of a few nanometers for alkali atoms.

On the contrary, at short distances, typically the atomic scale, atoms will experience a strong electron-exchange repulsive barrier [87]. As a result of the large range difference between the two contributions, the combined interaction potential, as sketched in Fig. 1.1, supports many vibrational bound-states (generally a few tens). Their binding energy can

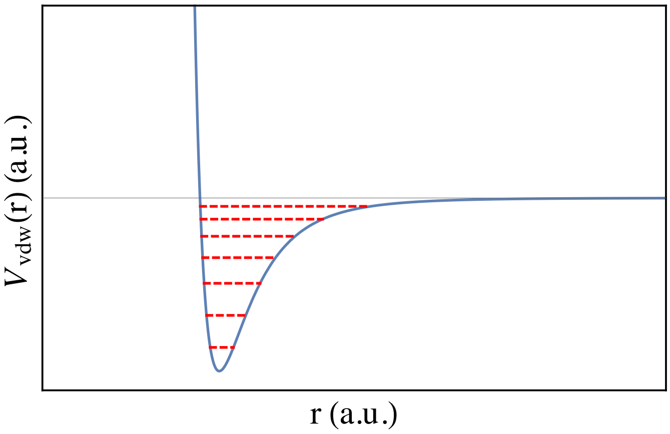

Figure 1.1: Schematic representation of a Van der Waals potential with associated bound states energies (red-dashed line).

be order of several hundred Kelvins and their typical size denoted R_* is smaller than l_{vdw}[1]. The presence of bound states allows for inelastic collisions when three atoms are within a distance R_*. We will discuss this process in more details in chapter 6.

In dilute gases where $l_{\text{vdw}} \ll n^{-1/3}$, with n the atomic density, we can expect that both inelastic collisions and elastic collisions should be rare events. We will see that the wave-like nature of atoms at low temperature can actually strongly enhance interactions but also potentially increase the deeply-bound molecule formation rate.

1.1.2 Scattering theory

The next step is to investigate how two atoms scatter[2]. In the center of mass frame, for two atoms of mass m, the following Schrödinger equation has to be considered

$$\left[-\frac{\hbar^2}{m}\Delta_{\mathbf{r}} + V(r)\right]\Psi(\mathbf{r}) = E\Psi(\mathbf{r}) \;, \tag{1.2}$$

where V is the interacting potential.

For negative energies $E < 0$, we should recover the bound states mentioned in the previous section. For $E > 0$, solutions are scattering states that we can search with the asymptotic form

$$\Psi(\mathbf{r}) \underset{r\to\infty}{\simeq} \mathrm{e}^{\mathrm{i}\mathbf{k}\cdot\mathbf{r}} + f_k(\mathbf{n})\frac{\mathrm{e}^{\mathrm{i}kr}}{r} \;, \tag{1.3}$$

where $\mathbf{n} = \mathbf{r}/r$ and f_k is the scattering amplitude.

The scattering states can be expanded onto the basis of partial spherical waves indexed by l the associated angular momentum quantum number. A centrifugal barrier term of order $l^2\hbar^2/ml_{\text{vdw}}^2 \gtrsim \mathrm{mK}$ strongly suppress partial waves with $l > 0$ at low temperature and the scattering is thus purely s-wave. Hence, in the low-energy limit, the scattering amplitude is isotropic and takes the form

$$f_k(\mathbf{n}) \underset{k\to 0}{\simeq} \frac{-1}{\frac{1}{a} + \mathrm{i}k - r_e k^2} \;, \tag{1.4}$$

---

[1] The shallowest bound state can however have drastically different binding energy and size as we will see in the following sections.

[2] An in-depth description of scattering theory for cold-atom systems can be found in [88].

where a is the (s-wave) scattering length and r_e the effective range. Both parameters depend on the precise shape of the interacting potential. In the limit $r_e k \ll 1$, only the knowledge of a single quantity, a, is needed to describe the scattering. Thus we can use a simplified interaction potential provided that it gives the same scattering length.
The differential scattering cross-section can be readily computed [3,4]

$$\frac{\mathrm{d}\sigma}{\mathrm{d}\Omega} = |f_k(\mathbf{n})|^2 \underset{k\to 0}{\simeq} a^2 \ . \tag{1.5}$$

Consequently, atoms can be seen as having an effective size of order a and the regime of strong interactions is achieved whenever $na^3 \gtrsim 1$. As we will see later in some "resonant" situations a can be orders of magnitude larger than l_{vdw} leading to the possibility of strong interactions in a dilute system, where $n^{-1/3} \gg l_{\mathrm{vdw}}$.
In the following we will investigate the behavior of the scattering length a in two important examples.

A Van der Waals potential

A simple way to describe the hard-core repulsion and the Van der Waals attraction at large distances is given by the following potential:

$$V(r) = \begin{cases} -C_6/r^6 & \text{if } r > b \\ \infty & \text{if } r \leq b \end{cases} \tag{1.6}$$

where b is the size of the hard-core potential. For this simple model we have the exact expression for the scattering length [87]

$$a = \bar{a}\,[1 - \tan(\Phi - 3\pi/8)] \ , \tag{1.7}$$

where $\bar{a} = 0.956 l_{\mathrm{vdw}}$ and

$$\Phi = \int_{r_c}^{\infty} \mathrm{d}r \sqrt{m|V(r)|/\hbar} = 2l_{\mathrm{vdw}}^2/b^2 \ . \tag{1.8}$$

Hence, we see that a should have the same order of magnitude as l_{vdw} but can be enhanced (or diminished) to extremely large (low) values via the tangent term in eq. (1.7), where the short-range part of the interaction comes into play.
The effective range is given by [89]

$$r_e = 2.92\bar{a}\left(1 - 2\frac{\bar{a}}{a} + 2\left(\frac{\bar{a}}{a}\right)^2\right) \ . \tag{1.9}$$

Here again, the magnitude of the effective range is essentially given by l_{vdw}. However, we can notice that the effective range r_e will diverge whenever the scattering length $a \to 0$.

---

[3] For indistinguishable particles, the (anti-)symmetrisation of the wave function imposes $\mathrm{d}\sigma = |f_k(\mathbf{n}) + \epsilon f_k(-\mathbf{n})|^2 \mathrm{d}\Omega$ with $\epsilon = 1$ for identical bosons and $\epsilon = -1$ for identical fermions. It leads to the famous result that identical fermions do not interact via a s-wave channel, $\mathrm{d}\sigma = 0$.

[4] For $a \to \infty$, σ will reach its maximal value $4\pi/k^2$ ($8\pi/k^2$ for identical bosons).

A box potential

The divergence of the scattering length is associated to the apparition of new bound state pulled in from the continuum. This can be readily seen with the example of an attractive box potential of size b:

$$V(r) = \begin{cases} 0 & \text{if } r > b \\ -v\frac{\hbar^2}{mb^2}\left(\frac{\pi}{2}\right)^2 & \text{if } r \leq b \end{cases} \tag{1.10}$$

This potential supports a bound state whenever $v > 1$ and a new bound state appears for $v = v_k = (1 + 2k)^2$, $k \in \mathbb{N}$. Away from those discrete values, the binding energies are of the order $\sim -\hbar^2/mb^2$ and the dimers extent are proportional to the box potential size $\sim b$, see Fig. 1.2. These bound-states can be used to model the deeply bound dimers of alkali atoms, by taking $b = R_*$.
By computing the low energy scattering state $k \to 0$ which has the asymptotic form $1 - a/r$ at large distance r, we can compute the scattering length a, it reads

$$a = b(1 - \frac{2}{\pi\sqrt{v}}\tan(\frac{\pi}{2}\sqrt{v}))\ , \tag{1.11}$$

which shows a periodic resonant enhancement each time a new bound state appears. In this case, it can be shown that the newly appeared bound state has a size which diverges as

$$\langle \mathbf{r} \rangle \underset{v \to v_k^+}{\sim} a/2\ , \tag{1.12}$$

see Fig. 1.2, and the binding energy

$$E_b \underset{v \to v_k^+}{\sim} -\hbar^2/ma^2\ . \tag{1.13}$$

In the zero-range limit, $a/b \to \infty$, the weakly-bound dimer wave function simplifies to the simple expression

$$\Psi(\mathbf{r}) = \frac{\mathrm{e}^{-r/a}}{r\sqrt{2\pi a}}\ . \tag{1.14}$$

The properties of the weakly bound state along with the associated divergence of the scattering length are universal. It will occur for any potential provided that it decreases sufficiently fast (and applies in particular to the potential mentioned in the previous section).

1.1.3 Pseudo-potential

The zero-range limit of (almost) any two-body problem will converge toward the same universal limit[5]. This universal limit can be described exactly using a simple model, the pseudo-potential. It is defined as

$$-\frac{\hbar^2}{m}\Delta_{\mathrm{r}}\Psi(\mathbf{r}) = E\Psi(\mathbf{r})\ . \tag{1.15}$$

---

[5] If the two-body potential vanishes fast enough.

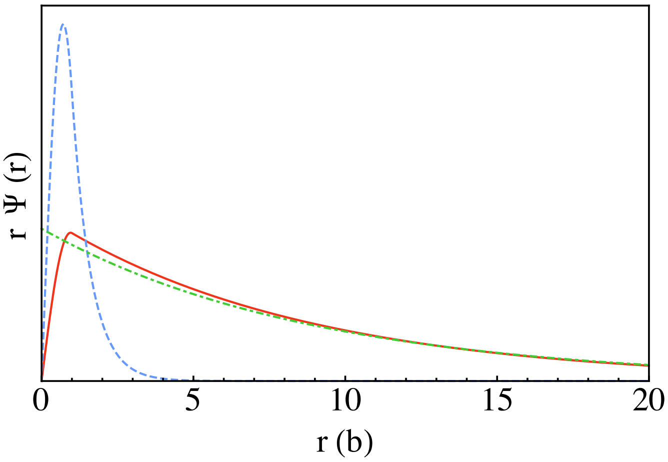

Figure 1.2: Bound-state wavefunctions for different trap depths v of a box potential. Red curve: Weakly bound state, $v = 1.1$, $a \simeq 8.90\ b$. Blue-dashed curve: Deeply bound state: $v = 3$, $a = 1.16\ b$. Green-dot-dashed curve: Weakly bound state in the zero-range limit with $a = 8.90\ b$.

for $\mathbf{r} \neq \mathbf{0}$.
In addition, the relative wavefunction should have the following behavior at short distances

$$\Psi(\mathbf{r}) \underset{r\to 0}{\simeq} A\left(\frac{1}{r} - \frac{1}{a}\right) . \tag{1.16}$$

The pseudo-potential is thus a zero-range potential and its effect is solely contained in the *Bethe-Peierls boundary condition* (1.16).
In momentum space, it leads to the high-momentum behavior

$$\Psi(\mathbf{k}) \underset{k\to\infty}{\sim} \frac{1}{k^2} . \tag{1.17}$$

The scattering amplitude is

$$f_k = \frac{-1}{\frac{1}{a} + \mathrm{i}k} . \tag{1.18}$$

Hence we can identify a as the usual scattering length and the effective range is $r_e = 0$. For positive a, there is a halo-dimer with energy $E_b = -\frac{\hbar^2}{ma^2}$ and wavefunction

$$\Psi(\mathbf{r}) = \frac{\mathrm{e}^{-r/a}}{r\sqrt{2\pi a}} . \tag{1.19}$$

1.1.4 Feshbach resonance

Along their simple description in terms of a single quantity, the scattering length a, another feature of the interactions in many cold-atom systems is their large tunability by the use of the so-called Feshbach resonance. It allows one to increase the scattering length to values far beyond the interparticle spacing and hence to reach strongly interacting regimes. An extended description of the physics behind Feshbach resonances can be found in [90, 88]. Here, we will restrict ourselves to a fairly short but synthetic description of its mechanism and give its important properties.

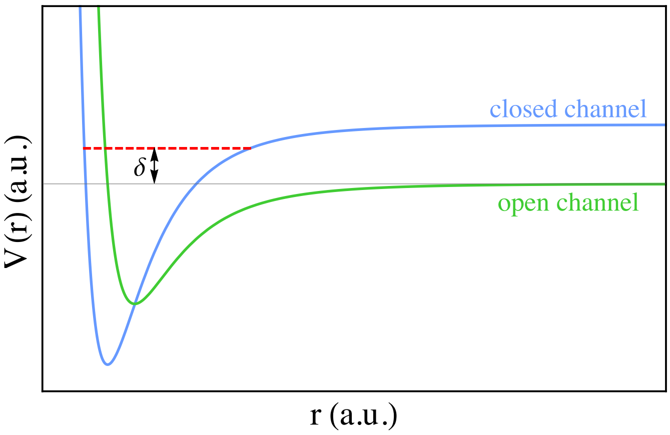

Figure 1.3: Schematic representation of two coupled channels that can give rise to a (magnetic) Feshbach resonance. The energy difference between the continuum threshold of the open channel and the bound-state of the open-channel, δ, can be tuned using a magnetic field thanks to the different magnetic moments of the two channels. As δ goes to 0, the bound-state becomes resonantly coupled to the open-channel diffusive states and lead to a divergence of the scattering length.

To begin with, we have to consider at least two interacting potentials through which the two atoms can scatter. For alkali atoms, those are played by the singlet and triplet potentials, V_s and V_t respectively. Both potentials have the same Van der Waals tail at large distance but can strongly differ at short distance. They can be added to form a (electron) spin dependent potential

$$V(r) = \frac{1}{4}\left(V_s(r) + 3V_t(r)\right) + \left(V_t(r) - V_s(r)\right)\frac{\mathbf{s}_1.\mathbf{s}_2}{\hbar^2}\ . \tag{1.20}$$

Another ingredient is the possibility to shift one potential respectively to the other. In the case of magnetic Feshbach resonances, this is done by applying constant external magnetic field. The primary effect will be a spin-Zeeman interaction

$$\mathcal{H}_Z = \gamma_e \mathbf{s}_1.\mathbf{B} + \gamma_e \mathbf{s}_2.\mathbf{B}\ . \tag{1.21}$$

Hence, the degeneracy between the triplet states is lifted while the singlet state energy is not affected. The relative energy between triplet and singlet channels can thus be tuned by changing the magnetic field. More generally, this will be possible every time the channels have different magnetic moments. The channel having the lowest energy at infinite spacing is then called the entrance or open channel, the others are said to be closed. Indeed, at low temperatures, atoms will only emerge from the entrance channel, as the others are not energetically accessible (since the energy difference results from hyperfine and Zeeman contributions $\gtrsim$ mK).

The last ingredient needed is a coupling between the open and closed channels. It is actually already present in the case of magnetic Feshbach resonances. Indeed, the hyperfine interactions (but not only) will lead to electronic eigenstates that are not fully spin-polarized. The initial incoming state is not a pure triplet and is thereby coupled to the closed channels.

Then, a Feshbach resonance occurs when the bound molecular state in the closed channel energetically approaches the scattering state in the open channel, see Fig. 1.3.

The magnetic resonances can be described using the following expression

$$a(B) = a_{bg}\left(1 - \frac{\Delta B}{B - B_0}\right) , \tag{1.22}$$

where a_{bg} is the background scattering length in the absence of coupling, B_0 is the resonance position, and ΔB its width.

The minimal description of a Feshbach resonance relies on a two-channel model and a natural question to ask is the role of the closed channel on the effective description of scattering between two atoms. This is characterized by the resonance strength parameter :

$$s_{res} \simeq \frac{l_{\mathrm{vdw}}}{r^\star} , \tag{1.23}$$

where $r^\star$ is an intrinsic length scale that is inversely proportional to the coupling strength of the resonance [90]. It allows to classify Feshbach resonances into two limiting cases. For $s_{res} \gg 1$, the resonance is open-channel-dominated, the scattering state projection onto the closed-channel resonant bound state is very small over the full width of the resonance. Hence, the scattering of atoms can be effectively described by a single channel model. This type of resonances are also called broad resonances and usually have a large width ΔB. The effective range r_e remains small, $\sim l_{\mathrm{vdw}}$, and interactions can be accurately described by the universal limit. As an example, for the well-known broad resonance in ^{6}Li near 832 G, the resonance strength is $s_{res} \simeq 59$ and the closed-channel fraction[6]$\sim 10^{-4}$ [90, 91] . The other limiting case, $s_{res} \ll 1$, is the closed-channel-dominated resonance, or narrow resonance. The closed-channel admixture is negligible only for a fraction of the resonance width. A single channel description of scattering is generally not possible. Furthermore, strong inelastic collisions occurs as the resonantly coupled bound state can decay easily to a deeply bound state.

1.2 Three-body problem

The next step toward the study of many-body systems is the three-body problem. Indeed, novel physics already appears when a third particle is added. With three atoms, an infinite sequence of universal three-body bound states called Efimov trimers can arise and have dramatic consequences on the many-body system. Also, the three-body problem is of great importance when dealing with molecule formation, since the process need at least three particles close to each other. In this section, we will review mainly the unitary case ($|a| = \infty$), where numerous analytical results were obtained. In particular, we will uncover the Efimov physics which plays a central role in strongly interacting Bose gases. Extended details on the three body problem can be found in the review [92] and in the thesis of F. Werner [93].

---

[6] In the two-body case we expect the closed-channel fraction to be exactly zero at resonance. The measured finite value comes from correlations with the many-body ensemble, see the Section 5.

1.2.1 Setting up the framework

As for the two-body problem, we have to solve a Schrödinger equation which now involves three particles, and can be readily expressed in the center of mass frame

$$\left[\frac{\hbar^2}{m}\left(\Delta_r+\Delta_\rho\right)+V(\mathbf{r},\boldsymbol{\rho})\right]\Psi(\mathbf{r},\boldsymbol{\rho})=E\Psi(\mathbf{r},\boldsymbol{\rho})\ , \tag{1.24}$$

where we have introduced the Jacobi coordinates

$$\mathbf{r} = \mathbf{r}_2-\mathbf{r}_1 \tag{1.25}$$

$$\boldsymbol{\rho} = \frac{2}{\sqrt{3}}\left(\mathbf{r}_3-\frac{\mathbf{r}_1+\mathbf{r}_2}{2}\right)\ , \tag{1.26}$$

$\mathbf{r}_i$, $i\in\{1,2,3\}$ being the three particles coordinates and V is the sum of the three two-body potentials.

1.2.2 Zero-range model

Now, in the zero-range limit, we can remove the interacting potential whenever $r\neq 0$ or $\pm\mathbf{r}/2+(\sqrt{3}/2)\boldsymbol{\rho}\neq\mathbf{0}$ and use a Bethe-Peierl condition (1.16) for each pair of atoms with potentially three different scattering lengths.

In the following we will only consider two specific cases that are relevant for the next chapters:

-Three identical bosons, which implies the particle-exchange condition

$$\hat{P}_{ij}|\Psi\rangle=|\Psi\rangle,\ \forall\, i,j \tag{1.27}$$

where $\hat{P}_{ij}$ transpose particles i and j.

-Two spin-up fermions ($i=1$ and 3) and a spin-down fermion ($i=2$), which imposes the condition

$$\hat{P}_{13}|\Psi\rangle=-|\Psi\rangle\ . \tag{1.28}$$

For both cases, due to their exchange symmetry one can only use a single Bethe-Peierl condition

$$\Psi(\mathbf{r},\boldsymbol{\rho})\underset{r\to 0}{\sim}\left(\frac{1}{r}-\frac{1}{a}\right)A(\boldsymbol{\rho})\ . \tag{1.29}$$

1.2.3 Efimov's ansatz

Let us first discuss the unitary case, $|a|=\infty$. It is convenient to introduce the hyperspherical coordinates $(R,\boldsymbol{\Omega})$. The hyperradius is:

$$R=\sqrt{\frac{r^2+\rho^2}{2}}\ , \tag{1.30}$$

by construction, it will vanish whenever the three particles get close to each others. $\mathbf{\Omega}$ is a set of three (hyper)angles $\mathbf{\Omega} = (\alpha, \hat{r}, \hat{\rho})$ with[7]

$$\begin{aligned} \alpha &= \arctan\left(\frac{r}{\rho}\right) && (1.31) \\ \hat{r} &= \frac{\mathbf{r}}{r} && (1.32) \\ \hat{\rho} &= \frac{\boldsymbol{\rho}}{\rho} \, . && (1.33) \end{aligned}$$

With this new set of coordinates, the Schrödinger equation (1.24) can be rewritten as

$$-\frac{\hbar^2}{2m}\Delta_{\mathbf{R}}\Psi(R,\mathbf{\Omega}) = E\Psi(R,\mathbf{\Omega}) \, , \tag{1.34}$$

where $\Delta_{\mathbf{R}}$ is the Laplacian operator on the hypersphere

$$\Delta_{\mathbf{R}} = \frac{1}{R^2}\left(\frac{\partial^2}{\partial R^2} + \frac{1}{R}\frac{\partial}{\partial R} + \frac{1}{R^2}T_{\mathbf{\Omega}}\right)R^2 \, , \tag{1.35}$$

and T_Ω is an operator that contains all the hyperangular dependence of the Laplacian (in a similar fashion as the angular momentum operator for the usual spherical Laplacian). In the absence of any length scale (i.e. unitarity with $|a| = \infty$), the problem is separable into a hyperangular and a hyperadial problem as shown by Efimov [94]. The three-body wavefunction can be written as

$$\Psi(R,\mathbf{\Omega}) = \frac{F(R)}{R^2}\phi(\mathbf{\Omega}) \, , \tag{1.36}$$

where F and ϕ are respectively solutions of the hyperradial and hyperangular problems.

1.2.4 Hyperangular problem

The hyperangular problem is an eigenvalue problem with boundary conditions. I.e, $\phi_{l,m,n}$ are the eigenfunctions of the hyperangular part of the Laplacian operator:

$$T_{\mathbf{\Omega}}\phi_{l,m,n}(\mathbf{\Omega}) = -s_{l,n}^2\phi_{l,m,n}(\mathbf{\Omega}) \, . \tag{1.37}$$

The boundary conditions given by the Bethe-Peierl condition eq. (1.29) and by imposing that Ψ should be finite at $\rho = 0$ lead to a quantization of $s_{n,l}$. The eigenvalues are solution of a transcendental equation [93] and can be indexed by two positive integers l and n, where l is the quantum number associated to the total relative angular momentum of the three particles. For the fermionic case, all $s_{n,l}$ are strictly positive. For the bosonic case, in the $l = 0$ channel (called Efimov channel), there exists a pure imaginary eigenvalue, $s_{0,0} \equiv \mathrm{i}s_0 \simeq \mathrm{i} \times 1.0062$, while all the others are shown to be strictly positive. Values for the lowest channels are listed in Table 1.1 (coming from [93]). As we will see in the next section, $s_{l,n}$ pilots the behavior of the three-body wavefunction at short distances.

---

[7] In terms of differentials we have $d^3r_1 d^3r_2 d^3r_3 = (3/2)^{3/2} d^3C R^5 dR d^5\Omega$ and $d^5\Omega = 2\sin^2(2\alpha) d\alpha d^2\hat{r} d^2\hat{\rho}$.

Three bosons		
l	n	$s_{l,n}$
0	0	$\mathrm{i} \cdot 1.0062$
	1	4.4653
1	0	2.8639
	1	6.4622

Three fermions		
l	n	$s_{l,n}$
0	0	2.1662
	1	5.1273
1	0	1.7727
	1	4.3582

Table 1.1: $s_{l,n}$ values in the "lowest" channels for the two discussed systems, taken from [93].

1.2.5 Hyperradial problem

From equations (1.34, 1.35, 1.37), we see that F is solution of the following equation

$$-F''(R) - \frac{1}{R}F'(R) + \frac{s_{l,n}^2}{R^2}F(R) = \frac{2mE}{\hbar^2}F(R)\ . \tag{1.38}$$

It can be seen as a Schrödinger equation for a fictitious particle living in two dimensions, where R is the distance to the origin and $s_{l,n}^2/R^2$ is an effective isotropic potential. We thus see that depending on the sign of $s_{l,n}^2$, the effective potential can be either repulsive or attractive and supports bound state (called Efimov trimers), see Fig. 1.4.

Universal channels

For $s_{l,n} \geq 0$, the three-body problem is universal. There only exist diffusive states described by a Bessel function $F(R) = AJ_{s_{l,n}}(kR)$, where $k^2 = 2mE/\hbar^2$, and with the following asymptotic behavior at short distances

$$F(R) \underset{R\to 0}{\sim} (kR)^{s_{l,n}}\ , \tag{1.39}$$

and long distances

$$F(R) \underset{R\to\infty}{\sim} A\mathrm{e}^{\mathrm{i}kR} + B\mathrm{e}^{-\mathrm{i}kR}\ . \tag{1.40}$$

Efimov channel

For s_0, $E > 0$ solutions of the hyperradial problem are linear combinations of Bessel functions:

$$F(R) = AJ_{\mathrm{i}s_0}(kR) + BJ_{-\mathrm{i}s_0}(kR)\ . \tag{1.41}$$

For $R \to 0$, $F(R) \sim R^{\pm\mathrm{i}s_0}$ has a singular behavior (oscillations with diverging frequency). For the three-body Efimovian problem to be hermitian, one has to introduce an additional boundary condition [95, 93], using a new quantity, the three-body parameter R_t:

$$F(R) \underset{R\to 0}{\sim} \sin\left[s_0 \ln\left(\frac{R}{R_t}\right)\right]\ , \tag{1.42}$$

which can be seen as imposing a node of the wavefunction at $R = R_t$. The introduction of this new parameter can be seen as a loss of universality, a is not the only relevant

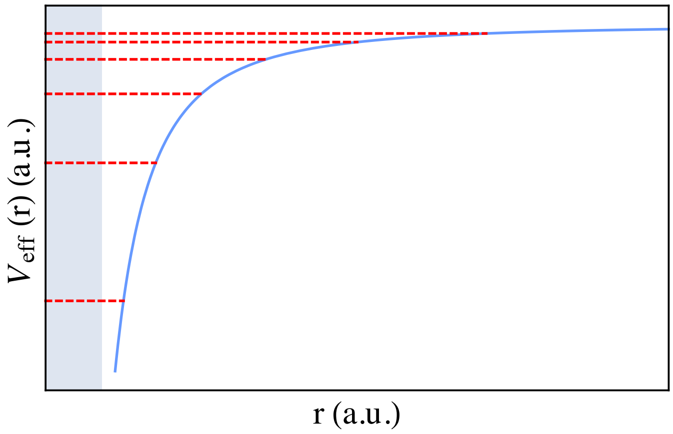

Figure 1.4: Schematic representation of the attractive effective potential in the Efimov channel and associated universal bound-states (red dashed lines). The blue-shaded area shows the region where the Efimov scenario breaks-down due to the short-range physics that cannot be neglected anymore. The geometric factor which relates the different energy levels, λ^2, is set to 2 for pratical convenience.

length scale for interactions in the zero-range limit. R_t depends on all the details of the two- and three-body potentials. Suprinsingly, it seems that for most Efimov resonances experiments, R_t has a universal behavior, $R_t = 8.9(4) l_{\mathrm{vdw}}$ [96].
The most interesting consequence of an Efimov channel is that it supports infinitely-many three-body bound-states (trimers) while two-body bound states are absent (at least at unitarity). Moreover, the absence of a length scale associated to the attractive potential (due to the particular -2 exponent) leads to a peculiar universal spectrum. Indeed, Efimov showed that two successive energy levels are connected via a geometric relation [38]

$$E_{n+1} = \frac{E_n}{\lambda^2} \, , \tag{1.43}$$

with $\lambda = \mathrm{e}^{\pi/s_0} \simeq 22.7$.
The boundary condition (1.42) will set the absolute positions of the levels. The spectrum is not bounded by below which should lead to a collapse of the wave function, as initially discovered by L.H. Thomas [97]. However, in realistic systems, the number of different trimers is finite due to both lower and upper bounds for their sizes.The nth Efimov trimer extent scales as λ^n. For large binding energies, the trimer size becomes comparable to the range of the two-body potential $\simeq l_{\mathrm{vdw}}$, in this case the short-range approximation is no longer valid and the Efimov scenario breaks down. For low binding energies, the trimer size becomes larger than interparticle distance $\simeq n^{-1/3}$ and will thus be affected by the interactions with surrounding atoms. In practice the number of accessible trimers is small[8] $\simeq \ln(n^{-1/3}/l_{\mathrm{vdw}})/\ln(22.7) \lesssim 3$.

1.2.6 Finite scattering length

In the previous sections, we gave results on the unitary three-body problem. Most of them relied on the use of Efimov anzats (1.36). For finite scattering length, the separability into

---

[8] For heteronuclear systems having large mass differences, there also exist an Efimov channel and the scaling parameter can be drastically smaller, e.g. for ^{6}Li-^{174}Yb$_2$, $\lambda \simeq 4.04$.

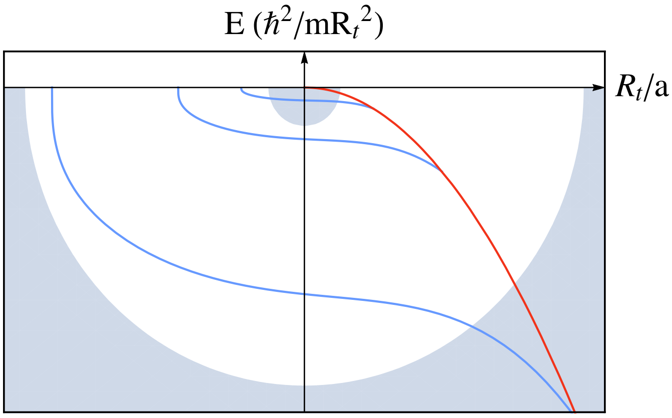

Figure 1.5: Efimov spectrum as a function of inverse scattering length. The Efimov trimers energy levels (blue curves) connect to the continuum threshold for negative a (and will lead to resonant three-body losses, see next chapter). For positive a they connect to the weakly-bound dimer level (red curve). The outer-shaded area represents the short-range physics dominated region where the Efimov scenario breaks down. The inner-shaded area shows the region where Efimov trimers are larger than the interparticle distance and interactions with other surrounding particles have to be taken into account.

a hyperangular and a hyperradial problem is no longer valid in the entire space. However, one can still apply its results in the universal sector, when $r_e \ll R \ll a$. Consequently, there still exists universal trimers away from unitarity but their number is reduced as $|a|$ is now a new upper bound for their size, see Fig. 1.5. By dimensional argument, the energy of the trimers takes the form

$$E_n = -\frac{\hbar^2}{mR_t^2} f_n(R_t/a) \ , \tag{1.44}$$

where the function f_n should obey the following scaling

$$f_n(x) = f_0(x/\lambda^n)/\lambda^{2n} \ , \tag{1.45}$$

for E_n to be scale invariant. More generally, quantities involving a/R_t will also share this scale invariance property that usually translates as a log-periodic behavior, $f(x) = f(\lambda x)$, signaling the underlying Efimov physics.

1.2.7 Adding more bodies

A natural question is to wonder whether there is an Efimov effect for systems involving more than three particles. Indeed, the existence of several infinite ladders of N-body bound states would lead to the introduction of as many N-body parameters which could limit the universal properties of the zero-range limit for interactions in a many-body ensemble. It was rapidly conjectured after Efimov discovery that no such effect was possible for more than three identical particles [98], however the general proof, if true, is still an ongoing work.

Recently, in the case of identical bosons, it was demonstrated that no Efimov effect was possible for four or more bosons [99]. Indeed, the introduction of a three-body parameter is expected to render all N-body problems well defined[9]. However, the unbounded by below Efimov trimers spectrum suggests that without introducing in the model a cut-off at short distance, the N-bosons system is at most meta-stable (Thomas collapse [97]).

For a spin 1/2 fermionic systems, there are no general results obtained for the N-body problem, but it was shown that a three-body Efimov effect could occur when the mass ratio between ↑ and ↓ is above some critical value, $m_\uparrow/m_\downarrow \simeq 13.607$ [81]. A four-body Efimov is also predicted to occur for a small mass ratio window $13.384 < m_\uparrow/m_\downarrow < 13.607$ [82]. However, for equal-mass fermions ensemble, no Efimov effect is predicted to occur at any level[10].

Consequently, it seems that except in some particular systems or conditions, the interactions in a many-body ensemble in the zero-range limit can be accurately described by the scattering length a and, in presence of an Efimov channel, a three-body parameter R_t.

1.3 Universal thermodynamics of the many-body problem

From the previous sections, we can conclude that in the vicinity of a Feshbach resonance and at low temperature it is possible to produce a many-body ensemble whose properties are universal, i.e they do not depend on the microscopic details associated with their constituent atoms. The equation of state and all thermodynamic quantities solely depends on a few variables: the density n, the temperature T, and the scattering length a and possibly the three-body parameter R_t. Hence, they can be directly compared to predictions of many-body theories as the Hamiltonian is completely determined. In this section dealing with the many-body problem, we illustrate this universality by quickly reviewing known results on the thermodynamical properties of the Bose and Fermi interacting ensembles and in particular on their equation of state. We will explore the effect of increasing interactions in bosonic systems, leading to the celebrated Gross-Pitaevskii equation, the Lee-Huang-Yang corrections, and the unitary Bose gas. Finally, we will describe the rich physics involved in the low temperature interacting Fermi gas, with its asymptotic regimes, the molecular Bose-Einstein condensate, the Barden-Cooper-Schriefer superfluid, and the unitary Fermi gas. But, to begin with, we will provide some results for non-interacting gases.

1.3.1 Ideal gases

The physics of a uniform ensemble of non-interacting identical particles at a temperature T is dictated by the comparison of the only two length-scales available, the mean interparticle distance $n^{-1/3}$ and the thermal de Broglie wavelength

$$\lambda_{th} = \sqrt{\frac{2\pi\hbar^2}{mk_BT}}\,, \tag{1.46}$$

which is a measure of the average size of a matter-wave packet. When $\lambda_{th} \gtrsim n^{-1/3}$, wave-packets start interfering and quantum effects are expected to occur. Equivalently,

---

[9] Universal N-body bound states are still possible, e.g. four-body bound states resonances were observed in the vicinity of the Efimov resonances [100].

[10] Yet, it is still mathematically unproven in three dimensions [101].

one can define a temperature scale,

$$T_n = \frac{\hbar^2}{2mk_B}(3\pi^2 n)^{2/3} \,, \tag{1.47}$$

which is exactly the same definition as the Fermi temperature $T_n = T_F$.
Quantum effects will occur whenever $T/T_n \lesssim 1$. At high temperature (or low density), the occupation number of each energy state (labelled by λ) is small ($\ll 1$) and can be described by a Boltzmann distribution

$$N_\lambda(\beta = 1/k_BT, \mu) = \mathrm{e}^{-\beta(\epsilon_\lambda - \mu)} \,, \tag{1.48}$$

where μ is the chemical potential. This leads to the the well-known equation of state

$$n\lambda_{th}^3 = \mathrm{e}^{\beta\mu} \,. \tag{1.49}$$

On the contrary, at low temperature, the quantum nature of the particles and in particular their exchange symmetry cannot be neglected.

Identical bosons

For identical bosons, we have

$$N_{\lambda,b}(\beta, \mu_b) = \frac{1}{\mathrm{e}^{\beta(\epsilon_\lambda - \mu_b)} - 1} \,, \tag{1.50}$$

with the constraint $\mu_b \leq \underset{\lambda}{\mathrm{Min}}[\epsilon_\lambda]$ (set to 0 in the following) for $N_{\lambda,b}$ to be always positive. For a 3D-uniform system, N_b bosons in a volume V, by assuming that all the states are weakly populated we have the equation of state

$$n_b\lambda_{th}^3 = Li_{3/2}(\mathrm{e}^{\beta\mu}) \,. \tag{1.51}$$

The equation predicts an upper bound for the phase-space density and is reached when $\mu = 0$ and all excited states are fully occupied. However, in this limit, the occupation number of the ground state is diverging and can be macroscopically populated. Hence, any additional particle will accumulate in the fundamental state leading to the famous Bose-Einstein condensation at low temperature/high density [11]. This occurs below the transition temperature given by

$$T_{c,b} = \frac{1}{(Li_{3/2}(1))^{2/3}} \frac{2\pi\hbar^2}{m_b k_B} \left(\frac{N_b}{V}\right)^{2/3} \simeq 0.69\, T_n \,, \tag{1.52}$$

The ground state occupation number N_c reads

$$N_c = N_b \left(1 - \left(\frac{T}{T_c}\right)^{3/2}\right) . \tag{1.53}$$

This textbook scenario for condensation was actually verified recently using ^{87}Rb atoms in a quasi uniform 3D potential [39].

---

[11] The occurence of Bose-Einstein condensation depends on the trap geometry and dimensionality. For a uniform system, it occurs in 3D at finite temperature and in 2D at $T = 0$ but not in 1D.

Identical fermions

For identical fermions, we have instead

$$N_{\lambda,f}(\beta,\mu) = \frac{1}{\mathrm{e}^{\beta(\epsilon_\lambda-\mu)}+1} , \tag{1.54}$$

and by definition it can only take values between 0 and 1. There is no phase transition at low temperature, but a smooth evolution toward a Fermi sea, where all low-energy states are occupied until there is no particle left to place.
At $T = 0$, the chemical potential is equal to the Fermi energy

$$\mu_f = E_f = k_B T_F , \tag{1.55}$$

and all states below E_f are occupied, while the others are empty. And finally, for $T \neq 0$ we have the equation of state

$$n_f \lambda_{th}^3 = -Li_{3/2}(-\mathrm{e}^{\beta\mu}) . \tag{1.56}$$

The uniform ideal Fermi gas was also recently studied experimentally in [40]. Using spin polarized ^{6}Li atoms in a uniform trap, they directly observed the appearance of a Fermi surface and the saturation of low-energy states at low temperature.

1.3.2 Interacting bosons

If we now include interactions, we have a new length-scale in our toolbox, the scattering length a [12]. A new dimension can be explored in the phase diagram and can be parametrized by na^3 or equivalently $1/k_F a$ where k_F is the Fermi wave-vector $k_F = (3\pi^2 n)^{1/3}$.

Mean-Field regime

For $na^3 \ll 1$ and $T \ll T_{c,b}$, interactions can be treated in the mean field approximation and atoms condense in the same macroscopic state. Contrarily to the non-interacting case, the condensate wavefunction $\phi(\mathbf{r})$ is density dependent and is described by the celebrated Gross-Pitaevskii equation:

$$\left(-\frac{\hbar^2}{2m}\nabla^2 + V(\mathbf{r}) + \frac{4\pi\hbar^2 a}{m} n(\mathbf{r})\right)\phi(\mathbf{r}) = \mu\phi(\mathbf{r}) , \tag{1.57}$$

where V is the trapping potential and $n = N|\phi|^2$.
For a uniform system, the chemical potential μ is now shifted by the interactions

$$\mu = gn . \tag{1.58}$$

where $g = 4\pi\hbar^2 a/m$.
The total energy density is then

$$\epsilon = \frac{1}{2} g n^2 . \tag{1.59}$$

The condensate is thus mechanically unstable if $a < 0$, since its energy decreases with increasing density. Along with its time dependent version (see chapter 4) the Gross-Pitaevskii equation sucessfully described all the results of early experiments on Bose-Einstein condensates, such as the density profiles of the cloud [102, 103] or the properties of vortices in rotating condensates [55, 56, 57].

---

[12] And of course, for large scattering length, we have R_t which comes into play.

Beyond Mean-Field corrections

For increasing interactions, quantum fluctuations of the low-energy Bogoliubov modes start depleting the condensate[13]. The associated corrections to the zero-temperature equations of state reads

$$\mu = gn\left(1+\frac{32}{3\sqrt{\pi}}\sqrt{na^3}+4(4\pi-3\sqrt{3})(\ln(na^3)+D)na^3+...\right)\ , \tag{1.60}$$

where the first term is the mean field term, the second term was first calculated by Lee, Huang, and Yang (LHY) in the 50's [104] and the next terms were calculated later on [105]. The LHY correction was quantitatively checked in several experiments [106, 107, 108]. The constant D was shown to be non-universal and to depend log-periodically on the three-body parameter R_t and is thus the first signature of emerging Efimov physics when increasing interactions[14]. This chemical potential corresponds to the following energy density

$$\epsilon = \frac{1}{2}gn^2\left(1+\frac{128}{15\sqrt{\pi}}\sqrt{na^3}+\frac{8}{3}(4\pi-3\sqrt{3})\left(\ln(na^3)+D-\frac{1}{3}\right)na^3+...\right)\ . \tag{1.61}$$

The unitary Bose gas

The unitary case ($a=\infty$) is a paradigmatic example of strongly correlated bosonic systems, and still represents an important theoretical as well as experimental challenge in cold atom systems. The stability and the precise nature of the degenerate unitary Bose gas is still an open theoretical problem and under intense investigation, e.g. for recent results see [109, 110, 111, 112].

By dimensional analysis, at unitarity and zero temperature, since the only length scales remaining are the density n and the three-body parameter R_t, we expect the equation of state to be of the form

$$\mu = \xi(n^{1/3}R_t)E_F = \xi(n^{1/3}R_t)\frac{\hbar^2}{2m}(3\pi^2 n)^{2/3}\ , \tag{1.62}$$

where ξ is a dimensionless log-periodic function for which only theoretical upper-bound or estimates are available [113, 114]. Up to some numerical function, we recognize here the equation of state of an ideal Fermi gas, all the effects of interactions are encapsulated in ξ. However, this "simple" picture of the degenerate unitary Bose gas is most probably strongly modified by the presence of resonant three-body recombination processes. At high temperatures, the unitary problem becomes tractable, rigorous approaches and exact results are available and some of them will be presented in chapter 7.

1.3.3 Interacting fermions: The BEC-BCS crossover

We now turn to the case of a balanced gas of fermions, in which the two spin-state are equally populated. Contrarily to the Bose gas, the interacting Fermi gas is stable for large values of the scattering length, positive and negative. At $T=0$, fermions of opposite

---

[13] Indeed, even at $T=0$, an interacting Bose gas is not fully condensed, to leading order the non-condensed fraction scales like $\sqrt{na^3}$.

[14] It has also an imaginary part to account for three-body recombinations toward shallow two-body bound states [92].

spins will pair up leading to the superfluidity of the ensemble. However, upon changing $1/k_F a$ over the range from $-\infty$ to $+\infty$, the nature of the pairing changes dramatically from a weak coupling BCS-type to molecular binding. Thus by tuning the interactions, the state of the fermionic gas interpolate between a molecular BEC and a BCS superfluid. In between, it crosses the unitary limit where the scattering length drops out and the properties of the gas become scale invariant. This realises the so-called BEC-BCS crossover proposed early by Leggett [115], Nozières and Schmitt-Rink [116] and confirmed by several recent theoretical approches [34], a fixed-node Monte-Carlo simulation [117] and experiments [118, 119]. In addition, the equation of state of the unitary Fermi gas at finite temperature is precisely known thanks to several experiments [120, 121].

BCS superfluid

In the regime of small negative scattering lengths $1/k_F a \to -\infty$, the fermions are weakly attracted to each-other and will form an ensemble of phase-coherent Cooper pairs. However, the energy contribution of the BCS pairing in the superfluid phase $\sim \Delta^2/E_f$ where $\Delta \sim \mathrm{e}^{-\pi/2k_F|a|}$ is the pairing gap, is exponentially small. Hence, the ground state energy of the BCS-superfluid is mainly given by

$$\epsilon = \frac{3}{5} n E_F \left(1 + \frac{10}{9\pi} k_F a + \frac{4(11 - 2\ln(2))}{21\pi^2} (k_F a)^2 + ...\right) , \tag{1.63}$$

where the first term is the energy of the ideal Fermi gas, the second is a mean-field shift and the next term was obtained by Galitskii, Lee and Yang in the 50's, in the context of repulsive hard-sphere fermions [122, 123]. The generalization of this expansion to attractive interactions was shown recently in [124].

Molecular BEC

In the regime of small positive scattering lengths, opposite-spin fermions are strongly attracted to each other and form tightly bound dimers of size $\sim a$ and binding energy $-\hbar^2/ma^2$. The dimers are composite bosons that condense at low temperature and can be described by a Gross-Pitaevskii equation for small scattering lengths. Consequently, the ground state energy reads

$$\epsilon = -\frac{\hbar^2}{ma^2} n_d + \frac{1}{2} g_d n_d^2 \left(1 + \frac{128}{15\sqrt{\pi}} \sqrt{n_d (c_d a)^3} + ...\right) , \tag{1.64}$$

where $n_d = n/2$ is the dimer density, $g_d = 2\pi\hbar^2 c_d a/m$ and $c_d a \simeq 0.6a$ is the dimer-dimer scattering length [77]. The first term is the binding energy density followed by the mean-field term and the LHY corrections [125].

Unitary Fermi gas

In the unitary limit, the scattering length drops out as a scaling parameter and we retrieve relations that are analog to the ideal Fermi gas. All the complexity of the interacting system is thus encapsulated in a few universal numerical constants. Indeed, the energy density can be expanded as

$$\epsilon = \frac{3}{5} n E_f (\xi - \frac{\zeta}{k_F a} + ...) . \tag{1.65}$$

The numerical constant ξ is the *Bertsch* parameter and was measured with high precision in [121], $\xi = 0.376(4)$. The other numerical constant ζ was extracted via the measurement of the equation of state in the crossover [118] and yields $\zeta = 0.93(5)$. A more precise measurement was done by performing a local Bragg-spectroscopy experiment and gives $\zeta = 0.87(3)$ [126]. The analytical or numerical calculation of those two parameters represent a challenging problem as they cannot be obtained by standard perturbative methods due to the lack of small parameters in the system. A review of the various theoretical and numerical approaches used for their calculation can be found in [34]. ζ is directly related to the unitary two-body contact C_2, a fundamental quantity that will be introduced in chapter 5. In chapter 8, we will exploit this relation to demonstrate a new method to measure ζ using few-body losses.

When varying the temperature, the unitary Fermi gas undergoes a superfluid to normal phase transition as observed in [120, 121]. The transition temperature was found to be $T_c \simeq 0.16T_F$. We will exploit this unusual large value to produce a fermionic superfluid by evaporating ^{6}Li atoms at resonance.

Chapter 2

Producing a dual Bose-Fermi superfluid

In this chapter, we describe the experimental apparatus that we use to produce a quantum degenerate mixture of Bose and Fermi gases. The current setup results from almost 20 years of continuous upgrading, repairing, and maintenance work starting from 1997. As the experiment is already described in great detail in the thesis of G. Ferrari [127], F. Schreck [128], L. Tarruel [129], S. Nascimbène [130], and I. Ferrier-Barbut [131] and no major changes were made in the past few years, we will provide here a short overview of the experiment and solely focus on the technical aspects which are useful for the rest of this mansucript.

2.1 General description

The general scheme of the setup is similar to many cold atom experiments. The overall idea is to cool a vapor of atoms down to quantum degeneracy via laser cooling and evaporative cooling. In our case, we use the two stable isotopes of lithium: the bosonic ^{7}Li and the fermionic ^{6}Li. A hot vapor beam ($500\,^\circ$C) is produced by heating lithium in an oven and letting the gas escape through a tube. The jet is slowed down by a Zeeman slower. The atoms are afterwards captured and further cooled ($\sim$ mK) in a magneto-optical trap (MOT) in the glass cell, see Fig. 2.1. Once the MOT is fully loaded (40 s), we elevate magnetically the atoms to an appendage of the glass cell. At this stage, the atoms are trapped in a strongly confining magnetic trap and sympathetic cooling is applied: The ^{6}Li atoms are cooled by thermal contact with evaporating ^{7}Li atoms. This cooling step ($\sim\ 50\,\mu$K) allows us to load efficiently the atoms in an optical dipole trap. Finally, we apply a second evaporative cooling step at high magnetic field in order to exploit a broad ^{6}Li Feshbach resonance. This time, ^{7}Li is sympathetically cooled by ^{6}Li. At the end of the evaporation ramp we reach a typical temperature of 100 nK and both ^{6}Li and ^{7}Li clouds are in the quantum degenerate regime.

2.2 The lithium atom

2.2.1 Atomic structure

Lithium is the lightest alkali element. A single electron occupies the outer shell and its atomic structure is thus quite simple. A schematic representation of the ground state and first excited states level structure for both isotopes is shown in Fig. 2.2. The Li ground

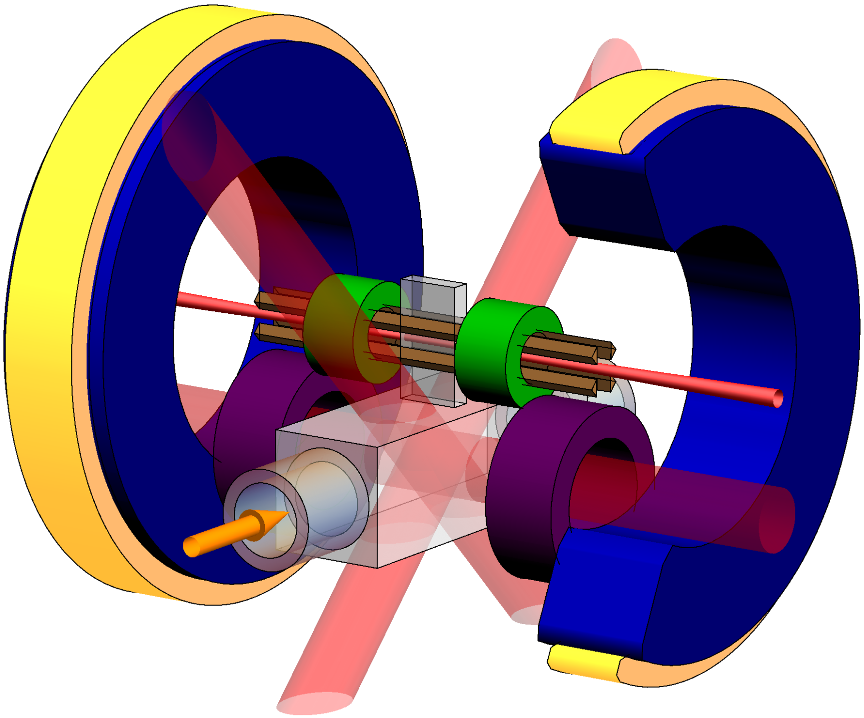

Figure 2.1: Schematic representation of the main parts of the experiment in the glass cell region. The yellow arrow indicates the atomic jet coming from the oven and the Zeeman slower assembly. The purple coils (MOT coils) and the three pairs of beams (large red beams) realize the magneto-optical trap. In the upper part of the cell, the appendage, atoms are first trapped in a Ioffe-Pritchard trap, created by the four Ioffe bars (brown bars), the pinch curve coils (green) and the Feshbach coils (blue). The final trap is composed of an optical dipole trap (red beam centered on the appendage) and a magnetic confinement provided mainly by the pinch-curve coils. The large bias field needed to go to the 832 G Feshbach resonance is provided by the Feshbach coils (blue). The offset coils (yellow) allow for rapid change of the bias field.

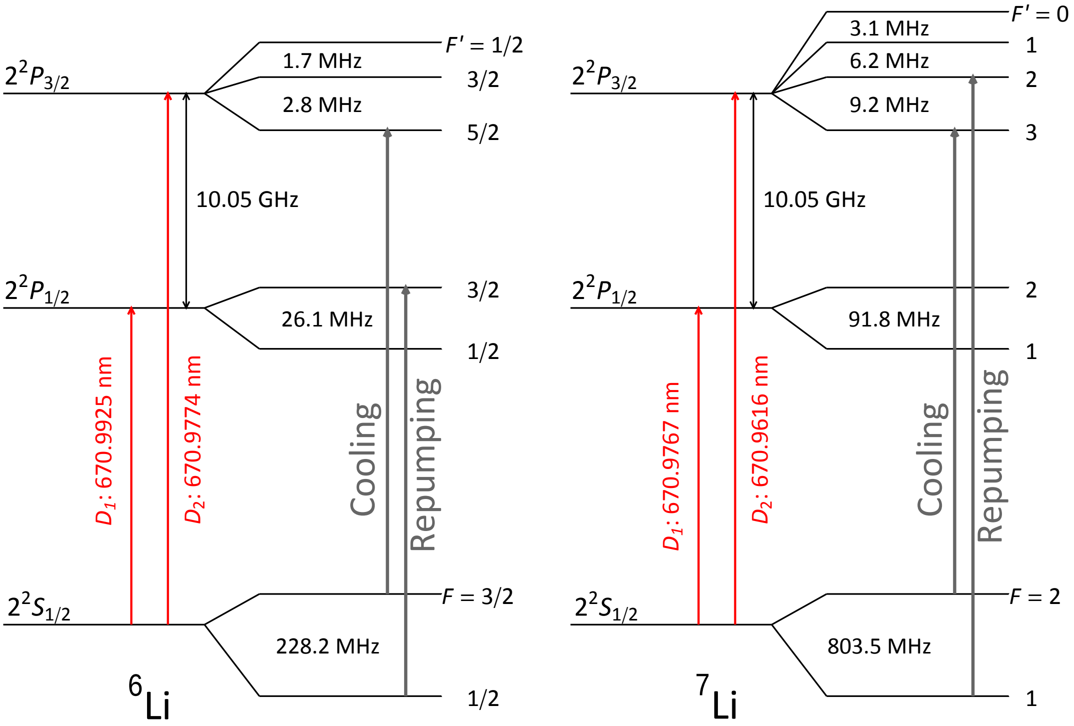

Figure 2.2: Energy level structure of the two Lithium isotopes, ^{6}Li and ^{7}Li. The transitions used for cooling and repumping for the MOT and the Zeeman slower are indicated in grey.

state is of $2s$ nature, while the first excited states is of kind $2p$. The splitting between the s and p states of the outer shell is large for alkali atoms and the associated transition (called the "D-line") lies in the visible and near infrared region. For lithium the $2s \to 2p$ transition is in the visible red spectrum, $\lambda_{\mathrm{Li}} = 671\,\mathrm{nm}$. The degeneracy between the $2^2P_{1/2}$ and $2^2P_{3/2}$ states is lifted by the spin-orbit coupling and leads to a fine-structure splitting of $\sim 10.05\,\mathrm{GHz}$. Hence, the D-line splits into two subfeatures: the D_1 and D_2 lines associated with the $2^2S_{1/2} \to 2^2P_{1/2}$ and $2^2S_{1/2} \to 2^2P_{3/2}$ transition respectively. Incidentally, the isotopic shift for $2s \to 2p$ transition is also equal to $\sim 10.05\,\mathrm{GHz}$ so that the D_1 line of ^{7}Li is extremely close to the D_2 line of ^{6}Li. Hyperfine coupling splits the different atomic levels even further. However due to a natural linewidth of $\Gamma \sim 5.9\,\mathrm{MHz}$, the hyperfine states of the $2^2P_{3/2}$ manifold cannot be completely resolved, see Fig. 2.2.

In Fig. 2.3, we show the magnetic field dependence of the energy levels of the $2^2S_{1/2}$ manifolds for both isotopes. In the following, we will label the associated states $|i_s\rangle$ with $i = 1, 2, ...$ starting from the lowest energy state at high field and the index s refers to the isotope ($s = \mathrm{b}$ for ^{7}Li and $s = \mathrm{f}$ for ^{6}Li). Since we will use the states $|1_\mathrm{f}\rangle$ and $|2_\mathrm{f}\rangle$ to produce a strongly interacting Fermi gas, they can be seen as the two states of a two-spin component Fermi gas, hence we will also use the common notation: $|\uparrow\rangle = |2_\mathrm{f}\rangle$ and $|\downarrow\rangle = |1_\mathrm{f}\rangle$.

2.2.2 Feshbach resonances

Lithium is characterized by a large number of Feshbach resonances that can be exploited to produce and study strongly interacting ensembles. In Fig. 2.4, we show the different resonances relevant for the different experiments discussed in this thesis. We use the large Feshbach resonance between the $|1_\mathrm{f}\rangle$ and $|2_\mathrm{f}\rangle$ states at 832.18 G [132] to produce a Fermi

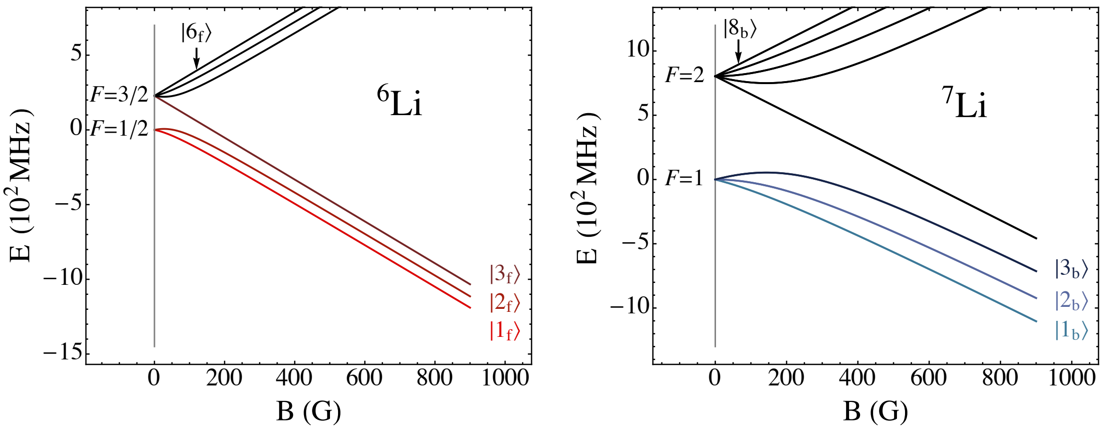

Figure 2.3: Magnetic field dependence of the energy levels of the $2^2S_{1/2}$ manifold of ^{6}Li and ^{7}Li.

superfluid. The state $|1_\mathrm{b}\rangle$ possesses a borad Feshbach resonance at 738.2 G which was previously used by our team to study the unitary Bose gas [36]. This state cannot be used to produce a BEC near the fermions Feshbach resonance, since it has a negative scattering length in the mentioned magnetic field region. In order to reach Bose condensation and superfluidity for the ^{7}Li cloud, we use the state $|2_\mathrm{b}\rangle$ which has mostly a positive scattering length in the region of the fermions Feshbach resonance. However, this state features two resonances, a narrow one at 845.5 G and a broad one at 893 G [74], which deteriorate the stability of the mixture in their vicinity. The scattering length between bosons and fermions is featureless at high magnetic fields and equals to $40.8\,a_0$ and is independent of the discussed spin states. This small scattering length value ensures that the two clouds are weakly coupled: Phase separation is only expected to occur for vanishing boson-boson scattering length, which in practice should happen (at low temperature) for magnetic fields lower than 720 G or in the vicinity of the zero-crossing near 845 G.

2.3 Laser system

Our laser system follows the MOPA (master-oscillator - power-amplifier) scheme. We use master lasers for frequency references and a series of injection-locked slave diodes and tapered amplifiers to amplify the total optical output power. We work with high-power laser diodes (Hitachi HL6545MG), with a maximal output power of 120 mW. At room temperature, the spectrum is centered around 660 nm, and the diodes need to be heated up to $70°$C to be able to reach lithium D-lines at ~ 671 nm. The diodes are thus mounted inside thermally isolated boxes and need to be regularly replaced due to their reduced lifetime.

We use external cavities in Littrow configuration for the master laser in order to stabilize their frequencies and reduce the modes linewidth. They are locked using saturated-absorption spectroscopy on the D_1 and D_2 lines of ^{6}Li and the D_2 line of ^{7}Li. We generate the different frequencies required for the experiment using several acousto-optic modulators. Optical power amplification is done by injection locking a dozen of slave diodes and using two tapered amplifiers[1]. All the different optical stages are decoupled from each

---

[1] The tapered amplifiers (TA) provide a larger power amplification than diodes (up to 500 mW), however

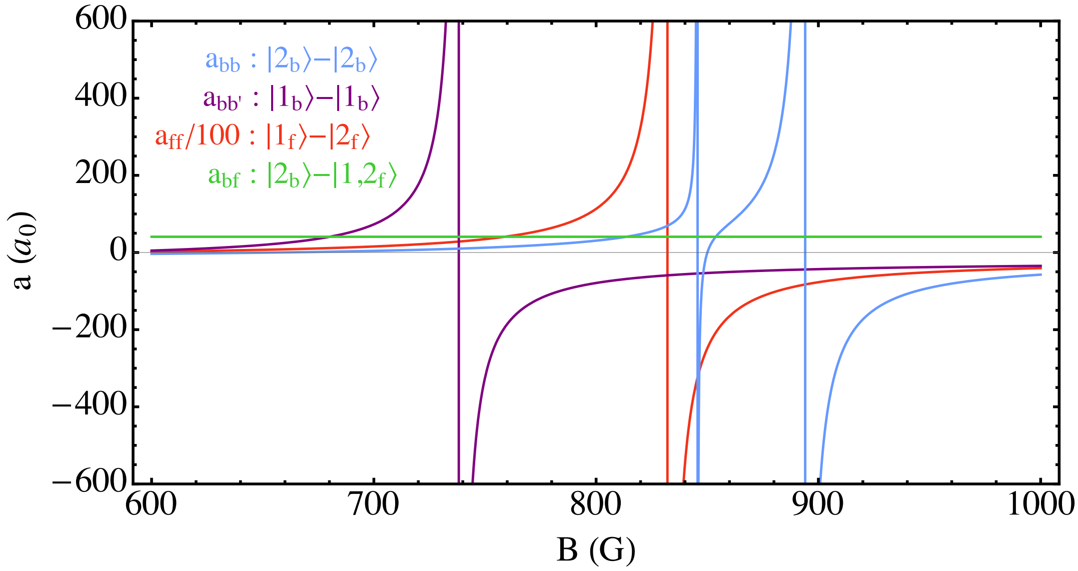

Figure 2.4: Magnetic field dependence for the different scattering lengths involved in our system.

other by means of optical fibers. This results in an optical power loss of 20-50% after each fiber, but minimizes the consequences of alignment drifts and therefore realignment work. The locking of the different diodes is monitored using three Fabry-Perot cavities. The first one is used to check the locking of the master diodes. The two others are for the locking of the MOT and Zeeman slower beams and also provide a useful reference for the beams alignment.

2.4 Loading the dual magneto-optical trap

2.4.1 The atomic beam source

The atomic beam is produced by heating a reservoir containing several grams of lithium (with natural isotopic abundance). The reservoir is connected to the rest of the vacuum chamber via a small tube that collimates the jet of atoms. The bottom of the reservoir is heated up to 400°C, the entrance of the collimation tube to 510 °C and its end to 190 °C. In this configuration, lithium is liquid at the bottom of the reservoir and a sufficient atomic flux leaves the oven. In principle, lithium cannot solidify in the tube and the temperature gradient allows lithium droplets to get back to the reservoir thanks to a temperature dependent surface tension. From time to time, the tube gets clogged and further heating (up to 600 °C) of the tube allows us to evaporate the undesired liquid. In order to guarantee an ultra-high vacuum in the main chamber, the atomic beam goes through two differential pumping stages before reaching the Zeeman slower, see Fig. 2.5.

---

the only 671 nm chips available on the market have an output mode which is highly non-gaussian and their output power tends to decrease rapidly with time (down to $250-300$ mW). Their replacement takes far more time than for diodes, as the beam shaping optical stage has to be redone entirely each time.

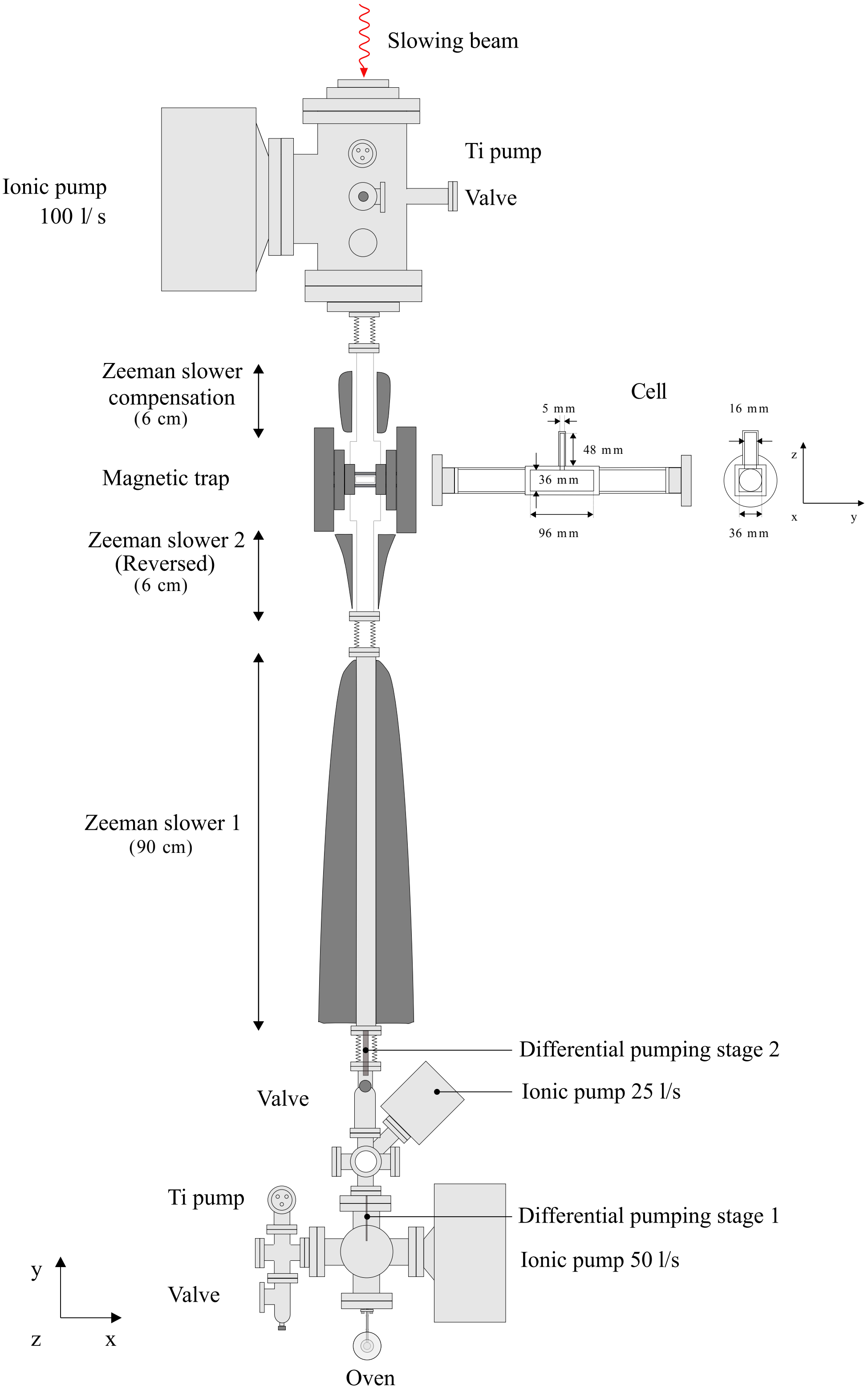

Figure 2.5: Overview of the vacuum system

2.4.2 The Zeeman slower

The oven produces a jet of atoms with a mean velocity of $1700\,\mathrm{m.s^{-1}}$. The MOT will only capture atoms with velocities less than the capture velocity $\sim 50\,\mathrm{m.s^{-1}}$. Therefore, we use a Zeeman slower which is a specific combination of counter-propagating bi-chromatic beam and a designed magnetic field in order to reduce the average atomic velocity. After each photon absorption event, the atom gets decelerated and quickly moves out of resonance due to the Doppler effect. This effect is compensated by the spatially-dependent magnetic field along the trajectory of the atoms provided by the coils. Indeed, the energy levels of the atoms are shifted by the Zeeman effect and the magnetic field is finely tailored so that the Zeeman shift constantly compensates the Doppler shift. Our Zeeman slower is in a spin-flip configuration consisting of two coils with opposite sign current, see Fig. 2.5, so that in between the two the magnetic field becomes zero and reversed, which avoids to have resonant light with the cold trapped atoms. The magnetic field between both ends goes from 800 G to -200 G and the Zeeman slower has a capture velocity of about $1100\,\mathrm{m.s^{-1}}$ [129].

Two laser beams are used to slow down ^{6}Li and ^{7}Li atoms (called principal beams). They are tuned to the $D_2 : F = 3/2,\, m_F = 3/2 \to F' = 5/2,\, m_F = 5/2$ and $D_2 : F = 2,\, m_F = 2 \to F' = 3,\, m_F = 3$ transitions respectively and shifted by -400 MHz to compensate the Doppler effect at the magnetic field zero crossing ($v \simeq 250\,\mathrm{m.s^{-1}}$). The ^{6}Li principal beam slightly deteriorates the slowing of ^{7}Li due to the ^{7}Li-D_1 ^{6}Li-D_2 coincidence, which finally forces a trade-off between the ^{6}Li and ^{7}Li flux. Two repumper beams are also necessary for the zero crossing region for the two following reasons: First, due to the narrow hyperfine structure of the $2^2P_{3/2}$ manifold, the open transitions $D_2 : F = 3/2 \to F' = 3/2$ and $D_2 : F = 2 \to F' = 2$ are excited and the atoms can fall in the $2^2S_{1/2}$ $F = 1/2$ and $F = 1$ states. Second, there is no adiabatic following near the zero crossing and atoms can flip to the "wrong" $m_{F'}$ states. We use the transitions $D_1 : F = 1/2 \to F' = 3/2$ and $D_2 : F = 1 \to F' = 2$ for ^{6}Li and ^{7}Li respectively, also shifted by -400 MHz in order to repump these depolarized atoms.

2.4.3 Magneto-Optical trap

The next step is to trap the slow atoms of the beam and further cool them down in a magneto-optical trap (MOT). It consists of three pairs of circularly polarized counter-propagating laser beams as depicted in Fig. 2.1 and a magnetic field gradient provided by one pair of coils. As a result, the atoms feel a combination of restoring and friction forces that trap them in the vicinity of the zero magnetic field region.

We use the $D_2 : F = 3/2 \to F' = 5/2$ and $D_2 : F = 2 \to F' = 3$ lines as cooling transitions for the ^{6}Li and ^{7}Li MOT respectively, similarly to the zeeman slower. We also need strong repumping beams to avoid loosing atoms that fall in the $2^2S_{1/2}$ $F = 1/2$ and $F = 1$ states. For this purpose we utilize the lines $D_1 : F = 1/2 \to F' = 3/2$ and $D_2 : F = 1 \to F' = 2$ of ^{6}Li and ^{7}Li respectively. The cooling beams are red-detuned by $\delta_{6\mathrm{P}} \simeq -6\Gamma$ for ^{6}Li and $\delta_{7\mathrm{P}} \simeq -7\Gamma$ for ^{7}Li, and the repumpers beams by $\delta_{6\mathrm{R}} \simeq -3\Gamma$ for ^{6}Li and $\delta_{7\mathrm{R}} \simeq -5.5\Gamma$ for ^{7}Li. Each beam has a $1/e^2$ diameter of 1.5cm and a peak intensity of about 2 mW/cm^2 (The on-resonance saturation intensity of the D_1 and D_2 lines are $I_{\mathrm{sat}} = 7.6$ mW/cm^2 and $I_{\mathrm{sat}} = 2.5$ mW/cm^2 respectively). The applied magnetic field gradient at the MOT is 25 G/cm.

In these conditions, we are able to load the dual-MOT in 40 s and it typically contains several 10^9 ^{7}Li atoms and 10^8 ^{6}Li atoms at a temperature of approximately 3 mK. In comparison, a single-isotope MOT can have twice as many atoms (by switching off the other MOT beams). In particular, the ^{6}Li cooling beams enhance the light-assisted inelastic collisions in the ^{7}Li MOT, and we tune its power to have a good balance between the two isotope numbers.

Once the dual-MOT is fully loaded, we perform a compressed-MOT phase. The cooling beams are brought closer to resonance ($\delta_{6\mathrm{P}} = -1.5\,\Gamma$ and $\delta_{7\mathrm{P}} = -5\,\Gamma$) and the repumping light intensities are ramped to zero in 8 ms. This results in all atoms being pumped in the lowest hyperfine manifold and a reduced temperature of $T \simeq 600\,\mu$K. We do not reach a temperature as low as the Doppler temperature $T_{\mathrm{D}} = \hbar\Gamma/2k_{\mathrm{B}} = 140\,\mu$K mainly because of the unresolved hyperfine structure of the $2^2P_{3/2}$ states and multiple photon scattering processes.

2.5 Magnetic trapping

2.5.1 Optical pumping

In order to trap magnetically the atoms, we perform an optical pumping step to transfer them into the the fully polarized states $|6_{\mathrm{f}}\rangle = |F = 3/2, m_F = 3/2\rangle$ and $|8_{\mathrm{b}}\rangle = |F = 2, m_F = 2\rangle$ of the second lowest hyperfine manifold (see Fig. 2.3). These states are low field seeking states, i.e their energy increases with increasing magnetic field. In addition, the two states are stable with respect to spin-exchange collisions.

To perform the optical pumping, we turn off the CMOT and illuminate the atoms with a combination of two circularly polarized beams in presence of a weak magnetic field (10 G) during 300 μs. The first beam is tuned to the $D_2 : F = 1 \to F' = 2$ transition and pumps the ^{7}Li atoms in the $F = 2$ manifold. The second beam is tuned close to the $D_1 : F = 2 \to F' = 2$ and $D_2 : F = 1/2 \to F' = 3/2$ lines. It achieves both the hyperfine pumping for ^{6}Li $F = 1/2 \to F = 3/2$ and the Zeeman pumping for ^{7}Li, since $|8_{\mathrm{b}}\rangle$ is a dark state in our scheme.

2.5.2 Lower magnetic trap and transfer to the appendage

After the optical pumping, we quickly turn on a quadrupole trap (within 2 ms) using the MOT coils (resulting in a magnetic field gradient of 200 G.cm^{-1} at 300 A). The atoms not in states $|6_{\mathrm{f}}\rangle$ and $|8_{\mathrm{b}}\rangle$ are lost by spin-exchange collisions and/or expelled by the magnetic trap. The overall efficiency of the optical pumping and magnetic trapping loading is typically 50% for ^{7}Li atoms and 30% for ^{6}Li atoms.

Next, we transport the cloud in the appendage of the cell: We simultaneously ramp up the current in the Feshbach coils and ramp down the current in the MOT coils in 500 ms so that the magnetic trap center is progressively elevated to the appendage. The cloud is transported over 6 cm and during the transfer approximately 50% of the atoms are lost, mainly due to collisions with the walls of the appendage.

Atoms are then transferred from the quadrupole trap to a Ioffe-Pritchard trap [133]: A strong magnetic radial confinement is provided by four bars placed near the appendage, a pair of coils (the pinch-curve coils) create a curvature along the axial direction, and finally another pair of coils (Feshbach coils) create an adjustable bias field (and only a small curvature). This creates a cigar-shaped harmonic trap with a non-zero minimum which avoid Majorana losses [134].

2.5.3 Doppler Cooling

In the Ioffe trap, the cloud has an initial temperature of $T \simeq 3\,\mathrm{mK}$. The collisional cross-section is cancelled at momenta corresponding to a temperature of $6\,m\mathrm{K}$ and is still weak at 3 mK [128]. Hence, to start evaporative cooling with better conditions (i.e. a larger collisional rate) we perform an additional Doppler cooling on ^{7}Li atoms. We send on the cloud a circularly polarized light beam red-detuned to the transition $D_2 : F = 2, m_F = 2 \rightarrow F' = 3, m_{F'} = 3$ at the corresponding bias field felt by the atoms (500 G). The beam will solely cool the atoms lying at the center of the trap and in the axial direction. The anharmonicity of the trap and at some point the elastic collisions will lead to a thermalization of the cloud in all spatial directions. This cooling procedure is repeated twice, with a stronger confinement and a smaller detuning the second time. As a result, the cloud has a temperature of $300\,\mu$K, with a loss of 25% ^{7}Li atoms, and the collisional rate is increased by a factor of ~ 16.

2.5.4 RF evaporation

The last step performed in the Ioffe-Pritchard trap is a radio-frequency evaporation of the ^{7}Li atoms. Evaporative cooling consists in removing the hottest atoms of the cloud so that the mean energy per particle is reduced and the phase-space density is increased [135]. The evaporation cannot be done with ^{6}Li atoms as they can neither collide via s-wave channel since they are spin-polarized in the $|6_\mathrm{f}\rangle$ state, nor via higher partial wave channels as they are already inhibited by the low temperature of the sample (The p-wave threshold for Li is $\sim$mK). ^{6}Li atoms are instead cooled by thermal contact with the ^{7}Li atoms that can be efficiently evaporated.

Here, the Ioffe-Pritchard is highly compressed and the bias field is maintained to a low value (5 G). A radio-frequency field blue-detuned with respect to the transition $|1_\mathrm{b}\rangle - |8_\mathrm{b}\rangle$ (803.5 MHz at $B = 0$) is sent on the cloud. As a result energetic ^{7}Li atoms are transferred to the high-field seeking state $|1_\mathrm{b}\rangle$ and expelled from the trap. Thanks to the smaller isotope hyperfine splitting of the $2^2S_{3/2}$ state of ^{6}Li (228.2 MHz), the RF-knife essentially only affect ^{7}Li atoms.

The RF-knife frequency is ramped from 1050 MHz down to 840 MHz in 22s. Typical final numbers are $N_6 = 2.5 \times 10^6$ and $N_7 = 0.5 \times 10^6$ at a temperature $T = 10\,\mu$K which correspond to a peak phase-space density of $\sim 10^{-1}$ for ^{6}Li atoms. These numbers strongly depends on the initial numbers of both species and in practice we adjust them by varying the population balance between the two MOT clouds.

2.6 Hybrid magnetic-optical trap

The Ioffe-Pritchard trap does not allow for an independent adjustment of the magnetic bias field and trap confinement. Hence, in order to profit from the 832 G Feshbach resonance of ^{6}Li where we can perform a second evaporation to quantum degeneracy, we load the atoms in a hybrid-magnetic optical trap resulting from the combination of a focussed 1073 nm beam and a axial magnetic curvature + bias field created by the pinch-curve and the Feshbach coils.

2.6.1 Trap description

The dominant effect of a far-detuned light beam on an atom is a shift of its energy levels proportional to the beam intensity (known as light shift or Stark shift) [136]. If the beam is red-detuned, the shift is negative for atoms in their ground state and they will be attracted by maxima of intensity. For lithium atoms, if the fine structure splitting of the 2^2P state is negligible with respect to the laser detuning, the dipole potential created by a beam is well described by the equation :

$$U_{\rm dip}(\mathbf{r}) = \frac{3\pi c^2}{2\omega_0^3}\frac{\Gamma}{\Delta}I(\mathbf{r}), \tag{2.1}$$

where c is the speed of light in the vacuum, ω_0 is the bare frequency of the atom's transition with linewidth Γ, $\Delta = \omega_{\rm L} - \omega_0$ is the laser detuning and $I(\mathbf{r})$ is the intensity profile. For a gaussian TEM$_{00}$ mode we have the profile

$$I(\mathbf{r}) = \frac{2P}{\pi w(z)^2}{\rm e}^{-2r^2/w(z)^2}, \tag{2.2}$$

with P is the laser power and $w(z) = w_0\sqrt{1+(z/z_R)^2}$, where w_0 is the beam waist and $z_R = \pi w_0^2/\lambda$ is the Rayleigh length. In the vicinity of the beam focus, $r \ll w_0$ and $z \ll z_R$, the dipole potential is harmonic. For an atom of mass m it reads

$$U_{\rm dip} = -U_0 + \frac{1}{2}m(\omega_r^2 r^2 + \omega_z^2 z^2) \tag{2.3}$$

with $U_0 = 3c^2\Gamma P/\omega_0^3|\Delta|w_0^2$ the potential depth, and $\omega_r = \sqrt{4U_0/mw_0^2}$, $\omega_z = \omega_r\lambda/\sqrt{2}\pi w_0$ the radial and axial trap frequencies respectively. Hence, the trap and therefore the clouds are highly elongated in the axial direction as depicted in Fig. 2.6.

In the experiments described in chapter 3 and 8, the beam waist is $w_0 = 27(2)\ \mu$m and $w_0 = 36(3)\ \mu$m respectively. Typical frequencies at high power (7 W) are $\omega_r \simeq 2\pi\times 7$ kHz and $\omega_z \simeq 2\pi \times 40$ Hz .

To increase the axial confinement at low optical power, a magnetic curvature is added using the pinch-curve coils and the Feshbach coils. For low-field seeker states, a magnetic minimum is superimposed to the beam waist while for high-field seeker states we create a saddle point with a maximum in the axial direction. Thanks to this magnetic confinement, the trap is highly harmonic in the axial direction (see section 2.9.3). Typical axial frequency provided by the magnetic curvature is $\omega_z = 2\pi \times 20$ Hz. In first approximation, the two lithium isotopes see the same trapping potential so that their trapping frequencies differ by a factor $\sqrt{m_7/m_6} = \sqrt{7/6}$.

2.6.2 Trap loading

We load atoms initially in the Ioffe-Pritchard trap to the dipole trap at relatively high-power[2] (7 W). Thanks to similar aspect ratios, the transfer between the two traps can be done efficiently with solely 20% atom loss.

---

[2] We observe increasing losses in the dipole trap when loading at higher power (thus higher density), probably due to dipolar losses in the state $|8_{\rm b}\rangle$. The associated loss rate coefficient $L_2 = 1.05(10) \times 10^{-14}\,{\rm cm}^3/{\rm s}$ was measured in [137].

2.6.3 Mixture preparation

In order to exploit the Feshbach resonance at 832G and to have a stable mixture of Bose and Fermi superfluid, we need to transfer the atoms in the states $|1_{\rm f}\rangle = |F = 1/2, m_F = 1/2\rangle$ and $|2_{\rm f}\rangle = |F = 1/2, m_F = -1/2\rangle$ for ^{6}Li and in the states $|2_{\rm b}\rangle = |F = 1, m_F = 0\rangle$ for ^{7}Li, see Fig. 2.3.

This is done by doing several radio-frequency transfers using the adiabatic passage technique. Atoms are dressed by a strong radio-frequency field whose frequency is varied across the transition resonance between the two involved levels. For slow enough frequency sweep, the atoms follow adiabatically the dressed state to eventually end up being in the target level.

The technique is repeated for three times. First at low field to do two transfers: $|8_{\rm b}\rangle \to |1_{\rm b}\rangle = |F = 1, m_F = 1\rangle$ and $|6_{\rm f}\rangle \to |1_{\rm f}\rangle = |F = 1/2, m_F = 1/2\rangle$ using a fixed frequency RF radiation of $827\,$MHz and $240\,$MHz respectively and ramping the bias magnetic field from 13 G to 4 G in 50 ms. Then, before crossing the Feshbach resonance at 750 G of the $|1_{\rm b}\rangle$ state, we perform a third transfer $|1_{\rm b}\rangle \to |2_{\rm b}\rangle$ at 656 G with a RF radiation whose frequency is swept from $170.9\,$MHz to $170.7\,$MHz in $10\,$ms. The typical efficiency of those transfers is 90% and is limited by decoherence effects due to atoms collisions, trap inhomogeneities or field fluctuations. Remaining atoms in the initial states $|8_{\rm b}\rangle$ and $|6_{\rm f}\rangle$ are expelled by the magnetic curvature that is now trapping high-field seeker states. $|1_{\rm b}\rangle$ atoms are lost by three-body recombination when crossing the 738.2 G Feshbach resonance.

Finally, a $|1_{\rm f}\rangle - |2_{\rm f}\rangle$ mixture is prepared by a doing a RF transfer at 835 G, the RF is swept from 76.25 MHz to 76.3 MHz. By varying the RF power or the sweep velocity, we can adjust the spin mixture according to the Landau-Zener formula:

$$P_{\rm tr} = 1 - {\rm e}^{-2\pi\Omega^2/\dot{\omega}}, \tag{2.4}$$

where $P_{\rm tr}$ is the transition probability, Ω is the Rabi frequency of the RF radiation and $\dot{\omega} = d\omega/dt$ is the frequency sweep velocity. To obtain a 50/50 mixture we typically do a 5 ms sweep implying a Rabi frequency of $\Omega \simeq 2\pi \times 600\,$Hz.

2.6.4 Evaporation at 835 G

As soon as some ^{6}Li atoms are transferred in the $|2_{\rm f}\rangle$ state, evaporative cooling is engaged. The collision rate between opposite spin fermions is extremely large ($\sim 10\,$kHz) thanks to a unitary limited scattering cross-section. As we have $\gamma_{66} \gg \gamma_{67} > \gamma_{77}$, where γ_{ij} is the collision rate between particles of type i and j, ^{7}Li atoms are essentially sympathetically cooled by the evaporating ^{6}Li atoms. The initial atoms numbers are typically $N_6 = 2\times10^6$ and $N_7 = 3\times10^5$ at a temperature $T = 45\,\mu K$ and a trap depth $U_0 \simeq 180\,\mu K$ ($P = 7\,$W). The trap depth is lowered exponentially with time. For our coldest samples, we go as low as $U_0 = 1.5\,\mu$K ($P = 60\,$mW) in 3 s. After waiting 1 s at constant trap depth, both clouds are thermalized and final numbers are typically $N_6 = 3 \times 10^5$, $N_7 = 4 \times 10^4$ and the temperature is $T \simeq 80 - 100\,$nK: both clouds are quantum degenerate. We provide in section 2.8 several evidence that both clouds are actually superfluid and a frictionless counterflow between the two clouds will be demonstrated in chapter 3. The mixture shows a good stability at low temperature with a typical lifetime of $\sim 5-10\,$s and will be studied in detail in chapter 8.

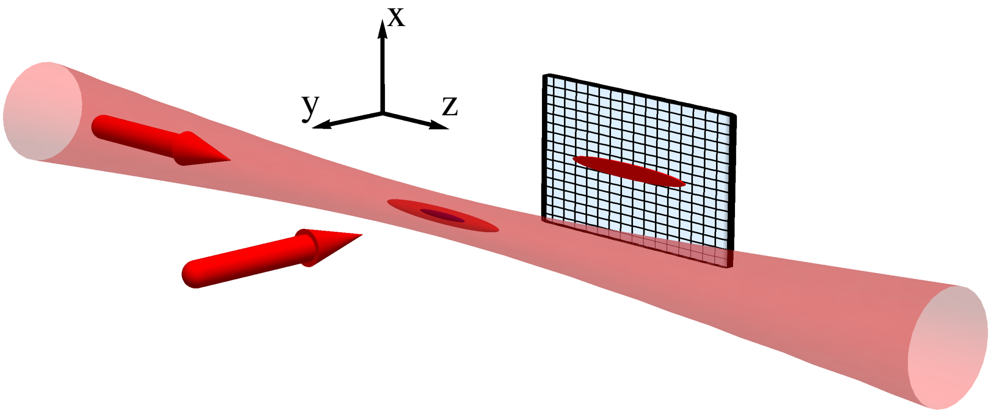

Figure 2.6: Schematic representation of the clouds trapped in the optical dipole trap. The arrows show the two different imaging directions. After passing through the clouds, and several optical components, the imaging light is collected on a camera shown as a grid.

2.7 Imaging

2.7.1 Absorption imaging

All the observables associated with the atomic clouds such as the temperature and atom numbers are obtained by imaging the atoms either in-situ (i.e when trapped) or after a time-of-flight expansion. Imaging of the atomic clouds is done by absorption imaging. A resonant probe is sent along a given direction (in the following examples the y-axis) on the atomic cloud that will partly absorb it. The intensity profile $I(x,z)$ of the probe after passing through the cloud is recorded on a camera, see Fig. 2.6. In order to cancel the inherent spatial inhomogeneity of the probe beam, a second image $I_0(x,z)$ is taken without the atomic cloud. For a probe with small intensity $I \ll I_{\text{sat}}$, according to the Beer-Lambert law the two intensity profiles are related by the formula

$$I(x,z) = I_0(x,z)\mathrm{e}^{-\sigma \int dyn(x,y,z)}, \tag{2.5}$$

where σ is the absorption cross-section and n the cloud's atomic density. Hence, the ratio of the two intensity profiles gives a direct access to the simply integrated density profile of the cloud.

For a resonant light beam with a narrow linewidth, the absorption cross-section reads $\sigma = 6\pi(\lambda/2\pi)^2C$ where C is the Clebsh-Gordan coefficient associated to the absorption transition and light polarization. However, we cannot rely on this theoretical value to count our atom numbers, inasmuch as several experimental imperfections can reduce drastically this cross-section. In particular, the imaging light linewidth is comparable to the atomic natural linewidth. Therefore, the absorption cross-section is measured experimentally, see section 2.9.3.

2.7.2 Imaging directions

In the appendage, the clouds can be imaged along two directions: Along the axial direction (the z-axis), parallel to the magnetic field direction and along a radial direction with

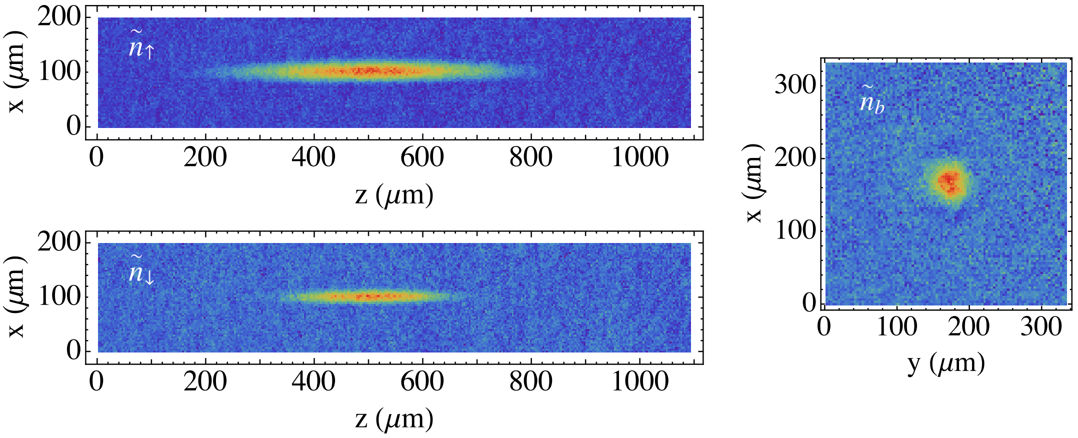

Figure 2.7: Examples of simply integrated density profiles $\tilde{n}$ obtained by absorption imaging. Here, the images are taken at 817 G after a full evaporation at 835 G. The two spin states of the fermions are imaged along the y-direction after a short time-of-flight expansion of $500\,\mu$s. The bosons are imaged along the z-direction after a longer time-of-flight expansion of 4.5 ms.

a σ^+ polarization and π polarization respectively in order to address the transitions listed in next section.

In the axial direction, the optical resolution is about $10\,\mu$m and cannot be used for in-situ imaging (the typical radial sizes for the clouds is 5-10 μm). However, thanks to the integration along the long axis of the clouds, this direction allows for the detection of small atoms numbers even after a long time-of-flight expansion.

In the radial direction, the resolution is $\simeq\ 5\,\mu$m. Again, we cannot resolve the in-situ spatial distribution of the clouds along the radial direction. By integrating over the remaining transverse direction, we retrieve accurate (doubly integrated) density profiles $\bar{n}(z) = \int dxdyn(x, y, z)$.

2.7.3 Imaging transitions

At low bias field (i.e to image atoms early in the sequence) we use the transitions

$$D_2: \quad F = 3/2 \ \rightarrow F' = 5/2, \tag{2.6}$$

$$D_2: \quad F = 2 \ \rightarrow F' = 3, \tag{2.7}$$

to image ^{6}Li atoms and ^{7}Li atoms respectively.
At high field, we use the closed transitions

$$D_2: \quad m_J = -1/2, m_I = 1 \quad \rightarrow m_{J'} = -3/2, m_{I'} = 0, \tag{2.8}$$

$$D_2: \quad m_J = -1/2, m_I = 0 \quad \rightarrow m_{J'} = -3/2, m_{I'} = -1, \tag{2.9}$$

$$D_2: \quad m_{J'} = -1/2, m_{I'} = 1/2 \quad \rightarrow m_{J'} = -3/2, m_{I'} = -1/2, \tag{2.10}$$

to image the states $|1_\mathrm{f}\rangle$, $|2_\mathrm{f}\rangle$, and $|2_\mathrm{b}\rangle$ respectively.

2.7.4 Double and triple imaging sequences at high field

In order to have access to both boson and fermion density distributions, the clouds are imaged sequentially. For the counterflow measurements presented in chapter 3, we image

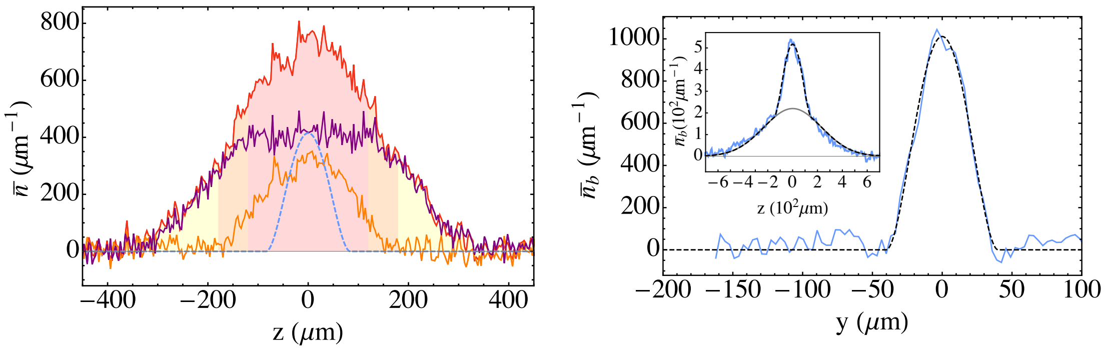

Figure 2.8: Examples of doubly integrated density profiles $\bar{n}$ corresponding to the images shown in Fig. 2.7 taken at 817 G after evaporation at 832 G. Left figure: quasi-in situ density profiles for the $|\uparrow\rangle$ (red line), $|\downarrow\rangle$ (orange line) states, and the difference (purple line). The plateau at the center of the difference profile (red region) indicates pairing between atoms with different spins, which corresponds to the superfluid region of the cloud. For smaller spin-imbalance, the superfluid core is larger. Right figure: Density profile of the bosons after time-of-flight (4.5ms) showing an almost pure Bose-Einstein condensate, the condensed fraction is superior to 80%, which corresponds to an upper-bound temperature of $120\,$nK. In the inset we show a typical in-situ boson density profile at higher temperature showing the bimodal signature of an emerging condensate. By fitting the thermal fraction by a gaussian we extract a temperature of $580(25)$ nK in agreement with a measured condensed fraction $N_{\mathrm{BEC}}/N_{\mathrm{b}} = 0.25(4)$.

the bosons and one state of the fermions in-situ along the radial direction using $50\,\mu$s imaging pulses separated by $10\,\mu$s. If we are interested in both fermionic spin states in situ density distribution we use a sequence of three imaging pulses. Both spin component of the fermionic gas are imaged in situ in the radial direction and the bosonic cloud after time of flight in the axial direction, see examples of images in Fig. 2.7. To avoid heating that can modify the density profiles, we use $10\,\mu$s pulses separated by $10\,\mu$s at low intensities $I/I_{\mathrm{sat}} = 0.06$ for the fermions. In any cases, reference images (providing I_0) are taken 20 ms later.

2.8 Evidence for superfluidity

By analyzing the density profiles obtained by absorption imaging such as the ones shown in Fig. 2.7, it is already possible to infer that both clouds are superfluid at the end of the evaporation.

2.8.1 Bose gas

Superfluidity in the Bose gas is signaled by the Bose-Einstein condensation which due to the interactions is described by a Thomas-Fermi profile. For a doubly integrated profile, it reads

$$\bar{n}_{\mathrm{BEC}}(z) = \bar{n}_0 \left(\mu_{\mathrm{b}} - \frac{1}{2} m_{\mathrm{b}} \omega_{z,\mathrm{b}}^2 z^2 \right)^2 , \tag{2.11}$$

where the central chemical potential reads

$$\mu_{\mathrm{b}} = \frac{\hbar\bar{\omega}_{\mathrm{b}}}{2}\left(15 N_{\mathrm{BEC}} a_{\mathrm{bb}}\sqrt{\frac{m_{\mathrm{b}}\bar{\omega}_{\mathrm{b}}}{\hbar}}\right)^{2/5}. \qquad (2.12)$$

with $\bar{\omega}_{\mathrm{b}} = (\omega_{z,\mathrm{b}}\omega_{r,\mathrm{b}}^2)^{1/3}$, a_{bb} the boson-boson scattering length, and N_{BEC} the number of condensed bosons. Hence, the cloud has an axial extent given by the Thomas-Fermi radius $R_{TF,z,\mathrm{b}} = 2\mu_{\mathrm{b}}/m_{\mathrm{b}}\omega_{z,\mathrm{b}}^2$ (and $R_{TF,r,\mathrm{b}} = R_{TF,z,\mathrm{b}}\omega_{z,\mathrm{b}}/\omega_{r,\mathrm{b}}$).

In Fig. 2.7, the bosons are imaged after a long time-of-flight expansion. Thanks to its hydrodynamic behavior, the BEC density distribution is modified by simple scaling factors and is thus described by a Thomas-Fermi profile with time dependent Thomas-Fermi radii. For a free expansion of duration t, the transverse radial Thomas Fermi radius of an elongated BEC reads [138]:

$$R_{TF,r,\mathrm{b}}(t) = R_{TF,r,\mathrm{b}}(0)\sqrt{1 + (\omega_{,r,\mathrm{b}}t)^2}. \qquad (2.13)$$

In our experiment, the expansion is done in the presence of a magnetic curvature, but its effect is negligible (few percents difference for a typical 5 ms time-of-flight). In Fig. 2.8, we show a doubly integrated profile of bosons after time-of-flight. We extract a radial Thomas-Fermi radius of $40\,\mu$m meaning an in-situ radius of $3\,\mu$m in the radial direction and $85\,\mu$m in the axial direction (see left panel of Fig. 2.8).

In terms of temperature, as there is no visible thermal fraction, we can only give an upper-bound for the cloud temperature. In a harmonic trap the condensed fraction $\rho = N_{BEC}/N_{\mathrm{b}}$ follows the equation

$$\rho = 1 - \left(\frac{T}{T_{c,\mathrm{b}}}\right)^3, \qquad (2.14)$$

where the transition temperature reads

$$k_B T_{c,\mathrm{b}} = \hbar\bar{\omega}_{\mathrm{b}}\left(\frac{N_{\mathrm{b}}}{\zeta(3)}\right)^{1/3}. \qquad (2.15)$$

Typically, the thermal fraction is no longer resolved for condensed fractions higher than $80\,\%$. Hence, we get a conservative upper bound temperature of 120 nK. At higher temperature, we can extract the temperature directly from the thermal fraction using a Gaussian fit (a polylog fit would give similar results). In the inset of Fig. 2.8, we show a Bose gas in situ density profile at intermediate temperature with a recognizable bimodal structure. By fitting the thermal wings we extract a temperature of $580(25)$ nK, and a condensed fraction of $0.27(4)\%$ in good agreement with the prediction of equation (2.14): $\rho = 0.30(4)$.

2.8.2 Fermi gas

Superfluidity of the strongly interacting Fermi gas can be inferred via several arguments. First, for a balanced unitary Fermi gas in a harmonic trap, the critical temperature was found to be $T_{c,\mathrm{f}} = 0.19\,T_{F,h}$ [139, 121] with $k_B T_{F,h} = E_{F,h} = \hbar\bar{\omega}_{\mathrm{f}}(3N_{\mathrm{f}})^{1/3}$ the Fermi temperature of the trapped Fermi gas. For typical fermion numbers $N_{\mathrm{f}} = 3\times10^5$ and trapping frequencies $\omega_{z,\mathrm{f}} = 18\,$Hz and $\omega_{r,\mathrm{f}} = 500\,$Hz, we get a transition temperature $T_{c,\mathrm{f}} = 150\,$nK which is above the typical upperbound temperature given by the condensate fraction of the Bose gas (120 nk).

Another evidence can be seen on the imbalanced Fermi gas such as in figs. 2.8. At low temperature, for small enough imbalance (i.e below the Clogston-Chandrasekhar limit [140, 141]), the cloud is composed of three different concentric layers (shown as three different colored regions in Fig. 2.8). At the core, the opposite spin fermions are paired and form a superfluid phase. Then, the second layer is a normal phase containing both spin states but with a strong imbalance, so that the minority atoms dressed by the majority form a gas of polarons. Finally, the outermost layer contains all the remaining majority atoms and forms an ideal Fermi gas. This structure can be directly seen on doubly integrated profiles thanks to the local density approximation. Indeed, under this assumption one can relate the local pressure P along the symmetry axis of the cloud to its doubly integrated density:

$$P(z, r = 0) = \frac{m\omega_r^2}{2\pi}\bar{n}(z). \tag{2.16}$$

Hence, using the Gibbs-Duhem identity $\partial P/\partial\mu = n$ we get the local density along the symmetry axis

$$n(z, r = 0) = -\frac{\omega_r^2}{\omega_z^2}\frac{1}{2\pi z}\frac{d\bar{n}}{dz} \tag{2.17}$$

In the superfluid core, the density of the two fermionic spin states are equal $n_\uparrow = n_\downarrow$ so that we get the following equation for the doubly integrated densities:

$$\frac{d(\bar{n}_\uparrow - \bar{n}_\downarrow)}{dz} = 0. \tag{2.18}$$

Therefore, full pairing of atoms in the core region is signaled by a plateau in the doubly integrated profiles. This is what is observed on the difference profile shown in Fig. 2.8. The superfluidity of paired atoms was demonstrated by observing vortices solely in the core region when the Fermi gas was put in rotation [59]. Furthermore, the observation of a well defined plateau implies that the temperature of the cloud is significantly below the transition temperature $T_{c,\mathrm{f}}$, as for intermediate temperature the superfluid can be slightly polarized [142]. Finally, the superfluid core size is given by the plateau length: in Fig. 2.8, the radius is $110\,\mu$m. For small imbalance, the radius is typically $300\,\mu$m. Finally, at unitarity and zero temperature, the balanced Fermi gas has a Thomas-Fermi profile:

$$\bar{n}_\mathrm{f}(z) = \bar{n}_{\mathrm{f},0}\left(\mu_\mathrm{f} - \frac{1}{2}m_\mathrm{f}\omega_{z,\mathrm{f}}^2 z^2\right)^{5/2}, \tag{2.19}$$

where the chemical potential reads $\mu_\mathrm{f} = \sqrt{\xi}E_{F,h}$.

2.9 Final trap calibrations

2.9.1 Magnetic field calibration

The precise knowledge of the magnetic field is essential for a fine tuning of the various different scattering lengths describing interactions in the system. As one of the Feshbach coils was replaced in 2015, we describe in this section its calibration at high-fieldt. We use the resonance frequency of the hyperfine transition $|1_\mathrm{b}\rangle \to |2_\mathrm{b}\rangle$ whose field dependence is known with great precision. At high field, the transition frequency is typically $175\,$MHz and has a field dependence of $\simeq\ 40\,$kHz/G. In practice, we measure transitions with a typical linewidth of $4\,$kHz, implying an upper bound for the magnetic field stability of $\sim$

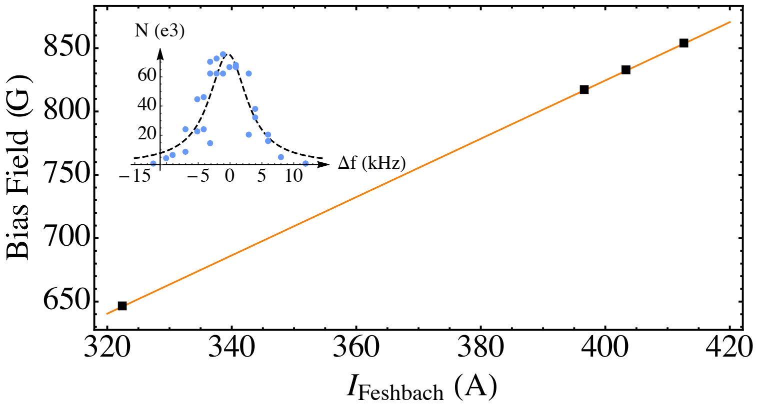

Figure 2.9: Bias field as a function of current in the Feshbach coils. The bias field is measured by looking at the radio-frequency resonance between the states $|1_{\mathrm{b}}\rangle$ and $|2_{\mathrm{b}}\rangle$ as shown in inset. A linear fit (orange line) to the different bias field measurements (black squares) gives a slope $B_{\text{Bias}}/I_{\text{Feshbach}} = 2.301(2)$ G/A.

0.1 G (see inset Fig. 2.9). Because of the large width of ^{7}Li and ^{6}Li Feshbach resonances, this precision is more than sufficient in our experiments. By repeating the measurement for different currents in the Feshbach coils, we can calibrate the coils, see Fig. 2.9. A linear fit gives a slope $B_{\text{Bias}}/I_{\text{Feshbach}} = 2.301(2)$ G/A.

2.9.2 Trap frequency calibration

In order to characterize the trapping potential we measure the associated frequencies by exciting the dipole mode of a cloud. This also allows us to check the harmonicity of the trap which is essential for the counterflow experiment described in the next chapter.

In the axial direction, we profit from the small position difference between the two curvature minima of the optical potential and the magnetic field. By slowly increasing the optical power, the cloud is adiabatically displaced toward the optical potential minimum and a sudden decrease of the power to its initial value will then make the cloud oscillate in the trap. In virtue of the Kohn's theorem, if the trap is harmonic the oscillations should last forever. In Fig. 2.10, we show two examples of dipole-mode oscillations. Measuring the oscillations over numerous periods allows for the extraction of the trap frequency with a high precision. Furthermore even for amplitude larger than the cloud size, no damping is visible over 1 s which validates the harmonic approximation in the axial direction.

In the radial direction, we excite the dipole mode by abruptly turning off the optical dipole trap for a short period of time ($500\,\mu$s), the slight displacement induced by the anti-trapping magnetic curvature and the gravity is enough to initiate radial oscillations of the cloud. In order to amplify the oscillations amplitude, we image the cloud after a time-of-flight (which typically increase the amplitude by a factor of 3). Depending on the isotope used and the temperature of the cloud, the oscillations can exhibit a fast damping or long-lived oscillations. In the case of a pure ^{7}Li BEC, there is no damping for amplitudes similar to the cloud sizes of the two isotopes ($8\,\mu$m amplitude while the fermions radial size is $10\,\mu$m). In contrast, the oscillations of a fermionic superfluid show a strong damping rate as it experiences more easily the anharmonicities of the trap due to its larger radial extent ($10\,\mu$m while the Bose gas has a typical radial extent of $3\,\mu$m).

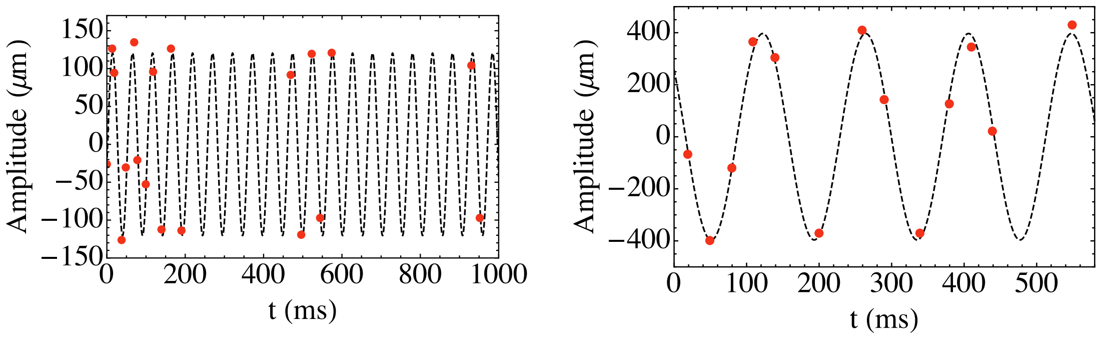

Figure 2.10: Examples of axial frequency measurements by exciting the dipole mode of the fermionic cloud. Left figure: typical oscillations in our shallowest trap, by measuring the oscillations over a few periods we extract a typical frequency of $\nu_{\mathrm{f,z}} = 19.61(5)$ Hz, the precision can be improved (generally up to a factor ~ 3) by increasing the number of measured periods of oscillation. At low optical power the axial confinement is mainly magnetic and highly harmonic, it allows for undamped oscillations of amplitude larger than the cloud size.

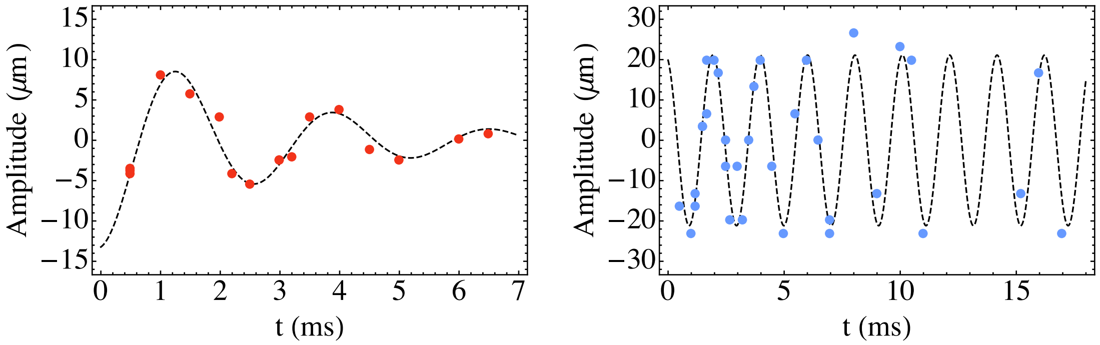

Figure 2.11: Examples of radial frequency measurements. At low optical power, a convenient method is to excite the cloud dipole mode by briefly shutting off the YAG laser. This induces oscillations of few micrometers amplitude in one of the radial directions. To amplify this movement, we measure the cloud position after time-of-flight. On the left figure we show the oscillations of the fermionic cloud showing a strong damping rate. On the contrary, oscillations of the ^{7}Li BEC show at most a weak damping (right figure).

2.9.3 Number calibration

Finally, as aforementioned, the experimental absorption cross-section of the atoms usually differs from the ideal theoretical estimate. In order to accurately count the atoms numbers, the cross-section is calibrated experimentally. At low temperature, the density profiles of our clouds are described by Thomas-Fermi profile and the extent of the clouds is thus related to their total atom number. Hence, provided the magnetic field and the trap frequencies are well known, we can calibrate the cross-section so that the total atom number obtained by integration of the density profil corresponds to the one obtained by measuring the Thomas-Fermi radius. For bosons in the state $|2_\mathrm{b}\rangle$ we use the equation (2.11), we find a correction $\alpha_\mathrm{cal} = 2.8(5)$. For the fermions in the states $|1_\mathrm{f}\rangle$ and $|2_\mathrm{f}\rangle$, we use the equation (2.19) and we find $\alpha_\mathrm{cal} = 1.9(5)$.

2.10 Conclusion

In this chapter, we have given an overview of the experimental setup that allows us to bring ^{6}Li and ^{7}Li vapors down to quantum degeneracy. While it is a rather complicated (and capricious) machine, it is largely compensated by its quite unique features:

- The tunability of interactions for both isotopes using their various broad Feshbach resonances. A direct consequence is the ability of producing new type of mixtures, such as our dual superfluid Bose-Fermi mixture that will be investigated in the next chapter.

- The possibility to use the ^{7}Li BEC to probe locally the strongly interacting Fermi gas which allows for a measurement of its temperature, equation of state and local two-body correlations as previously used in [139] and demonstrated in chapters 3 and 8 respectively.

Chapter 3

Counterflowing mixture of Bose and Fermi superfluids

The discovery of superfluidity goes back to 1938 when two teams in Oxford led by J.F Allen and A.D Misener and in Moscow led by P. Kapitsa reported the anomalous hydrodynamic behavior of liquid ^{4}He below 2.17 K [2, 3]. The fluid was showing no visible viscosity and could flow without friction through very small apertures. In analogy to the superconductors, Kapitsa baptised this type of intriguing fluid, a superfluid. It was soon conjectured that despite the strong interactions between ^{4}He atoms, superfluidity was related to Bose-Einstein condensation [143, 144]. The missing piece of puzzle connecting superfluidity to superconductivity was found in 1970 when the team of D. Osheroff, D. Lee, and R. Coleman managed to observe the superfluid behavior of liquid ^{3}He below a transition temperature of $2.49\,\mathrm{mK}$ [145]. Here, as ^{3}He atoms are fermions with attractive interactions, superfluidity arises via the Cooper pairing mechanism like for electrons in a superconductive metal as predicted by the BCS theory in 1957 [146, 6].

After those two discoveries of the superfluidity of bosonic ^{4}He and fermionic ^{3}He, the idea of studying a Bose-Fermi superfluid mixture rapidly emerged [147, 148]. However because of strong interactions between the two isotopes, ^{3}He-^{4}He mixtures contain only a small fraction of ^{3}He (typically 6%) which, so far, has prevented attainment of simultaneous superfluidity for the two species [149, 150]. With the advent of ultracold gases in the 90's, new possibilities to study superfluidity became available. In particular, it allowed for the study with unprecedented control of the phase coherence of these quantum fluids [43], the superfluid to Mott insulator transition [20], the Berezinskii Kosterlitz Thouless transition in reduced dimensions [48] or the BEC-BCS crossover [151, 78, 152]. Mixtures of degenerate gases were also produced such as Bose-Bose superfluid mixtures [153] or Bose-Einstein condensate immersed in a Fermi sea [128].

In this chapter, in the spirit of the historical experiments done on superfluid liquid helium, we describe the first observation of a counterflow between Bose and Fermi superfluids using our ^{6}Li-^{7}Li mixture. The counterflow is created by exciting center-of-mass oscillations. At low amplitude, the oscillations exhibit extremely low damping and a coherent energy exchange is observed between the two superfluids. These results can be captured within a sum-rule approach and interpreted in terms of a coupled-oscillator model. We then show how friction arises when the relative velocity between the Bose and Fermi gas is increased. A sharp onset of dissipation is observed above a certain critical velocity v_c that we measure in the BEC-BCS crossover. Our results are compared to the Landau criterion for superfluidity [154] and its generalization to a superfluid mixture [86].

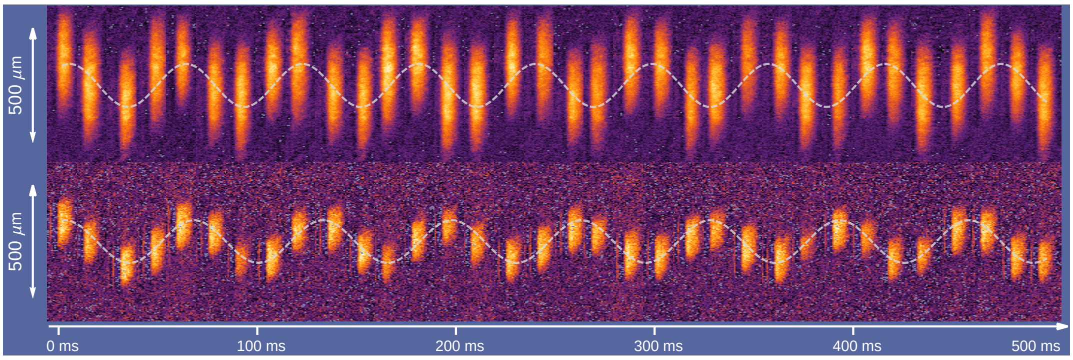

Figure 3.1: Center of mass oscillations of the two superfluids (^{6}Li top, ^{7}Li bottom) after being initially displaced from the trap center. In first approximation, the clouds oscillate at frequencies that differs by a factor $\sqrt{7/6}$. They thus progressively acquire a relative motion and get out of phase after ~ 4.5 periods. For an initial displacement of $100\,\mu$m, the maximal velocity between the two clouds is $1.8\,$cm/s.

The experiments have been described in great details in the thesis of I. Ferrier-Barbut [131], and M. Delehaye [155], to which we refer the interested reader. Therefore, we will deliberately focus on a simple description and emphasize the aspects that connect to the next chapter.

3.1 Creating a counterflow of Bose and Fermi superfluids

The full experimental sequence to cool our ^{6}Li-^{7}Li mixture down to double degeneracy is described in chapter 2. For the final cooling step, we start with ^{6} Li atoms in a balanced mixture of their two lowest hyperfine states $|1_\mathrm{f}\rangle$ & $|2_\mathrm{f}\rangle$ and ^{7}Li atoms spin polarized in the second lowest state $|2_\mathrm{b}\rangle$. The clouds are confined in a strong optical dipole trap, and by lowering the trap depth in the vicinity of the ^{6}Li Feshbach resonance we perform an extremely efficient evaporation and the clouds reach the dual degenerate regime. Typical final atoms numbers are $N_\mathrm{f} = 3 \times 10^5$ and $N_\mathrm{b} = 4 \times 10^4$ at a temperature $T \simeq 80\,$nK which is significantly below the critical temperatures for superfluidity of both gases, see section 2.8.

Contrary to liquid ^{3}He-^{4}He experiments, the Bose-Fermi interaction in our system is weak ($a_\mathrm{bf} = 40.8a_0$) and ensures that the superfluid mixture is stable with respect to phase separation. However, this also means that the effect of the interspecies coupling is difficult to see directly on the density profiles (and even more if the profiles are doubly integrated)[1]. As we will see, the small coupling between the two superfluids can be actually probed by counterflow experiment.

We create a relative motion between the two superfluids by exciting the center of mass oscillations of the two clouds, a scheme used previously for the study of mixtures of Bose-Einstein condensates [69, 156], mixtures of Bose-Einstein condensates and spin-polarized Fermi seas [157], spin diffusion in Fermi gases [158], or integrability in one-dimensional systems [159]. The oscillations are initiated by displacing the clouds from the trap center in the axial direction where the confinement is mostly magnetic and highly

---

[1] For example, the fermion central chemical potential μ_f is typically 20 times larger than the interspecies mean-field interaction term $g_\mathrm{bf}n_\mathrm{b}$, with $g_\mathrm{bf} = 2\pi\hbar^2 a_\mathrm{bf}/m_\mathrm{bf}$ and $m_\mathrm{bf} = m_\mathrm{b}m_\mathrm{f}/(m_\mathrm{b}+m_\mathrm{f})$. Hence, the deviation from the fermion density profile without interspecies coupling is typically a few percents.

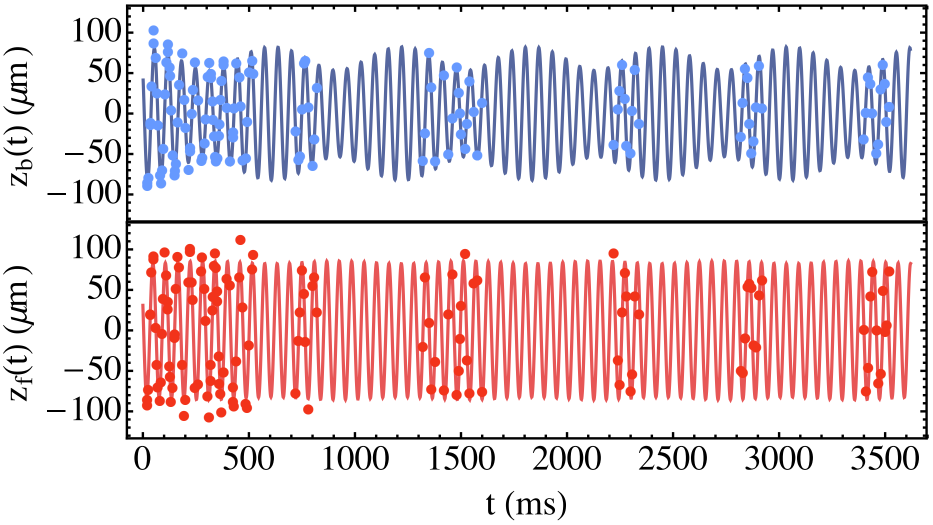

Figure 3.2: Example of low amplitude oscillations of the center of mass of the two superfluids (blue circles: bosons, red circles: fermions) taken at 835 G. Solid lines are fit to the data using the equations (3.7,3.8).

harmonic. At high field, both isotopes are in the Paschen-Back regime and have the same energy dependence with magnetic field so that both clouds feel the same trapping potential in the axial direction. As a consequence, due to the different atomic masses of the two clouds, the trapping frequencies are related by[2] $\omega_\mathrm{f}/\omega_\mathrm{b} = \sqrt{7/6} \simeq 1.08$. Hence, as depicted in Fig. 3.1, after being displaced by the same quantity, the clouds oscillate in the trap and progressively acquire a relative motion. The relative velocity reaches its maximal value after $\simeq 4.5$ periods. For an initial displacement of $100\,\mu$m, we have typically $v_\mathrm{rel,max} = 1.8\,$cm/s. The cloud positions are monitored during up to 4s, which represents ~ 60 periods of oscillations and we can determine the oscillations frequency with a typical precision of $\Delta\omega/\omega \lesssim 2 \times 10^{-2}$.

3.2 Low amplitude oscillations: Coherent energy exchange

For a small initial displacement (typically $\leq 100\,\mu$m), contrary to the large damping observed in the Bose-Bose mixtures [69], we observe long-lived oscillations of the Bose-Fermi superfluid mixture. They can extend up to $4\,$s with no visible damping, see fig (3.2) and our measurement is solely limited by the lifetime of the mixture. Furthermore, the oscillations of the mixture exhibits two features not observed in absence of one of the two isotopes. First, the ^{7}Li oscillation frequency $\tilde{\omega}_\mathrm{b}$ is downshifted by several percent, while the ^{6}Li frequency $\tilde{\omega}_\mathrm{f}$ is almost unchanged. At unitarity (832 G), we measure $\tilde{\omega}_\mathrm{b} = 15.00(2)$ and $\tilde{\omega}_\mathrm{f} = 16.80(2)$, while the associated bare trapping frequencies are $\omega_\mathrm{b} = 15.27(1)$ and $\omega_\mathrm{f} = 16.80(50)$. Second, we observe an amplitude modulation on the bosons oscillations at a frequency $\simeq (\tilde{\omega}_\mathrm{f} - \tilde{\omega}_\mathrm{b})/2\pi$, which implies a coherent energy exchange between the two superfluids.

---

[2] Because of a slight deviation from the Paschen-Back regime for ^{7}Li this ratio is 1.10 instead of 1.08.

3.2.1 Frequency shift

The small frequency shift observed for the boson oscillations comes from a modification of its confinement due to the interactions with the fermions. The Bose gas can be seen as a mesoscopic impurity immersed in the Fermi superfluid. Hence, the bosons see an effective potential which is the sum of the trapping potential $V(\mathbf{r})$ and the mean-field interaction $g_{\mathrm{bf}}n_{\mathrm{f}}(\mathbf{r})$, where n_{f} is the total fermion density, $g_{\mathrm{bf}} = 2\pi\hbar^2 a_{\mathrm{bf}}/m_{\mathrm{bf}}$, and $m_{\mathrm{bf}} = \frac{m_{\mathrm{b}}m_{\mathrm{f}}}{m_{\mathrm{b}}+m_{\mathrm{f}}}$ is the ^{6}Li/^{7}Li reduced mass. In first approximation we can neglect the back action of the bosons on the fermions, so that within the local-density approximation the density of the fermions is given by $n_{\mathrm{f}}(\mathbf{r}) = n_{\mathrm{f}}^{(0)}(\mu_{\mathrm{f}} - V(\mathbf{r}))$, where $n_{\mathrm{f}}^{(0)}(\mu)$ is the stationary equation of state (EoS) of the Fermi gas. Due to its small size $R_{\mathrm{TF,b}} \simeq 0.35R_{\mathrm{TF,f}}$, the BEC probes mainly the central density of the fermions. We can thus expand n_{f} around $\mathbf{r} = 0$, and we get

$$V_{\mathrm{eff}} = g_{\mathrm{bf}}n_{\mathrm{f}}(0) + V(r)\left[1 - g_{\mathrm{bf}}\left(\frac{dn_{\mathrm{f}}^{(0)}}{d\mu_{\mathrm{f}}}\right)_{r=0}\right]. \tag{3.1}$$

The effective potential is still harmonic and to first order the associated frequency is given by

$$\tilde{\omega}_{\mathrm{b}} \simeq \omega_{\mathrm{b}}\left[1 - \frac{1}{2}g_{\mathrm{bf}}\left(\frac{dn_{\mathrm{f}}^{(0)}}{d\mu_{\mathrm{f}}}\right)_{r=0}\right]. \tag{3.2}$$

The chemical potential of a unitary Fermi gas reads

$$\mu_{\mathrm{f}} = \xi\frac{\hbar^2}{2m_{\mathrm{f}}}(3\pi^2 n_{\mathrm{f}})^{2/3}. \tag{3.3}$$

Hence, in the weakly coupled limit the frequency shift is

$$\frac{\delta\omega_{\mathrm{b}}}{\omega_{\mathrm{b}}} = \frac{\omega_{\mathrm{b}} - \tilde{\omega}_{\mathrm{b}}}{\omega_{\mathrm{b}}} = \frac{13k_{F,h}a_{\mathrm{bf}}}{7\pi\xi^{5/4}}, \tag{3.4}$$

where $k_{F,h} = \sqrt{2\hbar m_{\mathrm{f}}\bar{\omega}_{\mathrm{f}}}(3N_{\mathrm{f}})^{1/3}$ is the Fermi momentum of a non-interacting harmonically trapped Fermi gas. For our experimental parameters $k_{\mathrm{F,h}} = 4.6 \times 10^6\,\mathrm{m}^{-1}$, eq (3.4) predicts a value $\omega_{\mathrm{b}} \simeq 2\pi \times 14.97\,\mathrm{Hz}$, in very good agreement with the observed value $15.00(2)\,\mathrm{Hz}$.

3.2.2 Amplitude modulation

To further understand the observed dynamics of the superfluids, it is necessary to include the back action of the bosons on the fermions. Experimentally, we remark that the initial displacement of the trap only excites the dipole modes of the cloud so that the underlying effective model should be a two-level system. In the absence of interspecies interactions, the two levels are the two dipole modes which get dressed when the coupling is turned on. Hence, the observed amplitude modulation on the boson oscillations comes from a beating between the two dressed modes. This modulation is a priori also present on the fermions but is smaller due to a larger inertia of the cloud $N_{\mathrm{f}}m_{\mathrm{f}} \gg N_{\mathrm{b}}m_{\mathrm{b}}$.

The observed center of mass oscillations of the mixture can be recovered using a phenomenological coupled oscillator model :

$$M_{\mathrm{f}}\ddot{z}_{\mathrm{f}} = -K_{\mathrm{f}}z_{\mathrm{f}} - K_{\mathrm{bf}}(z_{\mathrm{f}} - z_{\mathrm{b}}), \tag{3.5}$$

$$M_{\mathrm{b}}\ddot{z}_{\mathrm{b}} = -K_{\mathrm{b}}z_{\mathrm{b}} - K_{\mathrm{bf}}(z_{\mathrm{b}} - z_{\mathrm{f}}), \tag{3.6}$$

where $M_{\mathrm{b}} = N_{\mathrm{b}} m_{\mathrm{b}}$ ($M_{\mathrm{f}} = N_{\mathrm{f}} m_{\mathrm{f}}$) is the total mass of the ^{7}Li (^{6}Li) cloud, $K_{\mathrm{b}} = M_{\mathrm{b}} \omega_{\mathrm{b}}^2$ ($K_{\mathrm{f}} = M_{\mathrm{f}} \omega_{\mathrm{f}}^2$) is the spring constant of the axial magnetic confinement, and K_{bf} is a (weak) coupling constant describing the mean-field interaction between the two isotopes. To recover the correct frequency shift (eq. (3.2)), we take $K_{\mathrm{bf}} = 2K_{\mathrm{b}} \frac{\delta\omega_{\mathrm{b}}}{\omega_{\mathrm{b}}}$.

If we now solve these equations with the initial condition $z_{\mathrm{f}}(0) = z_{\mathrm{b}}(0) = d$, the beating between the two dressed modes is parametrized by two factors $\rho = N_{\mathrm{b}}/N_{\mathrm{f}}$ and $\varepsilon_m = \frac{2m_{\mathrm{b}}}{m_{\mathrm{b}} - m_{\mathrm{f}}} \frac{\delta\omega_{\mathrm{b}}}{\omega_{\mathrm{b}}}$. In our experiment, both factors are small and we can take the limit $\rho, \varepsilon_m \ll 1$, so that we get

$$\begin{aligned} z_{\mathrm{f}}(t) &= d\left[(1-\varepsilon_m \rho)\cos(\tilde{\omega}_{\mathrm{f}} t) + \rho\varepsilon_m \cos(\tilde{\omega}_{\mathrm{b}} t)\right], && (3.7) \\ z_{\mathrm{b}}(t) &= d\left[-\varepsilon_m \cos(\tilde{\omega}_{\mathrm{f}} t) + (1+\varepsilon_m)\cos(\tilde{\omega}_{\mathrm{b}} t)\right], && (3.8) \end{aligned}$$

with $\tilde{\omega}_{\mathrm{f}} \simeq \omega_{\mathrm{f}}$.

The predictions of eqs. (3.7, 3.8) agree well with experiment (Fig. 3.2). In particular, the amplitude modulation on the bosons oscillations is given by ε_m. Thanks to the large mass prefactor ($= 14$) in its expression, ε_m has a typical value of $\simeq 0.25$ at unitarity and it explains the observed amplitude modulation. This stems from the almost resonant bare frequencies of the two oscillators which allow for an efficient energy exchange despite a weak coupling.

3.2.3 Sum-rule approach

We can actually recover the equations (3.7, 3.8) within a fully quantum formalism, using a sum-rule approach [160, 161, 162]. The full derivation is given in appendix A. The sum-rule method is a variational approach that relates the properties of collective excitations (here the dressed dipole modes) to equilibrium properties of the system that can be computed using the local-density approximation. The principal result is that the squared frequencies of the two eigenmodes are given by the extrema of the following function

$$S : |\Psi\rangle \to k \frac{\langle \Psi | \Psi \rangle}{\langle \Psi | \mathcal{M} | \Psi \rangle}, \tag{3.9}$$

with $k = m_\alpha \omega_\alpha^2$ the (species independent) spring constant, $\Psi = (u_{\mathrm{b}}, u_{\mathrm{f}})$ is a 2-dimensional vector expressed in the basis of the two bare dipole modes and $\mathcal{M}$ is an effective mass operator given by

$$\mathcal{M}_{\alpha\beta} = \sqrt{m_\alpha m_\beta} \sqrt{\frac{N_\alpha}{N_\beta}} \frac{\partial \langle z_\alpha \rangle}{\partial b_\beta}, \tag{3.10}$$

with $\langle z_\alpha \rangle$ the mean displacement of species α when the trapping potential of species β is shifted by a quantity $b_\beta \mathbf{e}_z$. The extrema of S can be obtained by a diagonalisation of $\mathcal{M}$. Assuming $\partial_{b_{\mathrm{f}}} \langle z_{\mathrm{b}} \rangle \ll 1$, we get to first order

$$\begin{aligned} \tilde{\omega}_{\mathrm{f}} &= \omega_{\mathrm{f}} \left(1 - \frac{N_{\mathrm{b}}}{N_{\mathrm{f}}} \frac{\partial \langle z_{\mathrm{b}} \rangle}{\partial b_{\mathrm{f}}}\right) \simeq \omega_{\mathrm{f}}, && (3.11) \\ \tilde{\omega}_{\mathrm{b}} &= \omega_{\mathrm{b}} \left(1 - \frac{\partial \langle z_{\mathrm{b}} \rangle}{\partial b_{\mathrm{f}}}\right). && (3.12) \end{aligned}$$

The associated eigenmodes are the dressed dipole modes, and by expressing the initial condition over this eigenmode basis, one recovers the equations (3.7, 3.8).

Finally the crossed susceptibility term $\partial_{b_{\mathrm{f}}}\langle z_{\mathrm{b}}\rangle$ can be calculated using the local-density approximation

$$\begin{aligned} n_{\mathrm{b}}(\mathbf{r}) &= n_{\mathrm{b}}^{(0)}(\mu_{\mathrm{b}}^{(0)} - V(\mathbf{r}) - g_{\mathrm{bf}} n_{\mathrm{f}}(\mathbf{r})), & (3.13) \\ n_{\mathrm{f}}(\mathbf{r}) &= n_{\mathrm{f}}^{(0)}(\mu_{\mathrm{f}}^{(0)} - V(\mathbf{r} - b_{\mathrm{f}}\mathbf{e}_z) - g_{\mathrm{bf}} n_{\mathrm{b}}(\mathbf{r})). & (3.14) \end{aligned}$$

To first order in g_{bf}, we readily get

$$\frac{\partial\langle z_{\mathrm{b}}\rangle}{\partial b_{\mathrm{f}}} \simeq \frac{k g_{\mathrm{bf}}}{N_{\mathrm{b}}} \int d^3\mathbf{r}\, z^2 \frac{\partial n_{\mathrm{f}}^{(0)}}{\partial \mu_{\mathrm{f}}} \frac{\partial n_{\mathrm{b}}^{(0)}}{\partial \mu_{\mathrm{b}}}. \tag{3.15}$$

Assuming that the Bose gas is much smaller than the fermionic cloud , we can approximate this expression by

$$\frac{\partial\langle z_{\mathrm{b}}\rangle}{\partial b_{\mathrm{f}}} \simeq \frac{k g_{\mathrm{bf}}}{N_{\mathrm{b}}} \left(\frac{\partial n_{\mathrm{f}}^{(0)}}{\partial \mu_{\mathrm{f}}}\right)_{r=0} \int d^3\boldsymbol{r}\, z^2 \frac{\partial n_{\mathrm{b}}^{(0)}}{\partial \mu_{\mathrm{b}}}. \tag{3.16}$$

The integral can be calculated exactly, assuming a usual Thomas-Fermi distribution, so that we get the simplified expression

$$\frac{\partial\langle z_{\mathrm{b}}\rangle}{\partial b_{\mathrm{f}}} \simeq g_{\mathrm{bf}} \left(\frac{\partial n_{\mathrm{f}}^{(0)}}{\partial \mu_{\mathrm{f}}}\right)_{r=0}. \tag{3.17}$$

Hence, we recover the expression for the frequency shift given in equation (3.2).

3.2.4 Frequency shift in the crossover

Equation (3.2) allows us to predict the frequency shift of the Bose gas in the whole BEC-BCS crossover. More precisely, the frequency shift obeys a universal scaling

$$\frac{\delta\omega_{\mathrm{b}}}{\omega_{\mathrm{b}}} = k_{\mathrm{F,h}} a_{\mathrm{bf}} f\left(\frac{1}{k_{\mathrm{F,h}} a_{\mathrm{ff}}}\right). \tag{3.18}$$

where the function f is computed numerically using the zero temperature EoS of the interacting Fermi gas measured in [107] and is shown as a blue solid line in Fig. 3.3.
In addition to the unitary limit ($1/k_{\mathrm{F,h}} = 0$) where $f(0) = 13/7\pi\xi^{5/4}$, the two other asymptotic limits for the frequency shift can be understood easily. In the far BEC limit, the Fermi gas forms a molecular BEC whose size decreases with a_{ff} so that the mean field interaction seen by the bosons increases. In the mean field regime, we have $\partial n_{\mathrm{f}}/\partial\mu_{\mathrm{f}} = 2m_{\mathrm{f}} a_{\mathrm{dd}} \pi\hbar^2$, where $a_{\mathrm{dd}} = 0.6 a_{\mathrm{ff}}$ is the dimer-dimer scattering length [77]. Thus, we get

$$\lim_{1/k_{\mathrm{F,h}} a_{\mathrm{ff}} \to \infty} f(1/k_{\mathrm{F,h}} a_{\mathrm{ff}}) = 6.19 \frac{1}{k_{\mathrm{F,h}} a_{\mathrm{ff}}}. \tag{3.19}$$

Hence the frequency shift increases when going toward the BEC limit[3].
In the far BCS limit, the equation of state of the Fermi gas becomes that of a non-interacting Fermi gas and leads to the same frequency shift as at unitarity provided we set $\xi = 1$:

$$\lim_{1/k_{\mathrm{F,h}} a_{\mathrm{ff}} \to -\infty} f(1/k_{\mathrm{F,h}} a_{\mathrm{ff}}) = \frac{13}{7\pi}, \tag{3.20}$$

---

[3] However, we expect deviations from this mean-field result as the boson-dimer scattering length a_{bd} will differ from its mean-field expression $a_{\mathrm{bd}} = 2a_{\mathrm{bf}}$ in the deep BEC limit [163]. In our experiment, for the interaction parameter region we covered, the maximal deviation in frequency shift remains small $\lesssim 7\%$.

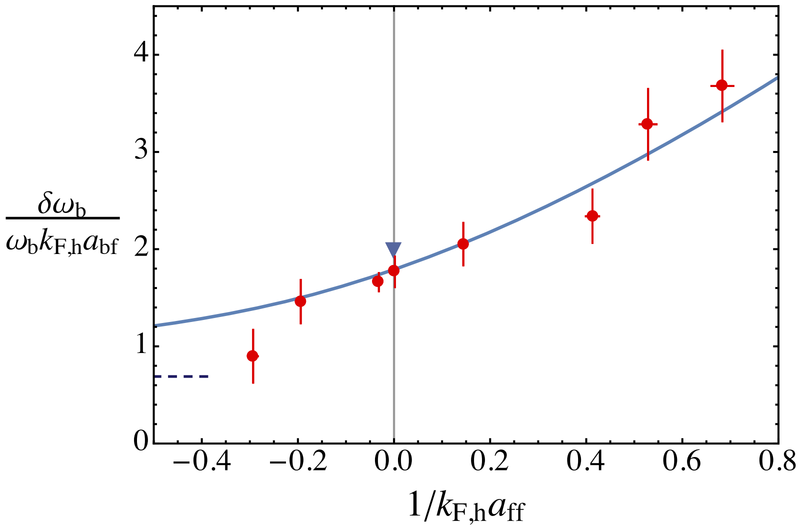

Figure 3.3: Relative frequency shifts for the bosons center of mass oscillations in the BEC-BCS crossover. The red circles are the experimental measurements, error bars represents 1-sigma uncertainty on the frequency measurment and the value of $k_{\mathrm{F,h}}$. Solid line is the model (eq. (3.18)) calculated using the EoS measured in [107]. The dashed line is the asymptotic frequency shift predicted in the BCS limit.

Therefore, we expect the frequency shift to reach a constant value in the BCS limit. To verify these predictions, we repeat the counterflow measurement for different magnetic field ranging from 780 G to 860 G where $1/k_{\mathrm{F,h}}a_{\mathrm{ff}}$ spans the interval$-0.4, +0.8$. The comparison is plotted in Fig. 3.3, and shows an excellent agreement between experiment and our model.

This demonstrates that precision measurements of collective modes of an impurity (the bosons) are a sensitive dynamic probe of equilibrium properties of a quantum many-body system. In chapter 8, we will also show that this same impurity can be also used as a probe for local quantum correlations in the many-body system by means of three-body recombinations. Finally, an interesting prospect that will be explored in the next chapter is to test if the sum rule model is also capable to describe the dynamics of two oscillating superfluids for stronger interspecies coupling.

3.3 Large amplitude oscillations: Friction and critical velocity

For small initial displacements of the clouds, we observed long-lived oscillations of their center of mass as expected in virtue of the frictionless flow property of superfluids. In sharp contrast, for amplitudes larger than a critical value the BEC oscillations are rapidly damped until a steady state regime is reached, as shown in Fig. 3.4. To extract the damping rate, we fit the data using equations (3.7, 3.8) with phenomenological time-dependent amplitudes d_α given by

$$d_{\mathrm{b}}(t) = (1+\delta_{\mathrm{b}}\mathrm{e}^{-\gamma_{\mathrm{b}}t})d, \tag{3.21}$$

$$d_{\mathrm{f}}(t) = (1+\delta_{\mathrm{f}}\mathrm{e}^{-\gamma_{\mathrm{f}}t})d. \tag{3.22}$$

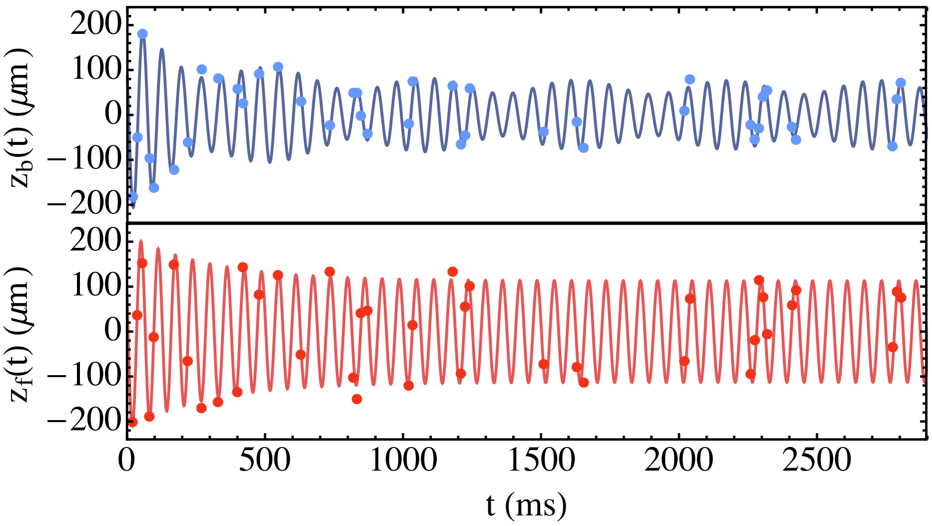

Figure 3.4: Example of center of mass oscillations taken a unitarity (832 G) with large initial displacements (200 μm). The oscillations are first rapidly damped until the relative velocity is lower than a critical relative velocity. Following oscillations are undamped. Solid lines are fit to the data using equations (3.7, 3.8) with time dependent amplitudes (eqs. (3.21, 3.22)).

Repeating the measurement for different initial displacements, hence different maximal relative velocities (estimated using the fits), we observe a well-defined threshold above which damping arises, see fig 3.5. We extract the associated critical velocity with a simple ad-hoc fit

$$\gamma_{\text{fit}} = A\Theta(v - v_c)((v - v_c)/v_{\text{F}})^p, \tag{3.23}$$

where Θ is the Heaviside function and $v_{\text{F}} = \sqrt{2k_{\text{B}}T_{\text{F,h}}/m_{\text{f}}}$ is the Fermi velocity. There is currently no theoretical model that provides a value for the exponent p. Nevertheless, a χ^2 test shows that for most of our data, the best fits are obtained for $p \simeq 1$. Hence we fix p to one and we estimate the uncertainty on v_c by allowing p to vary between 0.5 and 2. At unitarity we find $v_c = 0.42^{+0.08}_{-0.14} v_{\text{F}}$. As we will see in the following section, the critical velocity can be seen as a threshold for the creation of elementary excitations in the dual superfluid.

3.3.1 Simple and generalized Landau criterion for superfluidity

Another aspect of superfluidity predicted by Lev Landau [164], is the existence of a critical velocity above which an impurity moving through the superfluid starts to feel a friction force and its kinetic energy gets dissipated.

In the simple situation imagined by Landau, a microscopic impurity of mass m is moving trough an homogeneous superfluid at a constant speed. The first step for dissipation of the kinetic energy of the impurity is the emission of a single elementary excitation in the superfluid. Initially, the impurity has a velocity $\boldsymbol{v}$ and a kinetic energy $mv^2/2$. After the emission of an elementary excitation of momentum $\boldsymbol{p}$ and energy $\epsilon(\boldsymbol{p})$, by conservation of the total momentum, the new velocity of the impurity is $\boldsymbol{v} - \boldsymbol{p}/m$. Hence, by energy conservation the momentum of the elementary excitation has to fulfill the following

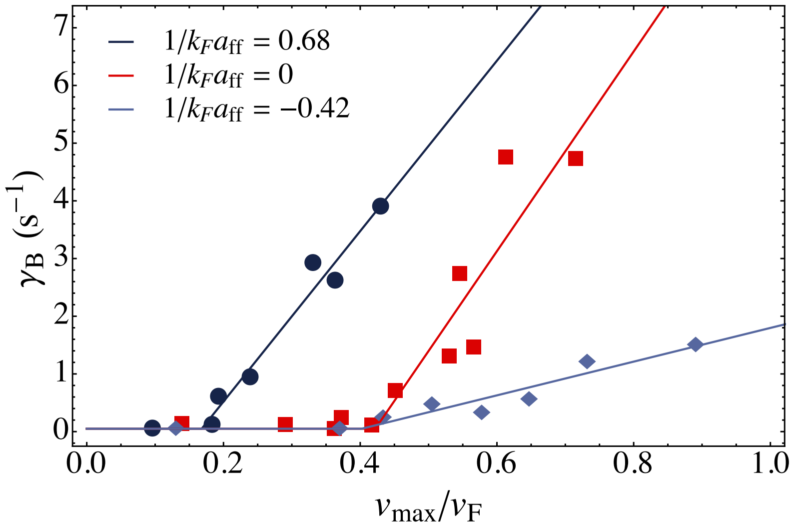

Figure 3.5: Damping rate for the BEC oscillations as a function of the maximal relative velocity between the superfluids and for three different interaction regimes. The solid lines are fit using equation (3.23) with $p = 1$.

equation

$$\boldsymbol{v}.\boldsymbol{p} = \frac{p^2}{2m} + \epsilon(\mathbf{p}). \tag{3.24}$$

Since $\boldsymbol{v}.\boldsymbol{p} \leq vp$, this equation admits solutions only if the velocity is above the Landau critical velocity :

$$v_c = \underset{\boldsymbol{p}}{\text{Min}} \left[\frac{\frac{p^2}{2m} + \epsilon(\boldsymbol{p})}{p} \right]. \tag{3.25}$$

In the limit of an infinite mass impurity, the critical velocity takes the simple expression

$$v_c = \underset{\boldsymbol{p}}{\text{Min}} \left[\frac{\epsilon(\boldsymbol{p})}{p} \right]. \tag{3.26}$$

The critical velocity can then be obtained graphically by finding the minimal slope possible among all the lines joining the origin (0,0) to a given point of the dispersion relation $(\boldsymbol{p}, \epsilon(\boldsymbol{p}))$. The homogeneous weakly interacting Bose gas has a convex dispersion relation and is linear at low momenta

$$\epsilon_{\rm b} \underset{p \to 0}{=} pc_{\rm b}. \tag{3.27}$$

Hence the critical velocity is just the sound velocity

$$v_{c,\rm b} = c_{\rm b} = \sqrt{\frac{g_{\rm bb} n_{\rm b}}{m_{\rm b}}}. \tag{3.28}$$

The case of the interacting Fermi gas is more complicated as it possesses two excitation branches: the bosonic collective excitations linear at low momenta and the gapped fermionic quasi-particles excitations. The value of the critical velocity depends on the precise shape of the two dispersion relations that actually strongly vary in the BEC-BCS crossover. A calculation of the fermion critical velocity was done in the limit of infinite mass impurity in [165] and was extended in [86] for any mass. In the BEC limit and up to unitarity, the critical velocity is given by the sound velocity of the Fermi gas

$$v_{\mathrm{c,f}} = c_{\mathrm{f}} = \sqrt{\frac{n_{\mathrm{f}}}{m_{\mathrm{f}}}\frac{\partial \mu_{\mathrm{f}}}{\partial n_{\mathrm{f}}}}, \tag{3.29}$$

which can be computed using the EoS. On the BCS side of the resonance, the collective excitations merge into the pair-breaking continuum and the critical velocity is given by the fermionic branch

$$v_{\mathrm{c,f}} = \left[\frac{1}{m_{\mathrm{f}}}\left(\sqrt{\Delta_{\mathrm{f}}^2 + \mu_{\mathrm{f}}^2} - \mu_{\mathrm{f}}\right)\right]^{1/2}, \tag{3.30}$$

where Δ_{f} is the gap parameter. For a finite mass impurity, the region where the critical velocity is given by the sound velocity is larger and can extend on the BCS side. Hence, the critical velocity is expected to be maximal around unitarity with a value close to the unitary sound velocity $\simeq 0.36\hbar k_{\mathrm{F}}/m_{\mathrm{f}}$.

In order to describe our experiment, the Landau criterion for superfluidity, eq. (3.25), has to be generalized to counterflowing superfluids. This extension was done in [86] where the method to calculate the new critical velocity is actually very similar to the case of a finite mass impurity. The minimal process for dissipation is the creation of one excitation in each superfluid with opposite momenta[4]. Hence, energy conservation implies

$$\epsilon_{\mathrm{f}}(-\boldsymbol{p}) + \epsilon_{\mathrm{b}}(\boldsymbol{p}) + \boldsymbol{p}.\boldsymbol{v} = 0 \tag{3.31}$$

where ϵ_{f} is an effective dispersion relation of the Fermi superfluid [86] and the term $\boldsymbol{p}.\boldsymbol{v}$ is the Doppler shift of the excitation of momentum $\boldsymbol{p}$ in the BEC.

Consequently, the generalized critical velocity is

$$v_{\mathrm{c}} = \underset{\boldsymbol{p}}{\mathrm{Min}}\left(\frac{\epsilon_{\mathrm{f}}(\boldsymbol{p}) + \epsilon_{\mathrm{b}}(\boldsymbol{p})}{p}\right). \tag{3.32}$$

According to [86], around unitarity and on the BEC side, the critical velocity is then the sum of the sound velocities

$$v_{\mathrm{c}} = c_{\mathrm{b}} + c_{\mathrm{f}}. \tag{3.33}$$

In [166], it was shown that in the hydrodynamic approximation, this critical velocity corresponds to the appearance of a dynamical instability in the counterflowing superfluids where excitations grow exponentially with time. They also calculated the reduction of the critical velocity when the interspecies coupling is increased[5]. Furthermore, it can also be shown that the friction force between the two superfluids is directly proportional to the dynamical structure factor of the fermionic superfluid [167].

---

[4] Two fermionic excitations in the Fermi superfluid if it involves breaking a pair, which is the dominant mechanism on the BCS side.

[5] The reduction of the critical velocity is driven by the parameter

$$\varepsilon_{\mathrm{bf}} = \frac{c_{\mathrm{bf}}^2}{c_{\mathrm{b}} c_{\mathrm{f}}}, \tag{3.34}$$

where

$$c_{\mathrm{bf}}^2 = \sqrt{\frac{n_{\mathrm{b}}}{m_{\mathrm{b}}}\frac{n_{\mathrm{f}}}{m_{\mathrm{f}}}\frac{\partial \mu_{\mathrm{b}}}{\partial n_{\mathrm{f}}}\frac{\partial \mu_{\mathrm{f}}}{\partial n_{\mathrm{b}}}}. \tag{3.35}$$

For $\varepsilon_{\mathrm{bf}} = 0$, the critical velocity is $c_{\mathrm{b}}+c_{\mathrm{f}}$ and goes to 0 when $\varepsilon_{\mathrm{bf}} \to 1$, which corresponds to the mechanical instability of the mixture (phase separation). In our experiment, we have $\varepsilon_{\mathrm{bf}} \sim 10^{-1} - 10^{-2}$, and the effect of the coupling on the critical velocity is negligible.

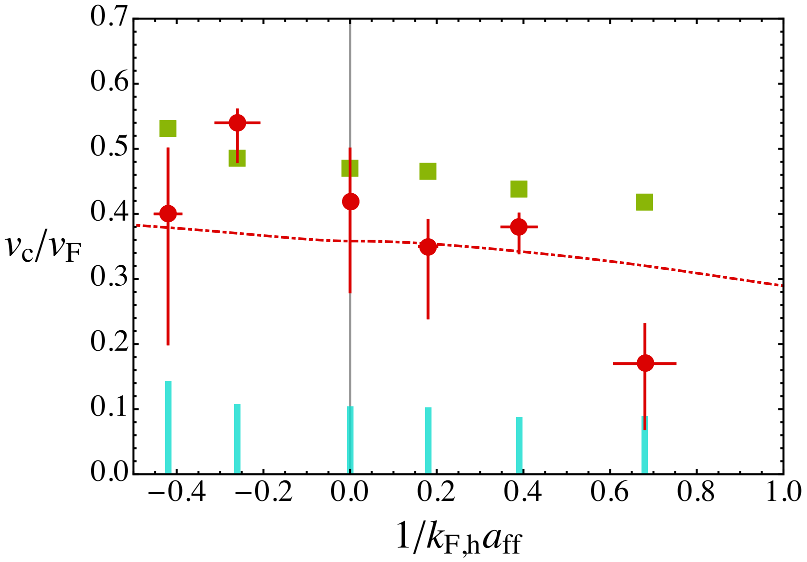

Figure 3.6: Critical velocity of the dual Bose-Fermi superfluid in the BEC-BCS crossover. Red circles: Experimental points obtained using the fit given by eq. (3.23) with p set to 1. Error bars are the variation of v_c when changing the power p from 0.5 to 2. Red dot dashed line: Sound velocity of the Fermi gas calcultated from its equation of state [168, 107]. Blue bars: calculated sound velocity of the Bose gas. Green squares: sum of the calculated sound velocities.

3.3.2 Critical velocity in the BEC-BCS crossover

In Fig. 3.6, we show the critical velocity extracted from the measurement of the oscillations damping rates in the BEC-BCS crossover. We compare them to the predictions of eqs. (3.28, 3.29, 3.33) using the central sound velocities for elongated superfluids $\bar{c}_{\alpha=\mathrm{b,f}}$ obtained by integration over the transverse degree of freedom[6]. $\bar{c}_\mathrm{b}$ does not depend on $1/k_\mathrm{F}a_\mathrm{ff}$ but rather on the associated magnetic field. It contributes typically to $20-25\%$ to the sum of the sound velocities and is clearly excluded as being the threshold for dissipation in our system. Instead, our data is compatible with a threshold for dissipation given by the fermionic sound velocity $\bar{c}_\mathrm{f}$ (i.e. the Landau criterion for a “rigid” impurity moving in the fermionic superfluid) or the sum of the two sound velocities $\bar{c}_\mathrm{b}+\bar{c}_\mathrm{f}$.

Despite the uncertainity of our measurements, this agreement is remarkable inasmuch as previous measurements of the fermionic critical velocity were systematically significantly lower than Landau’s prediction [171, 67]. In these studies, the friction was probed using a stirring laser beam that moves through the whole cloud including its non-superfluid part. In addition, the beam creates strong density modulation that allows for high-order process to be excited. Those factors limit a direct comparison to the ideal setup imagined by Landau [172].

---

[6] For a polytropic equation of state $\mu \propto n^\gamma$ and provided $\mu \gg \hbar\omega_r$, the 1D sound velocity is

$$\bar{c} = \sqrt{\frac{\gamma}{\gamma+1}\frac{\mu}{m}} = \frac{1}{\sqrt{\gamma+1}}c \tag{3.36}$$

For a BEC in the Thomas-Fermi regime, this gives $\bar{c} = c/\sqrt{2}$ [169]. For a unitary Fermi gas or in the BCS limit $\bar{c} = c/\sqrt{5}$ [170]

In our case, the BEC probes mainly the central density of the fermionic cloud thanks to its small size. Additionally, the critical velocity is always first reached when the centers of the clouds coincide as the ratio $v_{\mathrm{rel}}/c_{\mathrm{f}}$ is maximal in that position[7]. Furthermore, the weak repulsive coupling between the two superfluids ensures that vortex shedding or the generation of higher order excitations are strongly inhibited. Nevertheless several other factors are expected to affect the onset of dissipation in our system:

- The confinement in the radial direction induces a back-bending of the dispersion relation [173, 174]. This effect is expected to lower the critical velocity by a factor $(\mu/\hbar\omega_r)^{1/3}$. However, the associated high-frequency modes are localized on the edges of the cloud and due to the different sizes of our superfluids, the generation of those modes in the Fermi superfluid should be inhibited by their weak overlap with the BEC.

- The Landau criterion is a priori only valid at $T = 0$. The thermal fluctuations tend to smear out the onset of dissipation and therefore reduce the apparent critical velocity as demonstrated in [172]. This could explain the lower critical velocity observed on the BEC side of the resonance (780 G) where enhanced inelastic losses heat-up the cloud (see chapter 8).

- The oscillatory motion of the impurity is also expected to blur the threshold as it allows to create excitations at any speed. This effect is present in [67] where the stirrer has a circular motion and was shown to be an important reduction factor for the apparent critical velocity [172]. In the next chapter, we will look at how the non uniform motion affects the generation of excitations in a system similar to our counterflowing Bose-Fermi mixture.

Estimating the order of magnitude of these effects on the critical velocity is rather difficult, especially for the strongly interacting Fermi gas, but could potentially improve the agreement with the predicted value for our mixture $v_c = \bar{c}_{\mathrm{b}} + \bar{c}_{\mathrm{f}}$ (at unitarity and on the BEC side).

3.4 Conclusion

In this chapter, we presented experimental results on our counterflowing superfluids. The counterflow is created by exciting the dipole modes of the two clouds. For small initial displacements the oscillations are long-lived, providing a strong evidence of the superfluidity of our Bose-Fermi mixture. By carefully analyzing the BEC oscillations we observe a frequency shift and an amplitude modulation that demonstrate a coherent energy exchange between the two superfluids. The measured frequency shifts are well described by a sum-rule model and allow us to probe the EoS of the Fermi gas in the BEC-BCS crossover.

In a second part, we studied the oscillations at larger amplitude and observed an onset of dissipation characteristic of the generation of excitations in the system as predicted

---

[7] Indeed, for a polytropic equation state $\mu_{\mathrm{f}} \propto n_{\mathrm{f}}^{\gamma}$ and an oscillatory motion $z(t) = Z_0\mathrm{Cos}(\omega\mathrm{t})$, using the LDA we have

$$\frac{v(z)^2}{c_{\mathrm{f}}(z)^2} = \frac{v(0)^2}{c_{\mathrm{f}}(0)^2}\frac{1 - z^2/Z_0^2}{1 - z^2/R_{\mathrm{TF,z}}^2}, \tag{3.37}$$

which is maximum for $z = 0$ when $Z_0 \leq R_{\mathrm{TF,z}}$.

by the Landau criterion for superfluidity. The extracted critical velocities in the BEC-BCS crossover are remarkably high and compatible with theoretical predictions derived for ideal configurations. This can be partially explained by several properties that are unique to our system, in particular our impurity played by the BEC is weakly coupled to the Fermi gas and only locally probes its superfluid part. Two aspects of our system that can affect our measurement however remain to be explored: the effect of the finite temperature of the mixture and the non-uniform motion of the impurity. As it was done for the experiments presented in [67] with the numerical simulation done in [172], our results call for complementary studies. In the next chapter, we will partially fulfill that need by presenting the results of a Gross-Pitaevski simulation of two counterflowing BECs at zero temperature.

Chapter 4

Numerical simulation of counterflowing superfluids

In order to understand the frictionless nature of superfluidity, Landau investigated the thought experiment of a moving impurity in a superfluid. He conjectured the existence of a critical velocity above which dissipation nevertheless arises. As we have seen in the previous chapter, in its simplest form, this critical velocity marks the threshold beyond which the impurity can generate a stationary wake of elementary excitations. As such, it is a physical phenomenon similar to the Cherenkov radiation in electrodynamics [175], to a supersonic bang or to the generation of surface waves by an object moving at the surface of a liquid [176, 177]. However, the direct observation of such a treshold was shown to be challenging as in actual experiments other decay channels can strongly modify the response of the superfluid to the moving impurity. It was first observed that in the case of a strong perturbation, vortex shedding could supersede generation of elementary excitations [178, 179, 180, 181, 182]. Moreover, in trapped gases, density inhomogeneities [173, 174] and thermal fluctuations [183, 172, 184] can also strongly decrease the value of the critical velocity. Finally, the threshold is even completely smeared out when the impurity does not move at constant velocity [185, 172], just like accelerated charged particles radiate electromagnetic waves at any speed [186].

Despite all those mentioned potential limitations, we observe in our counterflow experiments thresholds for dissipation that are close to the expected value using the Landau criterion in the ideal case (i.e homogeneous superfluids moving at constant speed). This is surprising inasmuch as other measurements reported critical velocities below theoretical predictions [63, 66, 67]. Contrary to all other cold atom experiments where friction is probed using a stirring laser beam, our experiment uses two counterflowing superfluids and dissipation is expected to arise from a different mechanism [86] which might lead to a more robust threshold.

In order to gain more insight about the potentially original dynamics acting in our system, we started a collaboration with Philippe Parnaudeau, Atsushi Suzuki and Ionut Danaila from Laboratory Jacques Louis Lions to perform numerical simulations of counterflowing superfluids. The superfluids are interacting Bose-Einstein condensates modeled by two coupled Gross-Pitaevskii equations. This is a simplified situation where the strongly interacting Fermi gas is replaced by a Bose-Einstein condensate, an approximation that is valid on the molecular side of the fermionic Feshbach resonance. Like in the experiment, we simulate the dynamic of two harmonically trapped clouds initially displaced from their position at rest.

In this chapter, we describe the results obtained from the simulation and different phenomenological approaches used to interpret them. To begin with, we check the accuracy of the sum rule model introduced in the previous chapter to predict the full dynamics of the dipole mode oscillations. Then, with the help of a principal component analysis algorithm [187] we reveal the rich underlying dynamics of the collective modes excited during the counterflow. Using an hydrodynamic model, we are able to identify two mechanisms of excitation in our system. Firstly, in an analog manner to laser stirring beams, collective modes can be excited in a cloud by the perturbation potential created by the interactions with the other cloud. In the case of an oscillatory movement, we show that there is no threshold for the onset of dissipation, and the collective modes can be resonantly excited even at low velocity. The second mechanism is unique to counterflowing superfluids: pairs of modes from both superfluids can be parametrically excited. It is closely related to the generalized Landau criterion predicted for homogeneous counterflowing superfluids [166, 86]. Contrary to the first mechanism, an oscillatory movement does not destroy the threshold for excitation and a critical velocity is observed in our simulation like in our experiment.

4.1 Mathematical and numerical settings

In this section, we introduce the equations used to model the dynamics of two oscillating condensates in the simulation. We briefly explain the methods used to solve them. We also give all the parameters involved in the simulation.

4.1.1 Gross-Pitaevskii equations

The time evolution of a two-component Bose-Einstein condensate with complex macroscopic wave-functions $\psi_1(\mathbf{r},t)$ and $\psi_2(\mathbf{r},t)$ can be described by the coupled GP equations:

$$i\hbar\frac{\partial\psi_1}{\partial t} = \left[-\frac{\hbar^2}{2m_1}\nabla^2 + U(\mathbf{r},t) + N_1 g_{11}|\psi_1|^2 + N_2 g_{12}|\psi_2|^2\right]\psi_1, \tag{4.1}$$

$$i\hbar\frac{\partial\psi_2}{\partial t} = \left[-\frac{\hbar^2}{2m_2}\nabla^2 + U(\mathbf{r},t) + N_1 g_{21}|\psi_1|^2 + N_2 g_{22}|\psi_2|^2\right]\psi_2. \tag{4.2}$$

The number of particles N_i for each component is conserved and we have

$$\int_{\mathbb{R}^3}|\psi_1|^2 = 1, \quad \int_{\mathbb{R}^3}|\psi_2|^2 = 1. \tag{4.3}$$

The atomic mass of each component can be expressed as:

$$m_i = d_i m, \quad i = 1,2. \tag{4.4}$$

Interaction constants g_{ij} are defined as:

$$g_{ii} = 4\pi\hbar^2 a_{ii}/m_i, \tag{4.5}$$

and for $i \neq j$

$$g_{ij} = 2\pi\hbar^2 a_{ij}/\mu, \quad \text{with the reduced mass} \quad \mu = \frac{m_1 m_2}{m_1 + m_2}. \tag{4.6}$$

The a_{ij} are the s-wave scattering lengths and $a_{12} = a_{21}$.
The two BECs feel the same trapping potential:

$$U(\mathbf{r}, t) = \frac{m}{2} d_2 \left[\omega_\perp^2 (x^2 + y^2) + \omega_z^2 \left(z - z_c(t)\right)^2\right], \tag{4.7}$$

with

$$z_c(0) = z_0, \quad z_c(t) = 0,\ t > 0. \tag{4.8}$$

The two condensates having different atomic mass, displacing the center of the trap by the quantity z_0 will make them oscillate at different frequencies like in the experiment.

4.1.2 Dimensionless equations

In order to choose the relevant time and space resolution of the numerical simulation, the Gross-Pitaevskii equations have to be recast in a dimensionless form. The starting point is to consider a general length (x_s) and time (t_s) scales. Non-dimensional variables will be then

$$\tilde{\mathbf{x}} = \frac{x}{x_s}, \quad \tilde{t} = \frac{t}{t_s}, \quad \varphi_1 = \frac{\psi_1}{x_s^{-3/2}}, \quad \varphi_2 = \frac{\psi_2}{x_s^{-3/2}}. \tag{4.9}$$

We take the usual scalings

$$t_s = \frac{1}{\omega}, \quad x_s = a_{ho},\ a_{ho} = \sqrt{\frac{\hbar}{m\omega}}. \tag{4.10}$$

Hence, equations (4.1, 4.2) become (in the following we drop the ˜ notation for **r** and t):

$$i\frac{\partial \varphi_1}{\partial t} = \left[-\frac{1}{2d_1}\nabla^2 + U_a(\mathbf{r}, t) + \beta_{11}|\varphi_1|^2 + \beta_{12}|\varphi_2|^2\right]\varphi_1, \tag{4.11}$$

$$i\frac{\partial \varphi_2}{\partial t} = \left[-\frac{1}{2d_2}\nabla^2 + U_a(\mathbf{r}, t) + \beta_{21}|\varphi_1|^2 + \beta_{22}|\varphi_2|^2\right]\varphi_2, \tag{4.12}$$

with:

$$\left\{\begin{array}{lcl} U_a & = & \frac{d_2}{2}\left[\gamma_\perp^2 (x^2 + y^2) + \gamma_z^2 \left(z - b(t)\right)^2\right], \\ \beta_{11} & = & 4\pi \frac{1}{d_1}\frac{N_1 a_{11}}{a_{ho}}, \quad \beta_{12} = 2\pi \frac{d_1 + d_2}{d_1 d_2}\frac{N_2 a_{12}}{a_{ho}}, \\ \beta_{21} & = & 2\pi \frac{d_1 + d_2}{d_1 d_2}\frac{N_1 a_{12}}{a_{ho}}, \quad \beta_{22} = 4\pi \frac{1}{d_2}\frac{N_2 a_{22}}{a_{ho}}. \end{array}\right. \tag{4.13}$$

with $\gamma_\perp = (\omega_\perp/\omega)$, $\gamma_z = (\omega_z/\omega)$ and $b = z_c/a_{ho}$.

4.1.3 Numerical methods

The numerical simulation procedure can be decomposed in two parts, a preparation step where the initial wave functions are computed and the dynamics itself.

Initialization

As for the experiment, the clouds are initially in their ground state. In the Thomas-Fermi regime, the ground state of the coupled superfluids can be a priori calculated analytically. Here, we won't neglect the kinetic terms and instead compute the wave functions numerically. Stationary solutions have the form:

$$\varphi_i(\mathbf{r},t) = \exp(-i\mu_{g,i}t)\phi_i(\mathbf{r}), \quad i = 1,2, \tag{4.14}$$

with $\mu_{g,i}$ the global chemical potentials. Among these solutions, the ground state will minimize the total energy of the system $E(\phi_1,\phi_2)$, where

$$E(\phi_1,\phi_2) = \int_{\mathbb{R}^3} \sum_{i=1}^{2} \left[\frac{1}{2d_i}|\nabla\phi_i|^2 + U_a\,|\phi_i|^2 + \frac{1}{2}\sum_{j=1}^{2}\beta_{ij}|\phi_i|^2|\phi_j|^2 \right]. \tag{4.15}$$

To find such a solution, we use a pseudo-time (or imaginary time) propagation [188] by solving:

$$\frac{\partial\phi_1}{\partial t} = \left[\frac{1}{2d_1}\nabla^2 - U_a(\mathbf{r},t) - \beta_{11}|\phi_1|^2 - \beta_{12}|\phi_2|^2\right]\phi_1, \tag{4.16}$$

$$\frac{\partial\phi_2}{\partial t} = \left[\frac{1}{2d_2}\nabla^2 - U_a(\mathbf{r},t) - \beta_{21}|\phi_1|^2 - \beta_{22}|\phi_2|^2\right]\phi_2. \tag{4.17}$$

For the time discretization of these equations, we use a semi-implicit backward Euler method[188].

Real-time dynamics

For the real-time dynamics we use a second order time splitting method [188]. This method is used when two or more terms of the Hamiltonian do not commute, here A and B. For small time steps, their contribution can be calculated separately using the following formula:

$$\frac{\partial\psi}{\partial t} = (A+B)\psi \Longrightarrow \psi(x,t+\delta t) = e^{(A+B)\delta t}\psi(x,t) \tag{4.18}$$

$$\approx e^{A\delta t/2}e^{B\delta t}e^{A\delta t/2}\psi(x,t). \tag{4.19}$$

This particular choice is second order accurate in time t [189].
In our case

$$A_1 = i\frac{1}{2d_1}\nabla^2, \quad B_1 = -i\left[U_a(\mathbf{r},t) + \beta_{11}|\varphi_1|^2 + \beta_{12}|\varphi_2|^2\right], \tag{4.20}$$

$$A_2 = i\frac{1}{2d_2}\nabla^2, \quad B_2 = -i\left[U_a(\mathbf{r},t) + \beta_{21}|\varphi_1|^2 + \beta_{22}|\varphi_2|^2\right]. \tag{4.21}$$

The A_i and B_i operators are respectively diagonal in Fourier and real space. Their contribution can be computed easily by going back and forth in those spaces using Fourier pseudo-spectral methods.

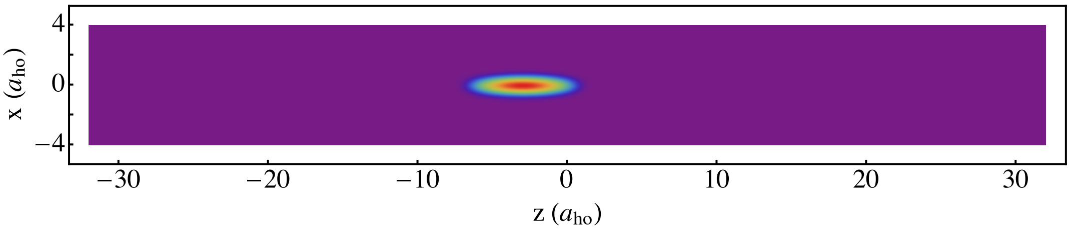

(a) $\tilde{n}_1(x, z)$

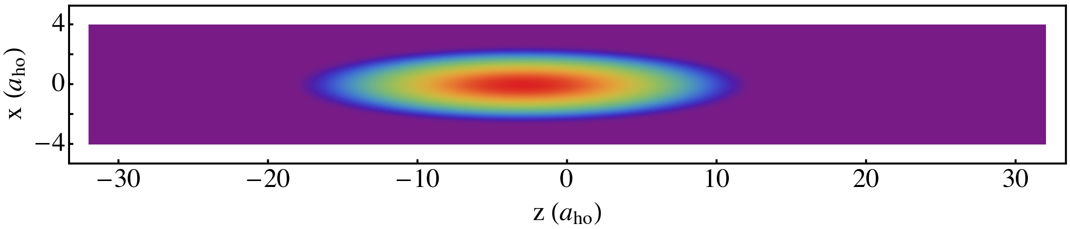

(b) $\tilde{n}_2(x, z)$

Figure 4.1: Simply integrated density profiles of the two initial wavefunctions $\tilde{n}_i(x, z) = \int dy\, n_i(x, y, z)$ for a simulation run with $b = 3$ and $\beta_{12}/\beta_{22} = 3.1 \times 10^{-3}$.

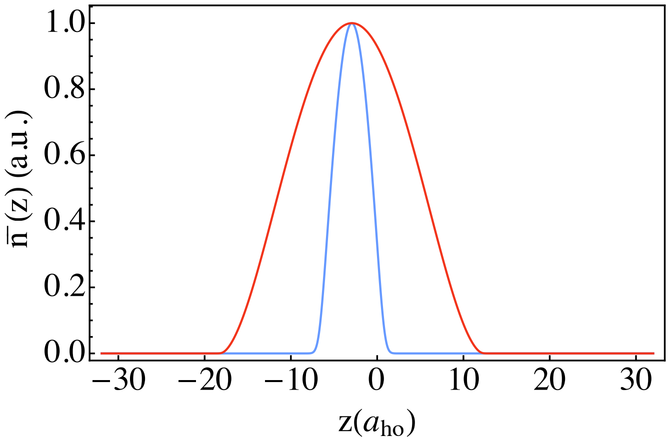

Figure 4.2: Doubly integrated density profiles of the two initial wavefunctions $\bar{n}_i(z) = \int dx\, dy\, n_i(x, y, z)$ for a simulation run with $b = 3$ and $\beta_{12}/\beta_{22} = 3.1 \times 10^{-3}$.

4.1.4 Simulation parameters

Fixed physical parameters

The parameters of the simulation are chosen to reproduce (but only partially) the experimental conditions described in the previous chapter. We consider a large and strongly interacting BEC and a small and weakly interacting BEC in a 3D harmonic trap elongated along one direction. For the clouds we thus took as fixed parameters

$$m = 6u, \quad d_1 = 7/6, \quad d_2 = 1.$$

$$N_1 = 2 \cdot 10^4, \quad N_2 = 6 \cdot 10^5$$

$$a_{11} = 40.83a_0, \quad a_{22} = 300a_0.$$

The masses are choosen to reproduce the bare trapping frequency difference in our mixture of ^{6}Li-^{7}Li, $\omega_\mathrm{b}/\omega_\mathrm{f} = \sqrt{6/7}$.
The dimensionless interacting parameters are then

$$\beta_{11} = 80.20, \quad \beta_{22} = 20621.52, \quad \beta_{12}/\beta_{21} = 30.$$

For the trapping frequencies, we choose

$$\omega_\perp = 2\pi \cdot 300\,\mathrm{Hz}, \quad \omega_z = 2\pi \cdot 50\,\mathrm{Hz},$$

Hence by setting $\omega = \omega_z$,

$$a_{ho} = 5.80 \cdot 10^{-6}\,\mathrm{m}.$$

We can estimate the size of the two condensates (Thomas-Fermi radii in units of a_{ho})

$$R_{\perp 1} = 0.81, \quad R_{z1} = 5.26,$$

$$R_{\perp 2} = 2.58, \quad R_{z2} = 15.47.$$

Examples of the simply integrated and doubly integrated density profiles of the initial wave functions are shown in figures 4.1 and 4.2 respectively . A Thomas-Fermi fit gives $R_{z1} = 4.47$ and $R_{z2} = 15.45$, close to the estimated values.

Numerical parameters

The space domain is chosen so that the clouds stay away from the boundaries during oscillations. We took

$$L_x = L_y = 8a_{ho}, \quad L_z = 64a_{ho}.$$

It allows us to have oscillations amplitude up to $\simeq 16a_{ho}$ along the z-direction, which is more than enough to have a relative velocity larger than the sum of the central sound velocities of the condensates (reached typically for $\simeq 5.5a_{ho}$).
For the space resolution we have

$$\Delta r = 1/2^4 a_{ho},$$

which corresponds to a grid of $128 \times 128 \times 1024$ computational points. The gradient of the phase φ of the wave function phase being proportional to the velocity, assuming a sinusoidal movement $R_{CoM} = b\, a_{ho}\mathrm{sin}(\omega_z t)$, we infer a phase resolution of $\Delta\varphi = b/2^4$. In order to capture both fast and slow dynamics present during the oscillations of the clouds, we used a refined time resolution $\Delta t = 5 \times 10^{-4}/\omega_z$ and a large number of steps $N_t = 4 \times 10^5$. This allows to simulate $\simeq 32$ periods of oscillations along the z-direction.

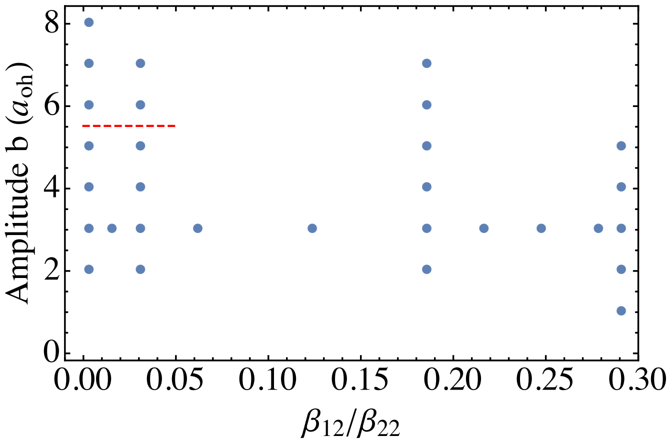

Figure 4.3: Summary of parameters for which simulations were performed (blue dots). The red dashed line shows the amplitude above which the critical velocity is expected to be reached in the limit of a vanishing coupling between the superfluids. For $\beta_{12}/\beta_{22} = 0.292$, we have $g_{12}^2/g_{11}g_{22} = 1$, which means that a homogeneous mixture of those superfluids is dynamically unstable and will demixe.

Simulation runs overview

Among all the possible configurations, we focused only on two parameters to vary:

- The initial displacement of the clouds, denoted as above by b. It will set the amplitude of the oscillations of the center of mass , and implicitly the relative speed between the clouds.

- The couplings between the two superfluids, β_{12} and β_{21}.

All in all, using the high-perfomance computing center of UPMC, we performed more than 30 simulation runs, which represents over 50000 hours of CPU time and teraoctets of data. A summary of parameters used for the simulations are shown in Fig. 4.3.

4.2 Low amplitude oscillations

The dynamics of oscillating condensates can be predicted using the sum rule method introduced in the previous chapter. As such, it provides a good test-bed to check the accuracy of the model using the numerical simulation data[1]. Similar to the experiment described in the previous chapter, the dipole mode oscillations are long-lived and the coupling between the superfluids will shift their frequencies from the bare trapping frequencies and modulate their amplitude. An example of center of mass evolution is shown in Fig. 4.4, as well as in Appendix C. We ran several simulations with interspecies coupling β_{12} encompassing two orders of magnitude. The frequency shifts and the amplitude

---

[1] It is also a good way to check the good behavior of the simulation, so that this comparison is actually a cross-validation of both the simulation and the model.

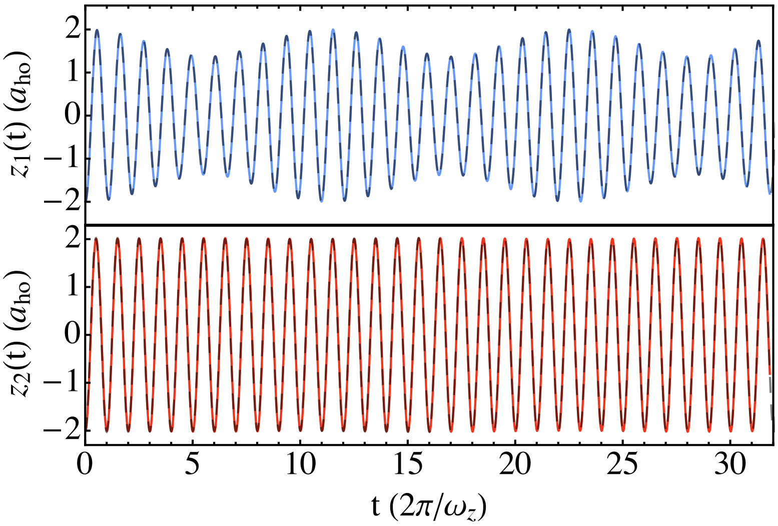

Figure 4.4: Example of low amplitude oscillations of the center of mass of the two superfluids ($b = 2$ and $\beta_{12}/\beta_{22} = 0.031$). The small atomic mass difference $(m_1{-}m_2)/m_1 \ll 1$ combined with a large atom number ratio $N_2/N_1 = 30$ induces a strong amplitude modulation of the small condensate oscillations ($i = 1$, in blue) while the oscillations of the large condensate are mostly not affected ($i = 2$, red). Dashed lines represent fits used to extract the frequency shifts and modulation factors.

modulation are extracted by fitting the center of mass using a sum of cosine functions

$$z_1(t) = \frac{b}{\alpha_{11} + \alpha_{12}} \left(\alpha_{11}\cos(\omega_1 t) + \alpha_{12}\cos(\omega_2 t)\right), \tag{4.22}$$

$$z_2(t) = \frac{b}{\alpha_{21} + \alpha_{22}} \left(\alpha_{21}\cos(\omega_1 t) + \alpha_{22}\cos(\omega_2 t)\right). \tag{4.23}$$

Results of the fit are displayed in Fig. 4.5a as blue dots. We will first compare them to the predictions of the sum-rule model restricted to the leading order term in β_{12} as we did for the experimental data. Then, as this first-order calculation will prove inaccurate for large interspecies coupling, we compute the exact solutions and compare them to the simulation points.

As explained earlier, the sum-rule method connects the dynamics of oscillating condensates with their static properties that are easier to compute. More precisely, it shows that all the dynamics can be derived knowing a single non-trivial quantity

$$\chi_{12} = \frac{\partial\langle z_1\rangle}{\partial b_2} \tag{4.24}$$

where $\langle z_1\rangle$ is the mean displacement along z of the cloud $i = 1$, when the trap center of the cloud $i = 2$ is shifted by a quantity $b_2\mathrm{e}_z$[2]. In our case, where the condensate $i = 1$ is smaller than the $i = 2$, it can be shown, assuming the local density approximation and as long as they are miscible, that we have

$$\chi_{12} = -\frac{\beta_{12}/\beta_{22}}{1 - \beta_{12}/\beta_{22}}. \tag{4.25}$$

---

[2] By symmetry, we have $\chi_{12} = N_2/N_1\chi_{21}$

In the limit $\beta_{12}/\beta_{22} = g_{12}/g_{22} \ll 1$, we recover the first order result used for the experimental data

$$\chi_{12} \simeq \frac{g_{12}}{g_{22}} = g_{12}\left(\frac{\partial n_2}{\partial \mu_2}\right)_{\mathbf{r}=0}. \tag{4.26}$$

For the frequency shifts we get

$$\tilde{\omega}_1 \simeq \omega_{z,1}\left(1 - \frac{1}{2}\frac{\beta_{12}}{\beta_{22}}\right), \tag{4.27}$$

$$\tilde{\omega}_2 \simeq \omega_{z,2}\left(1 - \frac{1}{2}\frac{N_1}{N_2}\frac{\beta_{12}}{\beta_{22}}\right). \tag{4.28}$$

First order theory is shown as black lines in figs. 4.5a,4.5b and is in good agreement with the simulation data only for low coupling. To go beyond the first order results and to predict the amplitude modulation, we now have to consider the effective mass operator $\hat{\mathcal{M}}$ provided by the sum rule method. Its eigenvectors and eigenvalues will give the two oscillation modes and their effective mass respectively. In matrix representation, $\hat{\mathcal{M}}$ takes the form

$$\mathcal{M} = \begin{pmatrix} m_1\left(1 - \frac{N_1}{N_2}\chi_{12}\right) & \sqrt{m_1 m_2}\sqrt{\frac{N_1}{N_2}}\chi_{12} \\ \sqrt{m_1 m_2}\sqrt{\frac{N_1}{N_2}}\chi_{12} & m_2\left(1 - \chi_{12}\right) \end{pmatrix}.$$

The new mode frequencies will then be given by

$$\tilde{\omega}_1 = \sqrt{\frac{m_1}{\tilde{m}_1}}\omega_{z,1}, \tag{4.29}$$

$$\tilde{\omega}_2 = \sqrt{\frac{m_2}{\tilde{m}_2}}\omega_{z,2}, \tag{4.30}$$

where $\tilde{m}_i$ is the eigenvalue of M that corresponds to m_i at low coupling. The associated eigenvectors will give the eigen-modes of oscillation $\tilde{\Psi}_i$ such that[3]

$$\begin{pmatrix} z_1(t) \\ z_2(t) \end{pmatrix} = \sum_{i=1}^{2} c_i \cos(\tilde{\omega}_i t)\tilde{\Psi}_i. \tag{4.31}$$

The coefficients c_i are fixed by the initial conditions $z_1(0) = z_2(0) = b$ (we also assumed that initial velocities are zero).

The complete sum rule method (orange lines) fits better the oscillations at larger coupling. While there is almost no difference for the frequency shift, there is however some visible discrepancy for the relative weight between the two modes. We can reproduce the simulation results almost exactly using a slightly different approach. Indeed, since at low amplitude we expect that only two modes are excited, the "dressed" dipole modes, the system should be completely analog to two coupled classical oscillators of frequency $\omega_{z,1}$ and $\omega_{z,2}$ and masses $M_1 = N_1 m_1$ and $M_2 = N_2 m_2$ are in this case coupled with a spring constant K_{12}. The equations of motion are in this case:

$$M_1\frac{d^2 z_1}{dt^2} = -M_1\omega_{z,1}^2 z_1 + K_{12}(z_2 - z_1), \tag{4.32}$$

$$M_2\frac{d^2 z_2}{dt^2} = -M_2\omega_{z,2}^2 z_2 + K_{12}(z_1 - z_2). \tag{4.33}$$

---

[3] with $\tilde{\Psi}_i = \begin{pmatrix} \sqrt{N_1/m_1} & 0 \\ 0 & \sqrt{N_2/m_2} \end{pmatrix} \Psi_i$, where $M\Psi_i = \tilde{m}_i\Psi_i$.

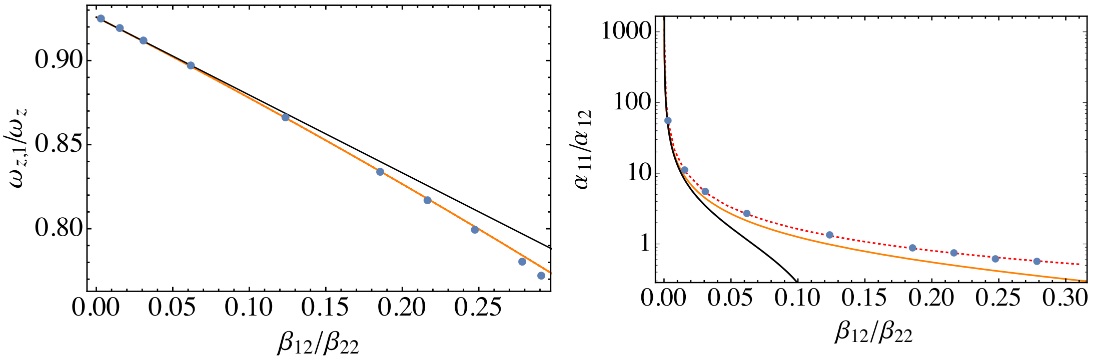

(a) (b)

Figure 4.5: Frequency shifts (a) and modulation factor (b) for the oscillations of the small condensate ($i = 1$) for different interspecies coupling. Blue dots: simulation data. Black line: first order perturbation theory. Orange line: non-perturbative sum rule method. Red dashed line: coupled harmonic oscillator analogy method. For the frequency shifts, the last two models give the same results.

To complete the analogy, we have to choose K_{12} so that it mimics the coupling between the two superfluids. Since the sum rule method suggested that χ_{12} was the driving parameter, we can express K_{12} as a function of the classical expression of χ_{12}, one finds

$$K_{12} = M_1 \omega_{z,1}^2 \frac{\chi_{12}}{1 - (1 + \frac{N_1}{N_2})\chi_{12}}. \tag{4.34}$$

Inserting the expression (4.25) in eq. (4.34), we are able to reproduce the dynamics of the oscillating condensates. Indeed, the results of this model are shown as red dashed lines in figs. 4.5a,4.5b and are in excellent agreement with the simulation points. The departure of the simulation data from the first order perturbation theory can be well accounted by a two level model, showing the underlying simplicity of the clouds dynamic at low amplitude. The sum rule method thus seems to provide the good frequencies but do not give the correct eigenmodes at large coupling; this means that while the product of the off-diagonal terms of the effective mass operator is correct, the matrix shouldn't be symmetric. This is actually a well known drawback of variational methods.

We didn't investigate the regime where superfluids are partially or completely phase-separated. In that case, the description in terms of two excited levels should fail since dipole oscillations could easily couple to some higher-order excitations. For homogenous superfluids with mean-field interactions, the mixture is unstable when $g_{12}^2/(g_{11}g_{22}) \geq 1$, which is equivalent in the numerical simulations to $\beta_{12}/\beta_{22} \geq 0.292$. We explore in the next section the case of oscillations with larger amplitudes where higher-order modes should be excited as well.

4.3 Large amplitude oscillations

The maximal relative velocity between the two superfluids during the oscillations is approximately given by $b(\tilde{\omega}_1 + \tilde{\omega}_2)$ and is reached when the clouds are out of phase. Based on what was observed in the experiment and predicted for homogeneous counterflowing superfluids [166, 86], dissipation is expected to occur in our system when $v_{\text{rel}} \geq \bar{c}_1 + \bar{c}_2$,

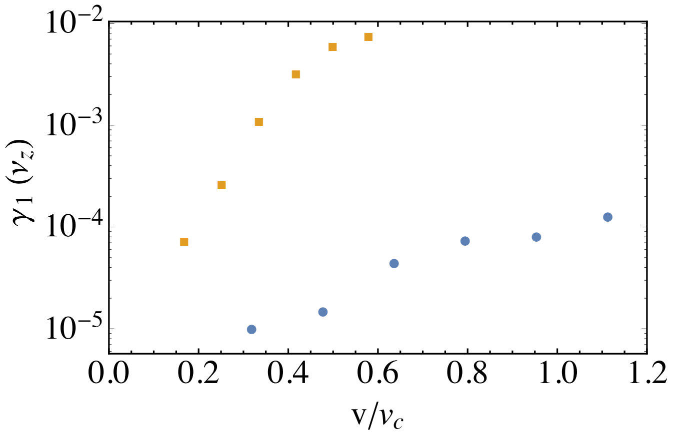

Figure 4.6: Damping rates for the center of mass $z_1(t)$ versus maximal relative velocity during the oscillations in units of the expected critical velocity $v_c = \bar{c}_1 + \bar{c}_2$. Blue dots: rates for the $\beta_{12}/\beta_{22} = 0.031$ simulation runs. Yellow squares: rates for the $\beta_{12}/\beta_{22} = 0.186$ simulation runs. The others runs ($\beta_{12}/\beta_{22} = 0.003$ and $\beta_{12}/\beta_{22} = 0.291$) showed a damping compatible with zero (i.e. in the fit error bars).

where $\bar{c}_{1,2}$ are the radially averaged central sound velocities. This velocity is attained with an initial displacement of $b \gtrsim 5.3$ (in units of a_{ho}) for small coupling between condensates. To explore this phenomenon we ran four sets of simulations for four different coupling parameters $\beta_{12}/\beta_{22} = \{0.003, 0.031, 0.186, 0.291\}$; for each set we varied the initial displacement around this predicted threshold for dissipation (see Fig. 4.3). At first sight, the obtained results show at most weak signals of dissipation in the system in sharp contrast with the experimental data. Nevertheless, using a principal component analysis (PCA) to look at small fluctuations in the clouds, we uncovered a rich set of phenomena that were at the beginning quite puzzling. In fact, the PCA gives us access to the dynamic of many collective modes excited during the counterflow. With the help of some theoretical modeling of our counterflowing superfluids, the behavior of most of the modes can be understood in terms of two mechanisms that we will discuss thoroughly in the next section.

4.3.1 First observations: The center of mass evolution

As in experiments, we can analyze the center of mass evolution to seek for dissipation related to the critical velocity. However, even at high oscillation amplitudes the simulation does not exhibit the strong damped motion observed in the experiment. Most of the runs showed an extremely weak decay rate $\gamma \lesssim 10^{-4}\omega_z$[4]. The only exception is for the $\beta_{12}/\beta_{22} = 0.186$ set of simulations where a damping was visible at large amplitude of oscillations and $\gamma \sim 10^{-2}\omega_z$, see Fig. 4.6. Additionally, the damping does not show any evidence of the existence of a threshold in relative velocity and seems featureless.

Nevertheless, by comparing oscillations at low and high amplitude we can observe some interesting features. A simple test is to look at rescaled oscillations differences $\Delta z_i = z_{i,b_1}(t)/b_1 - z_{i,b_2}(t)/b_2$, where z_{i,b_j} is the center of mass of the cloud i initially

---

[4] To extract the damping rate, we used the functions defined in (4.23) multiplied by an exponentially decaying term $\mathrm{e}^{-\gamma t}$.

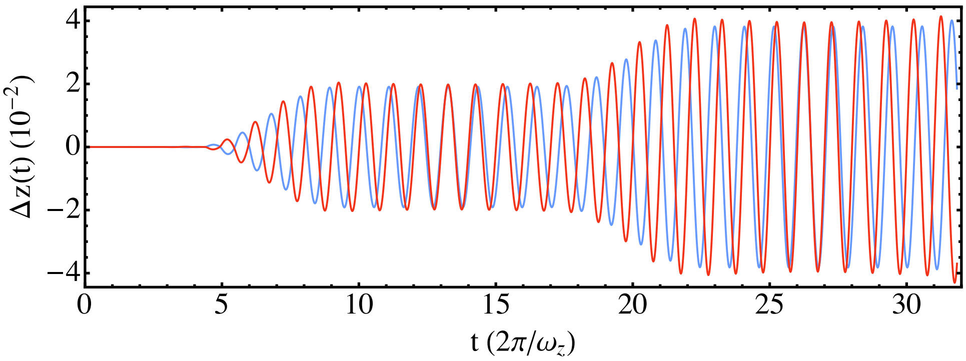

Figure 4.7: Rescaled amplitude difference $\Delta z = z_{i,b_1}(t)/b_1 - z_{i,b_2}(t)/b_2$ for $b_1 = 2$, $b_2 = 8$ and $\beta_{12}/\beta_{22} = 0.003$. Blue line: small condensate $i = 1$, Red line: large condensate $i = 2$ rescaled with a global factor $N_2/N_1 = 30$.

displaced by a quantity b_j. An example is shown in Fig. 4.7 for $b_1 = 2$, $b_2 = 8$ and $\beta_{12}/\beta_{22} = 0.003$. If the overall difference between these two runs is small, only a few percent, it shows a quite peculiar behavior. Indeed, for both clouds, the envelopes of Δz_1 and Δz_2 seem to be step-wise functions of time and equal up to a factor $N_2/N_1 = 30$. The growing of the oscillations starts after 5 periods and corresponds to a situation where the clouds are oscillating almost out of phase and have a large peak relative velocity. Since there is no damping for these runs, the increase seen for the Δz functions come mainly from a dephasing between the oscillations of the two considered simulation runs. Since changing the phase of an oscillator has no cost in energy, it means that the underlying source of this phenomenon is perturbing very weakly the dynamics.

If we now extract the instantaneous phase of the oscillations for different initial displacements, we observe the same behavior as for Δz_i, see Figs. 4.8a, 4.8b. The height of the steps increases non-linearly with the initial displacement and no clear plateaus are observed for the $b \leq 4$ simulation runs. Additionally, the phase difference start to grow earlier as the initial displacement is increased, see Fig. 4.8b. All these observations were done with $\beta_{12}/\beta_{22} = 0.003$, a case where the two superfluids are very weakly coupled. For larger couplings, the same plateau features can be observed at large amplitude but get smoothed as the inter-species interactions are increased (see appendix C).

As a conclusion, there is a weak but clear signal that something happens when the relative velocity between the superfluids is large, i.e. for a large initial displacement ($b \gtrsim 5$) and when the clouds are out of phase ($t \simeq 7 \times 2\pi/\omega_z$ and $t \simeq 21 \times 2\pi/\omega_z$). The next step is thus to understand what is the underlying source of these features observed from the center of mass oscillations.

4.3.2 Fluctuation analysis using a principal analysis component

The clouds images contain a handful of information but is dispersed in a a priori complex manner on a large set of variables, the pixels. One way to analyse them is to compute pre-determined quantities such as the center of mass, the size of the cloud, etc. By doing so, much of the information is washed out only to reveal a very specific one that might be not so relevant. In this context, a powerful method is the principal component analysis (PCA). The PCA is a *model free* algorithm to identify the main sources of fluctuations/correlations in a set of data and calculate their contribution. It greatly simplifies

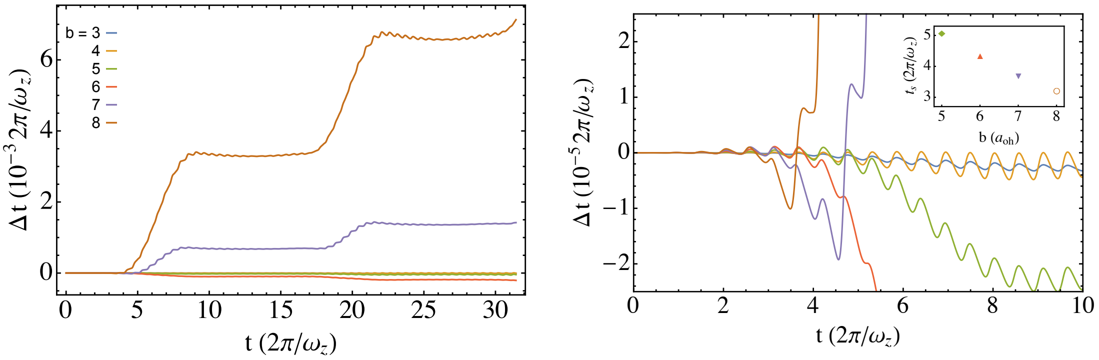

(a) (b)

Figure 4.8: Accumulated phase difference over time for different initial displacements but same coupling $\beta_{12}/\beta_{22} = 0.003$. The phase difference is calculated by comparing the phase of the oscillations to the one at low amplitude, $b = 2a_{ho}$. For $b \geq 5$, we can observe fast increases of the phase followed by well defined plateaus. The time at which the phase difference starts to increase, t_s, diminishes when the initial displacement increases, see the zoom on fig (b) and the associated inset.

the analysis since it provides the pertinent quantities to look at. Similarly to the procedure used in [187] to observe collective excitations in a 2D Bose gas, we apply the PCA to our density images to reveal the subtle phenomena at play in our system. In the following we will briefly discuss how the PCA is used and show some example of results.

Method

In short, the PCA is just the diagonalisation of a covariance matrix. The eigenvectors are the different orthogonal modes of fluctuations and the eigenvalues their relative importance. As input data for the PCA, we use integrated density profiles

$$\bar{n}_i(x, z, t) = \int dy\, n_i(x, y, z, t), \quad i = 1, 2. \tag{4.35}$$

which can be obtained in an experiment by absorption imaging.
All the profiles are arranged in a single matrix (one matrix per cloud)

$$M_i = (\bar{n}_i(r_k, t_l))_{k,l}, \quad k = 1 \dots N_p, \quad l = 1 \dots N_I. \tag{4.36}$$

so that each line of the matrix represents the time evolution of the density at a specific pixel. In practice we use $N_I = 4000$ images with $N_P = 128 \times 500$ pixels. The associated covariance matrix is then

$$C_i = \frac{1}{N_I - 1} \tilde{M}_i^T \tilde{M}_i, \tag{4.37}$$

where $\tilde{M}_i(k, l) = \bar{n}_i(r_k, t_l) - \langle \bar{n}_i(r_k) \rangle_t$ and $\langle ... \rangle_t$ is a time-average. C_i is thus a 4000×4000 symmetric and positive matrix. The diagonalization of C_i provides a set of N_I real eigenvalues $\lambda_{i,k}$ and normalized eigenvectors $P_{i,k}$ (the principal components). The spatial modes of fluctuations $\tilde{u}_{i,k}$ are then

$$\tilde{u}_{i,k} = \frac{1}{\sqrt{\lambda_{i,k}(N_I - 1)}} \tilde{M}_i P_{i,k}, \tag{4.38}$$

and their time evolution $a_{i,k}(t)$ are given by

$$a_{i,k}(t_l) = \sqrt{\lambda_{i,k}(N_I - 1)}P_{i,k}(l), \tag{4.39}$$

with $P_{i,k}(l)$ the l-th coefficient of the vector $P_{i,k}$. Hence, the density can be written as

$$\tilde{n}_i(r_k, t_l) = \langle \tilde{n}_i(r_k) \rangle_t + \sum_{p=1}^{N_I} a_{i,p}(t_l)\tilde{u}_{i,p}(r_k), \tag{4.40}$$

with the properties

$$\langle a_{i,k_1} | a_{i,k_2} \rangle_t = \sum_{l=1}^{N_I} a_{i,k_1}(t_l) a_{j,k_2}(t_l) = \lambda_{i,k_1}(N_I - 1)\delta_{k_1,k_2}, \tag{4.41}$$

$$\langle \tilde{u}_{i,k_1} | \tilde{u}_{i,k_2} \rangle_r = \sum_{l=1}^{N_P} \tilde{u}_{i,k_1}(r_l)\tilde{u}_{j,k_2}(r_l) = \delta_{k_1,k_2}. \tag{4.42}$$

In the limit of infinitesimal time steps and pixels we can write

$$\tilde{n}_i(x, z, t) = \langle \tilde{n}_i(x, z) \rangle_t + \sum_{p=1}^{\infty} a_{i,p}(t)\tilde{u}_{i,p}(x, z). \tag{4.43}$$

The PCA thus provides a decomposition of each image as a sum of modes. In the limit of small fluctuations, we can expect them to be associated to the elementary excitations of the superfluids[5]. However, in our case, the dipole mode is strongly excited by the initial displacement. To circumvent this problem we center each image on the cloud center of mass which filters out the dipole mode. Using 4000 images distributed on a total time span of 32 periods of dipole oscillations allows to have a frequency resolution of $\Delta\nu = \nu_z/32$ and maximal observable frequency of $\nu_{\max} = 62.5\nu_z$ [6].

Examples of output/Zoology of the PCA modes

Applied to our cloud images, the PCA gives for each of them a set of 4000 modes together with their associated eigenvalues and their temporal evolutions. This is clearly a lot of information, but most of it can be ignored. Indeed, only a limited number of modes play a non-negligible role in the fluctuations. This can be noticed on the distribution of the eigenvalues, usually at least 99% of the eigenvalues are 10^6 times smaller than the largest one as shown in Fig. 4.9 [7]. For each run, we typically limit our analysis to the 10-30 most populated modes given by the PCA. An example of mode we obtain using the PCA on the clouds images is shown in Fig. 4.10. More examples are shown in Appendix C. We observe various types of behavior that we can sort in 4 categories:

- Parametric modes. As we will describe it later on, a numbers of PCA modes exhibit a parametric type of behavior, i.e. they seem to emerge spontaneously from the noise after some time. In addition, they exhibit a dominant frequency peak in the Fourier space. Finally, these modes are observed for both clouds but only for large amplitudes of oscillations.

---

[5] And in the limit of a small coupling between the superfluids, since we compute a PCA on each cloud separately.

[6] Contrary to a Fourier analysis, spatial modes with frequency higher than $\nu_{\max}$ can also be identified by the PCA [187].

[7] The PCA is computed using double precision variables.

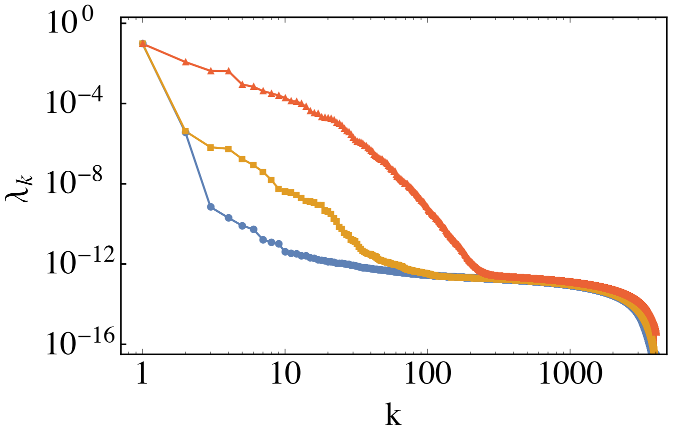

Figure 4.9: List of the eigenvalues given by the principal component analysis applied to the small cloud ($i = 1$) density images for three different simulations (same coupling $\beta_{12}/\beta_{22} = 0.003$). Blue dots: Initial displacement $b = 2$. Orange squares: Initial displacement $b = 5$. Red triangles: Initial displacement $b = 8$.

- Linearly forced modes. Again, this designation will be justified later. They usually display a quasi-periodic time evolution and a rich Fourier spectrum. They can be seen for both clouds at all amplitudes.

- The filtered dipole modes. The recentering process will typically make the condensates oscillate with a random amplitude of at most $1\text{px} = 1/16a_{ho}$. Still, the PCA is able to identify the dipole modes and they remain in the most populated modes if the superfluids are almost not perturbed by the oscillations. This is the case for many simulations especially those at low amplitude of oscillations where only a few modes are excited. The filtered dipole modes are easily recognizable due to their seemingly random time evolution.

- Harmonic modes. When subject to a perturbation, high order terms of the clouds response also contribute as modes identified by the PCA. For example, for a given perturbation along the z-axis $f_z(t)$, we have for the density $n(z + f_z(t)) - n(z) = f_z(t)\partial_z n(z) + \frac{1}{2}f_z^2(t)\partial_z^2 n(z) + ...$ The harmonic modes are simply related to the fundamental mode (spatial derivative and frequency harmonics) and can be easily identified.

Example of each types of modes are shown in Fig. 4.11. The two first categories are not completely exclusive since it is possible, in principle, for a mode to have both behaviors. Finally, to be completely exhaustive, there are also all the non-physical modes that are just associated to the numerical noise of the simulation and the spurious modes coming from a bad frequency resolution of the PCA (i.e. they are some unknown combinations of several physical modes). They actually constitute the major part of the weakly populated modes and is the PCA's main limitation to identify physical modes[8].

---

[8] The presence of high harmonics modes with a broad frequency spectrum prevent the PCA to identify weakly populated modes as they will share similar frequencies

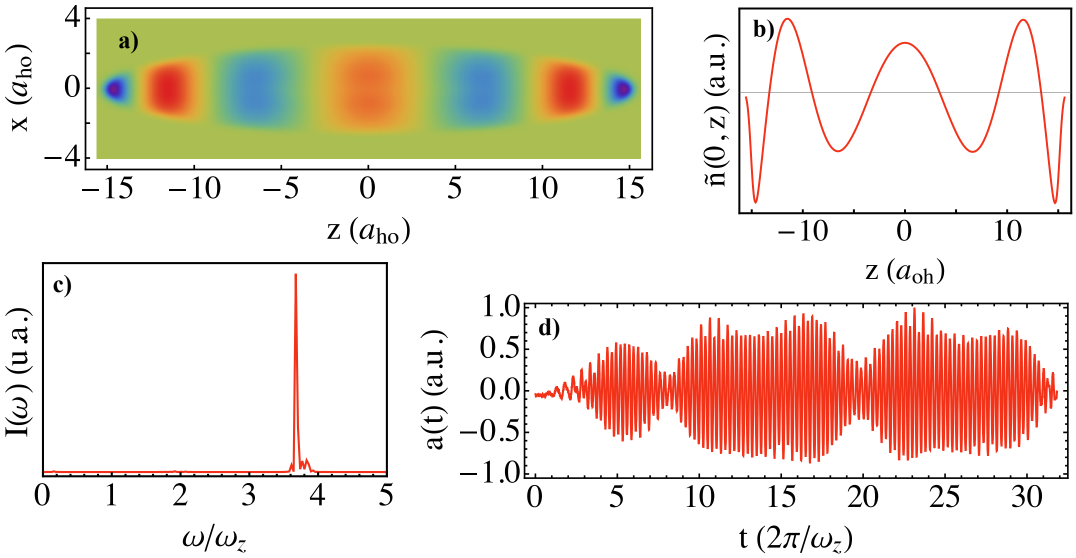

Figure 4.10: Example of a fluctuation mode identified by the PCA for the large cloud ($i = 2$). Its spatial structure is shown in a) and b). Its time evolution is shown in d) and its Fourier analysis in c). The number of spatial nodes is 6 and the mode oscillates at a frequency of $3.68\,\omega_z$.

4.3.3 PCA's modes versus collective excitations of the superfluids

The question is now whether the PCA modes can be related to the true elementary excitations of the superfluids or not. To answer this, we will compare them to theoretical models of collective excitations in elongated superfluids.

Hydrodynamic equations of a superfluid

In the hydrodynamic limit, the dynamic of a (single) superfluid is described by a set of two equations

$$m\frac{\partial \mathbf{v}}{\partial t} + \frac{m}{2}\nabla \mathbf{v}^2 = -\nabla\left(U + \mu\right), \tag{4.44}$$

$$\frac{\partial n}{\partial t} + \nabla(n\mathbf{v}) = 0, \tag{4.45}$$

where $\mathbf{v}$ is the velocity field and the chemical potential μ is defined locally so that the global chemical potential is $\mu_g = U + \mu$. The excitation spectrum can be obtained by considering small perturbations on top of the superfluid ground state:

$$\mathbf{v} = \mathbf{v}_0 + \delta\mathbf{v}, \tag{4.46}$$

$$n = n_0 + \delta n, \tag{4.47}$$

where $\mathbf{v}_0$ and n_0 are solutions of equations (4.44), (4.45) and we have the weak perturbation conditions $\delta n/n \ll 1$. In the center of mass frame, $\mathbf{v}_0 = \mathbf{0}$ and we have

$$m_i\frac{\partial \delta\mathbf{v}}{\partial t} = -\nabla\left(\frac{\partial \mu}{\partial n}\delta n\right), \tag{4.48}$$

$$\frac{\partial \delta n}{\partial t} = -\nabla(n_0\delta\mathbf{v})\ . \tag{4.49}$$

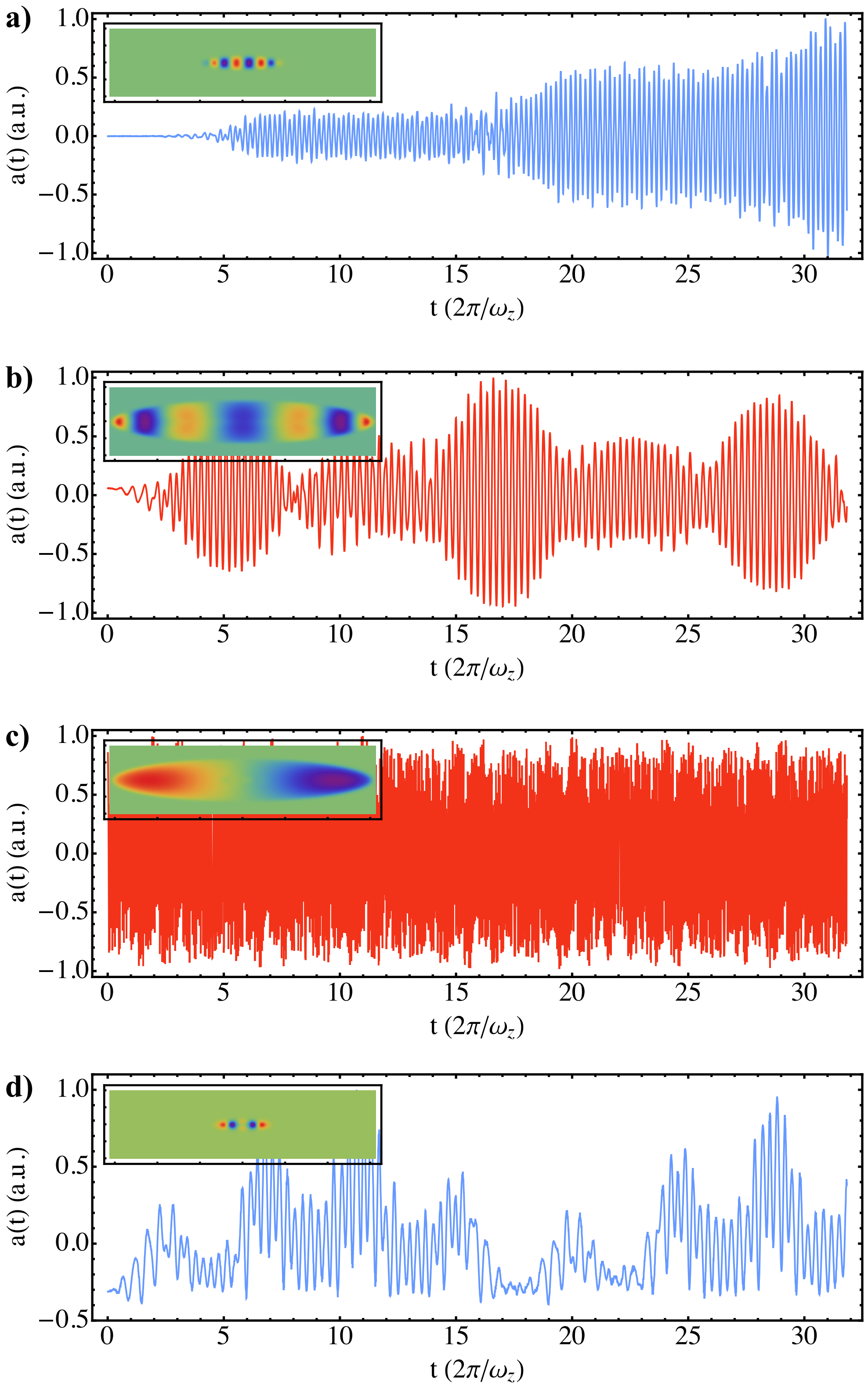

Figure 4.11: Examples of a mode's amplitude and spatial structure (inset) for each of the four categories listed in the main text. a) Parametric mode. b) Linearly forced mode. c) Filtered dipole mode. d) High order "clone" mode. (easily seen by its asymmetric time evolution with respect to the horizontal axis)

In terms of chemical potential shift $\delta\mu = \frac{\partial\mu}{\partial n}\delta n$ we get

$$\frac{\partial^2 \delta\mu}{\partial t^2} = \frac{1}{m}\frac{\partial\mu}{\partial n}\nabla(n_0\nabla\delta\mu)\ . \tag{4.50}$$

We can thus define an operator

$$\mathcal{L} = -\frac{1}{m}\frac{\partial\mu}{\partial n}\nabla(n_0\nabla)\ . \tag{4.51}$$

$\mathcal{L}$ is symmetric and positive for the scalar product

$$\langle\phi|\psi\rangle = \int d^3r \frac{\partial n}{\partial\mu}\phi^*\psi\ . \tag{4.52}$$

Therefore stationary solutions of equation (4.50) can be sought as an orthogonal set of eigenstates of $\mathcal{L}$, $(v_k)_k$ with

$$\mathcal{L}v_k = \omega_k^2 v_k\ , \tag{4.53}$$

where ω_k is the associated eigenfrequency.
And we have

$$n(\mathbf{r},t) = n_0(\mathbf{r}) + \sum_k a_k \cos(\omega_k t + \phi_k)u_k(\mathbf{r}), \tag{4.54}$$

where

$$u_k = \frac{\partial n}{\partial\mu}v_k. \tag{4.55}$$

Since the superfluids are Bose-Einstein condensates in the mean field regime, we have $\frac{\partial\mu}{\partial n} = g$. Hence, the scalar product, eq. (4.52), is the same as the one used by the PCA, and its modes can be expected to be the collective excitations [9].

Hydrodynamic modes of an elongated superfluid

To be more quantitative, it is useful to know the exact shape of the collective excitations and their frequency spectrum. In the case where $\omega_\perp \gg \omega_z$, relevant for many experimental systems and for our simulation, the low energy dynamics of a superfluid is essentially one-dimensional. In [169], the spectrum of hydrodynamic modes in a highly deformed trap was calculated. In the case where $\mu \gg \hbar\omega_\perp \gg \hbar\omega_z$, the cloud is in the Thomas-Fermi regime in both radial and axial directions and we have the following dispersion relation for the low energy modes:

$$\omega_k = \frac{1}{2}\sqrt{k(k+3)}\,\omega_z, \tag{4.56}$$

where k is a positive integer. In particular, $k = 1$ corresponds to the dipole mode $\omega_1 = \omega_z$ and $k = 2$ to the breathing mode $\omega_2 = \sqrt{5/2}\omega_z$. The corresponding solutions are the Gegenbauer polynomials[10] $G_n^{(3/2)}$. For $k \gg 1$, we recover a linear dispersion $\omega_k = k\,\omega_z/2$ and we have a simple expression for the corresponding solutions of eq. (4.53) using a WKB approximation [190]

$$\bar{v}_k(z) = \sqrt{\frac{2m\Delta\omega\bar{c}(z)}{\bar{n}_0(z)}}\cos\left[\int_0^z dz' \frac{\omega_k}{\bar{c}(z')} + k\frac{\pi}{2}\right], \tag{4.57}$$

---

[9] We are only interested in real solutions, so the complex conjugate is not relevant

[10] The Gegenbauer polynomials $G_n^{(m)}$ are solutions to the differential equation $(1-z^2)y'' - (2m+1)zy' + n(n+2m)y = 0$ and orthogonal for the scalar product $\langle f|g\rangle = \int_{-1}^{1} dz(1-z^2)^{m-1/2}fg$.

where the $\bar{\cdot}$ notation indicates a radially integrated quantity and $\Delta\omega^{-1} = R_z/2\pi\bar{c}(0)$ is the density of state. We have the following expressions for the radially integrated density

$$\bar{n}_0(z) = \bar{n}_0(0)\left(1 - \left(\frac{z}{R_z}\right)^2\right)^2, \tag{4.58}$$

and the radially averaged sound velocity

$$\bar{c}(z) = \bar{c}(0)\left(1 - \left(\frac{z}{R_z}\right)^2\right)^{1/2}, \tag{4.59}$$

with $\bar{c}(0) = \sqrt{\mu/2m}$ the radially averaged central sound density. Theses results are valid as long as $kR_\perp \ll R_z$, otherwise the radial degrees of freedom come into play. In particular the dispersion relation becomes sub-linear at large momentum [174, 191, 169]. In the simulation, the condition $\mu \gg \hbar\omega_\perp$ translates as $R_z \gg 3\sqrt{2}a_{ho} \simeq 3.5a_{ho}$ which is well satisfied for the large condensate ($R_{z,2} = 15.45a_{ho}$) but not for the small condensate ($R_{z,1} = 4.47a_{ho}$).
Another situation of interest is the regime where $\hbar\omega_\perp \gg (\mu - \hbar\omega_\perp) \gg \hbar\omega_z$, which corresponds to the case where the condensate occupies the lowest oscillator level in the radial direction. In that case, the dispersion relation is [192, 169]

$$\omega_k = \sqrt{\frac{k(k+1)}{2}}\,\omega_z, \tag{4.60}$$

and the associated eigenfunctions are Legendre polynomials. For large k, they can be described by similar WKB modes as in eq. (4.57). The small condensate ($i = 1$) should be better described by this second situation as we have $\hbar\omega_\perp \simeq 1.5(\mu_1 - \hbar\omega_\perp)$.

Comparison with the PCA's modes

Since we deal with a quasi one-dimensional geometry, the low-energy collective excitations can be indexed by their number of nodes. Thus, a PCA mode with k nodes should be equal to $\tilde{u}_k$ up to a normalization constant. As we have the relation[11]

$$\int \tilde{u}_k(x,z)dx \propto \left(1 - \left(\frac{z}{R_z}\right)^2\right)\bar{v}_k(z), \tag{4.61}$$

we can directly compare the PCA's mode of the large condensate ($i = 2$) to the solutions eq. (4.57) by a simple integration over the x axis. Some examples are shown in Fig. 4.12. The agreement is quite good but diminishes as k increases inasmuch as radial degrees of freedom were not taken into account by the model. For the small condensate, the Legendre polynomials fail to describe accurately the PCA's modes which are better described using an ad-hoc function $(1 - (z/R_z)^2)^{7/2}G_n^{(9/2)}(z/R_z)$. This discrepancy is probably due to the fact that the condition $\hbar\omega_\perp \gg \mu_1 - \hbar\omega_\perp$ does not hold.
Concerning the spectra, since some PCA's modes can exhibit a complex time evolution with multiple frequencies involved, we restrict the analysis to the modes where a single

---

[11] Indeed, in a regime where $\mu \gg \hbar\omega_\perp \gg \hbar\omega_z$, we have a similar relation as in eq. (4.55) for the doubly integrated modes: $\bar{u}_k = \bar{v}_k\partial_\mu\bar{n}$.

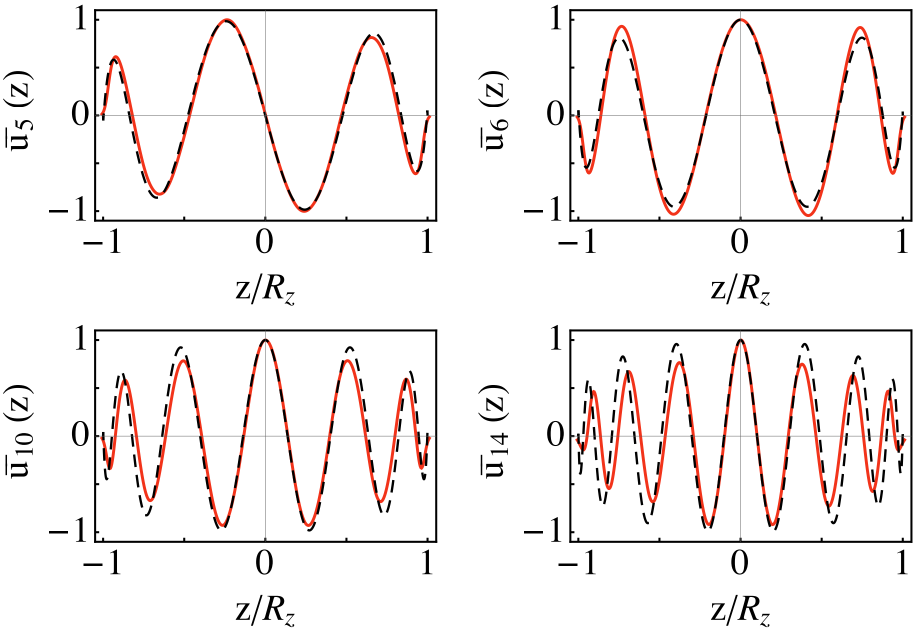

Figure 4.12: Comparison between PCA's mode of the large cloud $i = 2$ (red line) and the WKB modes of eq. (4.57) (black dashed line) for k =5, 6, 10, and 14.

dominant frequency peak is observed. The comparison to the two dispersion relations eq. (4.56,4.60) is displayed in Fig. 4.13 and shows good agreement between the measured and predicted frequencies. It confirms the one-dimensional character of the system but more importantly it shows that many of the PCA's modes are not just some numerical artifacts but true collective excitations in superfluids. All the associated information can be then used to study the dynamics of the system.

4.3.4 Linearly forced modes

We now move to the study of a particular category of observed modes during the oscillations of the two condensates, the linearly forced modes. To first order, a superfluid is just a moving perturbation potential for the other one and vice-versa. Hence, different collective modes are forced by this oscillating perturbation and depending on the spatial overlap and frequency matching it can be more or less enhanced. This is a realistic version of the Landau experiment where the perturbation is just a point-like impurity moving at constant speed in a homogeneous superfluid. However, an important difference is the absence of an associated critical velocity in our case. Indeed, as observed in the simulation and as we will justify below there is no velocity threshold for observing these linearly forced modes in our system. We will first derive a hydrodynamic model to explain this phenomenon and then use it to reproduce the observed behavior of some PCA's modes.

Hydrodynamic model for two coupled superfluids

As the modes identified by the PCA are hydrodynamic modes, we can restrict our analysis of the counterflowing Bose-Einstein condensates to an hydrodynamic approach. This is also useful as it can be also applied to more general superfluids.

We now have to consider the case of two coupled BECs labelled by $i, j \in \{1, 2\}$.

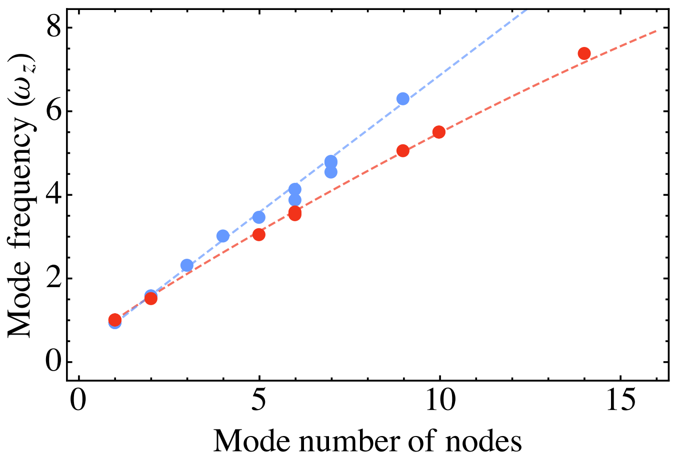

Figure 4.13: Frequency of PCA's modes versus their number of nodes. Blue circles : Small condensate's modes ($i = 1$). Red circles: Large condensate's modes ($i = 2$). Red dashed line: Dispersion relation for an elongated condensate with a large chemical potential $\mu \gg \hbar\omega_\perp$, eq. (4.56). Blue dashed line: Dispersion relation for an elongated condensate with a small chemical potential $\mu \sim \hbar\omega_\perp$, eq. (4.60).

They are described by a set of coupled hydrodynamic equations in their respective center of mass frame

$$m_i \frac{\partial \mathbf{v}_i}{\partial t} + \frac{m}{2}\nabla \mathbf{v}_i^2 = -\nabla\left(U_i + \mu_i + g_{ij} n_j\right), \tag{4.62}$$

$$\frac{\partial n_i}{\partial t} + \nabla(n_i \mathbf{v}_i) = 0 , \tag{4.63}$$

where n_j is a time dependent function $f(\mathbf{r} \pm \mathbf{r}_{\rm rel}(t))$ where $\mathbf{r}_{\rm rel}$ is the relative position between the two superfluids.

If the coupling between the superfluids is weak, we get to first order for the perturbations $\delta\mu_i = \mu_i - \mu_{i,0}$

$$\frac{\partial^2 \delta\mu_i}{\partial t^2} = -\mathcal{L}_i\left[\delta\mu_i + g_{ij}(n_{j,0} + \delta n_j)\right] , \tag{4.64}$$

with

$$\mathcal{L}_i = -\frac{1}{m_i}\frac{\partial \mu_i}{\partial n_i}\nabla(n_{i,0}\nabla) . \tag{4.65}$$

Again, we can express the chemical potentials as a sum of eigenstates of the operators $\mathcal{L}_i$, denoted $(v_{i,k})_k$

$$\delta\mu_i = \sum_k a_{i,k} v_{i,k} , \tag{4.66}$$

with

$$\mathcal{L}_i v_{i,k} = \omega_{i,k}^2 v_{i,k} \tag{4.67}$$

so that

$$\frac{d^2 a_{i,k}}{dt^2} + \omega_{i,k}^2 a_{i,k} = \omega_{i,k}^2 g_{ij}\left(\langle v_{i,k}|n_{j,0}\rangle_i + \langle v_{i,k}|\delta n_j\rangle_i\right) , \tag{4.68}$$

with

$$\langle\phi|\psi\rangle_i = \int d^3r \frac{\partial n_i}{\partial \mu_i}\phi^* \psi . \tag{4.69}$$

Furthermore, we have

$$\delta n_i = \frac{\partial n_i}{\partial \mu_i} \sum_k a_{i,k} v_{i,k} \ , \tag{4.70}$$

such that

$$\langle v_{i,k} | \delta n_j \rangle_i = \sum_q a_{j,q} \int d^3 r \frac{\partial n_i}{\partial \mu_i} \frac{\partial n_j}{\partial \mu_j} v^*_{i,k} v_{j,q} \ . \tag{4.71}$$

It follows immediately that

$$\frac{d^2 a_{i,k}}{dt^2} + \omega^2_{i,k} a_{i,k} = \omega^2_{i,k} g_{ij} \left(A_{i,k} + \sum_q B_{i,kq} a_{j,q} \right) \ , \tag{4.72}$$

with

$$\begin{aligned} A_{i,k} &= \langle v_{i,k} | n_{j,0} \rangle_i \ , & (4.73) \\ B_{i,kq} &= \int d^3 r \frac{\partial n_i}{\partial \mu_i} \frac{\partial n_j}{\partial \mu_j} v^*_{i,k} v_{j,q} \ , & (4.74) \end{aligned}$$

Again, we stress that the quantities $n_{j,0}$ and $v_{j,q}$ are time dependent functions $f(\mathbf{r} \pm \mathbf{r}_{\text{rel}}(t))$ where $\mathbf{r}_{\text{rel}}$ is the relative position between the two superfluids. Equations (4.72) can thus be seen as a set of coupled driven and parametric harmonic oscillators. The first term of the rhs is a forcing term and should be a priori dominant since excitations are considered to be weakly populated initially. However, the second term, which couples the modes of the two superfluids with time-dependent coefficients can lead to parametric-like resonant contributions and allow to explain the second class of observed PCA's modes, the parametric modes. Before that, let's study more thoroughly the physics associated to the first rhs term A_{ik}.

Homogeneous case

First, we can look at the ideal case imagined by Landau where the impurity is point-like (let assume the small condensate $i = 1$) and moving at constant speed $\mathbf{V}$ through an homogeneous superfluid ($i = 2$). Then the collective excitations are plane waves

$$v_{2,k} = \frac{1}{\sqrt{V}} \sqrt{\frac{\partial \mu_2}{\partial n_2}} \mathrm{e}^{i\mathbf{k}.\mathbf{r}}, \tag{4.75}$$

where V is a quantification volume.
The perturbation is a Dirac delta function $\propto \delta(\mathbf{r} - \mathbf{V}t)$ and we have

$$A_{2,k} \propto \mathrm{e}^{i\mathbf{k}.\mathbf{V}t}, \tag{4.76}$$

which is a simple oscillating forcing term.
The forcing is resonant when

$$\omega_{2,k} = \mathbf{k}.\mathbf{V}. \tag{4.77}$$

Since we have a linear dispersion relation $\omega_{2,k} = |\mathbf{k}| \, c_2$, where c_2 is the sound velocity, phonons can only be resonantly excited if

$$|\mathbf{V}| \geq c_2, \tag{4.78}$$

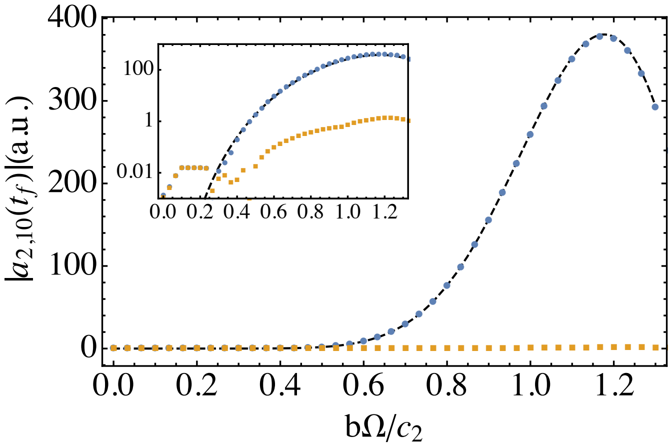

Figure 4.14: Amplitude of a collective mode (a plane wave) forced by a sinusoidal relative movement $\mathbf{r}_{\text{rel}} = b\sin(\Omega t)\mathbf{e}_z$ after $t_f = 200 \times 2\pi/\Omega$ with $|A_{k,2}| = 0.1$. Blue circles: resonant case $\omega_{2,k} = 10\Omega$ ($n = 10$). Yellow squares: non-resonant case $\omega_{2,k} = 9.99\Omega$. The black dashed line is the expected amplitude in the resonant case. The inset is the same data shown in log scale. The excitation growth rate peaks at $nb\Omega \simeq c_2$ but there is no threshold associated to the sound velocity.

which is the usual Landau criterion for superfluidity. Above this critical velocity excitations will grow linearly with time at a rate $\omega_{2,k}|A_{2,k}|/2$.
Now, for a sinusoidal relative movement $\mathbf{r}_{\text{rel}} = b\sin(\Omega t)\mathbf{e}_z$, we get

$$A_{2,k} \propto \mathrm{e}^{ik_z b\sin(\Omega t)} \propto \sum_{n=-\infty}^{+\infty} J_n(k_z b)\,\mathrm{e}^{in\Omega t}, \tag{4.79}$$

The appearance of Bessel functions here is not surprising but will have important consequences in the following. We will have a resonance whenever there exists a set $\{n, k\}$ such that $\omega_{2,k} = n\Omega$. This criterion is independent of the relative velocity between the superfluids and can therefore occur at any amplitude. In the resonant case, the amplitude of the excitation will grow as $\omega_{2,k}|A_{k,2}|J_n(k_z b)t$ as shown in Fig. 4.14 and is maximal around $b\Omega \simeq c_2$. Both in experiments and in our simulation the impurity has always a finite size s. It sets an upper bound for the validity domain of the Landau model: Only excitations with $|\mathbf{k}| \ll s$ will see a forcing term as in eq. (4.76). Additionally, the collective excitations in a trapped superfluid are quantized, so, a priori solely a small number of modes can be excited resonantly by the impurity.

Simulation case

Generally speaking, for any kind of density profile and collective modes, we can expand $A_{2,k}$ in powers of z_{rel}:

$$A_{i,k}(t) = \sum_{k=0}^{\infty} (\pm 1)^n \frac{z_{\text{rel}}^n}{n!} \langle v_{i,k}|\partial_z^n n_{j,0}\rangle_i, \tag{4.80}$$

with $\mathbf{r}_{\text{rel}}(t) = z_{\text{rel}}(t)\mathbf{e}_z$. Depending on the involved scalar products, $A_{i,k}$ can contain a large set of frequencies and therefore excite more or less resonantly a given mode.

Since the density profile is even, only odd/even terms will be non null for respectively an odd/even mode. Additionally, a Thomas-Fermi profile is a polynomial of degree two in position so that only the first three terms are non zero ($\partial_z^k n_{j,0} = 0$ for $k > 3$). In practice, higher-order terms can appear as the clouds are not perfectly in the Thomas-Fermi regime (which is the case for large interspecies coupling).

We should be able to reproduce all the linearly forced modes time evolution using the solution of

$$\frac{d^2a}{dt^2} + \omega^2 \left(a + \sum_k \alpha_k z_{\mathrm{rel}}^k \right) = 0, \tag{4.81}$$

where the α_k are numerical coefficients (they can be accurately estimated using models for the collectives modes introduced previously).

In the simple case where only one term of the sum is involved, the only unknown is the value of the mode frequency (but again it can be precisely estimated), the remaining unknown coefficient α_k is just a scaling factor. This configuration is expected to be relevant for the lowest frequency modes and for a small initial displacement so that high order terms can be neglected. Indeed, we are able to accurately reproduce the time evolution of the breathing mode ($k = 2$) of both clouds see Fig. 4.15 by using only the $z_{\mathrm{rel}}^2(t)$ term. It allows for the extraction of the breathing mode frequency with a good precision and we find $\omega_{1,2}/\omega_z = 1.490(3)$ and $\omega_{2,2}/\omega_z = 1.580(3)$ for the small condensate ($i = 1$) and large condensate ($i = 2$) respectively. They are in very good agreement with the expected frequencies $\omega_{1,2}/\omega_z = \sqrt{15/7} \simeq 1.464$ and $\omega_{2,2}/\omega_z = \sqrt{5/2} \simeq 1.581$ using eqs (4.56, 4.60).

Another interesting scenario is when there is a quasi resonance between a mode frequency and a combination of the two frequencies present in the dipole oscillations. In this particular scenario, the mode amplitude should increase linearly with time. This is what we observed for the mode $k = 10$ of the large cloud in two sets of simulations, $\beta_{22}/\beta_{12} = 0.003$ and $\beta_{22}/\beta_{12} = 0.031$. The measured mode frequency is $\omega_{2,10}/\omega_z = 5.697(3)$ (expected value is $\omega_{2,10}/\omega_z = \sqrt{65/2} \simeq 5.701$) which is close to $2 \times 1 + 4 \times \sqrt{6/7} \simeq 5.696$, a frequency that is present in the term z_{rel}^6. Similarly to the homogeneous situation, see Fig. 4.14, the mode's amplitude exhibits a Bessel-like behavior eq. (4.79) when varying the relative velocity as shown in Fig. 4.16. As β_{22}/β_{12} is increased and the frequencies of dipole oscillations are shifted, the resonance with this particular mode fades away and is not observed in the other simulations. However, some other resonances become possible and for $\beta_{22}/\beta_{12} = 0.186$, the $k = 6$ mode takes over as $\omega_{2,6} = 3.669(3)\omega_z \simeq 2(\tilde{\omega}_1 + \tilde{\omega}_2)$. In particular, it explains the unexpectedly large damping observed on the dipole oscillations for this particular set of simulations shown in Fig. 4.6.

Conclusion

This simple linear forcing model explains a large set of the observed PCA's modes. It demonstrates that linear forcing is one of the dominant phenomenon at play in our system. Contrary to the ideal Landau set up, the collective modes can be resonanlty excited even at low relative speed and the usual criterion for superfluidity $v_c = c_i$ is not observed in our system. It is mainly due to the oscillating behavior of the relative movement, as also pointed out in [172]. A comprehensive understanding of the resonance conditions is still open and depending on the atomic mass ratio and interaction parameters, some collective modes can be resonantly excited or completely absent during the dynamics. However, with a precise knowledge of the system's parameters and elementary excitations, one can

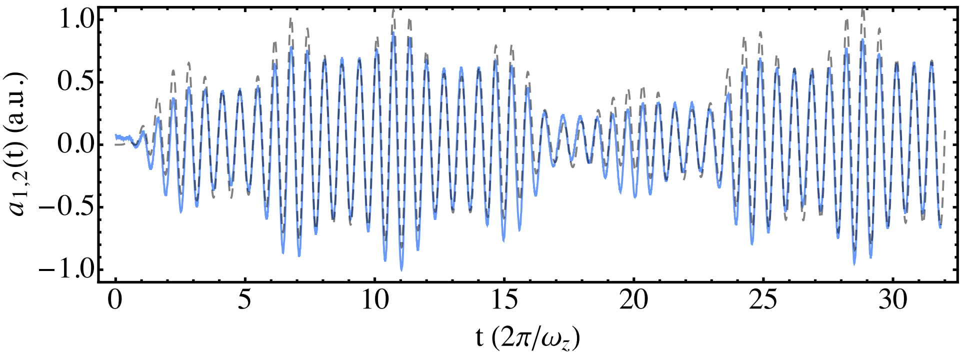

(a) $a_{1,2}(t)$

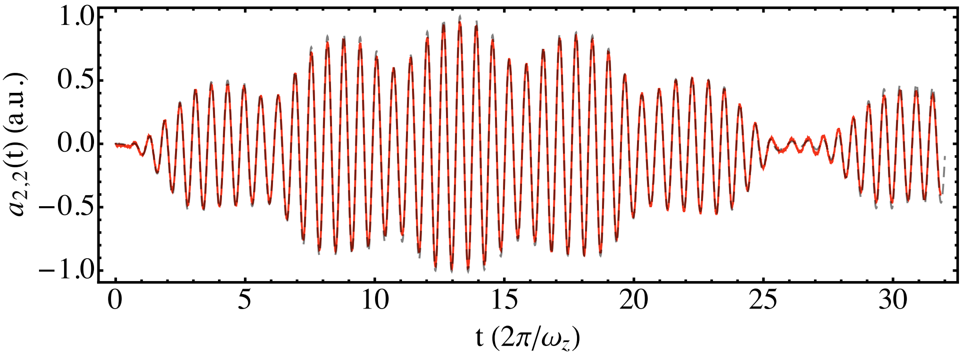

(b) $a_{2,2}(t)$

Figure 4.15: Time evolution of the breathing mode ($k = 2$) of both clouds for the simulation run $\beta_{22}/\beta_{12} = 0.291$ and $b = 1$. Blue line (fig (a)): breathing mode of the small condensate $i = 1$. Red line (fig (b)): breathing mode of the large condensate ($i = 2$). Dashed line is a fit using the solution of eq. (4.81) with only the α_2 coefficient being non-zero in the sum. The fit allows to extract the mode frequency with a good precision: we find $\omega_{1,2}/\omega_z = 1.490(3)$ and $\omega_{2,2}/\omega_z = 1.580(3)$ in good agreement with the predicted values $\omega_{1,2}/\omega_z = \sqrt{15/7} \simeq 1.464$ and $\omega_{2,2}/\omega_z = \sqrt{5/2} \simeq 1.581$.

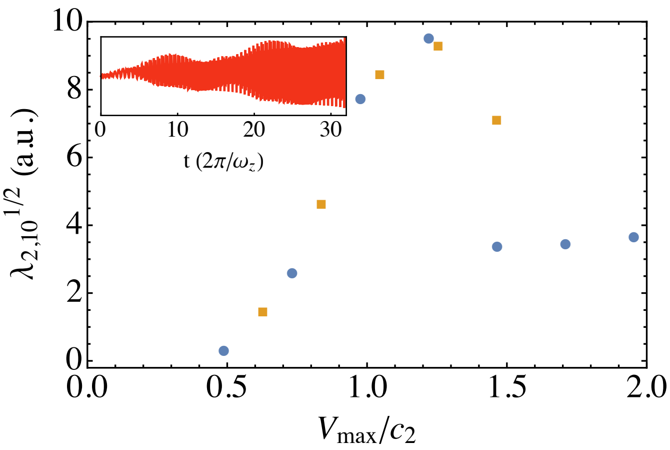

Figure 4.16: Eigenvalue of the mode $k = 10$ for the large cloud ($i = 2$) versus maximal relative velocity during the dipole oscillations for two simulation runs $\beta_{22}/\beta_{12} = 0.003$ (blue circles) and $\beta_{22}/\beta_{12} = 0.031$ (orange squares). Inset: example of associated time evolution showing the typical linear increase of the amplitude at resonance. The two data sets show a similar behavior to what is expected for a resonant mode in the homogeneous case as shown in Fig. 4.14.

predict when such resonance would happen. It might be possible to exploit this idea experimentally to excite some chosen high order mode via the dipole mode oscillations of the two superfluids.

4.3.5 Parametric modes

Another important class of mode that we observe in our simulation using the PCA are the so-called parametric modes. As we will show below, they originate from the second rhs term in eq. (4.72), $\sum_q B_{i,kq} a_{j,q}$, which couples modes of both superfluids and can lead to parametric resonances. In the homogeneous case and uniform relative speed, the parametric instability occurs only above a critical velocity equal to the sum of the sound velocities $v_c = c_1 + c_2$. Contrary to the linear forcing term, this threshold is preserved when the relative movement is not uniform anymore and the superfluids are not homogeneous. We believe that this mechanism explains the observation of a well defined threshold for dissipation in the counterflowing experiment and their large associated critical velocity.

Homogeneous case

For homogeneous superfluids moving with a constant and uniform relative velocity $\mathbf{V}$, the excitations are planes waves. We can compute the different terms in equations (4.72). From (4.74) and (4.75) we obtain:

$$B_{i,kq} = \left(\frac{\partial \mu_1}{\partial n_1}\frac{\partial \mu_2}{\partial n_2}\right)^{-1/2} \mathrm{e}^{i\mathbf{k}.\mathbf{V}t}\delta_{\mathbf{k},\mathbf{q}} \tag{4.82}$$

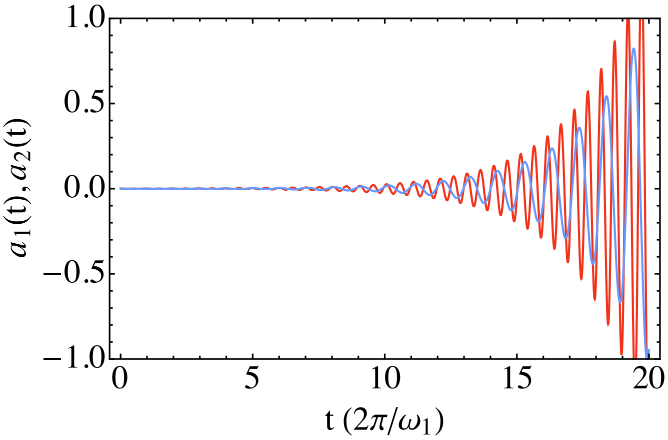

Figure 4.17: Evolution of two modes (1: red curve, 2: green curve) with frequencies $\omega_2 = 2\omega_1$ and coupled via a cosine term $\varepsilon\cos(\alpha(\omega_1+\omega_2)t)$ with $\varepsilon = 0.2$ and $\alpha = 0.98$. The amplitude increases exponentially.

and $A_{i,k} = 0$. Only modes with the same wave vector are coupled and equations (4.72) simplify to

$$\frac{d^2 a_{1,k}}{dt^2} + \omega_{1,k}^2 (a_{1,k} - \varepsilon \mathrm{e}^{i\mathbf{k}.\mathbf{V}t} a_{2,k}) = 0, \tag{4.83}$$

$$\frac{d^2 a_{2,k}}{dt^2} + \omega_{2,k}^2 (a_{2,k} - \varepsilon \mathrm{e}^{-i\mathbf{k}.\mathbf{V}t} a_{1,k}) = 0, \tag{4.84}$$

where

$$\varepsilon = \left(\frac{g_{12}^2}{\frac{\partial\mu_1}{\partial n_1}\frac{\partial\mu_2}{\partial n_2}} \right)^{1/2} . \tag{4.85}$$

These equations can be seen as coupled Mathieu's equation describing a parametric resonance between two modes, as illustrated in figure 4.17. In the limit $\varepsilon \to 0$, the instability occurs when[12]

$$|\mathbf{k}.\mathbf{V}| = \omega_{1,k} + \omega_{2,k}, \tag{4.86}$$

which readily gives the Landau criterion for superfluidity for the case of counterflowing superfluids. Indeed, to be able to create excitations in the system, a necessary condition is:

$$|\mathbf{V}| \geq c_1 + c_2. \tag{4.87}$$

We recover a critical velocity that is the sum of the two sound velocities $v_c = c_1 + c_2$, as found in [86]. Increasing the coupling ε will enlarge the instability window and we obtain the condition

$$\omega_{1,k} + \omega_{2,k} - \varepsilon\sqrt{\omega_{1,k}\omega_{2,k}} \leq |\mathbf{k}.\mathbf{V}| \leq \omega_{1,k} + \omega_{2,k} + \varepsilon\sqrt{\omega_{1,k}\omega_{2,k}}, \tag{4.88}$$

which gives a lower critical velocity

$$v_c = c_1 + c_2 - \varepsilon\sqrt{c_1 c_2}\ , \tag{4.89}$$

---

[12] There are no harmonic resonances as in the classical 1D Mathieu equation.

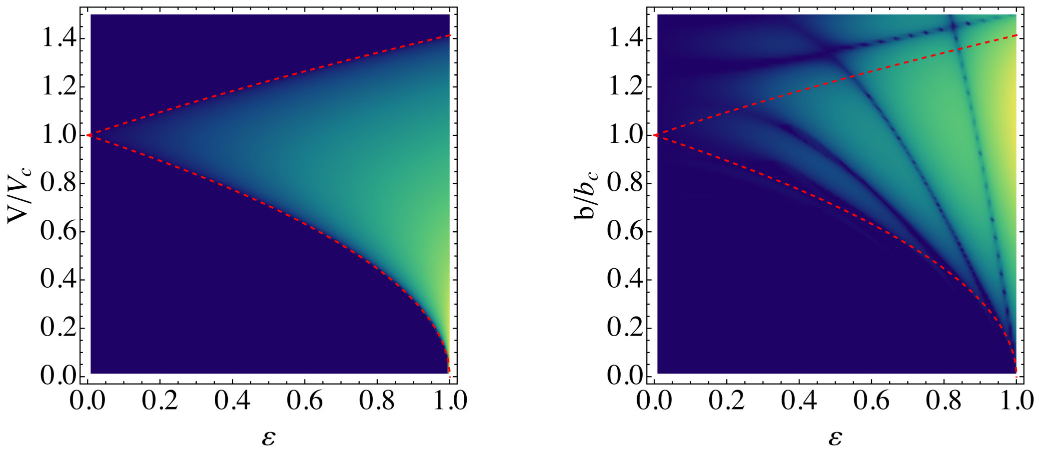

(a) Uniform relative movement

(b) Oscillating relative movement

Figure 4.18: Instability domain (yellow-green regions) of two coupled modes with same frequencies ω_k for two different types of counterflow: A uniform relative movement at speed $\mathbf{V} = V\mathbf{e}_z$ (with $V_c = 2\omega_k/|k_z|$) (a) and an oscillating relative movement with amplitude b and frequency $\Omega = \omega_k/10$ (with $b_c = 2\omega_k/|k_z|\Omega$) (b). Red dashed lines correspond to the limits of the instability domain in case of a uniform movement.

in agreement with the results of [166] in the limit $\varepsilon \ll 1$. In figure 4.18a, we show the parametric instability domain for two given coupled modes and where the two superfluids have the same sound velocity $c_1 = c_2 = c$. In this simple configuration, the domain boundaries are given by $v_\pm = 2c\sqrt{1 \pm \varepsilon}$. The domains can be calculated either by numerical integration of the differential equations eqs. (4.84, 4.83) or by using Floquet theory (numericals as well).

Generalisation to an oscillating relative movement

Since parametric instabilities develop within a time scale $\sim 1/(\varepsilon\omega)$, for $\Omega \ll \varepsilon\omega$ the relative velocity is slowly varying with time with respect to the growth of the instability. We can approximate the relative position as

$$\mathbf{r}_{\text{rel}}(t - t_0) = \mathbf{r}_0 + \mathbf{V}(t_0)t + ... \tag{4.90}$$

Thus, for $\varepsilon \ll 1$, high momentum excitations will spontaneously emerge if

$$\text{Max}|\mathbf{V}(t)| \geq c_1 + c_2. \tag{4.91}$$

and in particular, if $b\Omega \geq c_1 + c_2$ for a sinusoidal movement. In figure 4.18b, we show the parametric instability domains for two coupled modes with same frequency ($\omega = 10\Omega$) and same sound velocities c. The domain is very similar to the uniform velocity case, see Fig. 4.18a. An important difference is that the parametric instability regions are also present way above the critical velocity. This is also visible in figures 4.19a, 4.19b where we plot the range of amplitudes leading to a parametric resonance with respect to the mode frequency (black regions). Surprisingly, even at low frequency, where our previous argument should fail, the system continues to show an amplitude threshold above which the modes are parametrically unstable (which tends to 0 as $\omega/\Omega \to 0$).

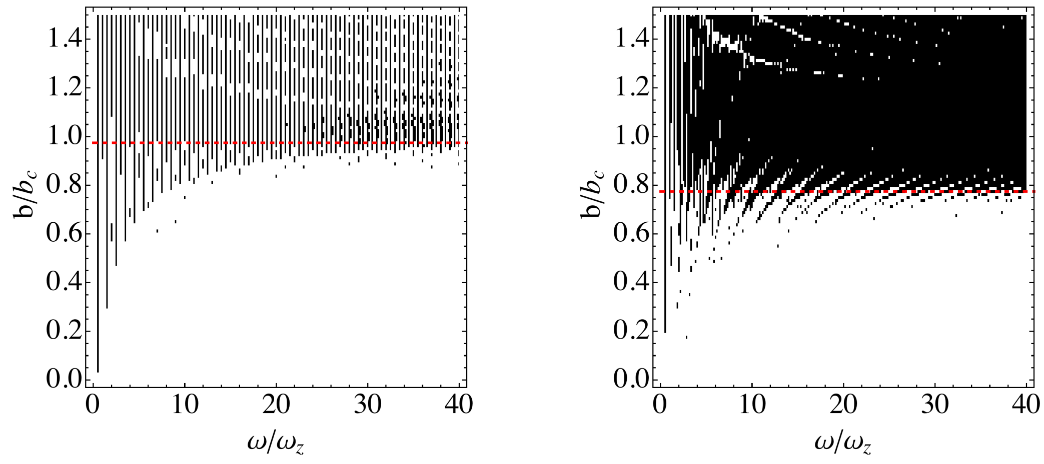

(a) $\varepsilon = 0.05$ (b) $\varepsilon = 0.4$

Figure 4.19: Instability domain (in black) of two coupled modes as a function of their common frequency ω when subject to an oscillating relative velocity $|V| = b\sin(\Omega t)$ for two different values of ε. Red dashed lines correspond to the critical amplitude reduced by a factor $\sqrt{1-\varepsilon}$ as in the uniform movement case ($c_1 = c_2$).

To go beyond this quasi-uniform motion approach and understand better the instability domains shown in figs 4.18b, 4.19a, 4.19b we have to look at the structure of the terms $B_{i,kq}$ in case of an oscillating motion $\mathbf{r}_{\text{rel}} = b\sin(\Omega t)\mathbf{e}_z$. Like we did for the term $A_{i,k}$, we can express $B_{i,kk}$ in terms of Bessel functions:

$$B_{i,kk} \propto \mathrm{e}^{ik_z b\sin(\Omega t)} \propto \sum_n J_n(k_z b)\,\mathrm{e}^{in\Omega t} \,. \tag{4.92}$$

$B_{i,kk}$ contains an infinite set of harmonic frequencies. For any given frequency Ω is thus possible to find a pair $\{\mathbf{k}, n\}$ such that $n\Omega = \omega_{1,k} + \omega_{2,k}$.

From this we could naively infer that there is no threshold in velocity or in oscillation amplitude for the onset of parametric instabilities and consequently no critical velocity. However, contrary to the linear forcing situation, the interplay between the different resonant terms leads to discrete and bounded instability regions.

It is possible, using a multi-scale approach, to compute analytically the instability domains in the limit $\varepsilon \to 0$ and in the symmetric situation where $\omega = \omega_{1,k} = \omega_{2,k}$. We find that the domains are given by the inequality, see Appendix B:

$$J_n(k_z b)^2 \geq (J_0(k_z b) \pm \frac{1}{\varepsilon}\delta\omega)^2, \tag{4.93}$$

where n is the closest integer to $2\omega/\Omega$ and $\delta\omega = n\Omega - 2\omega$.

For large values of n, using the stationary phase approximation, $J_n(k_z b)$ will take significant values when there exists a time t such that $k_z b\cos(\Omega t) - n = 0$, which is equivalent to $|\mathbf{k}.\mathbf{V}(t)| = 2\omega$ (neglecting $\delta\omega$) and we recover the criterion[13] (4.91.

In figure 4.20 is shown the evolution of two coupled high frequency modes in case of oscillating superfluids. While their amplitude remain constant at low relative speed, the

---

[13] Below v_c, there exists a finite number of small parametric domains, close to each node of $J_0(k_z b)$ as it can be seen in figs. 4.19a, 4.19b)

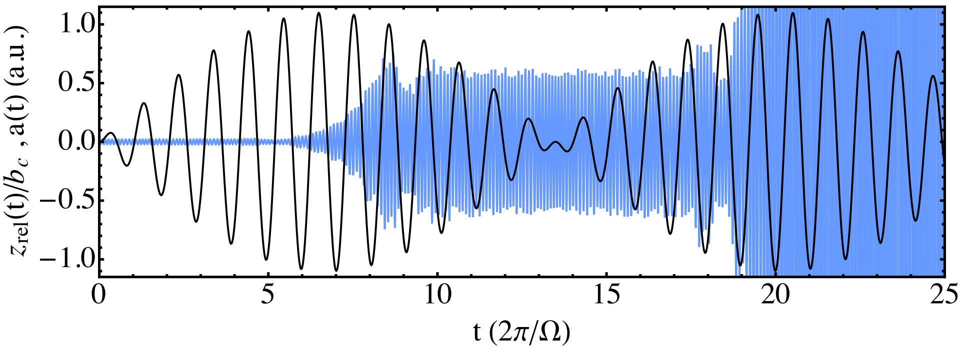

Figure 4.20: Dynamics of high frequency modes (blue curve) when the relative movement of the superfluids is oscillating $z(t) = b(\cos(\Omega t) - \cos(\sqrt{6/7}\Omega t))$ (black curve) with $b = 1.1b_c = 2.2\omega_k/k\Omega$, $\varepsilon = 0.21$ and $\omega_k = 10\Omega$. The modes are strongly excited when the amplitude of oscillations is maximal, i.e. when the relative velocity is close to the critical velocity.

modes are strongly excited when the relative instantaneous velocity is close to the critical velocity.

To sum up, the addition of a time dependent relative velocity does not suppress the parametric critical velocity contrary to the linear forcing case. For trapped superfluids, the number of low frequency modes being small, we can expect to see a threshold close to the generalized Landau criterion $v_c = c_1 + c_2$.

Extension to elongated condensates in a harmonic potential

In our simulation, the collective modes are not as simple as planes waves but they tend to be very similar for large k. We can expect the dynamics of the modes to be described by equations similar to eqs.(4.84). For elongated condensates such that $\mu_1, \mu_2 \gg \hbar\omega_\perp \gg \hbar\omega_z$ we can use the WKB solutions (4.57) to compute the mode overlap terms $B_{1,kq}$ and $B_{2,kq}$ (they are the same). After a few simplifications we get

$$\begin{aligned} g_{12}B_{1,kq} = \alpha \int_{-1}^{1} du\, w(u)w(\lambda(u-u_{\rm rel}))\cos\left[\frac{R_{z,1}\omega_{1,k}}{\bar{c}_1(0)}\arcsin(u) + k\frac{\pi}{2}\right] \times \\ \cos\left[\frac{R_{z,2}\omega_{2,q}}{\bar{c}_2(0)}\arcsin(\lambda(u-u_{\rm rel})) + q\frac{\pi}{2}\right], \end{aligned} \tag{4.94}$$

with $w(u) = (1-u^2)^{1/4}$, $\lambda = R_{z,1}/R_{z,2}$, $u_{\rm rel} = z_{\rm rel}(t)/R_{z,1}$ and

$$\alpha = 2\pi\frac{\omega_z}{\omega_\perp}\lambda^{-1/2}\left(\frac{g_{12}^2}{g_{11}g_{22}}\right)^{1/2}. \tag{4.95}$$

Since the superfluids do not have the same size, the integral is taken over the smallest ($i = 1$). The weight functions w are almost flat and slowly varying functions, especially for the largest of the two superfluids and their time dependence can be neglected. The overlap between the two modes will be important if

$$\forall u \in [-1,1], \quad \frac{R_{z,1}\omega_{1,k}}{\bar{c}_1(0)}\arcsin(u) = \frac{R_{z,2}\omega_{2,q}}{\bar{c}_2(0)}\arcsin(\lambda u), \tag{4.96}$$

This condition is well fulfilled (exactly for $\lambda = 1$) when

$$\frac{\omega_{1,k}}{\bar{c}_1(0)} \simeq \frac{\omega_{2,q}}{\bar{c}_2(0)}, \tag{4.97}$$

which means that the local central wavevectors of the two modes should be equal. Hence, we can write

$$g_{12} B_{1,kq} \simeq \frac{\alpha}{2} \cos\left(\frac{\omega_{2,q}}{\bar{c}_2(0)} z_{\text{rel}}(t) + (q-k)\frac{\pi}{2}\right). \tag{4.98}$$

Then, by using the same arguments and the slowly varying velocity assumption as in the previous section and equation (4.97), parametric instabilities should occur when (for $\alpha \to 0$)

$$\text{Max}\left|\frac{dz_{\text{rel}}}{dt}\right| \geq \bar{c}_1(0) + \bar{c}_2(0). \tag{4.99}$$

The critical velocity in the trapped system is thus equal to the sum of the radially averaged central sound velocities. This result was obtained using collective modes that are specific to a system of two elongated BECs but since the WKB approach is valid for a large class of elongated superfluids, we estimate that this result can be generalized to other types of superfluid mixtures including the Bose-Fermi mixture we studied experimentally.

Comparison with the PCA's modes

To sum up what we found in previous sections, we can list the important features that a parametric mode should display to be easily identified.

- The amplitude of a parametric mode starts to increase only when the relative velocity reaches the critical velocity. In our simulation, the critical velocity for small interspecies coupling is $v_c = \bar{c}_1(0) + \bar{c}_2(0)$ [14]. In practice we have, $\bar{c}_1(0) \simeq 0.25 v_c$ and $\bar{c}_2(0) \simeq 0.75 v_c$. In terms of clouds initial displacement, the critical velocity is reached for $b \simeq 5.3 a_{ho}$ (by neglecting the frequency shifts and the amplitude modulation caused by interspecies interactions) and we should see parametric modes only above this amplitude threshold.

- For each parametric mode in one superfluid, there exists its counterpart in the other superfluid which will have the same time evolution. They should have a good overlap and consequently similar wavevectors.

- A priori, this is valid only for high frequency modes with $\omega \gg \omega_z$.

In the simulation, the PCA's modes that we can consider to be excited parametrically, i.e. modes that appear suddenly out of the noise after a few center of mass oscillations, are indeed seen only for a large initial displacement generating a large relative velocity between the clouds. An example of time evolution is shown in Fig. 4.21. As expected, the mode amplitude seems to increase only when the relative velocity is above the critical velocity (gray regions). We observe this behavior mainly for two sets of simulation, in the $\beta_{12}/\beta_{22} = 0.003$ and $\beta_{12}/\beta_{22} = 0.031$ runs and typically for initial displacements $b \geq 5$. Above this amplitude threshold, all the most populated modes (largest eigenvalues

---

[14] The clouds are a priori in different regimes and the sound velocities have to be calculated differently : $\bar{c}_2(z=0) = c_2(\mathbf{r}=0)/\sqrt{2}$ [169] and $\bar{c}_1(0) = \sqrt{\omega_z^2 R_{1,z}^2/2}$ [193].

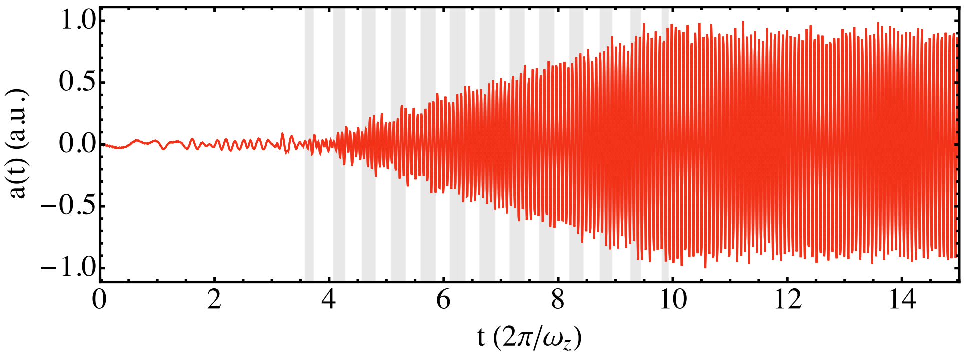

Figure 4.21: Example of a parametric-like behavior observed for a PCA mode of the large cloud ($i = 2$) in the simulation run $\beta_{12}/\beta_{22} = 0.003$ and $b = 8$. The grey regions shows the different time intervals where the relative velocity between the two clouds is above the expected critical velocity $v_c = \bar{c}_1(0) + \bar{c}_2(0)$.

λ) of the small cloud show a parametric-like growth (see an example in Appendix C). Indeed, the linear forcing terms are negligible for the small condensate since the perturbing potential (i.e the density profile of the other condensate) is almost flat, hence its collective modes will mainly be excited parametrically. Conversely, the large superfluid sees a sharper forcing potential and many of the PCA's modes are linearly forced even at high relative velocity. This makes the second requirement a bit difficult to prove, as the parametric modes can be hidden by the presence of strongly populated linearly forced modes. Nevertheless, the few observed parametric modes in the large cloud can be easily associated to a partner mode of the small cloud. They show an excellent overlap and a similar behavior in time as for the example displayed in Fig. 4.22.

The depletion of the fundamental state of a cloud into its collective modes can be quantified by looking at the sum of the eigenvalues given by the PCA

$$\sum_k \lambda_{i,k} \propto \langle (\tilde{n}_i - \langle \tilde{n}_i \rangle_t)^2 \rangle_t. \tag{4.100}$$

For the simulation runs with $\beta_{12}/\beta_{22} = 0.003$, since the modes in the small cloud are almost only excited parametrically, we observe a nice threshold in velocity above which the population of excited modes start to grow, see the blues circles data in Fig. 4.23. The threshold is located around $0.9v_c$ which tend to confirm our prediction of $v_c = \bar{c}_1 + \bar{c}_2$. For the $\beta_{12}/\beta_{22} = 0.031$ runs (yellow squares), the growth starts at low relative velocity, meaning that linearly forced modes already play an important role in the dynamics.

Finally, going back to the first observations made in section 4.3.1, the presence of plateaus in the re-scaled amplitude differences and in the accumulated phase differences was already an indication of the presence of parametric resonances between modes in our system.

Conclusion

We have shown in this section the possibility of parametric resonances between collective modes of the two clouds. It allows to explain the behavior of another large set of PCA modes. In the case of homogeneous superfluids with constant relative velocity, the resonance only occurs above a critical velocity equal to the sum of the sound velocities.

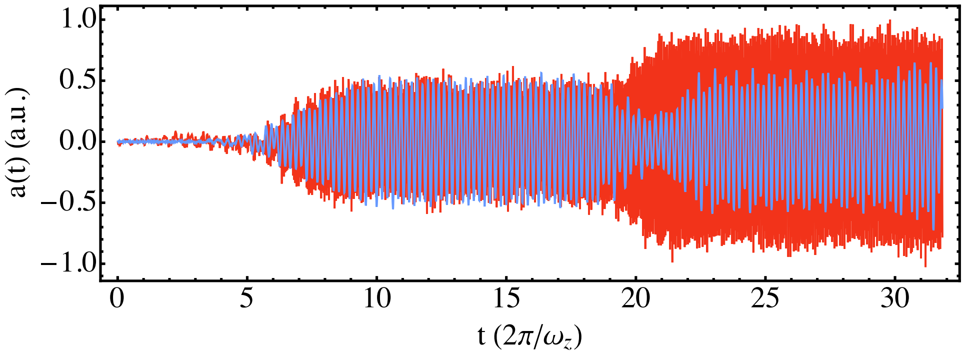

(a) $a_1(t)$ (blue curve) & $a_2(t)$ (red curve)

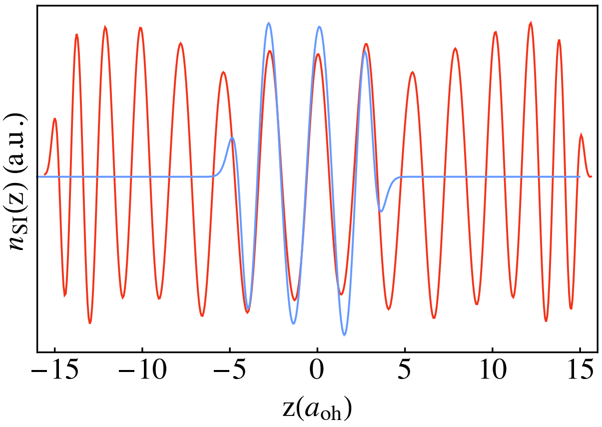

(b) $\tilde{u}_1(0,z)$ (blue curve) & $\tilde{u}_2(0,z)$(red curve)

Figure 4.22: Example of modes in both clouds that show the same parametric behavior (a) and have an excellent overlap (b). Taken from the simulation run $\beta_{12}/\beta_{22} = 0.003$ and $b = 5$.

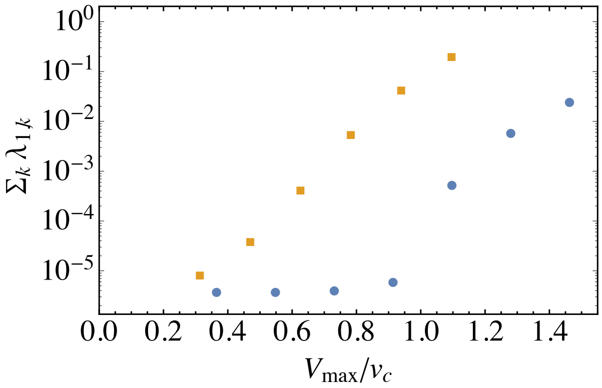

Figure 4.23: Variance of the small cloud $i = 1$ as a function of the maximal relative velocity during the oscillations. The variance characterizes the total population of collectives modes in the cloud. Blue circles: $\beta_{12}/\beta_{22} = 0.003$ simulation runs. We can observe a nice threshold (in logscale !) in velocity above which the variance start to grow. Orange squares: $\beta_{12}/\beta_{22} = 0.031$, no threshold is observed, as linearly forced modes are already present during the dynamic.

Interestingly and contrary to the linear forcing terms treated before, the effect of an oscillating velocity does not suppress the threshold.

4.4 Conclusion

In this chapter, we have presented the results of numerical simulations of two oscillating coupled Bose Einstein condensates. Firstly, the low amplitude oscillations of the clouds center of mass are well explained by the predictions of the sum rule method, validating the approach. Secondly, using a principal component analysis we revealed two mechanisms of mode excitation in superfluids. The first one is the linear response of a mode to a perturbation introduced by one superfluid. This process can occur even at small velocities and there is no associated critical velocity as also pointed out in [172]. The second mechanism, is a parametric resonance between modes of both superfluids. It occurs only at large relative velocity and connects to the Landau generalized critical velocity for homogeneous superfluids [166, 86]. We saw that for low coupling between the two condensates, the parametric excitation is the dominating mechanism for the small condensate, and it allows to observe a threshold for excitation close to the expected value $v_c = \bar{c}_1 + \bar{c}_2$. This mechanism is absent in all the experiments where dissipation is probed using a rigid perturbation such as laser beams.

These findings therefore suggest that the surprising large values of critical velocities observed in our Bose-Fermi counterflow experiment, as opposed to other reported values is due to the dominant presence of parametric excitations. Indeed, the Bose and Fermi superfluids are weakly coupled and we have typically [15] $\varepsilon \simeq 10^{-2}$, a value close to the $\beta_{12}/\beta_{22} = 0.003$ case in the simulation where $\varepsilon = 1.05 \times 10^{-2}$; a nice threshold in velocity is also observed for this case.

Additionally, this is an original application of the principal component analysis and demonstrates its strength to uncover the dynamics of collective modes in a superfluid. It is a model free approach and its results show good agreement with existing theories on collective modes in elongated traps.

There are still some open and unanswered questions that call for future works. First, why contrary to the experiment, the center of mass oscillations are not strongly damped for large relative velocity in the simulation ? Second, what are the consequences of a non-zero temperature in the system ? Finite temperature simulations of binary condensates are more involved but were recently developed [194, 195] and could also help understand better our experimental results. Third, can we observe directly in the experiment the dissipation mechanisms uncovered in the simulation ? The parametric growth of elementary excitation when the relative velocity crosses the critical velocity should lead to a temperature burst in the system and might be detected by a sudden appearance of a thermal fraction in the Bose gas. Finally, similarly to the experiment done in Cambridge [196], is there a turbulent cascade between modes that might explain the intriguing structure of the eigenvalues of the PCA shown in Fig. 4.10 ?

---

[15] ε is calculated using the formula [166]

$$\varepsilon^2 = \left(\frac{3}{\pi}\right)^{1/3} \frac{(m_f + m_b)^2}{\xi m_f m_b} \frac{a_{bf}^2 n_f^{1/3}}{a_{bb}} \tag{4.101}$$

where ξ is the Bertsch parameter.

Chapter 5

Contact relations

In chapter 1, we laid the basis of interactions in cold atomic ensembles, the two-body and three-body problems, and gave some results on the universal thermodynamic properties of some many-body system realized using cold atoms. Starting with the seminal works of S. Tan [197, 198] and M. Olshanii [199] in the years 2000, it was discovered that those thermodynamical observables are actually connected to various others microscopic and macroscopic quantities via a set of exact universal relations that hold for any interaction strength, temperature, number of atoms or trap geometry. Thus far, they all involve the same quantities, called the two-body contact and three-body contact which are intimately related to the few-body short-range correlations in the system. We will review those results in the context of two spin-component Fermi gas and Bose gas. Extended details of what will be presented here can be found in [197, 198, 200, 101, 201].

5.1 General framework

In the following we will treat two different cases:

– N identical bosons

– N fermions dispatched in two internal states: $\mid\uparrow\rangle$ (labelled by $i = 1, ..., N_\uparrow$) and $\mid\downarrow\rangle$ (labelled by $i = N_\uparrow + 1, ...N_\uparrow + N_\downarrow = N$).

In the zero-range model, the N-body Schrödinger equation for the orbital part of the many-body wavefunction reads

$$H\Psi(\mathbf{r}_1, ..., \mathbf{r}_N) = E\Psi(\mathbf{r}_1, ..., \mathbf{r}_N) \ , \tag{5.1}$$

with

$$H = -\frac{\hbar^2}{2m}\sum_{i=1}^{N}\Delta_{\mathbf{r}_i} \ . \tag{5.2}$$

which is just the Hamiltonian of a non-interacting ensemble of free particles. To account for contact-interactions, the wavefunction should obey the Bethe-Peierls contact condition for any pair of interacting particles i, j

$$\Psi(\mathbf{r}_1, ..., \mathbf{r}_N) \underset{r_{ij}\to 0}{\sim} \left(\frac{1}{r_{ij}} - \frac{1}{a}\right) A_{ij}\left(\mathbf{R}_{c,ij}, (\mathbf{r}_{k\neq i,j})\right) \ , \tag{5.3}$$

where $r_{ij} = |\mathbf{r}_i - \mathbf{r}_j|$, $\mathbf{R}_{c,ij} = (\mathbf{r}_i + \mathbf{r}_j)/2$ and A_{ij} is an unknown function[1]

Additionally, if Efimov effects are present, a second boundary limit has to be fulfilled for

---

[1] For fermionic systems, we have also $A_{ij} = 0$ if i, j particles have the same spin.

every triplet i, j, k of interacting particles

$$\Psi(\mathbf{r}_1, ..., \mathbf{r}_N) \underset{R_{ijk}\to 0}{\sim} \Phi(R_{ijk}, \mathbf{\Omega}_{ijk}) B_{ijk}\left(\mathbf{R}_{c,ijk}, (\mathbf{r}_{l\neq i,j,k})\right) \ , \tag{5.4}$$

with R_{ijk} and $\mathbf{\Omega}_{ijk}$ the hyperradius and hyperangle associated with particles i, j, k, $\mathbf{R}_{c,ijk} = (\mathbf{r}_i + \mathbf{r}_j + \mathbf{r}_k)/3$, B_{ijk} is an unknown function, and Φ reads

$$\Phi(R, \mathbf{\Omega}) = \frac{1}{R^2} \sin\left[|s_0| \ln\left(\frac{R}{R_t}\right)\right] \phi_{s_0}(\mathbf{\Omega}) \ . \tag{5.5}$$

Instead, if no Efimov effect is present, Ψ will be automatically of the form

$$\Psi(\mathbf{r}_1, ..., \mathbf{r}_N) \underset{R_{ijk}\to 0}{=} \frac{1}{R_{ijk}^{2-s_{l,n}}} \sum_{m=-l}^{l} \phi_{l,n,m}(\mathbf{\Omega}_{ijk}) B_{m,ijk}\left(\mathbf{R}_{c,ijk}, (\mathbf{r}_{l\neq i,j,k})\right) \ . \tag{5.6}$$

where $s_{l,n}$ is the lowest non-efimovian exponent.

5.2 The two and three-body contact

From these very general assumptions, it was discovered that one could deduce universal relations between different properties of the many-body system. Each time, the same intermediate quantity was used, the two-body contact C_2. In the context of two-spin component Fermi gas, the exact relations were first obtained by Shina Tan [197, 198], and the two-body contact is often called Tan's contact. Similar relations were then obtained using another quantity, the three-body contact C_3 [200, 101].

In a very abstract manner, one can define the two-body contact, C_2, using the following scalar product

$$(A^{(1)}, A^{(2)}) \equiv \sum_{i<j} \int \left(\prod_{k\neq i,j} d^3 r_k\right) d^3 R_{c,ij} A_{ij}^{(1)*}\left(\mathbf{R}_{c,ij}, (\mathbf{r}_{k\neq i,j})\right) A_{ij}^{(2)}\left(\mathbf{R}_{c,ij}, (\mathbf{r}_{k\neq i,j})\right) \ , \tag{5.7}$$

then[2]

$$C_2 \equiv \begin{cases} 2(4\pi)^2 (A, A) & \text{for identical bosons} \\ (4\pi)^2 (A, A) & \text{for 2-spin component fermions .} \end{cases} \tag{5.8}$$

The two-body contact can thus be seen as the squared-norm of the regular part of the many-body wave function when two particles get very close and is an extensive quantity. Similarly, we can define the three-body contact as[3]

$$C_3 \equiv \sum_{i<j<k} \int \left(\prod_{l\neq i,j,k} d^3 r_l\right) d^3 R_{c,ijk} \left|B_{ijk}\left(\mathbf{R}_{c,ijk}, (\mathbf{r}_{l\neq i,j,k})\right)\right|^2 \ . \tag{5.9}$$

It will be useful in the following chapters to use the intensive counterparts of C_2 and C_3, namely the contact densities $\mathcal{C}_2 = C_2/V$ and $\mathcal{C}_3 = C_3/V$, where V is the volume of the system. In the following sections, we will see how these quantities appear through different observables and gain more insight of what is the physical meaning of these contact parameters.

---

[2] The numerical factor is chosen so that C_2 can be defined in a unified manner by $C_2 \equiv \lim_{k\to\infty} k^4 n(\mathbf{k})$, as we will see later.

[3] If $l \neq 0$, there is an additional summation over $-l \leq m \leq l$.
Note also that with this definition C_3 dimension will depend on the considered channel, $[C_3] = 1/\mathrm{L}^{2(s_{n,l}+1)}$.

5.3 Relation to the tail of the momentum distribution

With the assumption of two-body contact interactions, and no Efimov effect, it seems intuitive that the large momentum properties of the N-body ensemble should be dominated by two-body physics, equivalently to the Bethe-Peierls condition at short interparticle distance in the real space. We will see that for the momentum distribution we will indeed recover two-body physics in the high-momentum limit but also that many-body physics will remain in the form of a prefactor which will be exactly the two-body contact C_2. Calculation will be shown for a system of spin 1/2 fermions, since no Efimov effect is present.

In first quantization, the momentum distribution in a given internal state σ is defined as

$$n_\sigma(\mathbf{k}) = \sum_{i:\sigma} \int \left(\prod_{l \neq i} d^3 r_l \right) \left| \int d^3 r_i \mathrm{e}^{-\mathrm{i}\mathbf{k}.\mathbf{r}_i} \Psi(\mathbf{r}_1, ..., \mathbf{r}_N) \right|^2 , \tag{5.10}$$

where $i : \sigma$ denotes the summation over all the fermions with a spin σ, and with the normalization

$$\int \frac{d^3 k}{(2\pi)^3} n_\sigma(\mathbf{k}) = N_\sigma . \tag{5.11}$$

In the large k limit, the Fourier transform integral is dominated by the contribution of the short-distance divergences (whenever $\mathbf{r}_i \to \mathbf{r}_j$):

$$\int d^3 r_i \mathrm{e}^{-\mathrm{i}\mathbf{k}.\mathbf{r}_i} \Psi(\mathbf{r}_1, ..., \mathbf{r}_N) \underset{k\to\infty}{\simeq} \int d^3 r_i \mathrm{e}^{-\mathrm{i}\mathbf{k}.\mathbf{r}_i} \sum_{j \neq i} \frac{1}{r_{ij}} A_{ij}(\mathbf{r}_j, (\mathbf{r}_{k \neq i,j})) . \tag{5.12}$$

Then, using the identity

$$\int d^3 r \mathrm{e}^{-\mathrm{i}\mathbf{k}.\mathbf{r}} \frac{1}{r} = \frac{4\pi}{k^2} , \tag{5.13}$$

we have

$$\int d^3 r_i \mathrm{e}^{-\mathrm{i}\mathbf{k}.\mathbf{r}_i} \Psi(\mathbf{r}_1, ..., \mathbf{r}_N) \underset{k\to\infty}{\simeq} \frac{4\pi}{k^2} \sum_{j \neq i} \mathrm{e}^{-\mathrm{i}\mathbf{k}.\mathbf{r}_j} A_{ij}(\mathbf{r}_j, (\mathbf{r}_{k \neq i,j})) , \tag{5.14}$$

where we can already see the high momentum limit $1/k^2$ signature of two-body physics, see eq. (1.17). Thus, we now have for the momentum distribution

$$n_\sigma(\mathbf{k}) \underset{k\to\infty}{\simeq} \frac{(4\pi)^2}{k^4} \sum_{i:\sigma} \int \left(\prod_{l \neq i} d^3 r_l \right) \left| \sum_{j \neq i} \mathrm{e}^{-\mathrm{i}\mathbf{k}.\mathbf{r}_j} A_{ij}(\mathbf{r}_j, (\mathbf{r}_{k \neq i,j})) \right|^2 . \tag{5.15}$$

By expanding the modulus squared, one see that it involves crossed terms that will vanish in the large-k limit, so that it simplifies to the following expression

$$n_\sigma(\mathbf{k}) \underset{k\to\infty}{\simeq} \frac{(4\pi)^2}{k^4} \sum_{i:\sigma, j \neq i} \int \left(\prod_{l \neq i} d^3 r_l \right) |A_{ij}(\mathbf{r}_j, (\mathbf{r}_{k \neq i,j}))|^2 . \tag{5.16}$$

We readily recognize the expression for the two-body contact[4]

$$k^4 n_\sigma(\mathbf{k}) \underset{k\to\infty}{\simeq} (4\pi)^2 (A, A) = C_2 . \tag{5.17}$$

---

[4] Since for fermions $\sum_{i:\sigma, j \neq i} = \sum_{i<j}$.

For identical bosons, the same relation holds

$$k^4 n_{\mathrm{b}}(\mathbf{k}) \underset{k\to\infty}{\simeq} 2(4\pi)^2(A,A) = C_2 \ . \tag{5.18}$$

but cannot be obtained in a simple manner as before. Indeed, due to the Efimov channel, the wave function is now also diverging whenever three particles get close, see eq. (5.5). This leads to a new contribution in the large momentum limit due to three-body physics:

$$n_{\mathrm{b}}(\mathbf{k}) \underset{k\to\infty}{\simeq} \frac{C_2}{k^4} + F(kR_t)\frac{C_3}{k^5} \ , \tag{5.19}$$

where F is a universal log-periodic function [200].
In fact, the $1/k^4$ tail appears also in one and two-dimensional systems [199, 101], and is independent of the statistical nature of the involved particles, thus the two-body contact is usually directly defined via the momentum tail:

$$C_2 \equiv \lim_{k\to\infty} k^4 n(\mathbf{k}) \ . \tag{5.20}$$

5.4 Relations to the pair and triplet distributions at short distances

The number of pair or triplet of atoms close together is a quantity that comes up in several phenomena and in particular in the formation of deeply-bound molecules which can strongly limit the stability of an interacting gas [5]. As it will be shown here, the contact parameter C_2 (respectively C_3) is directly related to the pair (resp. triplet) distribution at short distances.

5.4.1 Pair distribution

Intuitively again, we can expect the two-body correlations to be given by two body-physics at short distance (i.e. $\propto 1/r^2$) and guess that the prefactor should be, somehow, the two-body contact. The probability density of finding two fermions with opposite-spin at given positions is in second quantization:

$$g^{(2)}_{\uparrow\downarrow}(\mathbf{r}_\uparrow, \mathbf{r}_\downarrow) = \langle (\hat\Psi^\dagger_\uparrow \hat\Psi_\uparrow)(\mathbf{r}_\uparrow)(\hat\Psi^\dagger_\downarrow \hat\Psi_\downarrow)(\mathbf{r}_\downarrow)\rangle \ , \tag{5.21}$$

and in first quantization,

$$g^{(2)}_{\uparrow\downarrow}(\mathbf{r}_\uparrow, \mathbf{r}_\downarrow) = \sum_{i:\uparrow,j:\downarrow} \int \left(\prod_{k,\neq i,j} d^3 r_k\right) |\Psi(\mathbf{r}_1, ..., \mathbf{r}_i = \mathbf{r}_\uparrow, ..., \mathbf{r}_j = \mathbf{r}_\downarrow, ..., \mathbf{r}_N)|^2 \ . \tag{5.22}$$

The probability density of finding two opposite spin fermions separated by a vector $\mathbf{r}$ is then given by

$$G^{(2)}_{\uparrow\downarrow}(\mathbf{r}) = \int d^3 R_c \, g^{(2)}_{\uparrow\downarrow}\left(\mathbf{R}_c + \frac{\mathbf{r}}{2}, \mathbf{R}_c - \frac{\mathbf{r}}{2}\right) \ . \tag{5.23}$$

and for $r \to 0$ we readily have

$$G^{(2)}_{\uparrow\downarrow}(\mathbf{r}) \underset{r\to 0}{\sim} \frac{(A,A)}{r^2} = \frac{C_2}{(4\pi r)^2} \ . \tag{5.24}$$

---

[5] See next chapter.

Thus, if one measures the positions of all particles, the number of pairs of particles of opposite spin separated by a distance less than d is

$$N_{\uparrow\downarrow}(d) = \int_{r<d} d^3r\, G^{(2)}(\mathbf{r}) = \frac{C_2}{4\pi} d \,. \tag{5.25}$$

For identical bosons, the probability density of finding two bosons separated by a distance r has the same limit

$$G^{(2)}(\mathbf{r}) \underset{r\to 0}{\sim} \frac{2(A,A)}{r^2} = \frac{C_2}{(4\pi r)^2} \,. \tag{5.26}$$

and the number of pairs of particles separated by a distance less than d is then

$$N_{\text{pair}}(d) = \frac{1}{2!}\int_{r<d} d^3r\, G^{(2)}(\mathbf{r}) = \frac{C_2}{8\pi} d \,. \tag{5.27}$$

5.4.2 Triplet distribution

For the triplet distribution, we can apply the same reasoning. In the fermionic case of $(\uparrow\uparrow\downarrow)$ triplet, we have to look at

$$g^{(3)}_{\uparrow\uparrow\downarrow}(\mathbf{r}_1,\mathbf{r}_2,\mathbf{r}_3) = \langle \hat{\Psi}^\dagger_\uparrow(\mathbf{r}_1)\hat{\Psi}^\dagger_\uparrow(\mathbf{r}_2)\hat{\Psi}^\dagger_\downarrow(\mathbf{r}_3)\hat{\Psi}_\downarrow(\mathbf{r}_3)\hat{\Psi}_\uparrow(\mathbf{r}_2)\hat{\Psi}_\uparrow(\mathbf{r}_1)\rangle \,. \tag{5.28}$$

Then the number of triplets of hyperradius smaller than d is given by

$$N_{\uparrow\uparrow\downarrow} = \frac{1}{2!}\int_{R<d} d^3r_1 d^3r_2 d^3r_2 g^{(3)}_{\uparrow\uparrow\downarrow}(\mathbf{r}_1,\mathbf{r}_2,\mathbf{r}_3) \,, \tag{5.29}$$

which in the limit of small hyperradii gives

$$N_{\uparrow\uparrow\downarrow} \underset{d\to 0}{\simeq} \frac{1}{4}\left(\frac{3}{2}\right)^{3/2} d^2 \frac{d^{2s_{n,l}}}{1+s_{n,l}} C_3 \,, \tag{5.30}$$

where the non-usual dependence with d comes from eq. (5.6).
For identical bosons, one has to use instead the boundary (5.5), and one finds for the triplet number

$$N_{\text{triplet}} \underset{d\to 0}{\simeq} \frac{1}{16}\left(\frac{3}{2}\right)^{1/2} d^2 \left(1 - \text{Re}\left[\frac{(d/R_t)^{2is_0}}{1+is_0}\right]\right) C_3 \,. \tag{5.31}$$

5.5 Relation to the energy

The relation that probably raised the most interest connects the two-body contact and the derivative of the energy with respect to the inverse scattering length and is called the *adiabatic sweep theorem.*
For two-spin component fermions it reads

$$\frac{dE}{d(1/a)} = -\frac{\hbar^2 C_2}{4\pi m} \,. \tag{5.32}$$

For identical bosons, we have instead

$$\left(\frac{\partial E}{\partial(1/a)}\right)_{R_t} = -\frac{\hbar^2 C_2}{8\pi m} \,. \tag{5.33}$$

Their derivations using the standard tools introduced in section 5.1 is more involved and can be found in [201]. As a result, the knowledge of C_2 as a function of inverse scattering length determines the energy of the system by an integration starting from the non-interacting case at $a = 0$.
A similar relation was also demonstrated for the three-body contact in the case of identical bosons [200, 101]

$$\left(\frac{\partial E}{\partial(\ln(R_t))}\right)_a = \frac{\hbar^2}{m}\frac{\sqrt{3}s_0^2}{4}C_3 \,. \tag{5.34}$$

5.6 Extension to statistical mixtures

So far, we only discussed the case of pure states, but these relations can be generalized to the case of arbitrary statistical mixtures described by a density matrix operator $\hat{\rho} = \sum p_n|\Psi_n\rangle\langle\Psi_n|$[6]. In particular at thermal equilibrium, equation (5.32) now reads

$$\left(\frac{\partial F}{\partial(1/a)}\right)_T = -\frac{\hbar^2 C_2}{4\pi m} \,, \tag{5.35}$$

where F is the free energy and T is the temperature. It can also be written using the total internal energy U

$$\left(\frac{\partial U}{\partial(1/a)}\right)_S = -\frac{\hbar^2 C_2}{4\pi m} \,, \tag{5.36}$$

where S is the entropy.
This generalization to statistical mixture and in particular states at thermal equilibrium is a crucial feature of the contact relations. It means that they apply at any temperature, and for any phase (e.g. a superfluid or a Fermi-liquid phase) of the system. By measuring the local properties of the gas such as the two-body correlations at short distances, one can obtain information about the thermodynamics of the whole ensemble and conversely.
Using equation (5.36), we can actually compute the exact value of the contact provided we know the equation of state of the system we are interested in.

5.7 Conclusion

In this short chapter, we reviewed some important universal and exact relations that involve the two-body and three-body contacts. Numerous others relations were derived showing that the contact parameters actually play a central role in many of the most important probes for ultracold atoms. Notable examples where the two and three body contacts show up are the RF-spectroscopy where interacting atoms are transferred to a non interacting state [202, 203, 204, 205], photoassociation of atoms to form deeply-bound molecules [91, 206] or the structure factors measured by Bragg spectroscopy [207, 208, 209]. In the following chapter, we will show that inelastic losses are also intimately related to the contact parameters.

---

[6] Provided (but it's not the only requirement) the Ψ_n still satisfy the two-body contact condition 5.3 and, if there is an Efimov effect, the three body contact condition 5.5.

Chapter 6

Universal inelastic losses in cold gases

Cold atomic vapors are metastable systems. Indeed at such low temperatures their absolute ground-state is solid. To start solidifying, gaseous atoms need to find an "impurity" through which they can release their binding energy and form a cluster that will eventually contain all atoms of the vapor. In fact, the role of the impurity can be played by any atom of the vapor ensemble. In that way the first step of solidification would be the formation of a deeply-bound molecule resulting from the collision of three atoms. When the density is large, this inelastic process can drastically limit the lifetime of the atomic cloud. In this chapter, we will introduce the physics of three-body recombination in cold-atoms systems. We will show that interactions can strongly enhance or inhibit this process, and while it can severely limit the stability of the interacting system, it allows to probe the effects of interactions, such as the Efimov physics and quantum correlations at short distances.

6.1 Three-body recombination

Whenever three atoms collide, there is a probability that two of them will form a molecule. The released binding energy will be converted in momentum and the two final bodies will fly away from each other. This inelastic process is usually called a three-body recombination event. As said in chapter 1.1.1, the two-body Van der Waals potential possesses several bound states of size $R_* \lesssim l_{\rm vdw}$. Hence, the formation of deeply-bound molecules requires the three atoms to approach within a distance R_*. Classically, we then expect the recombination probability to scale as $(nR_*^3)^2$, which is a small parameter for dilute gases. The released energy is typically $\sim 10^2 - 10^4\,{\rm K}$ and is orders of magnitude larger than any relevant energy scale in ultracold systems. The kinetic energy imparted to the final products is thus enough for them to escape quickly from the confining potential. Consequently, we usually characterize three-body recombinations by a loss-rate coefficient Γ_3 and an associated differential equation

$$\frac{1}{N}\frac{dN}{dt} = -\Gamma_3(N). \tag{6.1}$$

In addition to atom losses, three-body recombinations can affect the rest of the gas in several other manners:

- It is a source of heating. Indeed, in a non-uniform trap, the maxima of densities are associated to minima of the trapping potential, so that three-body losses will mainly remove atoms which have low potential energies and thus increase the mean energy per particle of the system. In addition, three-body losses are in some situations more likely to occur when the kinetic energy of the particles is low, which reinforce the heating effect. In chapter 7, we describe and apply a model which takes into account both three-body recombinations and evaporative losses to describe the atom losses and temperature dynamics of a dilute unitary Bose gas.

- By removing preferentially a certain kind of particles (e.g. atoms with low kinetic energy, Feshbach molecules, etc ...), the three-body losses can modify the equilibrium properties of the gas. An original work on this topic will be discussed in chapter 7, where we compute the effect of the three-body losses on the momentum distribution of a dilute unitary Bose gas.
- At the quantum level, three-body losses can be seen as an absorptive boundary condition at short interparticle distances. If the absorption is too strong or for resonant cases, it can strongly affect the many-body wave function and break the universality of the zero-range model.

As we can intuitively guess, Γ_3 encompasses non-universal and complicated short-range physics that describes the formation of a molecule whenever three atoms are close to each other. In the zero-range limit, $a \gg l_{vdw}$, and assuming perturbative losses, the recombination rate also possess universal properties that will depend on the scattering length a and, if Efimov effects are present, on the three-body parameter R_t. The knowledge of the associated scaling laws is of utmost importance to determine the stability of a gas.

6.2 General principles

6.2.1 A general statement

As said earlier, the energy released by the formation of a deeply bound molecule exceeds by far all the energy scales of the system. As a consequence the momentum and energy conservation equations of the recombination are dominated by the final state. Indeed, if we label the three particles by $\alpha = 1, 2, 3$ and suppose the first two will recombine to form a molecule $\alpha = M$, we have the following energy and momentum conservation equations

$$k_1^2 + k_2^2 + k_3^2 = -\epsilon_b + \frac{1}{2}k_M^2 + k_3^2 \tag{6.2}$$

$$\mathbf{k}_1 + \mathbf{k}_2 + \mathbf{k}_3 = \mathbf{k}_M + \mathbf{k}_3' \tag{6.3}$$

where $\epsilon_b = 2mE_b/\hbar^2$ is the binding energy of the molecule.
In order for the rhs of the first equation to be positive we have $k_M^2/2 + k_3^2 \geq \epsilon_b$ and since the binding energy is larger than any typical energy scale $\epsilon_b \gg k_{th}^2, k_F^2$ we have in good approximation

$$\frac{1}{2}k_M^2 + k_3^2 = \epsilon_b \tag{6.4}$$

and finally

$$\mathbf{k}_M = -\mathbf{k}_3'. \tag{6.5}$$

The final state of the three-body system is completely decoupled from the momenta of the initial incoming particles. As a consequence, demonstrated in the next section, we have

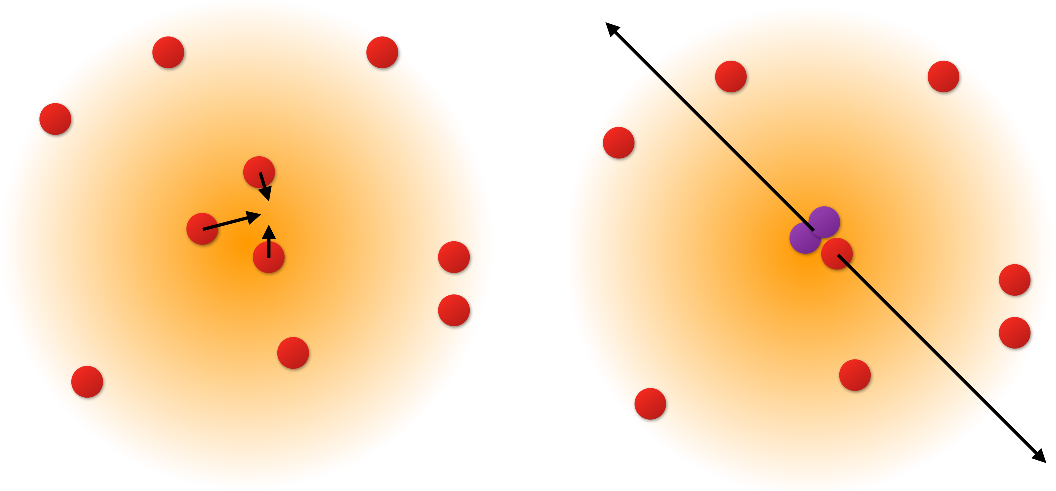

Figure 6.1: Sketch of a three-body recombination in a many-body system. Whenever three particles collide (left figure), there is a given chance that two of them form a deeply bound molecule (purple circles on the right figure). The large released binding energy exceeds greatly any energy scale involved in cold ensemble and the final state is independent of the initial momenta of the particles (black arrows). Therefore, the loss rate should be proportional to the probability to find triplet of atoms at short distances. This probability can be strongly modified by the interactions/correlations in the many-body system (depicted as orange shaded areas).

in a good approximation that the recombination rate is proportional to the probability of having the three particles within a distance R_*:

$$\Gamma_3 N_M = \gamma \int_{R<R_*} d^3r_1 d^3r_2 d^3r_3 \langle \widehat{\Psi}_1^\dagger(\mathbf{r_1}) \widehat{\Psi}_2^\dagger(\mathbf{r_2}) \widehat{\Psi}_3^\dagger(\mathbf{r_3}) \widehat{\Psi}_3(\mathbf{r_3}) \widehat{\Psi}_2(\mathbf{r_2}) \widehat{\Psi}_1(\mathbf{r_1}) \rangle \tag{6.6}$$

where γ is a constant that depends on the short-range physics and R is the hyperradius associated to the three particles and $\widehat{\Psi}_\alpha$ are the field operators for the atoms ($\alpha = 1, 2, 3$). It shows in a more explicit way that the losses are probing the few-body correlations of the ensemble at short distances. If the many-body wave function is unaffected by the losses, we can thus use directly all the contact relations introduced in the previous chapter to derive the loss rates. It is worth noticing that this same idea can be applied to describe light-assisted two-body losses [206, 91] or two-body inelastic scattering [210].

6.2.2 A justification using a microscopic model

We can actually derive an expression similar to equation (6.6) by considering a microscopic model for the three-body recombination. Assuming that the loss rate is small, we can compute it using perturbation theory. Similar approach to what will be described here can be found in an early work of Kagan *et al.* [84] and in our more recent publication [211]. We consider the three-body Hamiltonian

$$\widehat{H}_3 = \int d^3\boldsymbol{r}_1 d^3\boldsymbol{r}_2 d^3\boldsymbol{r}_3 g(\boldsymbol{\rho}_1, \boldsymbol{\rho}_2) \widehat{\Psi}_M^\dagger(\boldsymbol{r}_M)\, \widehat{\Psi}_3^\dagger(\boldsymbol{r}_3) \widehat{\Psi}_3(\boldsymbol{r}_3) \widehat{\Psi}_2(\boldsymbol{r}_2) \widehat{\Psi}_1(\boldsymbol{r}_1) + \text{h.c.}, \tag{6.7}$$

where $\widehat{\Psi}_M$ is the field operators for the molecule ($\alpha = M$) with $\boldsymbol{r}_M = (\boldsymbol{r}_1 + \boldsymbol{r}_2)/2$. $g(\boldsymbol{\rho}_1, \boldsymbol{\rho}_2)$ is a kernel describing the molecule formation and is expressed in term of Jacobi's coordinates $\boldsymbol{\rho}_1 = \boldsymbol{r}_1 - \boldsymbol{r}_2$ and $\boldsymbol{\rho}_2 = \boldsymbol{r}_3 - (\boldsymbol{r}_1 + \boldsymbol{r}_2)/2$. Its characteristic width is of the order of the typical size R_* of the deeply bound molecule and is assumed to be much smaller than the other relevant length scales of the problem (scattering length and inter-particle distance). Finally we assume for the sake of simplicity that all atomic species ($\alpha = 1, 2, 3$) have the same mass.

Assuming that the Hamiltonian $\widehat{H}_3$ can be treated perturbatively[1], the molecule formation rate (the number of recombinations per unit time) is given by Fermi's Golden Rule

$$\Gamma_3 N_M = \frac{1}{\hbar^2}\int_{-\infty}^{\infty} dt \langle i|\widehat{H}_3(0)\widehat{H}_3(t)|i\rangle \tag{6.8}$$

where

$$\widehat{H}_3(t) = \mathrm{e}^{i\widehat{H}_0 t/\hbar}\widehat{H}_3 \mathrm{e}^{-i\widehat{H}_0 t/\hbar}, \tag{6.9}$$

H_0 is the (complicated) Hamiltonian of the system without three-body recombinations, but contains deeply bound states.

If we now recast H_3 in momentum space by taking

$$\widehat{\Psi}_\alpha(\boldsymbol{r}) = \frac{1}{\sqrt{\Omega}}\sum_{\boldsymbol{k}} e^{i\boldsymbol{k}\cdot\boldsymbol{r}}\widehat{a}_\alpha(\boldsymbol{k}) \tag{6.10}$$

where Ω is a quantization volume, we have

$$\widehat{H}_3 = \frac{1}{\Omega^{3/2}}\sum_{\substack{\boldsymbol{k}_1,\boldsymbol{k}_2\\ \boldsymbol{k}_3,\boldsymbol{k}'_3}} \tilde{g}((\boldsymbol{k}_1-\boldsymbol{k}_2)/2,(\boldsymbol{k}'_3-\boldsymbol{k}_3))\widehat{a}_M(\boldsymbol{k}_M)^\dagger \widehat{a}_3(\boldsymbol{k}'_3)^\dagger \widehat{a}_3(\boldsymbol{k}_3)\widehat{a}_2(\boldsymbol{k}_2)\widehat{a}_1(\boldsymbol{k}_1) + \text{h.c.}, \tag{6.11}$$

with

$$\tilde{g}(\boldsymbol{q},\boldsymbol{q}') = \int d^3\boldsymbol{\rho}_1 d^3\boldsymbol{\rho}_2 e^{-i(\boldsymbol{q}\cdot\boldsymbol{\rho}_1+\boldsymbol{q}'\cdot\boldsymbol{\rho}_2)} g(\boldsymbol{\rho}_1,\boldsymbol{\rho}_2),$$

and $\boldsymbol{k}_M = \boldsymbol{k}_1 + \boldsymbol{k}_2 + \boldsymbol{k}_3 - \boldsymbol{k}'_3$ owing to momentum conservation.

If we then consider that the excited molecule and the fast atom have a free motion with energy $\hbar^2 k_M^2/4m - E_b$ and $\hbar^2 k_3'^2/2m$, respectively, then for each set of momenta, $H_3(t)$ will accumulate a phase

$$\exp\left[-i\frac{t}{\hbar}\left(\frac{\hbar^2 k_M^2}{4m} + \frac{\hbar^2 k_3'^2}{2m} - E_b + \Delta\right)\right], \tag{6.12}$$

where Δ is the energy gained or lost by removing three particles of the many-body ensemble. Since E_b is much larger than any typical single-particle energies of the initial state we can neglect Δ and we recover the two conditions (6.4) and (6.5). The time integral in (6.8) transforms as a Dirac delta function and if we note that the initial state does not contain any molecules and fast atoms we can rewrite the loss rate as

$$\Gamma_3 N_M \simeq \frac{2\pi}{\hbar\Omega^3}\sum_{\substack{\boldsymbol{k}_1,\boldsymbol{k}_2,\boldsymbol{k}_3\\ \boldsymbol{k}'_1,\boldsymbol{k}'_2,\boldsymbol{k}'_3}} \chi(\boldsymbol{k}_1-\boldsymbol{k}_2,\boldsymbol{k}'_1-\boldsymbol{k}'_2)\times \langle i|\widehat{a}_1(\boldsymbol{k}'_1)^\dagger\widehat{a}_2(\boldsymbol{k}'_2)^\dagger\widehat{a}_3(\boldsymbol{k}'_3)^\dagger\widehat{a}_3(\boldsymbol{k}_3)\widehat{a}_2(\boldsymbol{k}_2)\widehat{a}_1(\boldsymbol{k}_1)|i\rangle, \tag{6.13}$$

with

$$\chi(\boldsymbol{q},\boldsymbol{q}') = \frac{1}{\Omega}\sum_{\boldsymbol{k}'_3}\delta\left(\frac{3\hbar^2 {k'_3}^2}{4m} - E_b\right)\tilde{g}(\boldsymbol{q},\boldsymbol{k}'_3)\tilde{g}(\boldsymbol{q}',\boldsymbol{k}'_3)^* \tag{6.14}$$

---

[1] In practice, this is justified by a decay time longer than any other characteristic time scales.

Going back into real space and using the fact that thanks to momentum conservation, we must have $\boldsymbol{k}_1 + \boldsymbol{k}_2 + \boldsymbol{k}_3 = \boldsymbol{k}_1' + \boldsymbol{k}_2' + \boldsymbol{k}_3'$, we obtain

$$\begin{aligned}\Gamma_3 N_M \simeq \frac{2\pi}{\hbar} \int & d^3\boldsymbol{\rho}_1 d^3\boldsymbol{\rho}_2 G(\boldsymbol{\rho}_1, \boldsymbol{\rho}_2) \\ & \langle i|\widehat{\Psi}_1^\dagger(-\rho_2/2)\widehat{\Psi}_2^\dagger(\rho_2/2)\widehat{\Psi}_3^\dagger(0)\widehat{\Psi}_3(0)\widehat{\Psi}_2(\rho_1/2)\widehat{\Psi}_1(-\rho_1/2)|i\rangle\end{aligned} \tag{6.15}$$

with

$$G(\boldsymbol{\rho}, \boldsymbol{\rho}') = \frac{1}{\Omega^2} \sum_{\boldsymbol{q},\boldsymbol{q}'} \chi(\boldsymbol{q}, \boldsymbol{q}') e^{-i(\boldsymbol{q}\cdot\boldsymbol{\rho} + \boldsymbol{q}'\cdot\boldsymbol{\rho}')}. \tag{6.16}$$

Since G takes significant values for $\rho_1, \rho_2 \lesssim b$, we have essentially the same structure for the loss rate expression as in equation (6.6). In [84], this formalism was applied on a system of identical bosons and predicted that the three-body loss rate should decrease by a factor $3! = 6$ under the critical temperature for condensation because of the indistinguishability of the condensed bosons. It was thus thought as a strong signal to detect the famous phase transition not yet observed at that time. The prediction was actually verified later on in [44].

6.2.3 Application to some generic cases

Using the boundary conditions (5.3, 5.5, 5.6) introduced in the previous chapter we can directly relate the recombination rate to the two and three-body contact. If no Efimov effect is present we indeed have

$$\Gamma_3 n_M = \mathcal{C}_3 \frac{2\pi}{\hbar} \int d^3\rho_1 d^3\rho_2 \frac{G(\boldsymbol{\rho}_1, \boldsymbol{\rho}_2)}{(R_1 R_2)^{2 - s_{l,n}}} \tag{6.17}$$

where $\mathcal{C}_3$ is the three body-contact density and $R_{1,2} = \rho_{1,2}/\sqrt{2}$.
If instead, there is an Efimov channel, we have

$$\Gamma_3 n_M = \mathcal{C}_3 \frac{2\pi}{\hbar} \int d^3\rho_1 d^3\rho_2 \frac{G(\boldsymbol{\rho}_1, \boldsymbol{\rho}_2)}{(R_1 R_2)^2} \sin\left[|s_0| \ln\left(\frac{R_1}{R_t}\right)\right] \sin\left[|s_0| \ln\left(\frac{R_2}{R_t}\right)\right]. \tag{6.18}$$

If one kind of particle (here $\alpha = 3$) is weakly interacting with the two others, we readily get

$$\Gamma_3 n_M = \mathcal{C}_2 \frac{n_3}{8\hbar} \int d^3\rho_1 d^3\rho_2 \frac{G(\boldsymbol{\rho}_1, \boldsymbol{\rho}_2)}{\rho_1 \rho_2} \tag{6.19}$$

where $\mathcal{C}_2$ is the two-body contact density associated to particles $\alpha = 1, 2$ and n_3 is the density of the weakly coupled particles $\alpha = 3$.
The precise values of the integrals in equations (6.17, 6.18, 6.19) relies on short-range physics but are almost independent of external parameters, such as magnetic field, temperature, etc[2]. More importantly, all the effects of resonant interactions are decoupled

---

[2] If we assume the function G to be constant for $R \leq b$ and 0 otherwise, we can write (here for the non-Efimovian case) the loss rate as

$$\Gamma_3 n_M = \frac{\hbar}{m} \mathcal{C}_3 \frac{b^{2s_{n,l}}}{2s_{l,n} + 2} \alpha, \tag{6.20}$$

where α is a numerical constant. It shows explicitly that the intensity of the losses is given by comparing the three-body contact C_3 to the interaction range b (to some specific power).

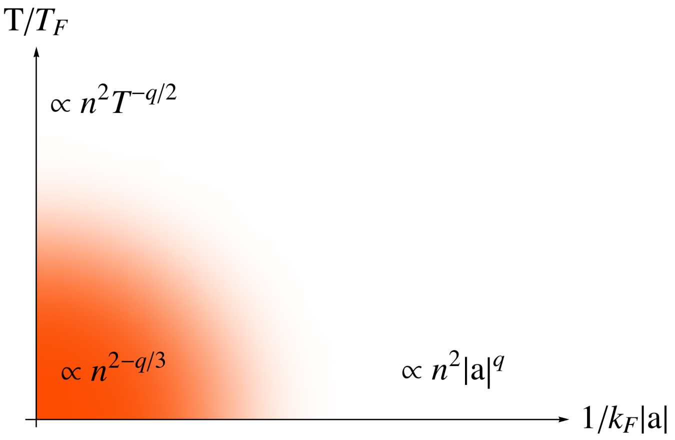

Figure 6.2: Simplified picture of the various scaling laws in density n, temperature T and scattering length a for the three-body loss rate $\Gamma_3 = \dot{n}/n$ for different asymptotic limits assuming a ideal system subject to three-body collisions without shallow bound states nor Efimov trimers. The red area shows the strongly correlated regime where three-body collisions are affected by the presence of surroundings atoms leading to a non-usual density dependence of the loss rate. The exponent q can be recovered using the contact theory.

from the short range physics and contained in a single prefactor that is again played by a contact parameter $\mathcal{C}_2$ or $\mathcal{C}_3$. All the dependence of the three-body loss rate on the system parameters T, n, a, and R_t is encapsulated in the contact parameter and we get simple differential equations of the form

$$\frac{dn_\alpha}{dt} = -\gamma\, \mathcal{C}_3 \;, \tag{6.21}$$

or for the case of a weak coupling between the third type of particles with the two others

$$\frac{dn_\alpha}{dt} = -\gamma\, n_3 \mathcal{C}_2 \;, \tag{6.22}$$

where γ is a numerical constant containing all the short-range physics.
With this simple formulation of three-body recombination, one can recover known results coming from few-body physics, such as the $\propto a^4$ dependence of the loss rate for weakly interacting bosons (see section 6.3) or the $1/a^{2.55}$ scaling for inelastic collisions between weakly bound dimers of fermions in the BEC limit (see section 8.4) [77].
Furthermore, it is worth emphasizing that this formalism allows one to describe losses in a strongly interacting many-body system as we have expressed the correlations in terms of the contact parameters. In particular, at low temperature and in the unitary limit, the only relevant length scale is given by the system density n and by dimensional analysis the loss rate will have a non trivial density dependence n^p where p differs from the usual values 2 or 3 (it can be a fractional or even an irrational number), as depicted in Fig.6.2. This results from the impossibility to isolate a set of three particles in a strongly interacting system, i.e their collisions are affected by the presence of surrounding atoms. Examples of unusual exponent p will be given in the following sections and an experimental confirmation shown in chapter 8.

6.2.4 Inelasticity parameter

To go beyond this perturbative approach we have to include the effects of three-body recombination on the many-body wave function. This is a priori a challenging task for a strongly correlated ensemble. For a set of three particles and in the case of an Efimov channel, Braaten and Hammer proposed to model the cumulative effects of all the two body-bound state as a simple absorptive boundary condition at short distance [92]. The hyperradial wave function can be seen as a superposition of an in-going and outgoing waves at short distances. Instead of having a purely reflective boundary condition with some phase-shift associated to the three-body parameter, they included a new factor depending on a single quantity, the inelasticity parameter η_* that will describe the fraction of triplet particles that is lost at short distances. This factor is not universal and will depend on the considered atomic species. The three-body contact condition becomes: $\exists\, B$ such that[3]

$$\Psi(\mathbf{R}) \underset{R\to 0}{\sim} \left[\left(\frac{R}{R_t}\right)^{-is_0} - \mathrm{e}^{-2\eta_*}\left(\frac{R}{R_t}\right)^{is_0}\right]\frac{B(\mathbf{\Omega})}{R^2}. \tag{6.23}$$

With this new assumption, the three-body recombination rate can be calculated non-perturbatively and allows one to describe loss resonances that occur when the energy of an Efimov trimer crosses the scattering threshold or a shallow two-body bound state [92, 212, 213].

In the limit of $\eta_* \to 0$ and if the system is far from a three-body recombination resonance, one should recover the perturbative result (6.21) with

$$\gamma \underset{\eta_*\to 0}{=} \eta_* 2\sqrt{3}\frac{\hbar}{m}|s_0|. \tag{6.24}$$

6.3 Scalings for the Bose gas

Three-body losses were historically first investigated on bosonic system, as it was potentially an important constraint to overcome in order to obtain a Bose-Einstein condensate. In the universal regime and low temperature, it was shown that the loss rate increases sharply with interactions as a^4 [214, 215], leading to an inevitable instability of the Bose gas when going toward strong interactions. Rapidly after, it was demonstrated both numerically and theoretically that there was some additional periodic resonant enhancement of the loss rate [216, 217]. It was then understood that the predicted resonant loss features were actually the signature of log-periodically emerging Efimov trimers [218, 219, 92], and their existence was confirmed experimentally by a first experiment with Cesium atoms [73], followed by several others using different atomic species [74, 75, 76].

Positive side of the resonance

Using the knowledge of the energy density of the low temperature interacting Bose gas, eq. (1.61) and the adiabatic sweep theorem, we can readily get the three-body loss rate

$$\frac{dn}{dt} = -\gamma\mathcal{C}_3 = -\gamma\frac{1}{s_0^2}\frac{64}{3\sqrt{3}}(4\pi - 3\sqrt{3})\left(\frac{\partial D}{\partial \ln(R_t)}\right)_a n^3 a^4, \tag{6.25}$$

---

[3] This condition is written for the three-body problem but can be readily generalized for any N-body wave function.

that we can rewrite as

$$\frac{dn}{dt} = -L_3 n^3, \tag{6.26}$$

with

$$L_3 = \frac{\hbar}{m} f\left(\frac{a}{R_t}\right) a^4, \tag{6.27}$$

and f is a numerical log-periodic function. We recovered the n^3 dependence as expected for recombinations involving three independent particles and the a^4 scaling law leading to strong losses for large scattering lengths[4], and we also obtained the log-periodic behavior coming from the Efimov physics.

Since the Efimov channel allows for atoms to be extremely close, the presence of deeply bound states can resonantly affect the many-body wave function. Thus, to compute the precise form of the loss-rate coefficient, it is convenient to introduce the inelasticity parameter η_* in the three-body contact condition, eq.(6.23). For positive scattering length $a > 0$, the log-oscillations are strongly suppressed by a factor $\mathrm{e}^{-2\pi s_0} \simeq 1/557$ as we have the expression [92]

$$f(a/R_t) = 64\pi^2(4\pi - 3\sqrt{3}) \frac{\mathrm{th}(\pi s_0)\mathrm{ch}(\pi s_0)\mathrm{ch}(\eta_*)\mathrm{sh}(\eta_*)}{\mathrm{sh}^2(\pi s_0 + \eta_*) + \sin^2(s_0 \ln(a/R_t) + \phi)}. \tag{6.28}$$

To be complete, there are three-body recombination occurring via the collision of a shallow dimer and a free atom. A loss resonance will take place whenever a trimer's energy reaches the atom-dimer threshold $E_b = -\hbar^2/ma^2$.

Negative side of the resonance

On the negative side of the Feshbach resonance, the three-body loss coefficient has much more prononced log-periodic oscillations [92]

$$L_3 = \frac{3590\,\mathrm{sh}(2\eta_*)}{\sin^2(s_0 \ln(a/a_-)) + \mathrm{sh}^2\eta_*} \frac{\hbar a^4}{m}, \tag{6.29}$$

with $s_0 \ln(a/a_-) = s_0 \ln(a/R_t) + 1.72(3)$.
The loss resonances are located at $a = a_- \mathrm{e}^{-n\pi s_0}$ and their width are given by the inelasticity parameter η_*. The observation of such resonances was used to prove for the first time the existence of the long sought Efimov trimers [73].

Unitary limit

At unitarity and $T = 0$ using the usual saturation argument $a \to n^{-1/3}$, we can expect the 3 body loss coefficient to be of the form

$$L_3 = \frac{\hbar}{m} f\left(\frac{n^{-1/3}}{R_t}\right) n^{-4/3}. \tag{6.30}$$

Thus the loss rate has the surprising fractional density dependence

$$\left(\frac{dn}{dt}\right)_{3\mathrm{b}} \propto -n^{5/3}. \tag{6.31}$$

---

[4] The a^4 scaling law can also be obtained by a simple dimensional argument assuming a n^3 dependence and forgetting about the short-range length scale, but it actually works because of the Efimov channel and $\mathcal{R}e(s_{0,0}) = 0$ for identical bosons: The short-range length scale only appears via log-periodic oscillations.

This expression might be drastically modified by resonant effect of losses on the many-body wave function. Nevertheless, the $5/3$ exponent was confirmed in a recent experiment at JILA [85].

The unitary problem is actually tractable in the high-temperature limit and it was found that [36, 213]

$$L_3 = \frac{72\sqrt{3}\pi^2\hbar(1-\mathrm{e}^{-4\eta_*})}{mk_{th}^6} \int_0^\infty \frac{(1-|s_{11}|^2)\mathrm{e}^{-k^2/k_{th}^2}kdk}{|1+(kR_t)^{-2is_0}\mathrm{e}^{-2\eta_*}s_{11}|^2}. \tag{6.32}$$

where $k_{th} = \sqrt{mk_BT}/\hbar$.

The s_{11} coefficient comes from a S-matrix formalism that describes how the long-range and short-range part of the three-body wave function connect. At unitarity, we have the expression $s_{11} = -\mathrm{e}^{-\pi s_0}2\mathrm{i}(\mathrm{s_0}\ln(2) + \arg\Gamma(1+\mathrm{is_0}))$ and $|s_{11}| = 0.04$ so that L_3 can be well approximated by

$$L_3 \simeq \frac{\hbar^5}{m^3}36\sqrt{3}\pi^2\frac{1-\mathrm{e}^{-4\eta_*}}{(k_BT)^2}. \tag{6.33}$$

We can remark a $1/T^2$ dependence of the loss rate, which could be obtained by assuming that the relevant length scale for interactions becomes λ_{th} when $a \to \infty$. This temperature dependence was confirmed by two experiments [36, 220] that will be discussed in more detail in the next chapter.

6.4 Conclusion

In this chapter, we have given a short overview of three-body recombination in cold gases. In particular, we have shown that the loss rate is directly related to the short-distance correlations in the atomic ensemble. In the universal regime, assuming that we can treat the losses perturbatively, we can indeed predict the loss rate scaling laws in density, temperature, and scattering length using our knowledge on the two-body and three-body contact of the system. Conversely, it shows that few-body losses can be used as a probe for the quantum correlations at play in a many-body system. In chapter 8, we will indeed use the link between three-body recombination and short-distance correlations to measure the local two-body contact of the unitary Fermi gas by looking at inelastic losses in our ultracold Bose-Fermi mixture. In chapter 7, we will describe how three-body losses modify the equilibrium properties of a dilute unitary Bose gas and how a dynamic competition can arise with evaporative losses.

Chapter 7

Inelastic losses in a strongly interacting Bose gas

The low temperature unitary Bose gas is under both experimental and theoretical intense investigation as it should display rich physics emerging from the interplay between strong many-body correlations and exotic Efimov few-body physics [37, 221, 222, 223, 224, 110, 85]. However, on the experimental side, its study is severely limited by the presence of resonant three-body recombination as shown in chapter 6. A way to overcome this challenge is to work at finite temperature where the three-body loss rate scaling as a^4 actually saturates when $a \gg \lambda_{\mathrm{th}}$, where λ_{th} is the thermal wavelength. Indeed, it was shown both theoretically and experimentally [36, 213] that at unitarity the three-body loss rate coefficient is given by

$$L_3 \simeq \frac{\hbar^5}{m^3} 36\sqrt{3}\pi^2 \frac{1 - \mathrm{e}^{-4\eta_*}}{(k_B T)^2}. \tag{7.1}$$

where η_* is the inelastic parameter characterizing the probability of forming a deeply bound molecule at short distance (see sections 6.2.4 and 6.3).
Thus the unitary Bose gas is metastable at high temperature as the three-body losses vanishes thanks to the $1/T^2$ scaling. More precisely, a quasi-equilibrium is ensured in presence of losses provided that the characteristic loss rate $\Gamma_3 = L_3 n^2$ is small in comparison to the elastic scattering rate $\Gamma_2 = n\sigma v$, where σ is the scattering cross-section and v the characteristic velocity of the atoms. At unitarity the scattering cross section follows a universal scaling $\sigma = \frac{1}{k^2}$, where k is the relative wave vector of two scattering particles. Plugging eq. (7.1) into the expression for Γ_3, we readily see that quasiequilibrium can be achieved as long as $(1 - \mathrm{e}^{-4\eta_*})n\lambda_{\mathrm{th}}^3$ is small, i.e. when the system is not too deeply in the quantum degenerate regime.

In this chapter we illustrate two consequences of the interplay between three-body inelastic losses and two-body collisions in a thermal unitary Bose gas, where a quasi-equilibrium is ensured and losses can be treated pertubatively . In a first part, we investigate the dynamic competition that can happen between two-body evaporation and three-body recombination. We develop a model that can describe accurately the full temperature and decay dynamics of the system. We identify a universal "magic" trap depth where, within some parameter range, evaporative cooling is balanced by recombination heating and the gas temperature stays constant. We apply the model for data coming from experiments done with two atomic species, ^{7}Li and ^{133}Cs, lying at the extreme ends of the (stable) alkaline group. We demonstrate that the dynamics are universal up to a single atomic-dependent factor, the inelasticity parameter η_*. In the second part, we explore the effect of three-body recombination on the equilibrium properties of the unitary Bose gas. Using a combination of Boltzmann's equation and virial expansion, we compute the effect of three-body losses and interactions on the momentum distribution of a dilute homogeneous unitary Bose gas. Our result are compared to the measurement made at JILA on a unitary gas of ^{85}Rb [37].

7.1 Universal loss dynamics

Along with the loss of all the colliding atoms, a three-body recombination also generates "anti-evaporative" heating as it occurs more frequently at the center of the trap (loss of atoms with small potential energy) and for particles with small momenta [36, 213]. With a rapidly increasing temperature, evaporative cooling can be reactivated and lead to a non trivial time dependence of the sample temperature. In particular, for a well chosen trap depth, the residual evaporation compensates for three-body loss heating and maintains the gas temperature constant. We will briefly present a model that describes this competition and then apply it to analyze the measured loss dynamics of unitary Bose gases prepared at various temperatures and atom numbers. The data come from two different experiments done at ENS with ^{7}Li atoms and previously published [36] and at Chicago (JFI) using ^{133}Cs atoms. The model allows to accurately extract the loss coefficients and we verify the universality of the $L_3 \propto 1/T^2$ scaling law. Extended details can be found in our publication [220].

7.1.1 The model

In the following we will consider a dilute unitary Bose gas trapped in a harmonic potential with a finite depth U. The cloud is described by a Maxwell Boltzmann distribution and the loss rate coefficient can be written as $L_3 = \lambda_3/T^2$, where λ_3 is a temperature independent constant.

Recombination decay and heating

As we have seen previously the atom number decay of a dilute (non-degenerate) Bose gas is given by the equation

$$\frac{dn}{dt} = -L_3 n^3. \tag{7.2}$$

Integrated over the system volume it reads

$$\frac{dN}{dt} = -\gamma_3 \frac{N^3}{T^5}, \tag{7.3}$$

where

$$\gamma_3 = \lambda_3 \left(\frac{m\bar{\omega}^2}{2\sqrt{3}\pi k_B} \right)^3, \tag{7.4}$$

with $\bar{\omega}$ the geometric mean of the trap frequencies.

Each loss of atom via a three-body recombination leads to an excess of $(5/3)k_B T$ of energy left in the sample[1]. Each atom carrying on average an energy $3k_BT$, we have the differential equation for the total energy of the system:

$$\frac{dE}{dt} = \left(3 - \frac{5}{3}\right) k_B T \frac{dN}{dt}, \tag{7.5}$$

Using the total energy expression $E = 3Nk_BT$, we get the differential equation for the temperature

$$\frac{dT}{dt} = \frac{5}{3}\frac{T}{3}\gamma_3 \frac{N^2}{T^5}. \tag{7.6}$$

Evaporative cooling

The evaporative cooling can be modeled using standard kinetic theory of gases [135]. Here, we suppose a 3 dimensional isothermal evaporation in a harmonic trap, for which analytic expressions can be derived. We have for the loss rate:

$$\dot{N} = -\Gamma_{\mathrm{ev}} N, \quad \Gamma_{\mathrm{ev}} = n_0 \sigma_U \bar{v} e^{-\eta} \frac{V_{\mathrm{ev}}}{V_{\mathrm{e}}}. \tag{7.7}$$

where $n_0 = N/V_e$ is the peak density, $\bar{v} = \frac{8k_BT}{\pi m}$ is the mean quadratic velocity, $\sigma_U = 16\pi\hbar^2/mU$ is the scattering cross-section [225], $\eta = U/k_BT$ is the trap depth, $V_e = (2\pi k_B T/m\bar{\omega}^2)^{3/2}$ is the effective volume of the sample, and the evaporative volume V_{ev} is defined by

$$\frac{V_{\mathrm{ev}}}{V_{\mathrm{e}}} = \eta - 4\frac{P(4,\eta)}{P(3,\eta)}, \tag{7.8}$$

with $P(a,\eta)$ being the incomplete Gamma function

$$P(a,\eta) = \frac{\int_0^\eta u^{a-1} e^{-u} \mathrm{d}u}{\int_0^\infty u^{a-1} e^{-u} \mathrm{d}u}. \tag{7.9}$$

The energy loss associated to the evaporation of atoms is given by

$$\frac{dE}{dt} = (\eta + \tilde{\kappa}) k_B T \frac{dN}{dt}, \tag{7.10}$$

where $\tilde{\kappa}$ is the mean excess energy an evaporated atom carries in addition to the trap depth energy in units of k_BT. For a harmonic trap it reads [135]

$$\tilde{\kappa} = 1 - \frac{P(5,\eta)}{P(3,\eta)} \frac{V_{\mathrm{e}}}{V_{\mathrm{ev}}}. \tag{7.11}$$

Using $E = 3Nk_BT$, we get the temperature differential equation

$$3\frac{\dot{T}}{T} = \frac{\dot{N}}{N}(\eta + \tilde{\kappa} - 3). \tag{7.12}$$

---

[1] This follows from [36, 213], where they calculate the three-body recombination rate for three scattering particles (plane waves at large distance) which is equivalent to computing the three-body contact C_3 of the associated system. It was shown that the loss rate coefficient is actually energy dependent, $L_3(E_{\mathrm{rel}}) \propto 1/E_{\mathrm{rel}}^2$ (where E_{rel} is the system energy in the center of mass frame), favoring the recombination of low momenta atoms. The energy lost per recombination event is then obtained by a thermal averaging of $L_3(E_{\mathrm{rel}})E_{\mathrm{tot}}$.

The above model allows to describe the evaporation in the ^{133}Cs experiment. However, for the ^{7}Li experiment the evaporation is two dimensional due to the magnetic axial confinement which has essentially an infinite trap depth. The description of a two-dimensional evaporation is a lot more involved and in pratice is done using Monte-Carlo simulations [226]. The analysis suggests that the 2D evaporation dynamics follows the same functional form as the well-established 3D model, but it requires a modification of the evaporation parameter:

$$\eta_{\text{eff}} = \eta + 1. \tag{7.13}$$

Combined equations

We can now combine the two processes of recombination heating eq. (7.3, 7.5) and evaporative cooling eq. (7.7,7.10) to get two coupled differential equations that will describe the temperature and atom number evolutions:

$$\begin{aligned} \frac{dN}{dt} &= -\gamma_3 \frac{N^3}{T^5} - \gamma_2 e^{-\eta} \frac{V_{\text{ev}}}{V_{\text{e}}} \frac{N^2}{T} & (7.14) \\ \frac{dT}{dt} &= \frac{T}{3} \left(\frac{5}{3} \gamma_3 \frac{N^2}{T^5} - \gamma_2 e^{-\eta} \frac{V_{\text{ev}}}{V_{\text{e}}} \left(\eta + \tilde{\kappa} - 3 \right) \frac{N}{T} \right). & (7.15) \end{aligned}$$

where $\gamma_2 = 16\hbar^2 \bar{\omega}^3 / \pi k_B U$.

The equations (7.15, 7.14) are solved numerically and an example with typical experimental settings is displayed in Fig. 7.1. We can see a non monotonous behavior of the temperature (orange line) showing the competition between evaporative cooling and recombination heating. The atom number decay is amplified by two-body evaporative losses with respect to three-body decay alone (red line). Thus, if not taken into account, evaporative cooling can lead to an important overestimation of the three-body loss coefficient. Due to its two-body nature, evaporative cooling is always dominant on the long term as the associated terms scale as N^2 while the three-body recombination terms scale as N^3. For short times, depending on the value of γ_2, γ_3, and U, the dynamics can be either dominated by one of the two processes or present in similar proportion leading to different dynamical behaviors. In particular, there exist a "magic" relative trap depth η_m, for which the first-order time derivative of the sample temperature vanishes, leading to an almost constant temperature over time. This property can be exploited to measure the temperature dependence of L_3, by doing decay measurements for different constant temperatures as done in [36]. The theoretical value of η_m is found by solving the equation $dT/dN = 0$. Up to a factor $(1 - \mathrm{e}^{-4\eta_*})$, η_m depends only on the phase-space density of the cloud $N(\hbar\bar{\omega}/k_B T)^3$. In that constant temperature situation, the ratio between the two body and three-body loss rates is given by

$$\frac{\dot{N}_{\text{2b}}}{\dot{N}_{\text{3b}}} = \frac{5}{3} \frac{1}{\eta_m + \kappa - 3} \tag{7.16}$$

which is $\sim 30\%$ for a typical relative trap depth $\eta_m = 8$.

For $\eta(t = 0) > \eta_m$, there is an initial phase with an increasing temperature (as in Fig.7.1) where evaporative cooling can be potentially neglected. With this model we are now able to accurately extract the loss coefficient L_3 by fitting the entire atom loss and temperature curves.

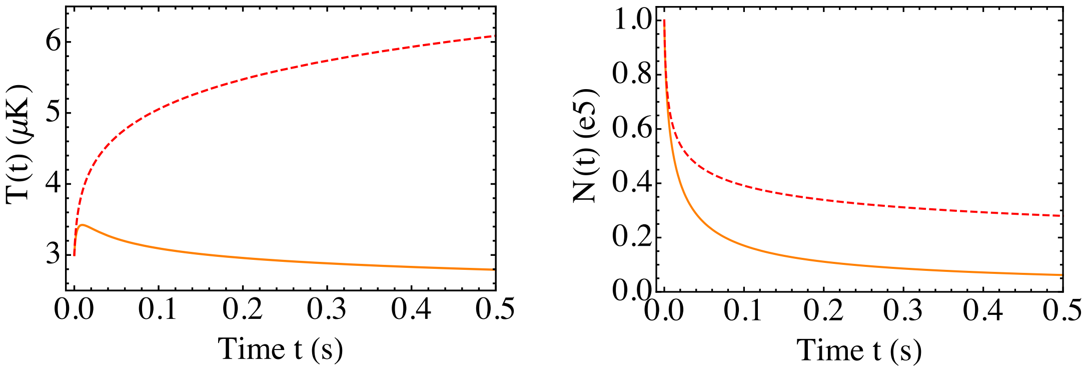

(a) Temperature evolution

(b) Decay of atom number

Figure 7.1: Example of temperature (a) and atom number decay (b) dynamics for typical experimental settings $N(0) = 10^5$, $T(0) = 3\,\mu\mathrm{K}$, $U/k_BT(0) = 9$, $\bar{\omega} = 2\pi \times 500\,\mathrm{Hz}$ and $\lambda_3 = 1 \times 10^{-20}\,\mu\mathrm{K}^2\,\mathrm{cm}^6$. The orange line is the full model (3-body losses + evaporation). The red dashed line is the model without evaporative cooling.

7.1.2 Analysis of the experimental data

The ^{7}Li and ^{133}Cs experimental setups are described in [36] and in [227] respectively. Both experiments follow a similar protocol. The Bose gas is first evaporated in a weakly interacting regime. The trap depth and frequencies are changed to reach a target temperature and density. Then the magnetic field is quickly ramped to unitarity. The clouds are imaged for different waiting times to measure $N(t)$ and $T(t)$. The ^{133}Cs Feshbach resonance at 47.8 Gauss and the ^{7}Li Feshbach resonance at 737.8 Gauss used in the experiments have very similar resonance strength parameters s_{res} = 0.67 and 0.80 respectively [228, 90]) and are in the intermediate coupling regime (neither in the broad nor narrow resonance regime).

Analysis of the N(T) trajectories

To analyze the data, we perform a coupled least-square fit[2] of the atom number and temperature trajectories, eqs. (7.15, 7.14), to the data. The only free fit parameters are the trap depth U and the three-body loss constant λ_3. In Fig. 7.2a, we present typical results for the evolution $T(N)$ in the case of ^{133}Cs. We show trajectories for different initial relative trap depths $\eta_{\mathrm{in}} = U/k_{\mathrm{B}}T_{\mathrm{in}}$. We also plot the relative temperature T/T_{in} as a function of the relative atom number N/N_{in} for the same data in Fig. 7.2b, and for ^{7}Li in Fig. 7.2c. Each data point results from the averaging of 5-10 measurements taken at a given waiting time t (or within a short time window), error bars are 1 standard deviation from the mean. The fits shown as solid lines in Fig. 7.2 are able to reproduce the different observed dynamics for a large variety of initial atom numbers and temperatures. The extracted values for the trap depth U are in good agreement with their calculated values using our knowl-

---

[2] We fit both temperature and atom number individually with solutions to the coupled differential equation set of eqs. (7.15, 7.14). For both fits, we use a common three-body loss coefficient λ_3, and a common trap depth U. The fitting is done by minimizing the weighted sum $\alpha\chi_T + \alpha^{-1}\chi_N$ by varying both the weighing factor α and the fit parameters. The quadratic deviations are defined as $\chi_{T,N} = \Sigma\sigma_{T,N}^2$ ($\sigma_{T,N}$ being the deviations of data and fit). This method accounts for the different amount of relative signal-to-noise ratio of both data sets.

edge on the trapping beams and magnetic fields. As an example, a comparison with ^{7}Li experiment calculated trap depth values is shown in Fig. 7.3.

Universality of three-body losses

Using the extracted values of λ_3, we can test the validity of the $L_3 \propto T^{-2}$ law for the three-body loss of unitary ^{7}Li and ^{133}Cs Bose gases. Thanks to the large mass ratio between the two atomic species $7/133 = 19$, we check the universality of the three-body loss rate over two orders of magnitude in temperature from $0.1\,\mu$K to $10\,\mu$K. We present in Fig. 7.4 the results for the rate coefficient L_3, which varies over approximately two orders of magnitude for both species. In order to emphasize universality, the loss data is plotted as a function of $(m/m_{\mathrm{H}})^3 T_{\mathrm{in}}^2$, where m_{H} is the hydrogen mass. In this representation, the unitary limit for any species collapses to a single universal line (dotted line in Fig. 7.4, cf. eq. (7.1)) up to the only remaining non-universal factor η^*.

The ^{7}Li results are obtained by reanalyzing the data used in [36] but also unpublished data where the temperature was not constant over time. This allows us to cover the 1-10μK temperature range. We find for the temperature-independent loss coefficient $\lambda_3 = 3.0(3) \times 10^{-20}\,\mathrm{cm}^6\mu\mathrm{K}^2\mathrm{s}^{-1}$ which is slightly higher than the previously measured value $\lambda_3 = 2.5(3)_{\mathrm{stat}}(6)_{\mathrm{syst}} \times 10^{-20}\,\mathrm{cm}^6\mu\mathrm{K}^2\mathrm{s}^{-1}$ found in [36] but compatible within the error bars. It is very close to the unitary limit $\lambda_3^{\mathrm{max}} \approx 2.7 \times 10^{-20}\,\mathrm{cm}^6\mu\mathrm{K}^2\mathrm{s}^{-1}$ and significantly larger than the predicted value $\lambda_3 \approx 1.5 \times 10^{-20}\,\mathrm{cm}^6\mu\mathrm{K}^2\mathrm{s}^{-1}$ using $\eta_* = 0.21$ measured in [229].

For ^{133}Cs dataset we find $\lambda_3 = 1.27(7) \times 10^{-24}\,\mathrm{cm}^6\mu\mathrm{K}^2\mathrm{s}^{-1}$ significantly below the unitary limit value $\lambda_3 \approx 2.68 \times 10^{-24}\,\mathrm{cm}^6\mu\mathrm{K}^2\mathrm{s}^{-1}$. We deduce a value of the previously unknown inelasticity parameter of the 47.8-G resonance $\eta_* = 0.098(7)$, which is comparable to the values found for other resonances in ^{133}Cs, in the range 0.06...0.19 [73, 230].

In eq. (7.1), we neglected the log periodic oscillations in temperature associated to the Efimov physics. The full expression is given in eq. (6.32) in chapter 6. Assuming a quasi-universal value of the three-body parameter for ^{133}Cs atoms $R_t = -9.73(3)l_{\mathrm{vdW}}$ [231] and $\eta_* = 0.098$, we expect a relative peak-to-peak amplitude of 7%, which is not resolved in the experimental data because of limited signal-to-noise ratio and temperature range. For ^{7}Li , the contrast is predicted to be even smaller $\sim 6\%$.

7.1.3 Conclusion

In this section, we have described a model that accounts for both three-body recombination heating and evaporative cooling in a dilute unitary Bose gas. It accounts for the various temperature and atom number decay behaviors observed experimentally. As such, it enables an independent determination of the trap depth and the method could be used for complex trap geometries. More importantly, it allows an accurate extraction of the three-body loss rate coefficient in presence of residual evaporation. By applying this model on the experimental data obtained for two different atomic species ^{7}Li and ^{133}Cs, we check the $L_3 \propto 1/T^2$ universal scaling law over two orders of magnitude in temperature. It is worth pointing out that the same scaling in temperature was observed for the unitary three-body contact C_3 using Ramsey interferometry [205] which confirms the proportionality between the two quantities that we have described in chapter 6. An interesting extent of this work would be to observe the small log-periodic oscillations of $L_3(T)$ signaling the underlying Efimov discrete scaling invariance of the unitary Bose gas.

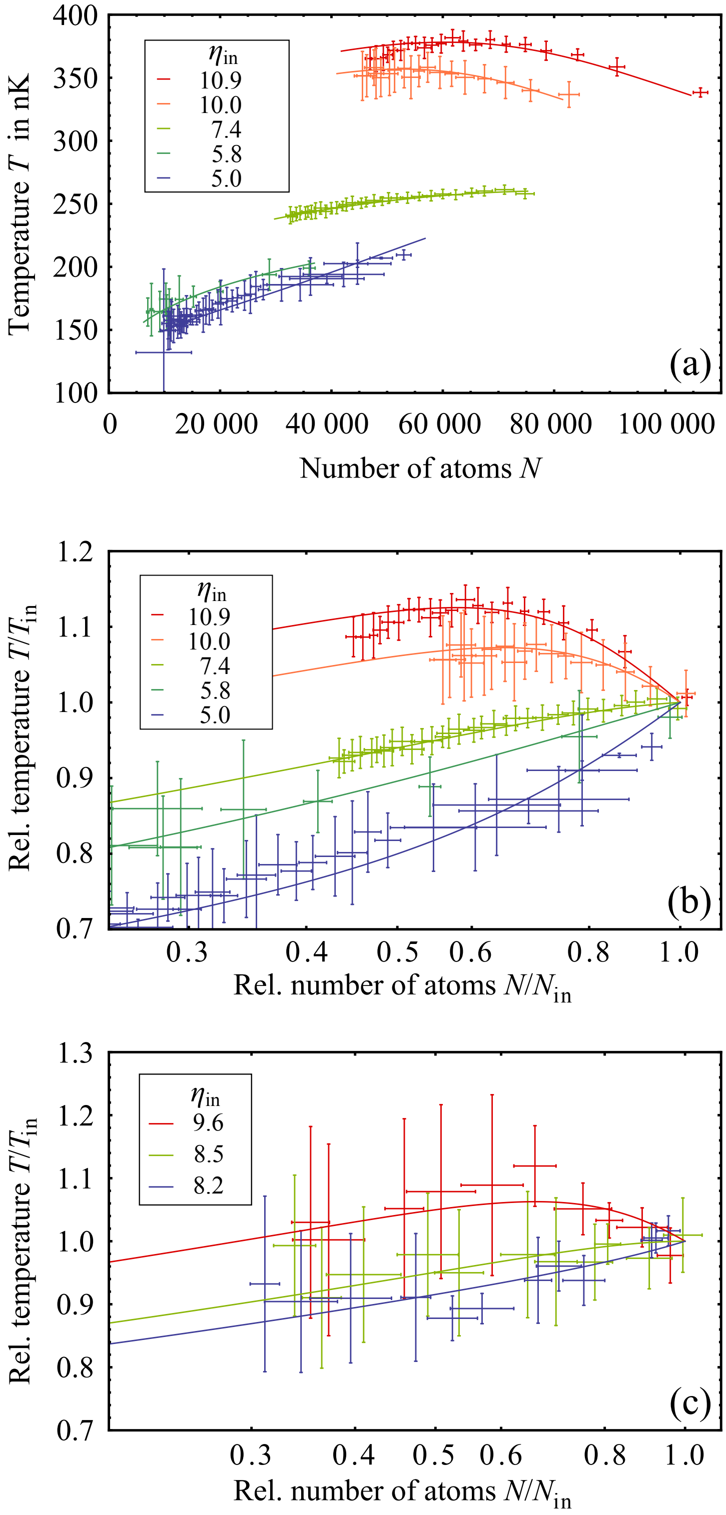

Figure 7.2: Example of temperature versus atom number trajectories for unitary ^{133}Cs atoms in (a) absolute and (b) relative numbers and for unitary ^{7}Li atoms (c). Solid lines are fits of the data using our model, and extracted initial relative trap depths $\eta_{\text{in}} = U/k_B T_{\text{in}}$ are given in the legend. The constant temperature behavior $dT/dN = 0$ is typically reached for $\eta \simeq 8.2$ and $\eta_{\text{eff}} \simeq 8.5$ for ^{133}Cs and ^{7}Li atoms respectively and can be seen on the green data sets. All errors bars represent 1 standard deviation.

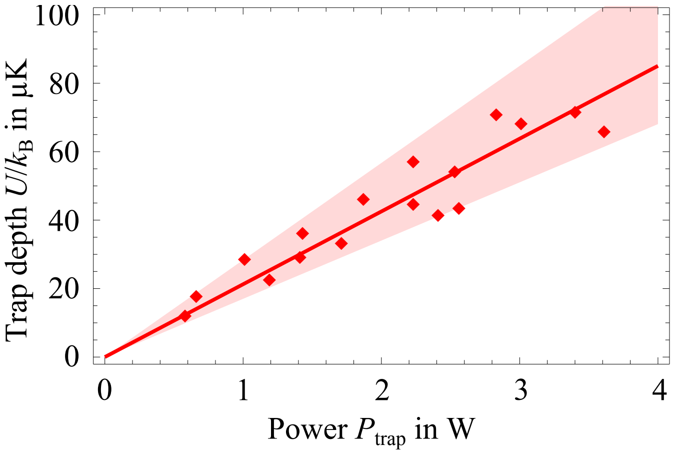

Figure 7.3: Absolute ^{7}Li trap depth results from the fits to our data (dots). The solid line indicates theoretical knowledge of our trap using the formula $U = 2\alpha P_i/\pi w^2$, with a waist $w = 38(1)\,\mu$m and a polarizability at 1071 nm $\alpha/k_B = 4.878 \times 10^{-13}\,\text{Kcm}^2\text{mW}^{-1}$. The shaded area accounts for the combined uncertainty of w_{R} and P_{trap}.

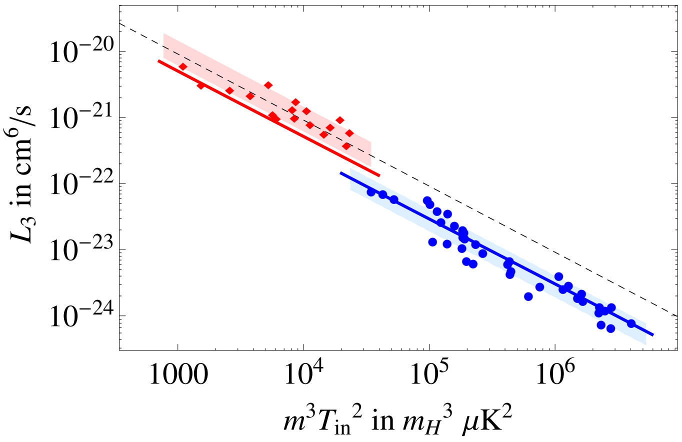

Figure 7.4: Temperature dependence of the three-body loss rate coefficient at unitarity for ^{7}Li (red) and ^{133}Cs (blue), with the respective standard deviations (shaded areas). On the horizontal axis, masses are scaled to the hydrogen atom mass m_{H}. The dashed line represents the unitary limit (eq. (7.1) with $\eta_* \to \infty$). For comparison, we show predictions of universal theory [36] with $\eta_* = 0.21$ for ^{7}Li [229] and fitted $\eta_* = 0.098(7)$ for ^{133}Cs as solid lines. The data confirms the universality of the $L_3 \propto T^{-2}$ law.

7.2 Momentum distribution of a dilute unitary Bose gas with three-body losses

The properties of the degenerate unitary Bose gas are generally investigated theoretically without considering the presence of resonant three-body losses. Yet, as we have shown in the chapter's introduction, the effects of three-body recombination on the equilibrium of the system are driven by the phase space density parameter $n\lambda_{\mathrm{th}}^3$. Hence, in the degenerate regime these effects are highly non perturbative and the question of whether the unitary Bose gas can be stable or not at low temperature is still debated. In this section, we investigate the imprint of 3-body losses on the momentum distribution of a unitary Bose gas in a controlled regime, i.e at high temperature where losses can be treated perturbatively and the unitary Bose gas described by a semi-classical approach using the Boltzmann's equation. To complete our approach we also compute the first virial correction associated with unitary interactions. We show that both effects deplete the center of the momentum distribution proportionally to the phase-space density of the gas and for realistic parameters, this depletion is dominated by three-body losses. Finally, we compare our result to the experiment done at JILA where they demonstrated universal dynamics of the momentum distribution of a unitary Bose gas towards a quasi-equilibirum state [37]. The following paragraphs are directly reproduced from our publication [232] with minor changes.

7.2.1 The model

We investigate the effect of 3-body losses on the momentum distribution of a unitary Bose gas using a semi-analytical resolution of Boltzmann's equation. Since Boltzmann's equation neglects all many-body correlations, our work is restricted to a low-phase space density regime where, as aforementioned, three-body losses can be treated perturbatively.

Starting point

Consider a homogeneous Bose gas that we describe by a phase space density $f(\boldsymbol{p})$. In the presence of losses, f is the solution of Boltzmann's equation that we write formally

$$\partial_t f = I_{\mathrm{coll}}[f] - \mathcal{L}_3[f], \tag{7.17}$$

where I_{coll} and $\mathcal{L}_3$ are non linear operators describing respectively the elastic collisions and the three-body losses. At low phase space density, we can neglect the bosonic stimulation and we have

$$I_{\mathrm{coll}}[f](\boldsymbol{p}_1) = \int \mathrm{d}^3\boldsymbol{p}_2 \mathrm{d}^2\boldsymbol{\omega}' \frac{\mathrm{d}\sigma}{\mathrm{d}\omega'} \frac{|\boldsymbol{p}_2 - \boldsymbol{p}_1|}{m} \left(f_3 f_4 - f_1 f_2\right). \tag{7.18}$$

Here, f_α stands for $f(\boldsymbol{p}_\alpha)$, $(\boldsymbol{p}_1, \boldsymbol{p}_2)$ (resp. $(\boldsymbol{p}_3, \boldsymbol{p}_4)$) are the incoming (outgoing) momenta satisfying energy and momentum conservation and $\mathrm{d}\sigma/\mathrm{d}\omega' = 8\hbar^2/|\boldsymbol{p}_1 - \boldsymbol{p}_2|^2$ is the differential scattering cross-section towards the outgoing solid angle $\boldsymbol{\omega}'$. From [36], the loss rate operator for a unitary Bose gas can be written as

$$\mathcal{L}_3[f](\boldsymbol{p}_1) = \int \mathrm{d}^3\boldsymbol{p}_2 \mathrm{d}^3\boldsymbol{p}_3 \frac{\mathcal{A}_3}{E_{123}^2} |\phi(\boldsymbol{\Omega}_3)|^2 f(\boldsymbol{p}_1) f(\boldsymbol{p}_2) f(\boldsymbol{p}_3), \tag{7.19}$$

where $E_{123} = (p_1^2 + p_2^2 + p_3^2)/2m - (\boldsymbol{p}_1 + \boldsymbol{p}_2 + \boldsymbol{p}_3)^2/6m$ is the energy in the center of mass frame of the three particles of momenta $(\boldsymbol{p}_1, \boldsymbol{p}_2, \boldsymbol{p}_3)$, $\mathcal{A}_3 = 2\pi^3(k_{\mathrm{B}}T)^2 L_3$ and $\phi(\boldsymbol{\Omega}_3)$ is the hyperangular wave-function describing the angular structure of the Efimov trimers that we normalize by the condition $\int \mathrm{d}^5\boldsymbol{\Omega}_3 |\phi(\boldsymbol{\Omega}_3)|^2 = 1$.

Linearisation and solving

In absence of losses the system thermalizes to a distribution G solution of $I_{\rm col}[G] = 0$. For a classical gas, the solution of this equation is a Gaussian distribution $G(n, E; p) = n\lambda_{\rm th}^3 e^{-\beta p^2/2m}/h^3$, where $\beta = 1/k_B T$ and $E = \int (G(p)p^2/2m) d^3\boldsymbol{p} = 3nk_B T/2$ is the energy density.

In the quasi-static regime $\gamma_3/\gamma_2 \ll 1$, three-body losses are small and we can use $\mathcal{A}_3$ as an expansion parameter. Since for $\mathcal{A}_3 = 0$ the system can reach a stationary thermal state, we expect the characteristic evolution time in the presence of losses to vary as $\mathcal{A}_3^{-1}$ and thus ∂_t must be considered to scale as $\mathcal{A}_3$. We write then $f = f_0 + f_1 + ...$ where $f_j \propto \mathcal{A}_3^j$. The expansion of eq. (7.17) to first order in $\mathcal{A}_3$, yields

$$\begin{aligned} I_{\rm coll}[f_0] &= 0 && (7.20)\\ \partial_t f_0 &= I'_{\rm coll}[f_1] - \mathcal{L}_3[f_0]. && (7.21) \end{aligned}$$

where $I'_{\rm coll}$ is the linearized collisional operator.
According to (7.20), f_0 is a Maxwell-Boltzmann distribution. However, since the system loses particles by three-body recombination, its atom number and its energy vary with time. We therefore have $f_0(p, t) = G(n_t, E_t; p)$. We then have in eq. (7.21)

$$I'_{\rm coll}[f_1] = \mathcal{L}_3[f_0] + \dot{E}\partial_E G + \dot{n}\partial_n G. \tag{7.22}$$

Take $f_1(p, t) = G(n_t, E_t; p)\alpha(p, t)$. eq. (7.22) then becomes

$$C[\alpha] = \frac{1}{G}\mathcal{L}_3[G] + \dot{E}\partial_E \ln(G) + \dot{n}\partial_n \ln(G). \tag{7.23}$$

with

$$\begin{aligned} C[\alpha] &= \frac{1}{G} I'_{\rm coll}[G\alpha] && (7.24)\\ &= \int {\rm d}^3\boldsymbol{p}_2 {\rm d}^2\boldsymbol{\omega}' f_0(\boldsymbol{p}_2) \frac{{\rm d}\sigma}{{\rm d}\omega'} \frac{|\boldsymbol{p}_2 - \boldsymbol{p}_1|}{m} (\alpha_3 + \alpha_4 - \alpha_1 - \alpha_2). && (7.25) \end{aligned}$$

and $\alpha_k = \alpha(\boldsymbol{p}_k)$ for $k = 1, \cdots 4$. The operator C is symmetric for the scalar product [233]

$$\langle \alpha | \alpha' \rangle = \int {\rm d}^3\boldsymbol{p} G(p)\alpha(p)\alpha'(p). \tag{7.26}$$

Due to energy and particle number conservation, the kernel of C is spanned by $\alpha(p) = 1$ and $\alpha(p) = p^2$. Finally, being a symmetric operator, its image is orthogonal to its kernel. To find the time evolution of the energy and the atom number, we project eq. (7.23) on 1 and p^2. Using the structure of the kernel of C, the collisional term vanishes and we obtain

$$\begin{aligned} \dot{n}_t &= -\langle 1 | \frac{1}{G}\mathcal{L}_3[G] \rangle && (7.27)\\ \dot{E}_t &= -\langle \frac{p^2}{2m} | \frac{1}{G}\mathcal{L}_3[G] \rangle. && (7.28) \end{aligned}$$

The explicit calculation of the rhs of these equations involves 9-dimensional integrals over the three momenta $(\boldsymbol{p}_1, \boldsymbol{p}_2, \boldsymbol{p}_3)$ in the three-body loss rate operator. This calculation can

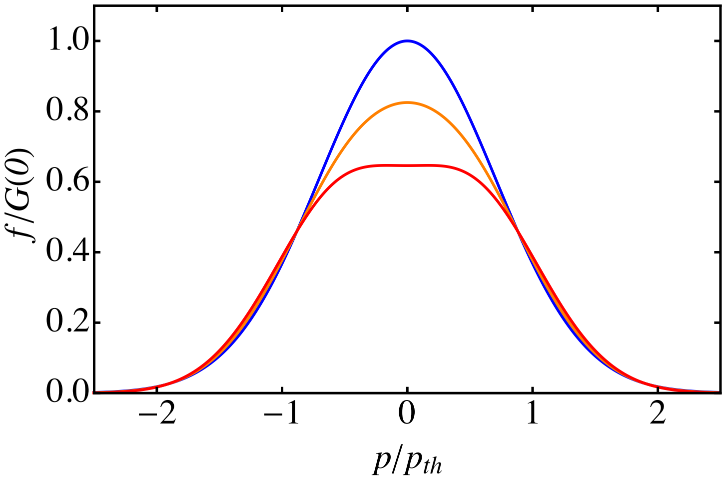

Figure 7.5: Deformation of the momentum distribution of a unitary Bose gas due to three-body losses. From top to bottom: $n\lambda_{\text{th}}^3(1-e^{-4\eta})=0$ (Blue, Boltzmann gas); $n\lambda_{\text{th}}^3(1-e^{-4\eta})=0.05$ (Orange) and $n\lambda_{\text{th}}^3(1-e^{-4\eta})=0.1$ (Red).

be performed analytically by introducing the momentum-space Jacobi coordinates, see Appendix D, and we finally obtain

$$\dot{n}_t = -L_3 n^3 \tag{7.29}$$

$$\dot{E}_t = -\frac{5}{9} E L_3 n^2. \tag{7.30}$$

where we recover the usual formula for three-body losses, as well as the recombination heating discussed in [36, 35].

To find α, we project eq. (7.23) on the range of C (ie orthogonally to $\mathrm{Span}(1,p^2)$). We then have

$$C[\alpha] = P\left[\frac{1}{G}\mathcal{L}_3[G]\right], \tag{7.31}$$

where P is the orthogonal projector on $\mathrm{Im}(C)$, and where we used the fact that $\ln G$ is a linear combination of 1 and p^2 and thus lies in the kernel of C and P.
Eq. (7.31) is solved numerically by decomposing its solution over a basis of orthogonal polynomials, see Appendix D. The results are displayd in Fig. 7.5, where we observe a flattening of the momentum distribution when the three-body losses strength is increased.

7.2.2 Comment on the depletion time scale

In the experiment described in [37], the cloud is not directly prepared in the quasi-static, strongly interacting state. Rather, the experimental sequence starts with a weakly interacting Bose-Einstein condensate in a regime where losses can be neglected. The magnetic field is then ramped quickly to unitarity where the system can relax towards the quasi-equilibrium described above. To get some insight on the relaxation of the system towards equilibrium, we consider the simpler case of a non-condensed gas for which the momentum distribution before the ramp is gaussian. We write as before $f=f_0+f_1$ with $f_1=f_{1,\text{qs}}+\delta f_1$, where $f_{1,\text{qs}}$ is the quasi-static solution and δf_1satisfies the initial condition $\delta f_1(p,t=0)=-f_{1,\text{qs}}(p;t=0)$, since at $t=0$, $f=f_0$. Expanding Boltzmann's Equation to first order in f_1 and using the properties of $f_{1,\text{qs}}$, we obtain for δf_1

$$\partial_t \delta f_1 = I'_{\text{coll}}[\delta f_1]. \tag{7.32}$$

This equation shows that the relaxation towards the quasi-static regime is solely driven by two-body collisions and occurs at a rate $\sim \gamma_2$. This may seem paradoxical since one would rather expect the three-body characteristic rate $\sim \gamma_3$. However, as far as the phase-space density is concerned, the depletion of f at low momenta is quite small since the relative decrease of the peak momentum density is $\propto n\lambda^3$. Since $1/\gamma_3$ is the time required to lose typically half the initial atom number, the dip should form on a time scale $\simeq n\lambda^3/\gamma_3 \simeq 1/\gamma_2$.

7.2.3 First virial correction

The three-body losses lead to a correction to the momentum distribution proportional to $n\lambda^3$. This scaling is similar to the first virial correction, and one may wonder if the three-body losses might not mask the effects of two-body interactions. To clarify this point, we calculated[3] the leading order corrections to the occupation number $\rho(p) = h^3 f(p)$ using the scheme presented in [234]. In the virial expansion, the leading order term corresponds to the ideal Boltzmann gas. In the grand canonical ensemble, this term reads $\rho^{(1)}(p) = ze^{-\beta\varepsilon_p}$, where z is the fugacity and $\varepsilon_p = p^2/2m$. The next order term is the sum of two contributions. The first one corresponds to Bose's statistics and is simply $\rho^{(2,a)}(p) = z^2 e^{-2\beta\varepsilon_p}$ while the second one is more involved and is due to interactions. Following [234], it is given by

$$\begin{aligned} \rho^{(2,b)}(p) = \frac{8\pi z^2}{m} \int_{\mathcal{C}_\gamma} \frac{\mathrm{d}s}{2\pi i} \int_0^{+\infty} \frac{\mathrm{d}P P^2}{2\pi^2} \frac{e^{-\beta s}}{\sqrt{-ms}} \\ \times \frac{e^{-\beta \frac{P^2}{4m}}}{\left[s + \frac{P^2}{4m} - \frac{p^2}{2m} - \frac{(P-p)^2}{2m}\right]\left[s + \frac{P^2}{4m} - \frac{p^2}{2m} - \frac{(P+p)^2}{2m}\right]} \end{aligned} \tag{7.33}$$

where $\mathcal{C}_\gamma$ is a Bromwich contour [235]. We note that this expression is simply twice that obtained for spin 1/2 fermions [234]. To convert this momentum distribution to the canonical ensemble, we use the virial expansion of the equation of state of the unitary Bose gas, $n\lambda_{\text{th}}^3 = z + 2b_2 z^2 + ...$, with $b_2 = 9/4\sqrt{2}$ [236]. We thus obtain

$$\rho(p) = n\lambda_{\text{th}}^3 e^{-\beta\varepsilon_p} + (n\lambda_{\text{th}}^3)^2 \left[\xi(\lambda_{\text{th}} p/\hbar) - 2b_2 e^{-\beta\varepsilon_p}\right], \tag{7.34}$$

where we took $\rho^{(2)}(p) = \rho^{(2,a)}(p) + \rho^{(2,b)}(p) = z^2 \xi(\lambda_{\text{th}} p/\hbar)$.

In Fig. 7.6, we compare the effect of 3-body losses with the virial corrections to the momentum distribution. We observe that for ^{7}Li, for which $\eta = 0.2$, the dip in the momentum distribution is dominated by three-body losses.

7.2.4 Comparison to the JILA experiment

We now turn to the quantitative comparison of our results with the experimental data presented in [37]. In this experiment an ultra-cold, weakly interacting Bose-Einstein condensate is ramped abruptly to the Feshbach Resonance and after a 100 μs-long waiting

---

[3] This calculation was carried out by Xavier Leyronas.

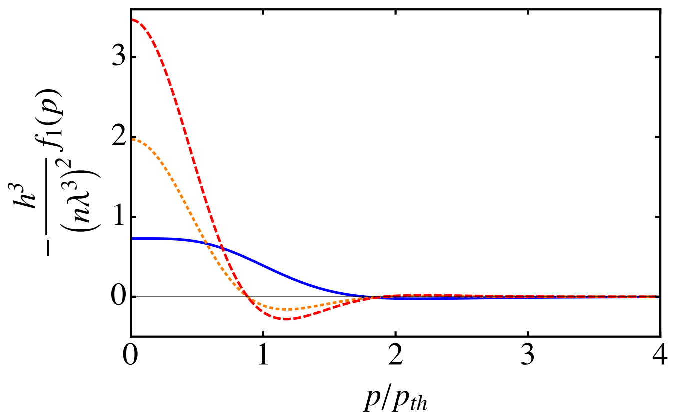

Figure 7.6: Correction to the Boltzmann gas: three-body losses vs interactions. The correction to Boltzmann's distribution is plotted for maximal three-body losses ($\eta = \infty$, red dashed line), $\eta = 0.2$, corresponding to ^{7}Li (Orange dotted line). The blue solid line corresponds to the correction eq. (7.34) due to Bose statistics and two-body interactions.

time, the system reaches a quasi-equilibrium characterized by the momentum distribution of Fig. 7.7. To compare this experiment with our results, we must first determine the temperature of the cloud and since the dynamics is very fast (in the experiment the trapping frequencies are a few Hz), it is most-likely inhomogeneous. We therefore assume a purely local heating and we consider that the thermalization mechanism depends only on elastic processes. Neglecting the initial scattering length, we conclude that the local temperature must scale like $T(\mathbf{r}) = CT_{n(\mathbf{r})}$ where C is a numerical constant and $T_n = \hbar^2(6\pi^2 n)^{2/3}/k_B m$. In other words, the phase-space density (or equivalently the fugacity) is homogeneous over the cloud. Furthermore, the dynamics being too fast for transport phenomena to occur, we can assume that the density profile is not affected by the thermalization. We can therefore average the predicted momentum distribution over the Thomas-Fermi density profile of the initial, weakly-interacting BEC and we fit the experimental data taking $\eta = 0.06$ and using the uniform fugacity z as the only fitting parameter, see Appendix D. In this way, we find a surprisingly good agreement between experiment and theory for $z = 0.6(1)$ (Note that as expected for such a small value of η, the three-body losses play only a small role in the wing of the momentum distribution). Using the virial expansion, this fugacity corresponds to temperature of 110 nK at the center of the trap. This temperature is much higher than that of the initial weakly interacting Bose gas and justifies universal thermalization hypothesis.

In principle, the virial expansion is valid only in the limit of vanishingly small fugacities, and its accuracy is therefore questionable in the present case. Even though there is no reliable way to assess the accuracy of the virial expansion for unitary Bose gases, we note that for the equation of state of the unitary *Fermi* gas, the first order virial expansion gives the correct result at a $\simeq 10\%$ level at $z = 0.6$ [139, 121]. If we assume that the same level of accuracy is achieved in the case of bosons, our calculation should provide a quantitative description of JILA's experiment. To further support our analysis we note that the temperature deduced from the virial expansion yields a three-body loss rate comparable to the one observed in [37].

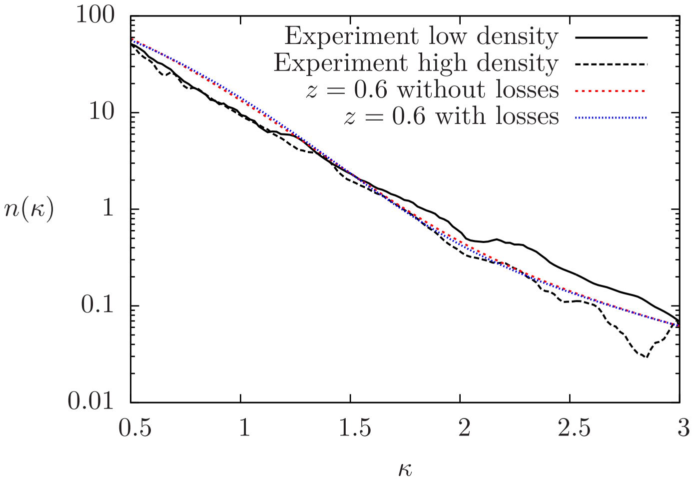

Figure 7.7: The dimensionless momentum occupation number for the unitary Bose gas in a semi log scale. $\kappa = p/\hbar k_n$ with $k_n \equiv (6\pi^2\langle n\rangle)^{1/3}$ and $\langle n\rangle$ the spatially-averaged density ($\langle n\rangle = 5.5 \times 10^{12}$ cm^{-3} and $\langle n\rangle = 1.6 \times 10^{12}$ cm^{-3}). The occupation number is normalized so that $\int n(\kappa)4\pi\kappa d\kappa = 8\pi^3$. The continuous line is the experimental result from Ref.[37] , the dashed line is the result of eq. (7.34) averaged over the initial density profile for $z = 0.6$, and the dotted line includes the effect of three-body losses. The fit is restricted to $\kappa > 0.5$ since for lower momenta, the momentum distribution never equilibrates.

7.2.5 Conclusion

The approach presented above provides a quantitative way to study unitary Bose gases in the dilute limit. In the case of the results presented in [37], we find that three-body losses are negligible and that the tail of the momentum distribution is well described by a first-order virial expansion at a fugacity $z = 0.6(1)$. This value raises a series of open questions: first, is it possible to derive this value from a purely microscopic model describing the dynamics of a Bose gas projected from a weakly interacting regime to unitarity. Second, is it really universal? In our work, we assumed that, after the ramp, the thermalization was only driven by the two body scattering length. However, for strongly interacting bosons, we know that three-body Efimov physics cannot be neglected and requires the introduction of the three-body parameter R_t. In this case, the fugacity would be a log-periodic function of the dimensionless parameter $k_F R_t$, as suggested in [224]. This assumption could be tested by reproducing JILA's experiment on different atoms to vary the value of R_t.

Chapter 8

Inelastic losses of a weakly coupled impurity immersed in a resonant Fermi gas

In a large quantum ensemble with strong interactions, correlations are highly non-trivial and their understanding represents a fundamental challenge in modern physics. As we have shown in chapter 5, short-range correlations present in a quantum gas are connected to various microscopic and macroscopic observables of the many-body system via the contact relations [199, 197, 198, 200, 101, 201]. For a two-component fermionic system, the two-body contact was measured via several observables: high momentum and RF tails [204, 237, 238, 239], structure factor [209, 240, 126], closed-channel fraction [91, 206] or equation of state [107, 241, 242]. In this chapter, we present a demonstration of the universal link between the fermionic two-body contact and inelastic losses of a weakly coupled impurity in a resonant Fermi gas by measuring the lifetime of our ^{6}Li/^{7}Li mixture. On the strongly attractive side of the fermionic Feshbach resonance, we recover known results on atom-dimer inelastic scattering [243, 244]. This first step allows us to calibrate the losses with respect to the two-body contact and to predict the loss rate anywhere in the BEC-BCS crossover. At unitarity, where the fermion-fermion scattering length diverges, we show that the loss rate is proportional to $n_{\rm f}^{4/3}$. This exponent differs from the generic integer case and signals non-trivial two-body correlations in the system. Moreover, our calibration done on the BEC side of the resonance, allows us to measure the local unitary two-body contact, in excellent agreement with measurements cited above.

8.1 Bose-Fermi losses scalings in the BEC-BCS crossover

Understanding the loss mechanisms in multi-component mixtures has been an important topic in the last few years, as more and more experiments were able to cool down several atomic species or several atomic states in a same trap. Pioneer works at Innsbruck using a ^{6}Li/^{40}K mixture [245] and at Washington using a ^{6}Li/^{174}Yb mixture [246] have studied the lifetime of an impurity (the fermionic ^{40}K and bosonic ^{174}Yb atoms respectively) immersed in a strongly interacting two-spin component Fermi gas. Both studies showed a good collisional stability of the mixture on the BCS side of the ^{6}Li Feshbach resonance and increasing losses when going toward the BEC side of the resonance.

In the strongly attractive limit of the BEC-BCS crossover, the fermions form halo-dimers of size $\simeq a_{\rm ff}$ and the relaxation occurs through two-body processes between one

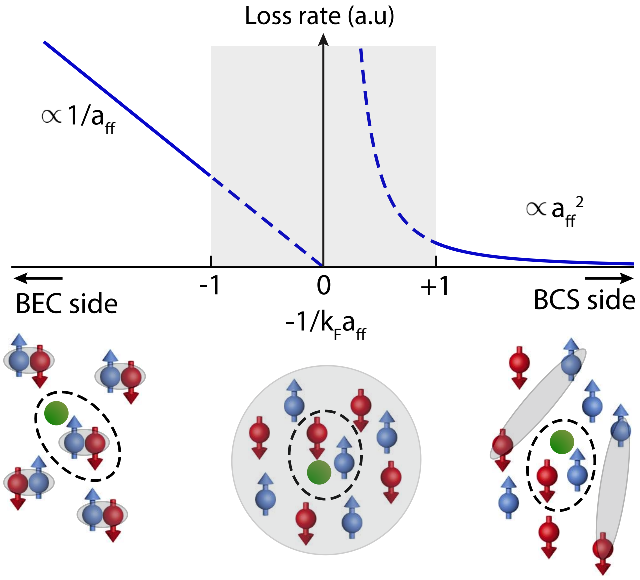

Figure 8.1: Sketch of inelastic decay of an impurity immersed in a Fermi gas with tunable interactions. On the BEC side, ↑ and ↓ fermions form tightly bound dimers and the decay mechanism can be effectively described as a two-body process involving the impurity (green disk) and a dimer. The loss rate scales as $1/a_{\mathrm{ff}}$[243, 244]. On the BCS side, the loss occurs through a three body-process and it scales as a_{ff}^2 in the mean-field limit [243]. The extrapolation of these two asymptotic behaviors towards the strongly correlated regime yields contradictory results (grey area).

such molecule and one impurity atom. The loss rate equations reads

$$\frac{dn_{\mathrm{i}}}{dt} = -L_2 n_{\mathrm{i}} n_{\mathrm{m}}, \tag{8.1}$$

where n_{i} and $n_{\mathrm{m}} = n_{\mathrm{f}}/2$ are the impurity density and molecule density respectively. This particular recombination process was studied previously in [244] with a mixture of ^{40}K atoms and ^{87}Rb Feshbach molecules. As a consequence of the enhanced overlap of the halo-dimer wavefunction with the deeply bound product molecules, the two-body loss rate was shown to scale as $1/a_{\mathrm{ff}}$ as predicted in [243].

On the BCS limit of the resonance, the fermions behave almost as isolated particles and the recombination can be described as a three-body process involving three distinguishable particles, one spin-up (↑), one spin-down fermion (↓) and one impurity atom. We can thus write the loss rate equation as

$$\frac{dn_{\mathrm{i}}}{dt} = -L_3 n_{\mathrm{i}} n_{\mathrm{f}}^2. \tag{8.2}$$

Three-body recombination between three distinguishable particles with large scattering lengths can lead to Efimov resonances as observed in a three-component mixture of ^{6}Li atoms [247, 248, 249]. Here, as the impurity is weakly coupled to the fermions, the loss rate scales simply as a_{ff}^2 [243], leading to vanishing losses in the BCS limit.

The two scalings we have described here allow us to explain the lifetime of an impurity immersed in a two-component Fermi gas in the two limits of the BEC-BCS crossover. However, as depicted in Fig. 8.1, they lead to an apparent paradox at unitarity where they predict by extrapolation either an increasingly long or a vanishingly small lifetime. In

	BEC	Unitary	BCS
$\frac{\dot{n}_\mathrm{i}}{n_\mathrm{i}}$	$\propto \frac{n_\mathrm{m}}{a_\mathrm{ff}}$[243]	$\propto n_\mathrm{f}^{4/3}$	$\propto a_\mathrm{ff}^2 n_\mathrm{f}^2$[243]
$\mathcal{C}_2$	$8\pi \frac{n_\mathrm{m}}{a_\mathrm{ff}}$	$\frac{2\zeta}{5\pi} k_F^4$	$4\pi^2 a_\mathrm{ff}^2 n_\mathrm{f}^2$

Table 8.1: Scaling of the impurity/fermion mixture loss rate and of Tan's contact density $\mathcal{C}_2 = C_2/V$ [197] in the BEC-BCS crossover. Both scalings are identical in the weakly and strongly attractive limits. As $k_\mathrm{F} = (3\pi^2 n_\mathrm{f})^{1/3}$, at unitarity $\mathcal{C}_2$ scales as $n_\mathrm{f}^{4/3}$. ζ is a dimensionless constant, $\zeta = 0.87(3)$ [126].

the two experiments [245, 246], a small decay could be observed at unitarity, but its interpretation was left over, as it was unclear what kind of recombination process could be at play. As a matter of fact, we can notice that by a simple dimensional argument assuming that the decay rate saturates for $a_\mathrm{ff} \simeq n_\mathrm{f}^{-1/3}$, the two asymptotic behaviors give the same scaling at unitarity $\dot{n}_\mathrm{i} \propto n_\mathrm{i} n_\mathrm{f}^{4/3}$, yielding a finite loss rate and an unusual fractional exponent on the fermions density.

In chapter 6, we have shown that provided inelastic decay processes can be treated perturbatively, the decay rate is directly proportional to the probability of finding three-particles within a distance R_*, where R_* is the typical size of the deeply bound molecule formed during the collision. As such, three-body recombination can be calculated in a unified manner for any interacting regime using the universal contact relations. In our specific situation, we have to consider $\rho_3(\boldsymbol{r}_\uparrow, \boldsymbol{r}_\downarrow, \boldsymbol{r}_\mathrm{i})$ the three-body probability distribution of the system. Assuming a weak coupling between the impurity and the fermions, we can factor it as $\rho_3(\boldsymbol{r}_\uparrow, \boldsymbol{r}_\downarrow, \boldsymbol{r}_\mathrm{i}) = \rho_\mathrm{f}(\boldsymbol{r}_\uparrow, \boldsymbol{r}_\downarrow)\rho_\mathrm{i}(\boldsymbol{r}_\mathrm{i})$. Finally, integrating over the positions of the three atoms we readily see that the three-body loss rate is proportional to Tan's Contact parameter C_2 of the fermions. Using our knowledge of the equation of state of the system (see section 1.3), we can calculate C_2 thanks to the adiabatic-sweep theorem

$$C_2 = -\frac{4\pi m_\mathrm{f}}{\hbar^2}\left(\frac{\partial F}{\partial(1/a_\mathrm{ff})}\right)_T. \tag{8.3}$$

where m_f is the fermion mass and F is the free-energy of the fermionic gas [199, 198]. The asymptotic expressions of C_2 at zero temperature in the BEC, BCS and unitary regimes are listed in Table 8.1. In the deep BEC limit, the free energy is dominated by the binding energy of the molecules $\hbar^2/m_\mathrm{f} a_\mathrm{ff}^2$; in the BCS regime C_2 is derived using the mean-field approximation [197]. At unitarity, the expression of the contact stems from the absence of any length scale other than the inter-particle distance and is proportional to $n_\mathrm{f}^{4/3}$. The dimensionless parameter ζ was determined both theoretically [117, 250, 251, 252, 253, 254] and experimentally [204, 107, 126, 240], the most recent measurement yields $\zeta = 0.87(3)$ [126]. Expressions listed in Table 8.1 confirm that the contact parameter and the impurity loss rate follow the same scalings with density and scattering length. Hence, the inelastic losses can be described in the whole BEC-BCS crossover by a single unifying equation

$$\frac{dn_\mathrm{i}}{dt} = -\gamma \mathcal{C}_2 n_\mathrm{i}, \tag{8.4}$$

where $\mathcal{C}_2 = C_2/V$ is the two-body contact density. As we have shown in chapter 6, the constant γ describes the coupling to deeply bound non-resonant states; hence γ has essentially no variation with magnetic field across the fermionic Feshbach resonance.

In the following, we will explore the consequences of equation (8.4) by measuring the lifetime of an ultracold Fermi-Bose mixture of ^{6}Li and ^{7}Li atoms. The impurity is a boson in our experiment and we now use the index $_\mathrm{b}$ instead of $_\mathrm{i}$ to denote the impurity.

8.2 Experiments on the BEC side

In this first series of experiments we check the prediction of eq.(8.4) on the BEC side: relaxation occurs dominantly via collisions between boson and fermionic dimers and the loss rate reads

$$\frac{dn_\mathrm{b}}{dt} = -\gamma\frac{8\pi}{a_\mathrm{ff}}n_\mathrm{m}n_\mathrm{b}. \tag{8.5}$$

The two clouds are prepared at a relatively high temperature and are well described by Maxwell-Boltzmann distributions which will greatly simplify the analysis. The experimental setup and the different cooling steps are described in chapter 2. In short, the ^{6}Li atoms are prepared in a spin mixture $\uparrow, \downarrow$ of $|1_\mathrm{f}\rangle$ and $|2_\mathrm{f}\rangle$ and the ^{7}Li atoms are transferred into the state $|2_\mathrm{b}\rangle$, see section 2.2.2. Importantly, the scattering length between bosons and fermions is $a_\mathrm{bf} = 40.8\,a_0$ and is equal for the $\uparrow, \downarrow$ states and it can be considered constant in the magnetic field range that we explored, 680-832 G. The atoms are confined in a hybrid magnetic/optical trap and are evaporated at the ^{6}Li Feshbach resonance until we reach the target temperature. We ramp the magnetic field to an adjustable value in 200 ms and wait for a variable time t. We then measure the atom numbers of the two species by in situ imaging or after time of flight.

8.2.1 Nature of the losses

In order to determine what is the dominant recombination mechanism for the bosons on the BEC side, we compare the boson losses for spin-balanced and spin-polarized fermionic samples. To do so, we measure the remaining number of atoms for two waiting times ($t_i = 0$ and t_f) and for different magnetic field values in the range $680 - 800\,$G. The experiment is done at a temperature $T \simeq 1.6\mu K$, with initial atom numbers $N_b \simeq 1.5 \times 10^5$ and $N_f \simeq 3 \times 10^5$, and trap frequencies $\nu_z = 26\,Hz$ and $\nu_r = 2.0\,kHz$. For each magnetic field value we record 3 to 5 images for each waiting time t_i and t_f.

In Fig. 8.2, we display the remaining fraction of bosons and fermions $N(t_f)/N(0)$ after a waiting time of $t_f = 1\,s$ for balanced fermions and $t_f = 1.5\,s$ for spin-polarized fermions with 90% polarization. We observe that with spin polarized fermions, bosons losses are highly suppressed indicating that in this magnetic field range bosonic three-body losses are negligible and that both spin states are needed to eliminate a boson. When the fermions are spin balanced we observe increasing losses for both bosons and fermions when going toward the deep BEC limit (low magnetic fields) as expected for losses dominated by boson-dimer and dimer-dimer recombination.

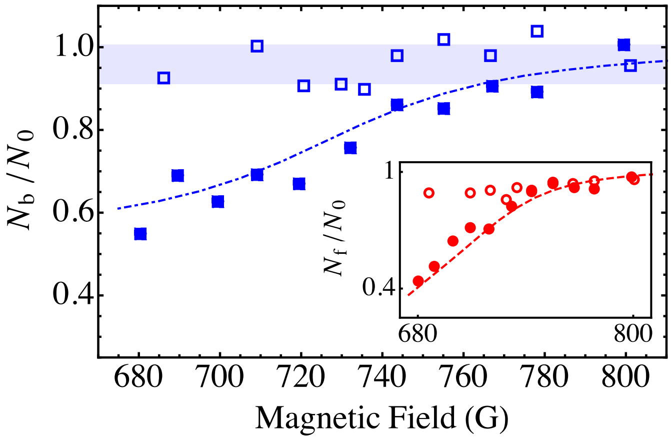

Figure 8.2: Remaining fraction of bosons (blue symbols) and fermions (red symbols, inset) after a 1 s and 1.5 s waiting time for spin-balanced (filled symbols), resp. 90% polarized (open symbols) fermions. The blue dash-dotted (red dashed, inset) curve is a coupled loss model describing the competition between boson fermion-dimer decay ($\propto 1/a_{\mathrm{ff}}$) and dimer-dimer decay ($\propto 1/a_{\mathrm{ff}}^{2.55}$) [77]. The blue-shaded area represents the 1σ fluctuations for the remaining fraction of bosons with spin-polarized fermions. The initial atom numbers are 3×10^5 for ^{6}Li and 1.5×10^5 for ^{7}Li at a temperature $T \simeq 1.6\,\mu$K with trap frequencies $\nu_z = 26$ Hz and $\nu_r = 2.0$ kHz.

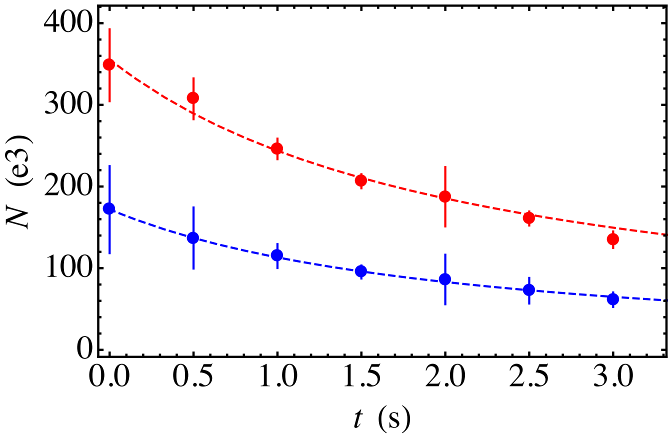

Figure 8.3: Example of atom losses at $B = 720$ G for a nondegenerate Bose-Fermi mixture at $T = 1.25\,\mu$K. Red circles: fermion decay. Blue circles: boson decay. Each circle is the average of 3 to 5 data points with their standard deviation. The red dashed curve is a fit of the fermion decay using eq. (8.11) to estimate $n_{\mathrm{f}}(t)$. The blue dashed curve is a fit to the boson decay using eq. (8.6) and the previously fitted $n_{\mathrm{f}}(t)$ to extract L_{bf}.

8.2.2 Loss coefficient measurement on the BEC side

In Fig. 8.3, we show a typical loss rate measurement at 720 G for a cold thermal Bose-Fermi mixture. Each point is the average of 3 to 5 data points[1]. On the BEC side of the ^{6}Li resonance, several processes can contribute to the loss of ^{6}Li atoms: atom-dimer and dimer-dimer inelastic collisions, evaporation losses and Bose-Fermi losses, resulting in a non-trivial time dependence. On the contrary, the ^{7}Li cloud will mainly lose atoms via Bose-Fermi losses, since evaporation losses and three-body losses are negligible due to the small ^{7}Li-^{7}Li scattering length in this region of magnetic field. We thus extract the interspecies decay rate by fitting the time evolution of the bosonic population

$$\dot{N}_b = -L_\mathrm{bf}\langle n_\mathrm{f}\rangle N_\mathrm{b} - \Gamma_v N_\mathrm{b}, \tag{8.6}$$

where $\langle\cdots\rangle$ represents the trap-average[2], and Γ_v is the one-body residual gas loss rate ($0.015\,\mathrm{s}^{-1}$) measured independently.

For $N_\mathrm{f}(t)$, we use instead a two-body decay function fitted to the measured decay of the fermions

$$N_\mathrm{f}(t) = \frac{N_0}{1+\alpha t}. \tag{8.11}$$

This method has the advantages to be independent of the boson number calibration contrary to a simultaneous fit of both boson and fermion using coupled differential equations and does not require a precise knowledge of all the mentioned decay channels for the fermions. The fits are shown as dashed lines in Fig. 8.3, the fermion decay (in red) is well reproduced by the ad-hoc function in eq. (8.11) and the fit for the bosons (in blue) gives for this measurement an interspecies decay constant $L_\mathrm{bf} = 1.33(24)\times 10^{-13}\mathrm{cm}^3.\mathrm{s}^{-1}$.

8.2.3 Molecule fraction

In our experiment we do not have direct access to the number of dimers in the fermionic cloud. However, in the weakly interacting regime $na_\mathrm{ff}^3 \ll 1$ (deep BEC side of the resonance), the molecular fraction $\eta = 2N_\mathrm{m}/(N_\mathrm{f}+2N_\mathrm{m})$ can be calculated using the law of mass-action [255]. We model the fermionic ensemble as a non-interacting mixture of

---

[1] The total number of points is often limited by the presence of long term drifts in atom numbers in our experiment. Also, due to our cooling scheme, the atom numbers of the two species are anti-correlated. It leads to enhanced number fluctuations with respect to a single atomic specie decay measurement.

[2] For thermal clouds we have the densities:

$$n_\mathrm{b}(\mathbf{r}) = N_b \frac{\bar{\omega}_\mathrm{b}^3}{(2\pi k_B T/m_\mathrm{b})^{3/2}} \mathrm{e}^{-\frac{m_\mathrm{b}}{2k_BT}(\omega_{r,\mathrm{b}}^2 r^2+\omega_{z,\mathrm{b}}^2 z^2)} \tag{8.7}$$

$$n_\mathrm{f}(\mathbf{r}) = N_\mathrm{f} \frac{\bar{\omega}_\mathrm{f}^3}{(\pi k_B T/m_\mathrm{f})^{3/2}} \mathrm{e}^{-\frac{m_\mathrm{f}}{k_BT}(\omega_{r,\mathrm{f}}^2 r^2+\omega_{z,\mathrm{f}}^2 z^2)} \tag{8.8}$$

It leads to

$$\langle n_\mathrm{f}\rangle = N_\mathrm{f} \frac{\lambda_r^2\lambda_z d^{3/2}}{(\frac{d}{2}\lambda_z^2+1)(\frac{d}{2}\lambda_r^2+1)^{1/2}} \left(\frac{m_\mathrm{f}\bar{\omega}_\mathrm{f}^2}{2\pi k_B T}\right)^{3/2} \tag{8.9}$$

With $\lambda_\alpha = \omega_{\alpha,b}/\omega_{\alpha,\mathrm{f}}$, $d = m_b/m_\mathrm{f}$.

In a good approximation we have $\lambda_\alpha = 1/d^{1/2} = \sqrt{6/7} \simeq 0.926$. It leads to the simplified expression:

$$\langle n_\mathrm{f}\rangle = N_\mathrm{f} \left(\frac{m_\mathrm{f}\bar{\omega}_\mathrm{f}^2}{6\pi k_B T}\right)^{3/2} \tag{8.10}$$

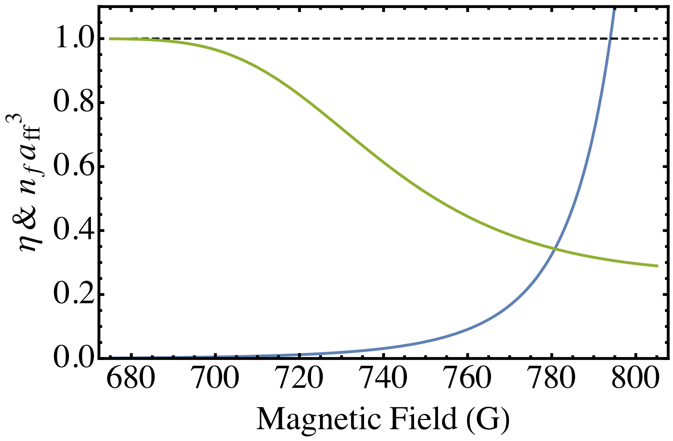

Figure 8.4: Calculated molecular fraction η (green) and $n_{\rm f}a_{\rm ff}^3$ (blue) versus magnetic field for a total number of fermions $N_{\rm f} = 3 \times 10^5$, a temperature $T \simeq 1.6\,\mu$K, and trap frequencies $\nu_z = 26\,$Hz and $\nu_r = 2.0\,$kHz. The model used to estimate η is valid for $n_{\rm f}a_{\rm ff}^3 \ll 1$

$N_{\rm m}$ molecules and $N_{\rm f}$ free atoms. The dimer-atom mixture can be considered to be at chemical equilibirum during the losses owing to the high formation rate of halo-dimers ($\simeq \hbar a_{\rm ff}^4/m_{\rm f}$)[214]. We thus simply write a chemical equilibrium condition between atoms and molecules in the trap at temperature T:

$$N_{\rm f} = \quad 2\left(\frac{k_{\rm B}T}{\hbar\bar{\omega}}\right)^3 Li_3(z) \tag{8.12}$$

$$N_{\rm m} = \quad \left(\frac{k_{\rm B}T}{\hbar\bar{\omega}}\right)^3 Li_3(z^2{\rm e}^{-E_b/k_{\rm B}T}) \tag{8.13}$$

where Li is a polylogarithm function, $z = {\rm e}^{\mu/k_{\rm B}T}$ the fugacity and $E_b = -\hbar^2/m_{\rm f}a_{\rm ff}^2$ the molecule's binding energy. The fugacity is calculated by imposing the total number of atoms in the trap $N_{tot} = N_{\rm f} + N_{\rm m}$.
In Fig. 8.4, we show typical values of the molecule fraction η in the BEC side of the resonance as well as the interaction parameter $n_{\rm f}a_{\rm ff}^3$ for the experimental conditions of Fig. 8.2. Together with the results shown in Fig. 8.2, it already indicates that boson-dimer recombination is the main loss mechanism for bosons in the deep BEC limit.

8.2.4 Bose-fermi losses versus molecular fraction and magnetic field

To verify our prediction of dominant boson-dimer losses we measure the Bose-Fermi loss rate $L_{\rm bf}$ at a fixed magnetic field ($720G$) for various molecule fractions. This fraction is varied by changing the temperature from $1\,\mu$K to $4\,\mu$K and ^{6}Li densities from $2 \times 10^{12}\,{\rm cm}^{-3}$ to $1.0 \times 10^{13}\,{\rm cm}^{-3}$. In practice, it is done by performing different evaporation ramps and trap recompression. The data in Fig. 8.5 shows that the boson loss-rate is indeed proportional to the molecule fraction of the fermionic cloud. A linear fit gives $L_{\rm bf} = (1.12(21)\eta + 0.14(13)) \times 10^{-13}{\rm cm}^3/{\rm s}$. It is thus now convenient to introduce the boson-fermion dimer molecule loss rate $L_{\rm bm}$ defined by $L_{\rm bm}\langle n_{\rm m}\rangle = L_{\rm bf}\langle n_{\rm f}\rangle$.

Finally, we can check the proportionality of $L_{\rm bm}$ with $1/a_{\rm ff}$ predicted in table 8.1 by repeating the loss measurements for different magnetic fields in the interval 690-800 G, see Fig. 8.6. From a linear fit to the data where interaction effects are negligible ($n_{\rm f}a_{\rm ff}^3 \leq 0.025$), we extract the slope $\gamma = 1.17(11) \times 10^{-27}\,{\rm m}^4.{\rm s}^{-1}$ entering in eq. (8.4). Since γ

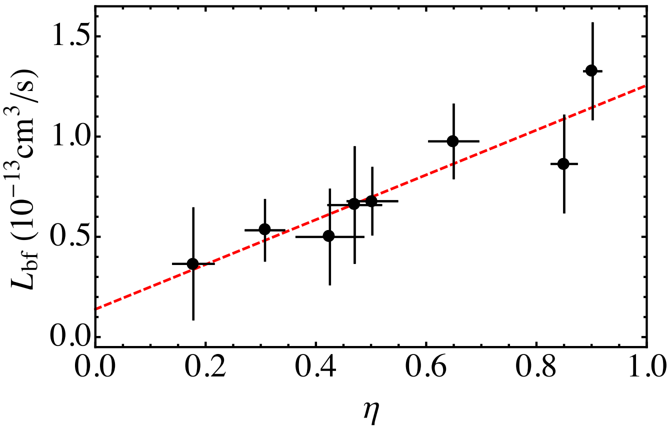

Figure 8.5: Boson-fermion loss rate vs molecule fraction. Circles: experimental data. The vertical error bars represent the statistical errors for L_{bf} from fitting the loss curves. The horizontal error bars represent the statistical errors on the molecule fraction due to ^{6}Li number fluctuations. The red dashed line is a linear fit to the data.

doesn't depend on the magnetic field we can now predict the loss rate anywhere in the BEC-BCS crossover using eq. (8.4).

8.3 Experiment at unitarity

We now move to the strongly interacting regime ($1/a_{\mathrm{ff}} = 0$). This is of particular interest as three-body recombination is now a many-body process and usual inelastic losses models based on solving the three-body problem are bound to fail as they cannot take into account the quantum correlations with the surrounding atoms. On the contrary, our modeling of inelastic decay in terms of two-body contact allows us to describe them in the unitary regime and equation (8.4) now reads

$$\frac{dn_{\mathrm{b}}}{dt} = -\gamma \frac{2\zeta}{5\pi}(3\pi^2 n_{\mathrm{f}})^{4/3} n_{\mathrm{b}}. \tag{8.14}$$

To check this prediction, we measure the boson decay rate at 832 G in the low temperature dual superfluid regime. The mixture is initially composed of about 40×10^3 fully condensed ^{7}Li bosons and 150×10^3 ^{6}Li spin-balanced fermions at a temperature $T \simeq 100\,\mathrm{nK}$ which corresponds to $T/T_{\mathrm{F}} \simeq 0.1$ where T_{F} is the Fermi temperature.

8.3.1 Loss coefficient measurement

In Fig. 8.7, we show a typical loss rate measurement in the dual superfluid regime at unitarity. The atoms are now closer to the boson Feshbach resonance located at 845.5 G and bosonic three-body losses are no longer negligible. Loss by evaporation are negligible for the bosons as they were sympathetically cooled by the fermions and $U \simeq 20\mu_{\mathrm{b}}$, where U is the trap depth and μ_{b} the bosons chemical potential. The time dependence of the boson number is then given by

$$\dot{N}_{\mathrm{b}} = -L_{\mathrm{b}}\langle n_{\mathrm{b}}^2\rangle N_{\mathrm{b}} - \Gamma_{\mathrm{bf}} N_{\mathrm{b}} - \Gamma_{\mathrm{v}} N_{\mathrm{b}}. \tag{8.15}$$

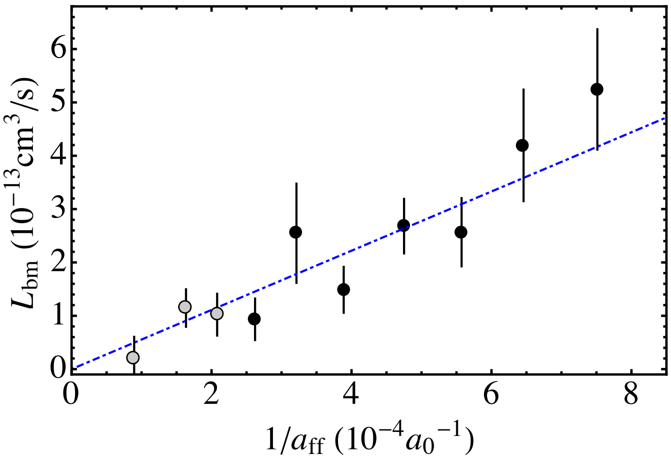

Figure 8.6: Boson-dimer loss rate vs inverse scattering length. The blue dot-dashed line is a linear fit to the data with $n_{\rm f}a_{\rm ff}^3 \leq 0.025$ (black circles), providing $\gamma = 1.17(11) \times 10^{-27}\,{\rm m}^4.{\rm s}^{-1}$, see eq. (8.4).

In order to measure the Bose-Fermi loss rate $\Gamma_{\rm bf}$ we first extract the loss coefficient $L_{\rm b}$ associated to three-boson recombination. For this purpose, we measure the decay of a BEC alone and fit its time dependence using the following equation

$$\dot{N}_{\rm b} = -L_{\rm b}\langle n_{\rm b}^2\rangle N_{\rm b} - \Gamma_v N_{\rm b}. \tag{8.16}$$

We restrict the measurement over a period of time for which the thermal fraction surrounding the BEC is not visible. We thus assume that the ^{7}Li cloud density is given by a Thomas-Fermi distribution[3].We typically have $L_{\rm b}\langle n_{\rm b}^2\rangle = 0.1 - 0.4\,{\rm s}^{-1}$, and $L_{\rm b} = 0.11(1) \times 10^{26}\,{\rm cm}^6.\,{\rm s}^{-1}$ consistent with the model of [257].

For our experimental conditions, the predicted Bose-Fermi loss rate is expected to share the same order of magnitude $\Gamma_{\rm bf} \simeq 0.15\,{\rm s}^{-1}$. However, due to the stronger dependence in bosons density the three-body recombination constitutes the main source of losses, typically $\sim 80\%$ of the lost bosons. The experimental challenge is to be able to detect the 20% supplementary contribution coming from Bose-Fermi losses (the difference between the light blue and blue dashed curves shown in Fig. 8.7). In comparison, the Fermi gas does not suffer from severe losses, and Bose-Fermi recombination should represent a decrease of $\sim 10\%$ of the total atom number. Yet, we do not use the fermion decay to measure $\Gamma_{\rm bf}$ given the larger numbers fluctuations and potential remaining evaporative losses ($\mu_{\rm f} \simeq 0.5U$) which are difficult to estimate[4].

8.3.2 Density dependence of the loss rate

Repeating decay measurements for different fermion numbers and trap confinement, we are able to test the expected $n_{\rm f}^{4/3}$ dependence of the Bose-Fermi loss rate at unitarity

---

[3] We take as in [256]

$$\langle n_{\rm b}^2\rangle = \frac{7}{6}\left(\frac{15^{2/5}}{14\pi}\right)^2\left(\frac{m_{\rm b}\bar{\omega}_{\rm b}}{\hbar\sqrt{a_{\rm bb}}}\right)^{12/5} N_{\rm b}^{4/5}, \tag{8.17}$$

where $\bar{\omega} = (\omega_r^2\omega_z)^{1/3}$.

[4] In addition, three-fermion recombination are present and of unknown magnitude.

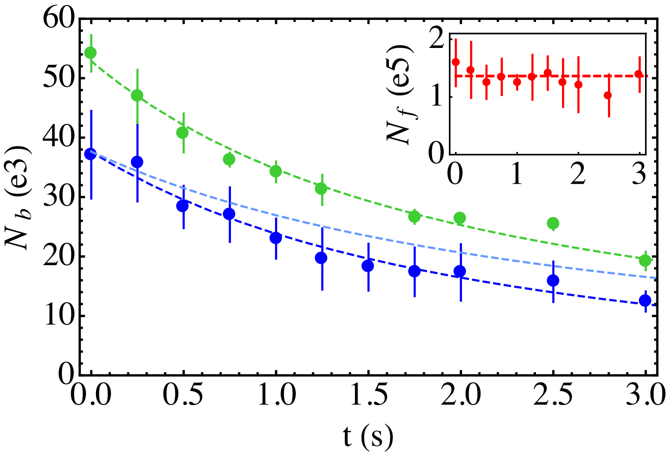

Figure 8.7: Example of atom loss at $B = 832.1\,\mathrm{G}$ in the dual superfluid regime. Green circles: BEC without fermions. Blue circles: BEC in presence of the fermionic superfluid. Each circle is the average of 3 to 5 data points with their standard deviation. Green dashed curve: fit to the decay of the BEC alone using eq. (8.16) providing the three body loss coefficient L_b. Blue dashed curve: fit to the BEC with fermions using eq. (8.15) which gives $\Gamma_\mathrm{bf} = 0.14(4)\,s^{-1}$. Light blue dashed curve: expected BEC decay without Bose-Fermi losses. Inset: the number of ^{6}Li atoms for the same time duration (red circles). As it is nearly constant we use the mean number of ^{6}Li atoms shown as a red dashed line to compute the peak density of the fermionic superfluid during the losses.

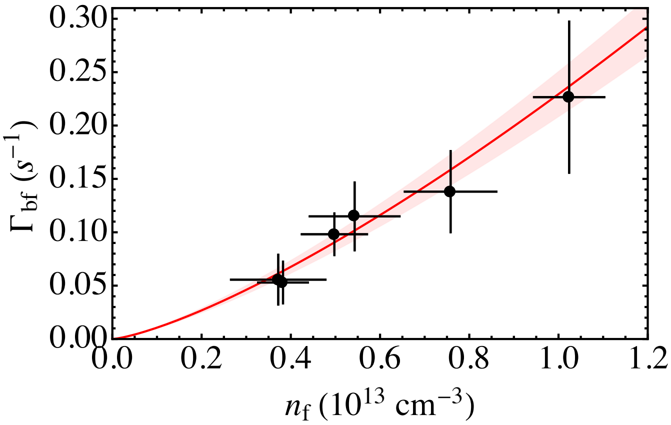

Figure 8.8: Boson loss rate versus fermion central density at unitarity, $n_\mathrm{f} = n_\mathrm{f}(0)$. Circles: experimental data. The red line is the $n_\mathrm{f}^{4/3}$ prediction of eq. (8.20) without any adjustable parameter. The red shaded area represents the $1\,\sigma$ uncertainty resulting from the error on γ.

(central column in Table 8.1). In practice we varied fermion central density by a factor ~ 3 from $0.3 \times 10^{13}\,\mathrm{cm}^{-3}$ to $1 \times 10^{13}\,\mathrm{cm}^{-3}$, as for strong confinements we are limited by rapid three-body losses for the bosons. Γ_{bf} is assumed to be constant since $n_{\mathrm{f}} \propto \sqrt{N_f}$ does not vary significantly during the measurement duration, see Fig. 8.7. In this dual superfluid regime, the size of the BEC is much smaller than that of the fermionic superfluid and the BEC will mainly probe the central density region $n_{\mathrm{f}}(r = 0)$. However, it is not truly a point-like probe, and introducing the ratio ρ of the Thomas-Fermi radii for bosons and fermions, we obtain the finite size correction for eq. (8.14)[5]:

$$\Gamma_{\mathrm{bf}} = \gamma\, C_2(0)\, (1 - \frac{6}{7}\rho^2), \tag{8.20}$$

where[6] $C_2(0) = \frac{2\zeta}{5\pi}(3\pi^2 n_{\mathrm{f}}(0))^{4/3}$, and the last factor in parenthesis amounts to 0.89(3). The prediction of eq. (8.20) is plotted as a red line in Fig. 8.6 and is in excellent agreement with our measurements without any adjustable parameter. Alternatively, a power-law fit An^p to the data yields an exponent $p = 1.36(15)$ which confirms the $n_{\mathrm{f}}^{4/3}$ predicted scaling at unitarity. Finally fixing p to $4/3$ provides the coefficient A and a value of the homogeneous contact $\zeta = 0.82(9)$ in good agreement with previous measurements, $\zeta = 0.87(3)$ [126].

8.4 Concluding remarks and perspectives

We have shown in this chapter that equation (8.4) stating the proportionality of the impurity loss rate to the fermions two-body contact could accurately predict the inelastic losses in our Bose-Fermi mixture both in weakly and strongly interacting regimes. Indeed, on the BEC side, we recovered known results on atom-halo-dimer inelastic collisions [243, 244], and at unitarity, we observed the unusual $n_{\mathrm{f}}^{4/3}$ dependence of the loss rate indicating the non-trivial two-body correlations at play in the system. Furthermore, our localized impurity in the center of the resonant Fermi gas allowed us to measure a local two-body contact in excellent agreement with previous measurements.

Our method thus demonstrates that impurity losses can be used as a quantitative probe for short-range correlations in a many-body system. An interesting extent of this work is

---

[5] The slight reduction of the Bose-Fermi losses due to the BEC finite size is computed using the local density approximation:

$$\frac{\langle n_{\mathrm{f}}^{4/3}(\mathbf{r})\rangle_{\mathrm{BEC}}}{n_{\mathrm{f}}^{4/3}(0)} = \frac{\int d^3r n_{\mathrm{b}}(\mathbf{r}) n_{\mathrm{f}}^{4/3}(\mathbf{r})}{n_{\mathrm{f}}^{4/3}(0) \int d^3r n_{\mathrm{b}}(\mathbf{r})}. \tag{8.18}$$

Introducing the Thomas-Fermi radii $R_{\mathrm{TF,b}}$ and $R_{\mathrm{TF,f}}$, we find

$$\frac{\langle n_{\mathrm{f}}^{4/3}(\mathbf{r})\rangle_{\mathrm{BEC}}}{n_{\mathrm{f}}^{4/3}(0)} = 1 - \frac{6}{7}\left(\frac{R_{\mathrm{TF,b}}}{R_{\mathrm{TF,f}}}\right)^2 + \frac{5}{21}\left(\frac{R_{\mathrm{TF,b}}}{R_{\mathrm{TF,f}}}\right)^4. \tag{8.19}$$

In practice, we have $\rho = R_{\mathrm{TF,b}}/R_{\mathrm{TF,f}} \simeq 0.35(5)$ for all the data sets as it weakly depends on the total atoms numbers of both clouds.

[6] The peak density of a trapped unitary Fermi gas is related to its total atom number via the formula

$$n_{\mathrm{f}}(0) = \frac{4\sqrt{N_{\mathrm{f}}}}{\sqrt{6}\pi^2\xi^{3/4}}\left(\frac{\bar{\omega}_{\mathrm{f}} m_{\mathrm{f}}}{\hbar}\right)^{3/2}, \tag{8.21}$$

where $\xi = 0.376(4)$ is the Bertsch parameter measured with high precision in [121].

to measure the two-body contact of the unitary Fermi gas at finite temperature, whose behavior is still largely debated[7] near the normal-superfluid transition [258]. More generally, our results are another illustration of the universal behavior of three-body recombination for large scattering lengths as we have shown in chapter 6. The $1/T^2$ and $n^{-4/3}$ scaling laws of the three-body loss coefficient L_3 of the unitary Bose gas at high and low temperatures respectively are other remarkable observed examples [36, 85]. Similarly, another interesting perspective would be to measure the decay of the unitary Fermi gas. Indeed, the loss rate should be proportional to the three-body contact of the unitary Fermi gas, which is to our knowledge only known at high temperature. By dimensional argument, we can however predict its scaling at zero temperature $\dot{n}_\mathrm{f} \propto n_\mathrm{f}^{2.85}$ (see the perspective section in the conclusion chapter).

Finally, this unified description of impurity losses in the BEC-BCS crossover also provides a framework to interpret the experimental data on ^{6}Li/^{40}K mixture [245] and ^{6}Li/^{174}Yb mixture [246] mentioned at the beginning of the chapter. In appendix E, we analyze the data presented in [245].

---

[7] In [258], a sharp decrease of the two-body contact is observed near the transition temperature. However, as the unitary Fermi gas belongs to the 3D XY universality class, the contact is expected to be continuous and its derivative finite [259].

Conclusion

Summary

The results presented in this thesis can be divided into two parts that illustrate complementary aspects of interacting quantum gases. The first part consider the dynamical properties of a mixture of superfluids while the second part deals with inelastic losses in a strongly correlated gas.

To investigate the hydrodynamic property of our mixture, we excited the dipole modes of the clouds to initiate a counterflow between them. At low relative velocity, the oscillations are long lived demonstrating the superfluid behavior of the ensemble. Furthermore, we observed a coherent energy exchange between the clouds signaled by a frequency shift and an amplitude modulation of the boson oscillations. These observations can be fully captured using a sum-rule approach which can be interpreted in terms of two coupled oscillators. We then measured for various interaction strengths in the BEC-BCS crossover a critical velocity above which dissipation occurs. The extracted values are found to be close to the sum of the sound velocities of the two clouds as it can be expected for two homogeneous counterflowing superfluids [86, 166] and the sound velocity of the fermions. This is surprising in as much as several factors and phenomena usually tend to reduce the critical velocity in experiments and make a direct comparison to ideal models difficult [172]. Hence, to complete our experimental findings, we performed a numerical simulation of two counterflowing Bose-Einstein condensates. Similarly to the experiment, the coupled-oscillator model could accurately describe the dynamics of the clouds at low relative velocity, even for large interspecies coupling. To investigate the dynamics for larger oscillation amplitude, we used a principal component analysis to reveal the collective modes dynamics at play in the system. We uncovered two mechanisms of dissipation. One is analogue to the simple Landau mechanism corresponding to the emission of a single excitation in the superfluid by a rigid impurity which doesn't show any activation threshold when the relative motion is oscillatory. The second one corresponds to the generalized Landau criterion where excitations are created in both superfluids [86, 166]. Contrary to the first scenario, this mechanism presents a threshold behavior that remains when the relative velocity is oscillating in time. For low interspecies coupling we expect the second mechanism to dominate, which could explain why we observed such nice onset of dissipation in our experiments.

In a second part, we considered the inelastic losses in our cold gases. We showed theoretically, that the three-body recombination rate is proportional to the few-body correlations at short distances. Using the universal contact relations it is thus possible to relate the loss rate to several microscopic and macroscopic quantities of the system such as the equation of state of the gas. With this, we can predict the loss rate in various regimes and in particular for strongly correlated systems where few-body processes cannot be isolated

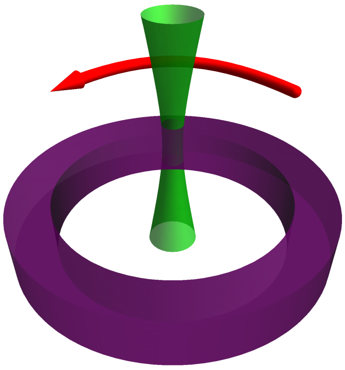

Figure 8.9: Schematic view of a mixture of superfluids in a ring trap (purple) that could be created using a ring shaped dipole trap for radial confinement and a sheet trap for vertical confinement. A counterflow between the two species can be created by a stirring laser (green) with a well chosen wavelength.

from the many-body environment. As a matter of fact for resonant interactions, this leads to an unusual dependence on density or temperature of the loss rate, that we illustrated on two cases.

We first considered the case of the unitary Bose gas, where interactions between bosons are resonant. Its stability is hindered by strong three-body recombination. In a first part, we presented a model taking into account both three-body recombination and evaporation to describe the atom losses and temperature dynamics in a dilute unitary Bose gas. It allows for a quantitative measurement of the three-body loss rate and the method is applied to results obtained by our team (^{7}Li) and Cheng Chin's group at Chicago (^{133}Cs). This analysis confirms the $1/T^2$ universal behavior of the losses at unitarity found in [36]. In a second part, we studied theoretically the effect of three-body losses and interactions on the momentum distribution of a homogeneous unitary Bose gas in the dilute limit. We compared it to the results at JILA on a gas of ^{85}Rb.

Finally, we presented a study of inelastic losses in our ultracold Bose-Fermi mixture. One possible inelastic decay channel is via the recombination of two different spin states fermions and a boson. The associated loss rate is then proportional to the Tan's contact parameter of the Fermi gas. We verified this prediction by probing the recombination rate in our ^{7}Li/^{6}Li mixture in both the thermal and dual-superfluid regimes. When the interactions between fermions become resonant, we showed that the loss rate is proportional to $n_f^{4/3}$, where n_f is the fermionic density. This unusual exponent signals strong correlations among fermions.

Perspectives

The work presented in this thesis can be extended in several directions, here we focus on two compelling ideas that could be tested in near future in our group.

Superfluid counterflow in a ring trap

As we have seen in chapter 3 and 4, non-uniform densities and an oscillatory relative motion hinder the analysis of a superfluid counterflow. An interesting way to extend our study of counterflowing superfluids is to repeat the experiment (and possibly the numerical simulations) in a better suited environment: a ring trap, as depicted in Fig. 8.9. It could allow for a counterflow with a quasi-constant velocity and with a uniform density in the direction of motion. The ring trap can be realized by various means [260, 261, 262, 263]. As in [261, 262], it could be made with a combination of red detuned beams creating a ring shaped dipole trap for the radial confinement and a sheet trap for vertical confinement. Another possibility is to use blue detuned beams to create repulsive walls in order for the clouds to be also homogeneous in the radial direction [39, 40].

Metastable currents with long persisting times can be prepared by several methods. As it was done in [261, 260], a rotation can be induced on the atoms by a transfer of the orbital momentum of a Laguerre-Gauss (LG) beam to the atoms by a two-photon Raman process. This necessitates two internal states and hence could be done on a Bose gas provided the states have convenient scattering properties (positive scattering lengths for the BEC to be stable, which is not always the case for ^{7}Li). The created rotation frequency is $l \times \Omega_0$ where l is the orbital angular momentum of the LG beam and $\Omega_0 = \hbar/mR^2$ is the rotational quantum, with R the ring radius. For lithium atoms in a ring of radius of $30\,\mu$m, with $l = 10$ as used in [261], the flow velocity is about $\simeq 0.5$ cm/s. Hence, this might not be enough to reach the predicted critical velocity $c_\mathrm{b} + c_\mathrm{f}$ which for typical densities ($10^{13}\,\mathrm{cm}^{-3}$) should be on the order of a few cm/s. The other existing strategy is to use a stirring laser beam [262]. This creates a so-called weak link that allows the superfluid to gain angular momentum via the phase slip phenomenon that occurs every time the stirring frequency is close to a multiple of the rotational quantum [262]: A vortex-antivortex pair is nucleated in the vicinity of the beam and separates to reach the confinement walls. The net result is an increase of the winding number l by one unit. In order to create a counterflow between two superfluids, the stirring beam has to affect only one specie. This might prove difficult for a ^{6}Li-^{7}Li mixture due to similar transition frequencies, but could be implemented more easily with different element mixtures e.g. ^{6}Li-^{41}K [264] using a blue-detuned beam close to the ^{6}Li D-lines.

The onset of dissipation could be detected by the appearance of a dynamical instability in the clouds density [166], or by a rapidly decaying relative velocity. The ring geometry can also be used to probe the superfluid fraction by measuring the fraction of atoms put in motion by a weakly perturbing stirring potential. Finally, another phenomenon that could observed is the Andreev-Bashkin effect [148] initially predicted for the superfluid ^{3}He-^{4}He mixture. Due the strong interspecies interaction, the ^{3}He atoms are dressed by the surrounding ^{4}He atoms and form quasiparticles with a large effective mass so that a superfluid flow of ^{3}He atoms should also transport a substantial mass of ^{4}He atoms. This non-dissipative drag might be observable in a superfluid cold atom mixture close to an interspecies Feshbach resonance. In particular it could be seen as a shift of the rotational quantum Ω_0 due to the effective mass of the superfluid particles.

Measuring the three-body contact of a strongly interacting Fermi gas

Another strongly correlated system where three-body loss rate should exhibit exotic scaling is the resonant Fermi gas itself (without impurities). Contrary to the interacting Bose gas, the 2-spin component interacting Fermi gas does not suffer from severe three-body recombination close to the Feshbach resonance. The probability to find two fermions with the same spin at short distances is strongly reduced by the Pauli exclusion principle (and also from the absence of an Efimov channel[8]). Inelastic losses in the degenerate regime were investigated experimentally in [78, 79, 80] and theoretically in [77, 265, 266]. The different inelastic processes are well understood in the two asymptotic limits of the BEC-BCS crossover, but the unitary regime still lacks both theoretical and quantitative experimental investigation.

Before considering the resonant case, it is useful to start first with the two limits of the crossover. On the BEC side, the losses are dominated by two-body processes, dimer-dimer and atom-dimer collisions. Indeed the vanishing size of the weakly bound dimer which scale like a strongly enhances the probability to find closeby triplets of fermions. On the BCS side, the size of the Cooper pairs being large $\sim 1/k_F$, losses are described by three-body processes which require p-wave collisions and vanish for $|a| \to 0$. Following a suggestion from Félix Werner, one can predict the precise scaling in density and scattering length for the loss rates using dimensional arguments on the three-body contact[9]. For a wave function in a given three-body channel characterized by the parameter $s_{l,n}$ (given in table 1.1) the three-body contact density $\mathcal{C}_3$ has the dimension $L^{-2s_{l,n}-5}$ where L is a length (see section 5.2). Since we can infer the scaling of $\mathcal{C}_3$ on the density we can deduce its dependence on the other variables.

BEC limit

For the dimer-dimer collisions we can consider a four-body wavefunction composed of two dimers. The dimers collide dominantly via a two-body s-wave channel at low temperature. However, a triplet subset of those four particles can undergo a p-wave collision while having a total orbital angular momentum still equal to zero [77]. The dominant relaxation process is thus via the $l = 1$, $n = 0$ channel which has the lowest exponent $s_{1,0} \simeq 1.77$. Hence, we have

$$\frac{dn_d}{dt} \propto -n_d^2 a^{-2s_{1,0}+1} \simeq -n_d^2 a^{-2.55}. \tag{8.22}$$

Atom-dimer collisions are also dominantly s-wave and the relaxation will occur via the $l = 0$, $n = 0$ channel with $s_{0,0} \simeq 2.17$. We then have

$$\frac{dn_d}{dt} = \frac{dn_a}{dt} \propto -n_a n_d a^{-2s_{0,0}+1} \simeq -n_a n_d a^{-3.34}. \tag{8.23}$$

This process is actually negligible at low temperatures ($T \ll E_b$) as the Fermi gas is fully molecular in the far BEC limit and the atom-dimer loss rate decreases faster than the dimer-dimer loss rate when going to unitarity. The lifetime of an ultracold mixture of molecules and atoms of ^{40}K was measured in [78, 79]. They found a scaling a^p with $p = -2.3(4)$ for the loss rate in agreement with the dimer-dimer predicted exponent $p \simeq -2.55$ [77].

BCS limit

Three-body s-wave collisions of three unbound fermions are strongly supressed by the Pauli principle, see [267]. The main relaxation process is via p-wave collisions and thus

---

[8] For mass-imbalanced fermionic system there can exist an Efimov channel and resonant losses can happen via p-wave collisions.

[9] Or equivalently by looking at the probability of finding three fermions within a vanishing hyperradius.

through the channel $l = 1$, $n = 0$ and the exponent $s_{1,0} \simeq 1.77$. Hence,

$$\frac{dn_a}{dt} \propto -n_a^3 |a|^{-2s_{1,0}+4} \simeq -n_a^3 |a|^{0.45}. \tag{8.24}$$

We neglected the effects of Cooper pairing which actually tend to enhance the losses [266] but is a subleading contribution. The exponent on the scattering length $p \simeq 0.45$ is within less than a factor two to what was measured experimentally in [80] where they found an exponent $p = 0.79(14)$.

Unitary limit

The most interesting case and yet unexplored is the unitarity regime. At zero temperature, the only remaining length scale is $1/k_F$ so that we have the unusual density dependence of the loss rate

$$\frac{dn}{dt} \propto -\sum_{l,n} \alpha_{l,n} n^{(2s_{l,n}-5)/3} \tag{8.25}$$

In principle both s-wave and p-wave collisions are possible, but relaxation will mainly occur via the channel which has the lowest exponent $s_{l,n}$, here $s_{1,0} \simeq 1.77$, as the others channels contribution are smaller by a factor $(nb^3)^{(s_{l,n}-s_{1,0})2/3} \ll 1$. We can thereby expect like for the unitary Bose gas another fractional density dependence of the loss rate:

$$\frac{dn}{dt} \propto -n^{2.85} \tag{8.26}$$

At high temperature, the many-body correlations are negligible, we should recover the n^3 scaling so that

$$\frac{dn}{dt} \propto -\frac{n^3}{T^{0.23}}. \tag{8.27}$$

These exotic scaling laws predicted at both low and high temperatures remain to be confirmed experimentally. More generally, measuring the inelastic losses in a strongly interacting Fermi gas would provide information about its three-body correlations at short distance or equivalently its three-body contact C_3 for which there are currently no theoretical estimates. Furthermore, by performing a calibration of the losses on the BEC or the BCS side like we did in chapter 8 for the impurity losses, it should be possible to measure the precise value of C_3. Its determination might prove useful for characterizing the effect of three-body interactions that are expected to occur between neutrons in the crust of neutron stars [268].

Appendix A

Derivation of the coupled oscillator model using the sum-rule approach

In this appendix we provide the derivation of equations (3.7, 3.8) using the sum rule method as given in our publication [269].

The dynamics of the system is described by a Hamiltonian

$$\widehat{H} = \sum_{i,\alpha} \left[\frac{\widehat{p}_{\alpha,i}^2}{2m_\alpha} \right] + U(\boldsymbol{r}_{\alpha,i}), \tag{A.1}$$

where $\alpha = \mathrm{b}, \mathrm{f}$ labels the isotopes, and U describes the total (trap+interaction) potential energy of the cloud.

Consider the operators $\widehat{F}_\alpha = \sum_{i=1}^{N_\alpha} \widehat{z}_{\alpha,i}$, where $z_{\alpha,i}$ is the position along z of the i-th atom of species $\alpha = \mathrm{b}, \mathrm{f}$ and take $\widehat{F}(d_\mathrm{f}, d_\mathrm{b}) = \sum_\alpha d_\alpha \widehat{F}_\alpha$ an excitation operator depending on two mixing coefficients (d_α). We introduce the moments S_p defined by

$$S_p = \sum_n (E_n - E_0)^p \left| \langle n | \widehat{F} | 0 \rangle \right|^2,$$

where $|n\rangle$ and E_n are the eigenvectors and the eigenvalues of the Hamiltonian $\widehat{H}$ (by definition $|0\rangle$ is the ground state and E_0 is its energy). Using the Closure Relation and first order perturbation theory, S_1 and S_{-1} can be calculated exactly and we have

$$S_1 = -\sum_\alpha \frac{\hbar^2}{m_\alpha} N_\alpha d_\alpha^2, \tag{A.2}$$

$$S_{-1} = -\frac{1}{k} \sum_{\alpha,\beta} d_\alpha d_\beta N_\alpha \frac{\partial \langle z_\alpha \rangle}{\partial b_\beta}, \tag{A.3}$$

where k is the restoring force of the axial magnetic trap and $\langle z_\alpha \rangle$ is the center of mass position of atoms α in the presence of a perturbing potential $-k \sum_\beta b_\beta \widehat{F}_\alpha$ corresponding to a shift of the trapping potential of species β by a distance b_β. $\langle z_\alpha \rangle$ satisfies two useful conditions. First, using Hellmann-Feynman's theorem, the matrix $N_\alpha \partial_{b_\beta} \langle z_\alpha \rangle = \partial^2_{b_\alpha b_\beta} \widehat{H}$ is symmetric. Secondly, if we shift the two traps by the same quantify $b_\beta = b$, the center of mass of the two clouds move by $\langle z_\alpha \rangle = b$. Differentiating this constraint with respect to b yields the condition $\sum_\beta \partial_{b_\beta} \langle z_\alpha \rangle = 1$.

Experimentally, we observe that only two modes are excited by the displacement of the trap center. We label $|n = 1\rangle$ and $|n = 2\rangle$ the corresponding modes and we take

$\hbar\omega_n = E_n - E_0$, with, by convention, $\omega_1 \leq \omega_2$. We thus have for any set of mixing parameters $(d_\mathrm{f}, d_\mathrm{b})$,

$$\hbar^2\omega_1^2 \leq \frac{S_1}{S_{-1}} \leq \hbar^2\omega_2^2. \tag{A.4}$$

To find the values of the two frequencies ω_1 and ω_2, one thus simply has to find the extrema of S_1/S_{-1} with respect to d_f and d_b. Using the sum rules (A.2) and (A.3), we see that

$$\frac{S_1}{S_{-1}} = \hbar^2 k \frac{\sum_\alpha N_\alpha/m_\alpha d_\alpha^2}{\sum_{\alpha,\beta} N_\alpha d_\alpha d_\beta \frac{\partial\langle z_\alpha\rangle}{\partial b_\beta}}. \tag{A.5}$$

This expression can be formally simplified by taking $d'_\alpha = d_\alpha\sqrt{N_\alpha/m_\alpha}$ and $\Psi = (d'_\mathrm{f}, d'_\mathrm{b})$. We then have

$$\frac{S_1}{S_{-1}} = \hbar^2 k \frac{\langle\Psi|\Psi\rangle}{\langle\Psi|\mathcal{M}|\Psi\rangle}, \tag{A.6}$$

where the scalar product is defined by $\langle\Psi|\Psi'\rangle = \sum_\alpha \Psi_\alpha\Psi'_\alpha$ and the effective-mass operator is given by

$$\mathcal{M}_{\alpha\beta} = \sqrt{m_\alpha m_\beta}\sqrt{\frac{N_\alpha}{N_\beta}}\frac{\partial\langle z_\alpha\rangle}{\partial b_\beta}. \tag{A.7}$$

With these notations, the frequencies $\omega_{i=1,2}$ are given by $\omega_i = \sqrt{k/\tilde{m}_i}$, where $\tilde{m}_i$ is an eigenvalue of $\mathcal{M}$.

In the weak-coupling limit, the cross-terms $\partial_{b_\beta}\langle z_\alpha\rangle$ $(\alpha \neq \beta)$ are small and using their symmetry properties, we can write $\mathcal{M}$ as $\mathcal{M}_0 + \mathcal{M}_1$ with

$$\mathcal{M}_0 = \begin{pmatrix} m_\mathrm{f} & 0 \\ 0 & m_\mathrm{b} \end{pmatrix}, \tag{A.8}$$

$$\mathcal{M}_1 = \begin{pmatrix} -m_\mathrm{f}\frac{\partial\langle z_\mathrm{f}\rangle}{\partial b_\mathrm{b}} & \sqrt{m_\mathrm{f} m_\mathrm{b}}\sqrt{\frac{N_\mathrm{b}}{N_\mathrm{f}}}\frac{\partial\langle z_\mathrm{b}\rangle}{\partial b_\mathrm{f}} \\ \sqrt{m_\mathrm{f} m_\mathrm{b}}\sqrt{\frac{N_\mathrm{b}}{N_\mathrm{f}}}\frac{\partial\langle z_\mathrm{b}\rangle}{\partial b_\mathrm{f}} & -m_\mathrm{b}\frac{\partial\langle z_\mathrm{b}\rangle}{\partial b_\mathrm{f}} \end{pmatrix}. \tag{A.9}$$

Since the matrix $\mathcal{M}$ is symmetric we can use the usual perturbation theory to calculate its eigenvalues and eigenvectors. We have to first order

$$\tilde{m}_1 = m_\mathrm{f}\left(1 - \frac{\partial\langle z_\mathrm{f}\rangle}{\partial b_\mathrm{b}}\right), \tag{A.10}$$

$$\tilde{m}_2 = m_\mathrm{b}\left(1 - \frac{\partial\langle z_\mathrm{b}\rangle}{\partial b_\mathrm{f}}\right). \tag{A.11}$$

Using the symmetry of $N_\alpha\partial_{b_\beta}\langle z_\alpha\rangle$, we see that in the experimentally relevant limit $N_\mathrm{f} \gg N_\mathrm{b}$, we have $\partial_{b_\mathrm{f}}\langle z_\mathrm{b}\rangle \gg \partial_{b_\mathrm{b}}\langle z_\mathrm{f}\rangle$. Thus the frequency of ^{6}Li is essentially not affected by the coupling between the two species. To leading order, we can identify ω_1 (ω_2) with $\tilde{\omega}_\mathrm{b}$ $(\tilde{\omega}_\mathrm{f})$ and we have

$$\tilde{\omega}_\mathrm{f} \simeq \omega_\mathrm{f}, \tag{A.12}$$

$$\tilde{\omega}_\mathrm{b} \simeq \omega_\mathrm{b}\left(1 + \frac{1}{2}\frac{\partial\langle z_\mathrm{b}\rangle}{\partial b_\mathrm{f}}\right). \tag{A.13}$$

To calculate the frequency $\tilde{\omega}_{\rm b}$ we need to know the crossed-susceptibility $\partial_{b_{\rm f}}\langle z_{\rm b}\rangle$. Since this is in equilibrium quantity, we can calculate it using the local-density approximation. We then obtain

$$\frac{\partial\langle z_{\rm b}\rangle}{\partial b_{\rm f}}=\frac{kg_{\rm bf}}{N_{\rm b}}\int d^3\boldsymbol{r}\,z^2\left(\frac{\partial n_{\rm f}}{\partial\mu_{\rm f}}\right)\left(\frac{\partial n_{\rm b}}{\partial\mu_{\rm b}}\right) \tag{A.14}$$

In the limit $N_{\rm b}\ll N_{\rm f}$, the bosonic cloud is much smaller than the fermionic cloud. We can therefore approximate this expression by

$$\frac{\partial\langle z_{\rm b}\rangle}{\partial b_{\rm f}}\simeq\frac{kg_{\rm bf}}{N_{\rm b}}\left(\frac{\partial n_{\rm f}}{\partial\mu_{\rm f}}\right)_0\int d^3\boldsymbol{r}\,z^2\left(\frac{\partial n_{\rm b}}{\partial\mu_{\rm b}}\right) \tag{A.15}$$

where the index zero indicates that the derivative is calculated at the center of the trap. The integral can be calculated exactly and we finally obtain

$$\frac{\partial\langle z_{\rm b}\rangle}{\partial b_{\rm f}}=g_{\rm bf}\left(\frac{\partial n_{\rm f}}{\partial\mu_{\rm f}}\right)_0, \tag{A.16}$$

where we recover eq. (A.13) from chapter 3.

To get the dynamics of the system after the excitation, we need to calculate the eigenvectors of the matrix $\mathcal{M}$. Note $\Psi_i=(d'_{i,\rm f},d'_{i,\rm b})$ the eigenvector associated to the eigenvalue ω_i. Using once more first order perturbation theory, we have

$$\Psi_1=\begin{pmatrix}1\\ \frac{\sqrt{m_{\rm f}m_{\rm b}}}{m_{\rm f}-m_{\rm b}}\sqrt{\frac{N_{\rm b}}{N_{\rm f}}}\frac{\partial\langle z_{\rm b}\rangle}{\partial b_{\rm f}}\end{pmatrix}, \tag{A.17}$$

$$\Psi_2=\begin{pmatrix}\frac{\sqrt{m_{\rm f}m_{\rm b}}}{m_{\rm b}-m_{\rm f}}\sqrt{\frac{N_{\rm b}}{N_{\rm f}}}\frac{\partial\langle z_{\rm b}\rangle}{\partial b_{\rm f}}\\ 1\end{pmatrix}, \tag{A.18}$$

from which we deduce the vectors $\tilde{\Psi}_{i=1,2}=(d_{i,\rm f},d_{i,\rm b})$ giving the excitation operator $\widehat{F}(d_{i,\rm f},d_{i,\rm b})$. More precisely

$$\tilde{\Psi}_1=\sqrt{\frac{m_{\rm f}}{N_{\rm f}}}\begin{pmatrix}1\\ \frac{m_{\rm b}}{m_{\rm f}-m_{\rm b}}\frac{\partial\langle z_{\rm b}\rangle}{\partial b_{\rm f}}\end{pmatrix}, \tag{A.19}$$

$$\tilde{\Psi}_2=\sqrt{\frac{m_{\rm b}}{N_{\rm b}}}\begin{pmatrix}\frac{m_{\rm f}}{m_{\rm b}-m_{\rm f}}\frac{N_{\rm b}}{N_{\rm f}}\frac{\partial\langle z_{\rm b}\rangle}{\partial b_{\rm f}}\\ 1\end{pmatrix}. \tag{A.20}$$

Note d the initial displacement of the two species and expand the initial condition $Z=(z_{\rm f}(0),z_{\rm b}(0))=(d,d)$ over the basis $\{\tilde{\Psi}_1,\tilde{\Psi}_2\}$ as $Z=\sum_i c_i\tilde{\Psi}_i$. Since by construction the operator $\widehat{F}(d_{i,\rm f},d_{i,\rm b})$ excites solely the mode ω_i we must have at time t $Z(t)=\sum_i c_i\cos(\omega_i t)\tilde{\Psi}_i$ (we assume that the initial velocities are zero). After a straightforward calculation, we get

$$z_{\rm f}(t)=d\left[\frac{(1-\varepsilon_m\rho\eta)\cos(\omega_1 t)+\eta\rho\varepsilon_m(1+\varepsilon_m)\cos(\omega_2 t)}{1+\varepsilon_m^2\rho\eta}\right], \tag{A.21}$$

$$z_{\rm b}(t)=d\left[\frac{-\varepsilon_m(1-\varepsilon_m\rho\eta)\cos(\omega_1 t)+(1+\varepsilon_m)\cos(\omega_2 t)}{1+\varepsilon_m^2\rho\eta}\right], \tag{A.22}$$

with $\eta = m_{\rm f}/m_{\rm b}$, $\rho = N_{\rm b}/N_{\rm f}$, and $\varepsilon_m = m_{\rm b}/(m_{\rm b}-m_{\rm f})\partial_{b_{\rm f}}\langle z_{\rm b}\rangle$.
In experimentally relevant situations, we have $\varepsilon_m \ll 1$, $\rho \ll 1$ and $\eta \simeq 1$, we can thus approximate the previous equations by

$$z_{\rm f}(t) \simeq d\left[(1-\varepsilon_m\rho)\cos(\tilde{\omega}_{\rm f}t) + \rho\varepsilon_m\cos(\tilde{\omega}_{\rm b}t)\right] \tag{A.23}$$

$$z_{\rm b}(t) \simeq d\left[-\varepsilon_m\cos(\tilde{\omega}_{\rm f}t) + (1+\varepsilon_m)\cos(\tilde{\omega}_{\rm b}t)\right], \tag{A.24}$$

and where according to Eq. (A.13), we can take

$$\varepsilon_m = \frac{2m_{\rm b}}{m_{\rm b}-m_{\rm f}}\left(\frac{\tilde{\omega}_{\rm b}-\omega_{\rm b}}{\omega_{\rm b}}\right). \tag{A.25}$$

Appendix B

Instability domains of modified 2D Mathieu's equations

In this appendix, we compute the parametric instability domains associated to the following modified Mathieu's equations:

$$\frac{d^2u}{dt^2} + u + \varepsilon \mathrm{e}^{i\alpha\cos(\Omega t)} v = 0, \tag{B.1}$$

$$\frac{d^2v}{dt^2} + v + \varepsilon \mathrm{e}^{-i\alpha\cos(\Omega t)} u = 0. \tag{B.2}$$

If we introduce the new variables $r = u + v^*$ and $s = u - v^*$ we have the uncoupled differential equations

$$\frac{d^2r}{dt^2} + r + \varepsilon \mathrm{e}^{i\alpha\cos(\Omega t)} r^* = 0, \tag{B.3}$$

$$\frac{d^2s}{dt^2} + s - \varepsilon \mathrm{e}^{i\alpha\cos(\Omega t)} s^* = 0, \tag{B.4}$$

which will have the same solutions provided $\varepsilon \to -\varepsilon$.
Since parametric instabilities develop in a time scale given by ε, in the limit $\varepsilon \ll 1$ we can adopt a multi-scale analysis. Here, let's introduce two timescales $\tau_0 = t$ and $\tau_1 = \varepsilon t$ and write our general solution as a perturbation series solution dependent both on τ_0 and τ_1:

$$r(t) = \sum_{n=0}^{\infty} \varepsilon^n r_n(\tau_0, \tau_1). \tag{B.5}$$

We will also look at frequencies close to an a priori resonant one ω_0 such that $\Omega = \omega_0 + \varepsilon\omega_1$.
For a function $f(\tau_0, \tau_1)$ we have the identity

$$\frac{d^2f}{dt^2} = \frac{\partial^2 f}{\partial \tau_0^2} + 2\varepsilon \frac{\partial^2 f}{\partial \tau_0 \partial \tau_1} + \varepsilon^2 \frac{\partial^2 f}{\partial \tau_1^2}. \tag{B.6}$$

Then to 0-order in ε, the equation (B.3) gives

$$\frac{\partial^2 r_0}{\partial \tau_0^2} + r_0 = 0. \tag{B.7}$$

The solutions can be written as

$$r_0(\tau_0, \tau_1) = A(\tau_1)\mathrm{e}^{i\tau_0} + B(\tau_1)\mathrm{e}^{-i\tau_0}. \tag{B.8}$$

If we now plug in these solutions into (B.3), we can look at the first order terms in ε and we obtain the equation

$$\frac{\partial^2 r_1}{\partial \tau_0^2} + r_1 + 2i\left(\frac{\partial A}{\partial \tau_1}\mathrm{e}^{i\tau_0} - \frac{\partial B}{\partial \tau_1}\mathrm{e}^{-i\tau_0}\right) + \mathrm{e}^{i\alpha\cos(\omega_0\tau_0+\omega_1\tau_1)}\left(A^*(\tau_1)\mathrm{e}^{-i\tau_0} + B^*(\tau_1)\mathrm{e}^{i\tau_0}\right) = 0 \tag{B.9}$$

We can recognize the equation of an harmonic oscillator forced by oscillating terms. For the solution r_1 to not diverge on a time scale τ_0 and the multiscale approach to be valid, there shouldn't be any resonant terms.
Using the identity

$$\mathrm{e}^{i\alpha\cos(\omega_0\tau_0+\omega_1\tau_1)} = \sum_k i^k J_k(\alpha)\mathrm{e}^{ik\omega_0\tau_0}\mathrm{e}^{ik\omega_1\tau_1} \tag{B.10}$$

we will have a resonance whenever there exist an integer k such that $k\omega_0 = 2$.
In other words the resonant frequencies are

$$\omega_{0,n} = \frac{2}{n}\,, \qquad n \in \mathbb{N}. \tag{B.11}$$

To cancel the resonance we need that

$$\begin{aligned} 2i\frac{\partial A}{\partial \tau_1} + \quad & i^n J_n(\alpha)\mathrm{e}^{in\omega_1\tau_1}A^* + J_0(\alpha)B^* && = 0, && \text{(B.12)}\\ -2i\frac{\partial B}{\partial \tau_1} + \quad & J_0(\alpha)A^* + (-i)^n J_n(\alpha)\mathrm{e}^{-in\omega_1\tau_1}B^* && = 0. && \text{(B.13)} \end{aligned}$$

By introducing the new variables $a = \exp^{-in\omega_1\tau_1/2}A$ and $b = \exp^{in\omega_1\tau_1/2}B$, we get a time independent set of differential equations

$$\begin{aligned} 2i\frac{\partial a}{\partial \tau_1} - n\omega_1 a + \quad & i^n J_n(\alpha)a^* + J_0(\alpha)b^* && = 0, && \text{(B.14)}\\ -2i\frac{\partial b}{\partial \tau_1} - n\omega_2 b + \quad & J_0(\alpha)a^* + (-i)^n J_n(\alpha)b^* && = 0. && \text{(B.15)} \end{aligned}$$

If we now consider the set a, b, a^*, b^* as independent variables, we have to solve

$$\frac{d}{dt}\begin{pmatrix} a \\ b \\ a^* \\ b^* \end{pmatrix} = \frac{i}{2}\begin{pmatrix} -n\omega_1 & 0 & i^n J_n(\alpha) & J_0(\alpha) \\ 0 & n\omega_1 & -J_0(\alpha) & -(-i)^n J_n(\alpha) \\ -(-i)^n J_n(\alpha) & -J_0(\alpha) & n\omega_1 & 0 \\ J_0(\alpha) & i^n J_n(\alpha) & 0 & -n\omega_1 \end{pmatrix}\begin{pmatrix} a \\ b \\ a^* \\ b^* \end{pmatrix}. \tag{B.16}$$

The eigenvalues of the matrix are

$$\lambda_{\pm,\pm} = \pm\frac{i}{2}\sqrt{(J_0(\alpha) \pm n\omega_1)^2 - J_n(\alpha)^2}. \tag{B.17}$$

We will thus have a parametric instability if

$$J_n(\alpha)^2 \geq (J_0(\alpha) \pm n\omega_1)^2. \tag{B.18}$$

The eigenvalues can be obtained numerically using a Floquet method. A comparison for two mode frequencies is displayed in fig.(B.1) and shows an excellent agreement. We also recover similar instability domains in the $(\alpha, 1/\Omega)$ plane as shown in fig.(B.2).

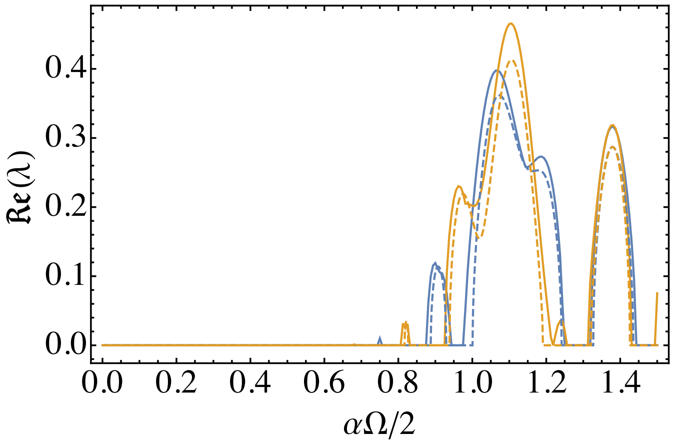

Figure B.1: Real part of $\lambda_{\pm,\pm}$ as a function of the amplitude α for $\omega_1 = 0$. Blue line: n=20, Yellow line: n=22. Dashed lines represent the eigenvalue obtained numerically using Floquet theory on eqs.(B.1,B.2).

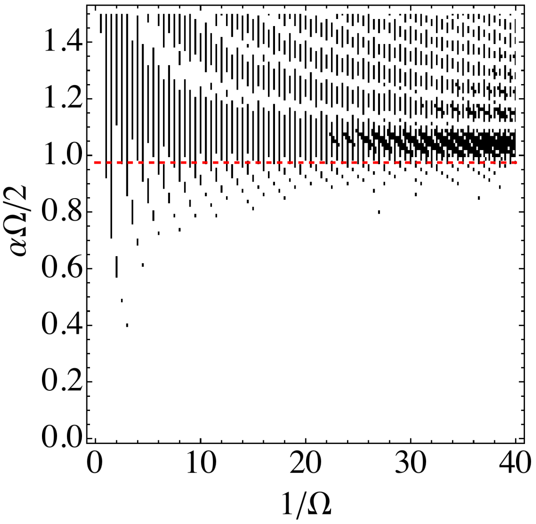

Figure B.2: Instability domains (in black) in the $(\alpha, 1/\Omega)$ space for $\varepsilon = 0.05$. Red dashed line correspond to the critical velocity predicted in the uniform movement case.

Appendix C

Numerical simulation of counterflowing superfluids: supplemental data

In this appendix, we present supplemental data in order for the reader to have a larger overview of the different signals obtained from the numerical simulation itself but also from the principal component analysis. This is of course not exhaustive.

In fig.(C.1), we present the center of mass oscillations of both clouds for different interspecies couplings β_{12}/β_{22}.

In fig.(C.2), we show the rescaled amplitude difference $\Delta z = z_{i,b_1}(t)/b_1 - z_{i,b_2}(t)/b_2$ for different interspecies coupling β_{12}/β_{22}.

In figs.(C.3,C.4,C.5,C.6) we show some typical results obtained from the PCA. We display the 5 most populated modes for each cloud for two different simulation runs.

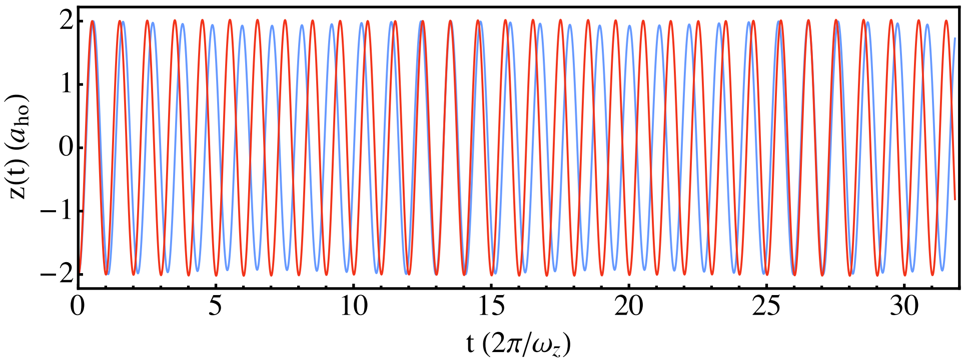

(a) $\beta_{12}/\beta_{22} = 0.003$

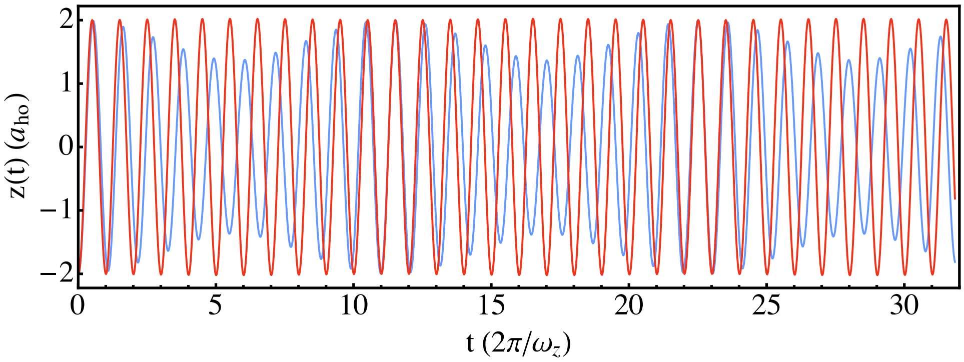

(b) $\beta_{12}/\beta_{22} = 0.031$

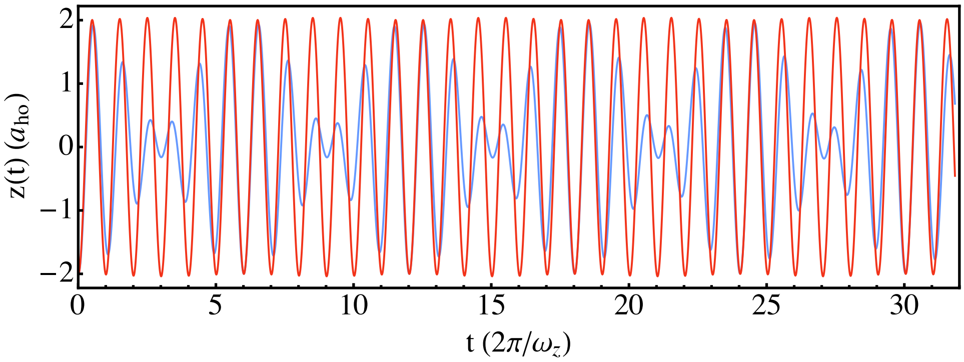

(c) $\beta_{12}/\beta_{22} = 0.186$

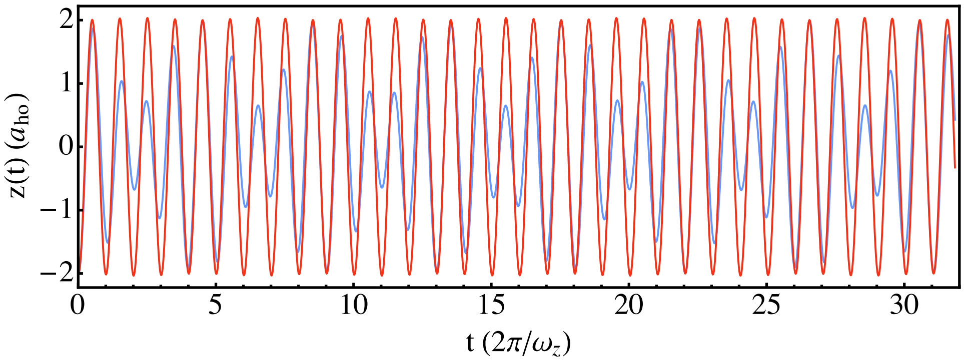

(d) $\beta_{12}/\beta_{22} = 0.291$

Figure C.1: Center of mass oscillation of both clouds ($i = 1$ in blue, $i = 2$ in red) for different interspecies coupling β_{12}/β_{22} and same initial dispalcement $b = 2$.

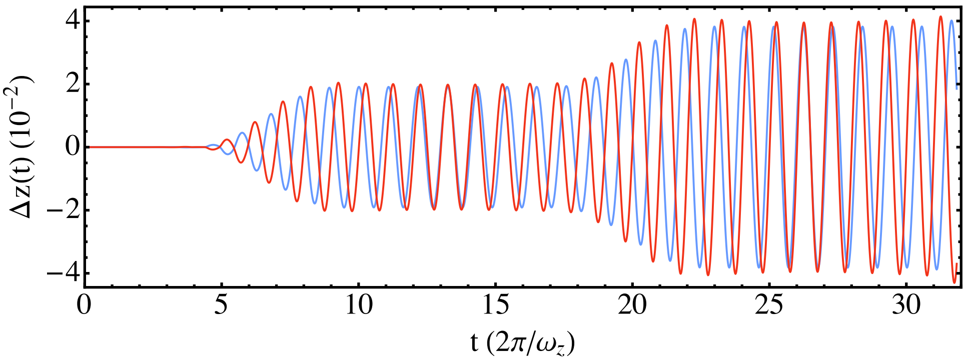

(a) $\beta_{12}/\beta_{22} = 0.003$, $b_1 = 2$, and $b_2 = 8$

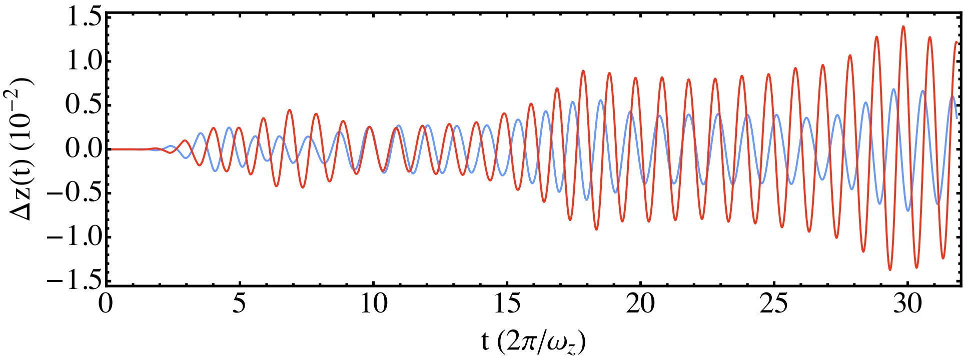

(b) $\beta_{12}/\beta_{22} = 0.031$, $b_1 = 2$, and $b_2 = 7$

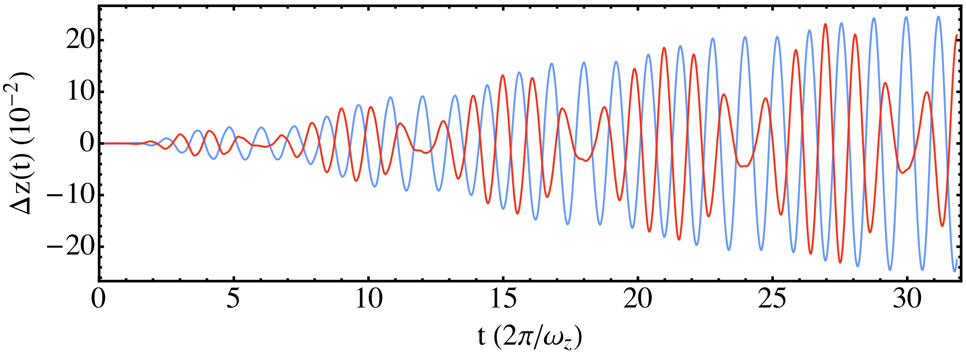

(c) $\beta_{12}/\beta_{22} = 0.186$, $b_1 = 2$, and $b_2 = 7$

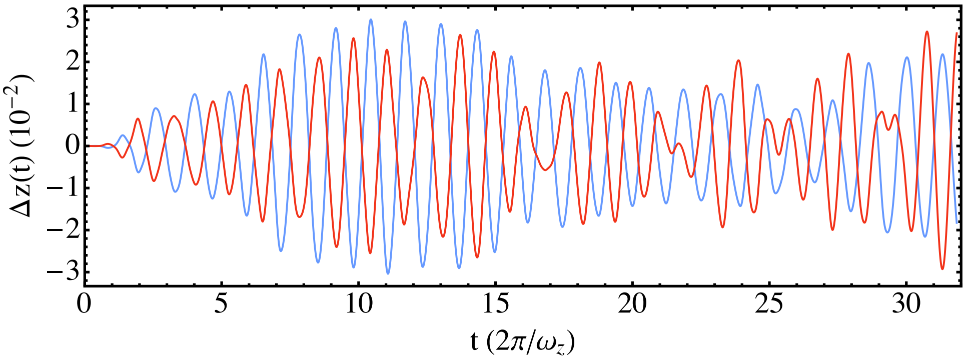

(d) $\beta_{12}/\beta_{22} = 0.291$, $b_1 = 1$, and $b_2 = 5$

Figure C.2: Rescaled amplitude difference $\Delta z = z_{i,b_1}(t)/b_1 - z_{i,b_2}(t)/b_2$ for different interspecies coupling β_{12}/β_{22}. Blue line: small condensate $i : 1$, Red line: large condensate $i = 2$ rescaled with a global factor $N_2/N_1 = 30$.

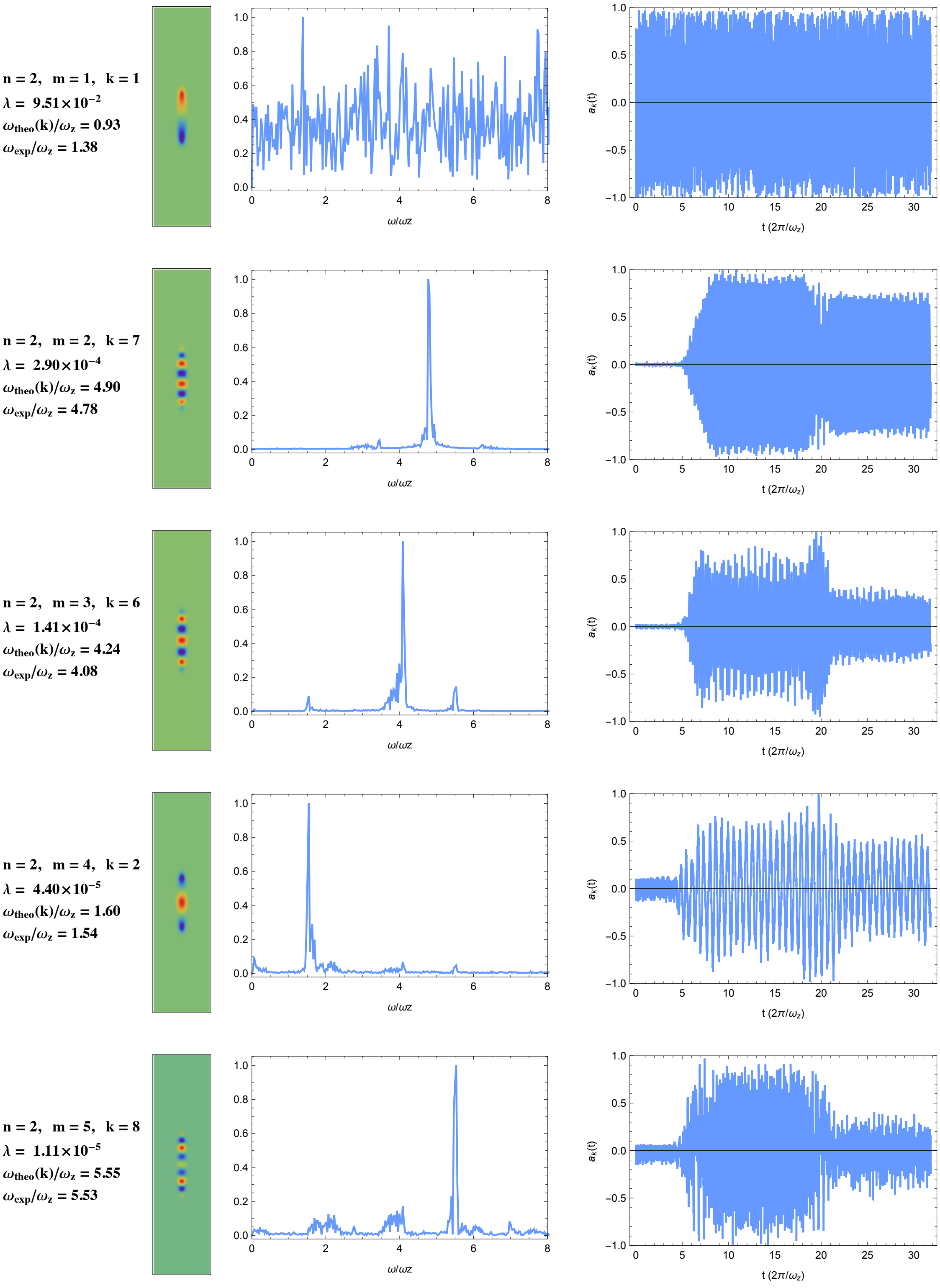

Figure C.3: First five PCA's modes for the small cloud $i = 1$ and the simulation run $\beta_{12}/\beta_{22} = 0.003$, $b = 6$. From left to right figures: Mode's parameters: λ is the associated covariance matrix's eigenvalue. k is the extracted number of nodes which allows to predict the mode frequency ω_{theo}. ω_{exp} is the frequency of the highest peak in the fourier spectrum. The spatial mode structure. The associated fourier spectrum. Mode time evolution.

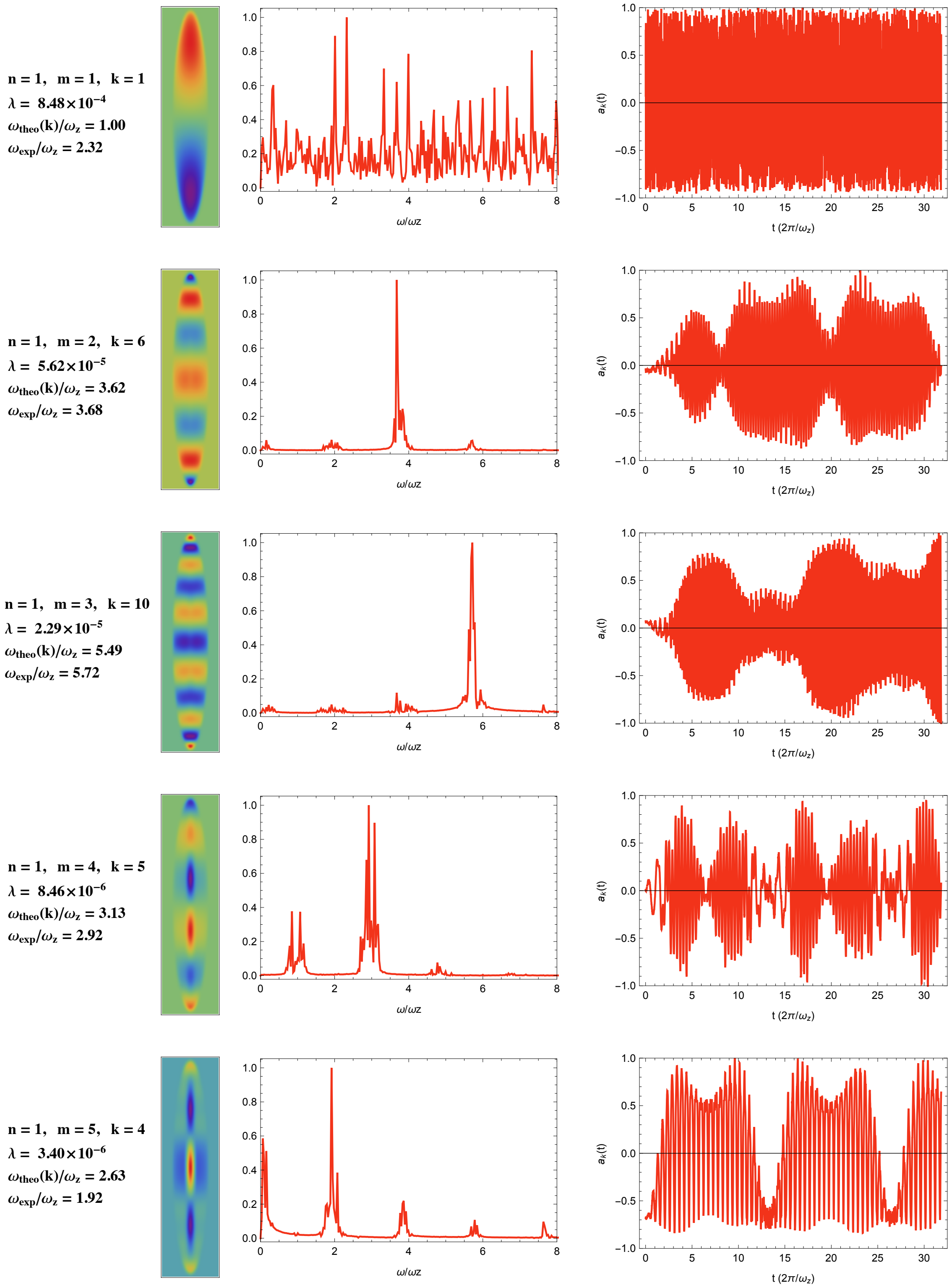

Figure C.4: First five PCA's modes for the large cloud $i = 2$ and the simulation run $\beta_{12}/\beta_{22} = 0.003$, $b = 6$. From left to right figures: Mode's parameters: λ is the associated covariance matrix's eigenvalue. k is the extracted number of nodes which allows to predict the mode frequency ω_{theo}. ω_{exp} is the frequency of the highest peak in the fourier spectrum. The spatial mode structure. The associated fourier spectrum. Mode time evolution.

$n = 2,\ m = 1,\ k = 1$
$\lambda = 1.24\times10^{-1}$
$\omega_{theo}(k)/\omega_z = 0.93$
$\omega_{exp}/\omega_z = 8.92$

$n = 2,\ m = 2,\ k = 2$
$\lambda = 2.59\times10^{-2}$
$\omega_{theo}(k)/\omega_z = 1.60$
$\omega_{exp}/\omega_z = 1.82$

$n = 2,\ m = 3,\ k = 3$
$\lambda = 3.84\times10^{-3}$
$\omega_{theo}(k)/\omega_z = 2.27$
$\omega_{exp}/\omega_z = 2.67$

$n = 2,\ m = 4,\ k = 4$
$\lambda = 5.65\times10^{-4}$
$\omega_{theo}(k)/\omega_z = 2.93$
$\omega_{exp}/\omega_z = 3.68$

$n = 2,\ m = 5,\ k = 7$
$\lambda = 3.56\times10^{-4}$
$\omega_{theo}(k)/\omega_z = 4.90$
$\omega_{exp}/\omega_z = 4.49$

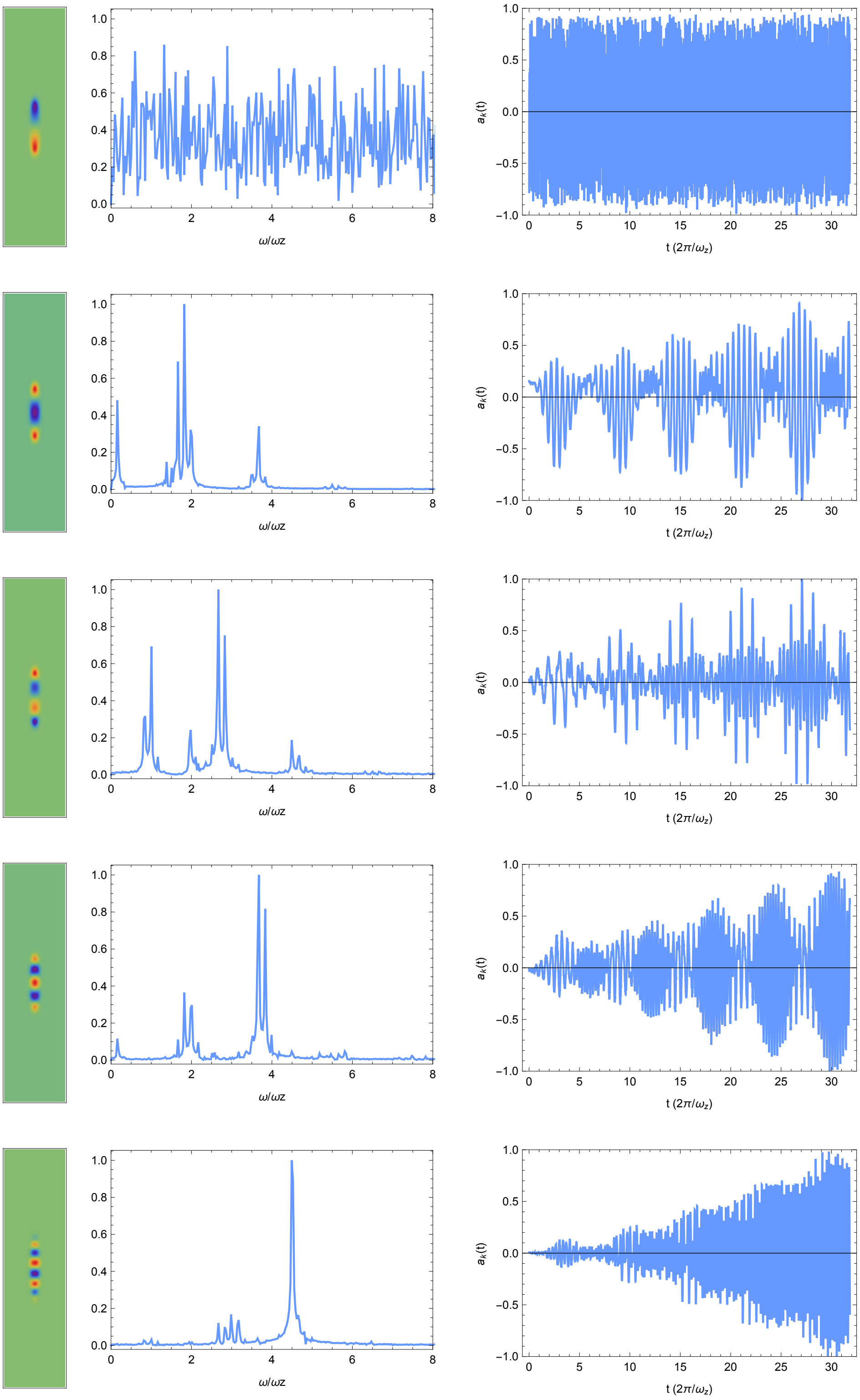

Figure C.5: First five PCA's modes for the small cloud $i = 1$ and the simulation run $\beta_{12}/\beta_{22} = 0.186$, $b = 4.$. From left to right figures: Mode's parameters: λ is the associated covariance matrix's eigenvalue. k is the extracted number of nodes which allows to predict the mode frequency ω_{theo}. ω_{exp} is the frequency of the highest peak in the fourier spectrum. The spatial mode structure. The associated fourier spectrum. Mode time evolution.

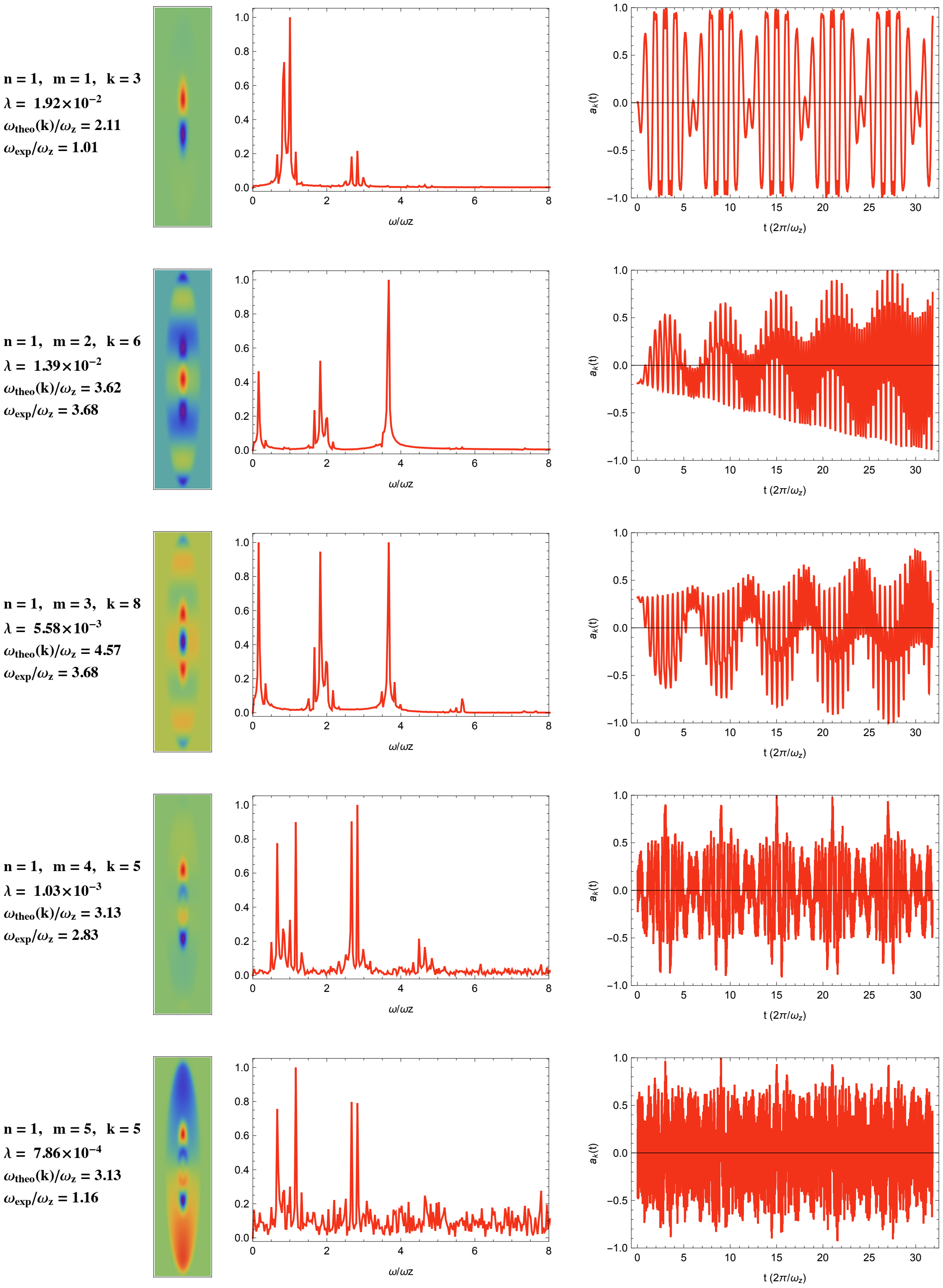

Figure C.6: First five PCA's modes for the large cloud $i = 2$ and the simulation run $\beta_{12}/\beta_{22} = 0.186$, $b = 4$. From left to right figures: Mode's parameters: λ is the associated covariance matrix's eigenvalue. k is the extracted number of nodes which allows to predict the mode frequency ω_{theo}. ω_{exp} is the frequency of the highest peak in the fourier spectrum. The spatial mode structure. The associated fourier spectrum. Mode time evolution.

Appendix D

Momentum distribution of a dilute unitary Bose gas: Supplemental material

In this appendix, we reproduce without modifications the supplemental material of article [232] given in section 7.2 .

D.1 Derivation of the loss equations

The coefficient $\langle 1|\frac{1}{G}\mathcal{L}_3[G]\rangle$ can be written as

$$\langle 1|\frac{1}{G}\mathcal{L}_3[G]\rangle = \left(\frac{n\lambda_{\text{th}}^3}{h^3}\right)^3 \int \mathrm{d}^3\boldsymbol{p}_1\mathrm{d}^3\boldsymbol{p}_2\mathrm{d}^3\boldsymbol{p}_3 \frac{\mathcal{A}_3}{E_{123}^2}|\phi(\boldsymbol{\Omega}_3)|^2 e^{-\beta E_{\text{tot}}} \tag{D.1}$$

where $E_{\text{tot}} = (p_1^2 + p_2^2 + p_3^2)/2m$. We then define three new momentum variables which are conjugated to Jacobi coordinates in real space and verify

$$\begin{aligned} \boldsymbol{p}_1 &= \frac{\boldsymbol{P}}{3} - \frac{\boldsymbol{\Pi}_1}{a} - \frac{a\boldsymbol{\Pi}_2}{2} && \text{(D.2)} \\ \boldsymbol{p}_2 &= \frac{\boldsymbol{P}}{3} + \frac{\boldsymbol{\Pi}_1}{a} - \frac{a\boldsymbol{\Pi}_2}{2} && \text{(D.3)} \\ \boldsymbol{p}_3 &= \frac{\boldsymbol{P}}{3} + a\boldsymbol{\Pi}_2. && \text{(D.4)} \end{aligned}$$

with $a = (4/3)^{1/4}$.
The energy in the center of mass frame is then $E_{123} = \Pi^2/2\mu$ with $\Pi^2 = \Pi_1^2 + \Pi_2^2$ and $\mu = m/\sqrt{3}$ while the total energy is $E_{\text{tot}} = P_{\text{G}}^2/6m + \Pi^2/2\mu$. The jacobian of such a change of variables is equal to one and we have the differential transformation

$$\mathrm{d}^3\boldsymbol{p}_1\mathrm{d}^3\boldsymbol{p}_2\mathrm{d}^3\boldsymbol{p}_3 = \mathrm{d}^3\boldsymbol{P}_{\text{G}}\Pi^5\mathrm{d}\Pi\frac{1}{2}\sin^2(2\alpha)\mathrm{d}\alpha\mathrm{d}^2\hat{\Pi}_1\mathrm{d}^2\hat{\Pi}_2 \tag{D.5}$$

where $\hat{\Pi}_i = \boldsymbol{\Pi}_i/\Pi_i$ and $\alpha = \arctan(\Pi_1/\Pi_2) \in [0;\pi/2]$.
It can be rewritten in terms of the hyperangular differential $\mathrm{d}^5\boldsymbol{\Omega}_3 = 1/2\sin^2(\alpha)\mathrm{d}\alpha\mathrm{d}^2\hat{\Pi}_1\mathrm{d}^2\hat{\Pi}_2$.
We thus obtain a new form for the integral

$$\langle 1|\frac{1}{G}\mathcal{L}_3[G]\rangle = \left(\frac{n\lambda_{\text{th}}^3}{h^3}\right)^3 \int \mathrm{d}^3\boldsymbol{P}_{\text{G}}\Pi^5\mathrm{d}\Pi\mathrm{d}^5\boldsymbol{\Omega}_3 \frac{\mathcal{A}_3}{E_{123}^2}|\phi(\boldsymbol{\Omega}_3)|^2 e^{-\beta E_{\text{tot}}}. \tag{D.6}$$

Using the normalization condition on $\phi(\mathbf{\Omega}_3)$ we are left with Gaussian integrals which are straightforward to calculate. We then get $\dot{n}_t = -L_3 n^3$.

To calculate $\langle \frac{p^2}{2m} | \frac{1}{G} \mathcal{L}_3[G] \rangle$ we use the fact that it can be written as

$$\langle \frac{p_1^2}{2m} | \frac{1}{G} \mathcal{L}_3[G] \rangle = \left(\frac{n\lambda_{\mathrm{th}}^3}{h^3} \right)^3 \int \mathrm{d}^3\boldsymbol{p}_1 \mathrm{d}^3\boldsymbol{p}_2 \mathrm{d}^3\boldsymbol{p}_3 \frac{E_{\mathrm{tot}}}{3} \frac{\mathcal{A}_3}{E_{123}^2} |\phi(\mathbf{\Omega}_3)|^2 e^{-\beta E_{\mathrm{tot}}}. \tag{D.7}$$

Therefore we can use the same change of variables to get rid of the hyperangular dependence and finally retrieve the loss equation $\dot{E}_t = -5EL_3 n^2/9$.

D.2 Decomposition of the solution over the Laguerre Polynomial basis

In this section, we solve the Eq.

$$C[\alpha] = P \left[\frac{1}{G} \mathcal{L}_3[G] \right] \tag{D.8}$$

In the spirit of Chapman-Enskog's expansion, we expand α on a basis of orthogonal polynomials for the scalar product

$$\langle \alpha | \beta \rangle = \int d^3\boldsymbol{p} G(p) \alpha(p) \beta(p). \tag{D.9}$$

Such a basis can be expressed in terms of the generalized Laguerre polynomials [270]

$$q_k(p) = \sqrt{\frac{\sqrt{\pi} k!}{2n\Gamma(k+3/2)}} L_k^{(1/2)}(\beta p^2/2m) \tag{D.10}$$

By definition, q_0 and q_1 lie in $\mathrm{Ker}(C)$ and as such will not contribute to the expansion. Take $\alpha(p) = \sum_{k\geq 2} a_k q_k(p)$, where the coefficients a_k are real numbers, Eq. (D.8) is then equivalent to the infinite set of linear equations

$$\sum_{k'\geq 2} a_{k'} \langle q_k | C[q_{k'}] \rangle = \langle q_k | \frac{1}{G} \mathcal{L}_3[G] \rangle, \tag{D.11}$$

for $k \geq 2$. In these equations, the coefficients $\langle q_k | C[q_{k'}] \rangle$ can be calculated analytically to arbitrary order, while the complex form of the Efimov wave-function allows only for a numerical calculation of the projection of the loss term on this polynomial basis. We solve this equation by truncating the indices (k, k') to a value k_{max}. We observe in Fig. (D.1) that the convergence is very fast and that the first order result ($k_{\mathrm{max}} = 2$) gives the correct answer within a few percent accuracy.

D.3 Calculation of C

The coefficients $\langle q_k | C[q_{k'}] \rangle$ can be expressed as follow $\langle q_k | C[q_{k'}] \rangle = -n\hbar^2 \sqrt{\pi\beta/m^3} \mathcal{C}_{kk'}$, $\mathcal{C} = (\mathcal{C}_{kk'})$ being a matrix with purely numerical coefficients. Those coefficients can be

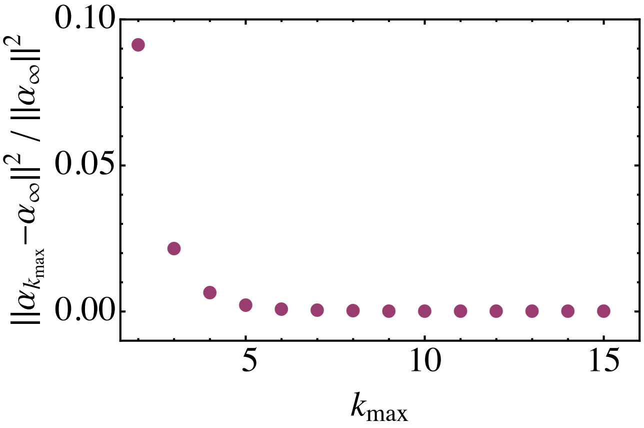

Figure D.1: Convergence of the numerical solution of Eq. (D.11). We estimate the error on the solution using the norme $\|\alpha\|^2 = \langle\alpha|\alpha\rangle$ and we compare the solution of Eq. (D.11) obtained by truncation at $k = k_\text{max}$ with the "true" result corresponding to $k_\text{max} = 15$.

calculated analytically to arbitrary order. As a "proof", all the coefficients to a value $k_{max} = 6$ are shown below:

$$\mathcal{C} = \begin{pmatrix} 0 & 0 & 0 & 0 & 0 & 0 \\ 0 & 0 & 0 & 0 & 0 & 0 \\ 0 & 0 & \frac{256}{45} & \frac{64}{15}\sqrt{\frac{2}{21}} & \frac{32}{15\sqrt{21}} & \frac{8}{9}\sqrt{\frac{10}{231}} \\ 0 & 0 & \frac{64}{15}\sqrt{\frac{2}{21}} & \frac{288}{35} & \frac{8\sqrt{2}}{5} & \frac{428}{63\sqrt{55}} \\ 0 & 0 & \frac{32}{15\sqrt{21}} & \frac{8\sqrt{2}}{5} & \frac{14908}{1575} & \frac{533}{35}\sqrt{\frac{2}{55}} \\ 0 & 0 & \frac{8}{9}\sqrt{\frac{10}{231}} & \frac{428}{63\sqrt{55}} & \frac{533}{35}\sqrt{\frac{2}{55}} & \frac{209863}{20790} \end{pmatrix} \quad \text{(D.12)}$$

D.4 Momentum distribution in a harmonic trap

The virial expansion of the momentum distribution was derived for a uniform system and we need to take into account for the fact that in [37] the density is not uniform. Since the quasi-equilibration time is much shorter than any collective mode period we can assume that the density is given by the Thomas-Fermi density of the initially weakly interacting Bose Einstein condensate $n(r) = n(0)\,(1 - r^2/R^2)$. The density at the center $n(0)$ and the Thomas-Fermi radius R are related to the total atom number N, the initial scattering length a and the harmonic oscillator length a_{ho} thanks to $n(0) = (15)^{2/5}/(8\pi)\frac{1}{a_{ho}^2 a}(\frac{Na}{a_{ho}})^{2/5}$ and $R = (15Na_{ho}^4 a)^{1/5}$. The two-body scattering rate being large compared to the inverse of typical experimental time, we assume locally thermal equilibrium. For dimensional reasons, the temperature at radius r is proportional to the degeneracy temperature at density $n(r)$. Therefore we have $k_B\,T(r) = C\,\hbar^2\,(6\pi^2 n)^{2/3}/m$ with C a dimensionless constant. Hence we have a uniform phase-space density $n(r)\lambda_{th}(r)^3 = D$, with D a dimensionless constant.

D is related to the the fugacity $z = e^{\mu/(k_B T)}$ through the equation of state

$$D \;=\; z + 2\,b_2\,z^2 + \cdots \quad \text{(D.13)}$$

Therefore we find that the *fugacity is uniform* in the cloud.

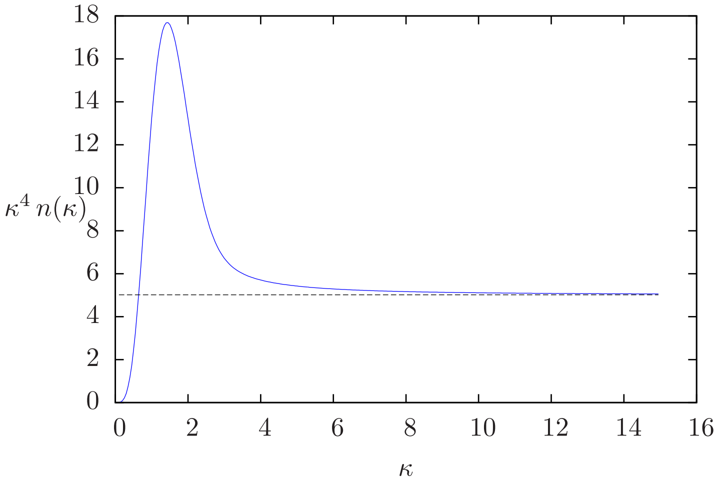

Figure D.2: The product $\kappa^4\, n(\kappa)$ from Eq.D.15 and $z = 0.5$.

In order to calculate the momentum occupation number in the cloud, we have to integrate on space the result for a homogeneous system, keeping track of the fact that the temperature and the chemical potential are non-uniform. The sum of the three contributions to the momentum occupation number $\rho^{(2)}(p)$ of order z^2 is denoted by $f_2(p\, \lambda_{th}/\hbar)$. This includes Bose statistics correction, interaction effects and three-body losses. Therefore we have locally for the momentum occupation number, up to second order in fugacity

$$\rho(p; r) \;=\; z\, e^{-\frac{p^2}{2mk_BT(r)}} + z^2\, f_2(p\, \lambda_{th}(r)/\hbar) \tag{D.14}$$

with $k_BT(r) = \frac{2\pi\, n(0)^{2/3}}{m\, D^{2/3}}\left(1 - r^2/R^2\right)^{2/3}$ and z is related to D in Eq.D.13. The results of Ref.[37] are given for dimensionless wave vector κ defined by $p = \hbar\, k_n\, \kappa$ and $k_n \equiv \left(6\pi^2\langle n\rangle\right)^{1/3}$, with $\langle n\rangle$ a spatial average density. For a Thomas-Fermi profile, we easily get $n(0) = A\, k_n^3$, with $A = 5/(12\pi^2)$. Moreover the dimensionless wave vector occupation number $n(\kappa)$ should be normalized such that $4\pi \int_0^{+\infty} d\kappa\, \kappa^2\, n(\kappa) = 8\pi^3$. In this way, we find for the dimensionless momentum distribution

$$n(\kappa) = \frac{15}{2\,A}\int_0^1 du\, u^2 \{ z\, e^{-\frac{D^{2/3}}{4\pi\, A^{2/3}}\frac{1}{(1-u^2)^{2/3}}\kappa^2} + z^2\, f_2\left(\frac{D^{1/3}}{A^{1/3}}\frac{1}{\left(1-u^2\right)^{1/3}}\kappa\right)\}$$

In Fig.D.2, we show the product $\kappa^4\, n(\kappa)$ for $z = 0.5$. From Eq.D.15, we find this product should tend to $\simeq 5.018$. We also notice that this asymptotic value is not reached for κ equals 3.

Appendix E

Analysis of impurity losses of the Innsbruck experiment.

We present in this appendix, a quick analysis of the data presented in [245], where they measured the decay rate of an impurity (^{40}K atoms, denoted i) immersed in a strongly interacting Fermi gas (^{6}Li atoms) accross the BEC-BCS crossover, see fig.(E.1) (taken from [245]). The Fermi gas is in the superfluid regime as $T/T_{\rm F} = 0.15$. According to what we have presented in chapter 6 and 8, the loss rate $\Gamma = \dot{n}_{\rm i}/n_{\rm i}$ is given by the two-body contact of the interacting Fermi gas. On the BEC side, far from the resonance we thus have $\Gamma = \gamma 4\pi \langle n_{\rm f}\rangle / a_{\rm ff}$, where the brackets denotes the averaging over the impurity density distribution. Applied to the data point taken at 730 G we get $\gamma = 3.4(5) \times 10^{-27}{\rm m}^4.{\rm s}^{-1}$ (at 690 G, the mixture suffers from strong dimer-dimer losses (see fig. 1 of the paper) and the impurity decay seem to be underestimated). However, as the scattering length is still large ($\simeq 2500\, a_0$) , $k_F a_{\rm ff}$ is close to 1 and the value of γ is an upper estimation. In the far BCS limit we have instead $\Gamma = \gamma 4\pi^2 \langle n_{\rm f}^2\rangle a_{\rm ff}^2$. Using the data point with the highest magnetic field (1190 G) we get $\gamma = 2.1(5) \times 10^{-27}{\rm m}^4.{\rm s}^{-1}$. Similarly to the BEC data point, the scattering length is still large ($\simeq -2700\, a_0$), the value of γ is underestimated. At unitarity and at zero temperature we should have

$$\Gamma = \gamma \frac{2\zeta}{5\pi} (3\pi^2)^{4/3} \langle n_{\rm f}^{4/3} \rangle \ , \tag{E.1}$$

where $\zeta = 0.87(3)$ is a dimensionless constant.
In the experiment, at resonance, the peak density is $n_{\rm f,peak} = 2 \times 2.1 \times 10^{12}\,{\rm cm}^{-3}$. Moreover, as they give $n_{\rm f,peak}/\langle n_{\rm f}\rangle = 1.7$ and $n_{\rm f,peak}^2/\langle n_{\rm f}^2\rangle = 2.4$, we can take by extrapolation $n_{\rm f,peak}^{4/3}/\langle n_{\rm f}^{4/3}\rangle = 1.9$. The measured unitary loss rate is $\Gamma = 0.07(2){\rm s}^{-1}$ and we thus get $\gamma = 2.5(5) \times 10^{-27}{\rm m}^4.{\rm s}^{-1}$. We did not take into account the corrections to the two-body contact coming from the finite temperature of the mixture that can slightly modify this result.

The extracted values of γ in the three asymptotic regimes of the BEC-BCS crossover shows at most a weak variation with the magnetic field. The data presented in [245] is thus consistent with losses proportional to the two-body contact. A more refined analysis including the beyond mean-field corrections to the contact could improve the agreement. Interestingly, the value of γ found here for the ^{40}K/^{6}Li mixture share the same order of magnitude than what we have measured for our ^{7}Li/^{6}Li mixture $\gamma = 1.17(11) \times 10^{-27}{\rm m}^4.{\rm s}^{-1}$.

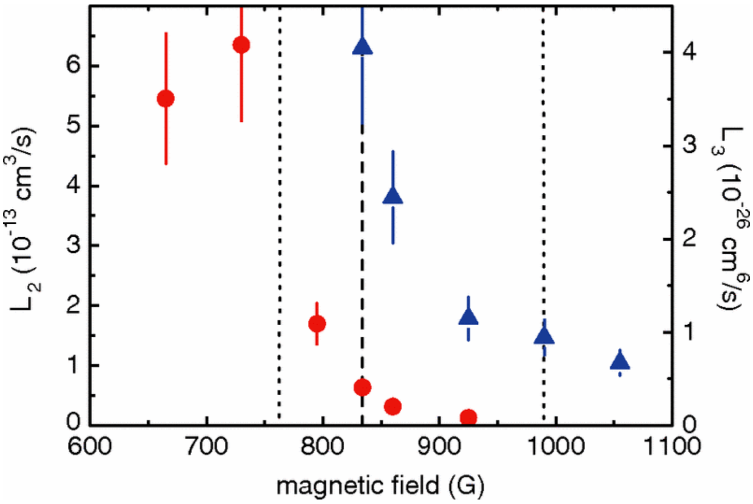

Figure E.1: ^{40}K impurity decay rate in the BEC-BCS crossover, taken from [245]. The decay is fitted either by a two-body loss term or a three-body loss term. Red circles: two-body loss rate coefficient $L_2 = \Gamma/\langle n_{\mathrm{f}}\rangle$. Blue triangles:three-body loss rate coefficient $L_3 = \Gamma/\langle n_{\mathrm{f}}^2\rangle$. The dashed black line marks the unitary limit where $1/a_{\mathrm{f}} = 0$. The dotted lines indicates the strongly interacting regime, where $|k_F a_{\mathrm{ff}}| \geq 1$.

List of publications

- "A mixture of Bose and Fermi superfluids"
  Igor Ferrier-Barbut, Marion Delehaye, Sébastien Laurent, Andrew T. Grier, Matthieu Pierce, Benno S. Rem, Frédéric Chevy, and Christophe Salomon
  Science, **345**, 1035-1038 (2014)

- "Momentum distribution of a dilute unitary Bose gas with three-body losses"
  Sébastien Laurent, Xavier Leyronas, and Frédéric Chevy
  Physical Review Letters, **113**, 220601 (2014)

- "Critical velocity and dissipation of an ultracold Bose-Fermi counterflow"
  Marion Delehaye, Sébastien Laurent, Igor Ferrier-Barbut, Shuwei Jin, Frédéric Chevy, and Christophe Salomon
  Physical Review Letters, **115**, 265303 (2015)

- "Universal loss dynamics in a unitary Bose gas"
  Ulrich Eismann, Lev Khaykovich, Sébastien Laurent, Igor Ferrier-Barbut, Benno S. Rem, Andrew T. Grier, Marion Delehaye, Frédéric Chevy, Christophe Salomon, Li-Chung Ha, and Cheng Chin
  Physical Review X, **6**, 021025 (2016)

- "Connecting few-body inelastic decay to quantum correlations in a many-body system: a weakly coupled impurity in a resonant Fermi gas"
  Sébastien Laurent, Matthieu Pierce, Marion Delehaye, Tarik Yefsah, Frédéric Chevy, and Christophe Salomon
  Physical Review Letters, **118**, 103403 (2017)

A mixture of Bose and Fermi superfluids

Igor Ferrier-Barbut, Marion Delehaye, Sébastien Laurent, Andrew T. Grier, Matthieu Pierce, Benno S. Rem, Frédéric Chevy, and Christophe Salomon

Science, **345**, 1035-1038 (2014)

collisions. An analysis with some similarities to ours for the bright debris disk of HD 172555 (*20*) found that dust created in a hypervelocity impact will have a size slope of ~ –4, in agreement with the fits of (*10*) to the IR spectrum of ID8.

After the exponential decay is removed from the data ("detrending"), the light curves at both wavelengths appear to be quasi-periodic. The regular recovery of the disk flux and lack of extraordinary stellar activity essentially eliminate coronal mass ejection (*21*) as a possible driver of the disk variability. We employed the SigSpec algorithm (*22*) to search for complex patterns in the detrended, post-impact 2013 light curve. The analysis identified two significant frequencies with comparable amplitudes, whose periods are P_1 = 25.4 ± 1.1 days and P_2 = 34.0 ± 1.5 days (Fig. 3A) and are sufficient to qualitatively reproduce most of the observed light curve features (Fig. 3B). The quoted uncertainties (*23*) do not account for systematic effects due to the detrending and thus are lower limits to the real errors. Other peaks with longer periods in the periodogram are aliases or possibly reflect long-term deviation from the exponential decay. These artifacts make it difficult to determine whether there are weak real signals near those frequencies.

We now describe the most plausible interpretation of this light curve that we have found. The two identified periods have a peak-to-peak amplitude of ~6×10^{-3} in fractional luminosity, which provides a critical constraint for models of the ID8 disk. In terms of sky coverage at the disk distance inferred from the IR SED, such an amplitude requires the disappearance and reappearance every ~30 days of the equivalent of an opaque, stellar-facing "dust panel" of radius ~110 Jupiter radii. One possibility is that the disk flux periodicity arises from recurring geometry that changes the amount of dust that we can see. At the time of the impact, fragments get a range of kick velocities when escaping into interplanetary space. This will cause Keplerian shear of the cloud (*24*), leading to an expanding debris concentration along the original orbit (supplementary text). If the ID8 planetary system is roughly edge-on, the longest dimension of the concentration will be parallel to our line of sight at the greatest elongations and orthogonal to the line of sight near conjunctions to the star. This would cause the optical depth of the debris to vary within an orbital period, in a range on the order of 1 to 10 according to the estimated disk mass and particle sizes. Our numerical simulations of such dust concentrations on moderately eccentric orbits are able to produce periodic light curves with strong overtones. P_2 and P_1 should have a 3:2 ratio if they are the first- and second-order overtones of a fundamental, which is consistent with the measurements within the expected larger errors (<2σ or better). In this case, the genuine period should be 70.8 ± 5.2 days (lower-limit errors), a value where it may have been submerged in the periodogram artifacts. This period corresponds to a semimajor axis of ~0.33 astronomical units, which is consistent with the temperature and distance suggested by the spectral models (*10*).

Despite the peculiarities of ID8, it is not a unique system. In 2012 and 2013, we monitored four other "extreme debris disks" (with disk fractional luminosity $\geq 10^{-2}$) around solar-like stars with ages of 10 to 120 My. Various degrees of IR variations were detected in all of them. The specific characteristics of ID8 in the time domain, including the yearly exponential decay, additional more rapid weekly to monthly changes, and color variations, are also seen in other systems. This opens up the time domain as a new dimension for the study of terrestrial planet formation and collisions outside the solar system. The variability of many extreme debris disks in the era of the final buildup of terrestrial planets may provide new possibilities for understanding the early solar system and the formation of habitable planets (*25*).

REFERENCES AND NOTES

1. R. Helled *et al.*, in *Protostars and Planets VI*, H. Beuther, R. Klessen, C. Dullemond, T. Henning, Eds. (Univ. of Arizona Press, Tucson, AZ, 2014), in press; available at http://arxiv.org/abs/1311.1142.
2. M. C. Wyatt, *Annu. Rev. Astron. Astrophys.* **46**, 339–383 (2008).
3. K. Righter, D. P. O'Brien, *Proc. Natl. Acad. Sci. U.S.A.* **108**, 19165–19170 (2011).
4. S. N. Raymond, E. Kokubo, A. Morbidelli, R. Morishima, K. J. Walsh, in *Protostars and Planets VI*, H. Beuther, R. Klessen, C. Dullemond, T. Henning, Eds. (Univ. of Arizona Press, Tucson, AZ, 2014), in press; available at http://arxiv.org/abs/1312.1689.
5. R. M. Canup, *Annu. Rev. Astron. Astrophys.* **42**, 441–475 (2004).
6. M. Ćuk, S. T. Stewart, *Science* **338**, 1047–1052 (2012).
7. R. M. Canup, *Science* **338**, 1052–1055 (2012).
8. H. Y. A. Meng *et al.*, *Astrophys. J.* **751**, L17–L21 (2012).
9. D. R. Soderblom, L. A. Hillenbrand, R. D. Jeffries, E. E. Mamajek, T. Naylor, in *Protostars and Planets VI*, H. Beuther, R. Klessen, C. Dullemond, T. Henning, Eds. (Univ. of Arizona Press, Tucson, AZ, 2014), in press; available at http://arxiv.org/abs/1311.7024.
10. J. Olofsson *et al.*, *Astron. Astrophys.* **542**, 90–115 (2012).
11. P. Artymowicz, *Astrophys. J.* **335**, L79–L82 (1988).
12. G. G. Fazio *et al.*, *Astrophys. J. Suppl. Ser.* **154**, 10–17 (2004).
13. D. Jewitt, H. Matthews, *Astron. J.* **117**, 1056–1062 (1999).
14. J. A. M. McDonnell *et al.*, *Nature* **321**, 338–341 (1986).
15. D. Perez-Becker, E. Chiang, *Mon. Not. R. Astron. Soc.* **433**, 2294–2309 (2013).
16. P. H. Warren, *Geochim. Cosmochim. Acta* **72**, 3562–3585 (2008).
17. B. C. Johnson, H. J. Melosh, *Icarus* **217**, 416–430 (2012).
18. M. C. Wyatt, W. R. F. Dent, *Mon. Not. R. Astron. Soc.* **334**, 589–607 (2002).
19. B. Zuckerman, I. Song, *Astrophys. J.* **758**, 77–86 (2012).
20. B. C. Johnson *et al.*, *Astrophys. J.* **761**, 45–57 (2012).
21. R. Osten *et al.*, *Astrophys. J.* **765**, L44–L46 (2013).
22. P. Reegen, *Astron. Astrophys.* **467**, 1353–1371 (2007).
23. T. Kallinger, P. Reegen, W. W. Weiss, *Astron. Astrophys.* **481**, 571–574 (2008).
24. S. J. Kenyon, B. C. Bromley, *Astron. J.* **130**, 269–279 (2005).
25. S. Elser, B. Moore, J. Stadel, R. Morishima, *Icarus* **214**, 357–365 (2011).
26. T. Naylor *et al.*, *Mon. Not. R. Astron. Soc.* **335**, 291–310 (2002).
27. R. D. Jeffries, T. Naylor, C. R. Devey, E. J. Totten, *Mon. Not. R. Astron. Soc.* **351**, 1401–1422 (2004).

ACKNOWLEDGMENTS

H.Y.A.M, K.Y.L.S., and G.H.R. thank R. Malhotra and A. Gáspár for valuable discussions. This work is based on observations made with the Spitzer Space Telescope, which is operated by the Jet Propulsion Laboratory (JPL), California Institute of Technology, under a contract with NASA. Support for this work was provided by NASA through an award issued by JPL/Caltech and by NASA grant NNX13AE74G. All data are publicly available through the NASA/IPAC Infrared Science Archive.

SUPPLEMENTARY MATERIALS

www.sciencemag.org/content/345/6200/1032/suppl/DC1
Supplementary Text
Figs. S1 to S4
References (*28*–*45*)

23 April 2014; accepted 15 July 2014
10.1126/science.1255153

SUPERFLUIDITY

A mixture of Bose and Fermi superfluids

I. Ferrier-Barbut,* M. Delehaye, S. Laurent, A. T. Grier,† M. Pierce, B. S. Rem,‡ F. Chevy, C. Salomon

Superconductivity and superfluidity of fermionic and bosonic systems are remarkable many-body quantum phenomena. In liquid helium and dilute gases, Bose and Fermi superfluidity has been observed separately, but producing a mixture in which both the fermionic and the bosonic components are superfluid is challenging. Here we report on the observation of such a mixture with dilute gases of two lithium isotopes, lithium-6 and lithium-7. We probe the collective dynamics of this system by exciting center-of-mass oscillations that exhibit extremely low damping below a certain critical velocity. Using high-precision spectroscopy of these modes, we observe coherent energy exchange and measure the coupling between the two superfluids. Our observations can be captured theoretically using a sum-rule approach that we interpret in terms of two coupled oscillators.

In recent years, ultracold atoms have emerged as a unique tool to engineer and study quantum many-body systems. Examples include weakly interacting Bose-Einstein condensates (*1*, *2*), two-dimensional gases (*3*), and the superfluid-Mott insulator transition (*4*) in the case of bosonic atoms, and the crossover between Bose-Einstein condensation (BEC) and fermionic superfluidity described by the the theory of Bardeen, Cooper, and Schrieffer (BCS) for fermionic atoms (*5*). Mixtures of Bose-Einstein condensates were produced shortly after the observation of BEC (*2*), and a BEC mixed with a single-spin state Fermi sea was originally observed in (*6*, *7*). However, realizing a mixture in which both fermionic and bosonic species are superfluid has been experimentally challenging. This has also been a long-sought goal in liquid helium, where superfluidity was achieved separately in both bosonic ^{4}He and fermionic ^{3}He. The double superfluid should undergo a transition between s-wave and p-wave Cooper pairs as the ^{3}He dilution is varied (*8*). However, because of strong interactions between the two isotopes, ^{3}He-^{4}He mixtures contain only a small fraction of ^{3}He (typically 6%) which, so far, has prevented attainment of simultaneous superfluidity for the two species (*8*, *9*).

Here we report on the production of a Bose-Fermi mixture of quantum gases in which both species are superfluid. Our system is an ultracold gas of fermionic ^{6}Li in two spin states mixed with ^{7}Li bosons and confined in an optical dipole trap. Using radio-frequency pulses, we prepare ^{6}Li atoms in their two lowest hyperfine states $|1_\mathrm{f}\rangle$ and $|2_\mathrm{f}\rangle$, whereas ^{7}Li is spin polarized in the second-to-lowest state $|2_\mathrm{b}\rangle$ (*10*). For this combination of states, in the vicinity of the ^{6}Li Feshbach resonance at a magnetic field of 832 G (*11*), the scattering length of the bosonic isotope a_b = $70a_0$ (a_0 is the Bohr radius) is positive, preventing collapse of the BEC. The boson-fermion interaction is characterized by a scattering length $a_\mathrm{bf} = 40.8a_0$ that does not depend on magnetic field in the parameter range studied here. At resonance, the Fermi gas exhibits a unitary limited collision rate, and lowering the optical dipole trap depth leads to extremely efficient evaporation. Owing to a large excess of ^{6}Li atoms with respect to ^{7}Li, the Bose gas is sympathetically driven to quantum degeneracy.

The two clouds reach the superfluid regime after a 4-s evaporation ramp (*10*). As the ^{7}Li Bose gas is weakly interacting, the onset of BEC is detected by the growth of a narrow peak in the density profile of the cloud. From previous studies on atomic Bose-Einstein condensates, we conclude that the ^{7}Li BEC is in a superfluid phase. Superfluidity in a unitary Fermi gas is notoriously more difficult to detect because of the absence of any qualitative modification of the density profile at the phase transition. To demonstrate the superfluidity of the fermionic component of the cloud, we slightly imbalance the two spin populations. In an imbalanced gas, the cloud is organized in concentric layers, with a fully paired superfluid region at its center, where Cooper pairing maintains equal spin populations. This ^{6}Li superfluid core can be detected by the presence of a plateau in the doubly integrated density difference (*12*). Examples of density profiles of the bosonic and fermionic superfluids are shown in Fig. 1, where both the Bose-Einstein condensate (blue circles) and the plateau (black diamonds in the inset) are clearly visible. Our coldest samples contain $N_\mathrm{b} = 4 \times 10^4$ ^{7}Li atoms and $N_\mathrm{f} = 3.5 \times 10^5$ ^{6}Li atoms. The absence of a thermal fraction in the bosonic cloud indicates a temperature below $0.5T_\mathrm{c,b}$, where $k_\mathrm{B}T_\mathrm{c,b} = 0.94\hbar\overline{\omega}_\mathrm{b}N_\mathrm{b}^{1/3}$ is the critical temperature of the ^{7}Li bosons, and $\overline{\omega}_\mathrm{b}$ ($\overline{\omega}_\mathrm{f}$) is the geometric mean trapping frequency for ^{7}Li (^{6}Li). Combined with the observation of the ^{6}Li plateau, this implies that the Fermi cloud is also superfluid with a temperature below $0.8T_\mathrm{c,f}$. Here, $T_\mathrm{c,f}$ is the critical temperature for superfluidity of a spin-balanced, harmonically trapped Fermi gas at unitarity, $T_\mathrm{c,f} = 0.19T_\mathrm{F}$ (*13*), and $k_\mathrm{B}T_\mathrm{F} = \hbar\overline{\omega}_\mathrm{f}(3N_\mathrm{f})^{1/3}$ is the Fermi temperature. The superfluid mixture is very stable, with a lifetime exceeding 7 s for our coldest samples.

As seen in Fig. 1, the Bose-Fermi interaction is too weak to alter significantly the density profiles of the two species (*14*). To probe the interaction between the two superfluids, we study the dynamics of the mass centers of the two isotopes (dipole modes), a scheme used previously for the study of mixtures of Bose-Einstein condensates (*15*, *16*), mixtures of Bose-Einstein condensates and spin-polarized Fermi seas (*17*), spin diffusion in Fermi gases (*18*), or integrability in one-dimensional systems (*19*). In a purely harmonic trap and in the absence of interspecies interactions, the dipole mode of each species is undamped and can therefore be measured over long time spans to achieve a high-frequency resolution and detect small perturbations of the system. We excite the dipole modes by shifting the initial position of the ^{6}Li and ^{7}Li clouds by a displacement d along the weak direction z of the trap (*10*). We then release them and let them evolve during a variable time t, after which we measure their positions. By monitoring the cloud oscillations during up to 4 s, we determine their frequencies with high precision ($\frac{\Delta\omega}{\omega} \lesssim 2 \times 10^{-3}$). In the absence of the other species, the oscillation frequencies of ^{6}Li and ^{7}Li are, respectively, $\omega_\mathrm{f} = 2\pi \times 16.80(2)$ Hz and $\omega_\mathrm{b} = 2\pi \times 15.27(1)$ Hz. In the axial direction, the confinement is mostly magnetic, and at high magnetic field, both species are in the Paschen-Back regime, where the electronic and nuclear spin degrees of freedom are decoupled. In this regime, the magnetic confinement mostly results from the electronic spin and is therefore almost identical for the two isotopes. The ratio $\omega_\mathrm{f}/\omega_\mathrm{b}$ is then very close to the expected value $\sqrt{7/6} \simeq 1.08$ based on the ratio of the atomic masses (*20*).

Contrary to the large damping observed in the Bose-Bose mixtures (*15*), we observe long-lived oscillations of the Bose-Fermi superfluid mixture at frequencies ($\tilde{\omega}_\mathrm{b}$, $\tilde{\omega}_\mathrm{f}$). These oscillations extend over more than 4 s with undetectable damping (Fig. 2 and fig. S2). This very weak dissipation is only observed when the initial displacement d is below 100 μm, corresponding to a maximum relative velocity $v_\mathrm{max} = (\tilde{\omega}_\mathrm{b} + \tilde{\omega}_\mathrm{f})d$ below 18 mm/s $\simeq 0.4\ v_\mathrm{F}$, where $v_\mathrm{F} = \sqrt{2k_\mathrm{B}T_\mathrm{F}/m_\mathrm{f}}$. In this situation, the BEC explores only the central part of the much broader Fermi cloud. When $v_\mathrm{max} > v_\mathrm{c} = 0.42^{+0.05}_{-0.11}v_\mathrm{F} = 20^{+2}_{-5}$ mm/s, we observe a sharp onset of damping and heating of the BEC compatible with the Landau criterion for breakdown of superfuidity (Fig. 2C) (*10*). For comparison, the sound velocity of an elongated Fermi gas at its center is $v_\mathrm{s}' = \xi^{1/4}v_\mathrm{F}/\sqrt{5} = 17$ mm/s (*21*), where $\xi = 0.38$ is the Bertsch parameter (*5*, *13*). The measured critical velocity v_c is very close to v_s' and is clearly above the BEC sound velocity of $\simeq$5 mm/s at its center.

Two striking phenomena are furthermore observed. First, whereas the frequency $\tilde{\omega}_\mathrm{f}$ of ^{6}Li oscillations is almost unchanged from the value in the absence of ^{7}Li, that of ^{7}Li is downshifted

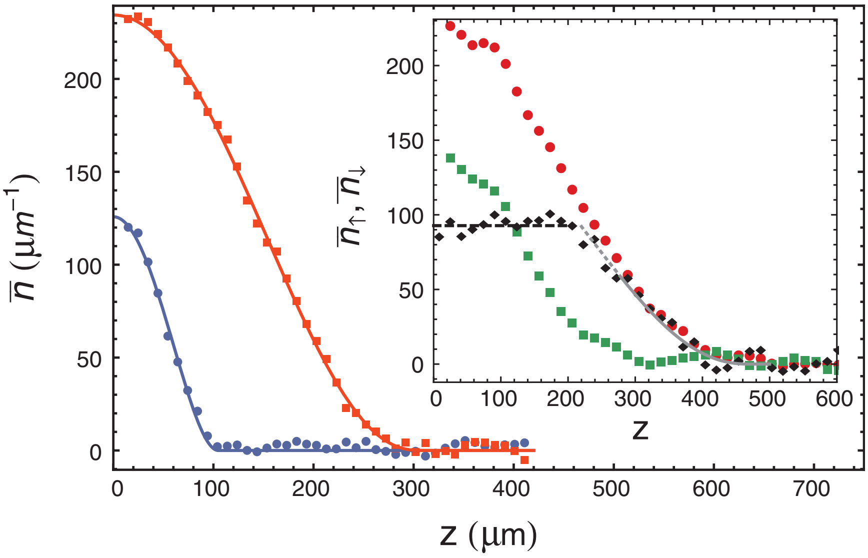

Fig. 1. Density profiles in the double superfluid regime. $N_\mathrm{b} = 4 \times 10^4$ ^{7}Li atoms and $N_\mathrm{f} = 3.5 \times 10^5$ ^{6}Li atoms are confined in a trap at a temperature below 130 nK. The density profiles $\bar{n}_\mathrm{b}$ (blue circles) and $\bar{n}_{\mathrm{f},\uparrow}$ (red squares) are doubly integrated over the two transverse directions. The blue (red) solid line is a fit to the ^{7}Li (^{6}Li) distribution by a mean-field (unitary Fermi gas) EoS in the Thomas-Fermi approximation. Inset: Spin-imbalanced Fermi gas ($N_{\mathrm{f},\uparrow} = 2 \times 10^5$, $N_{\mathrm{f},\downarrow} = 8 \times 10^4$) in thermal equilibrium with a BEC. Red circles: $\bar{n}_{\mathrm{f},\uparrow}$; green squares: $\bar{n}_{\mathrm{f},\downarrow}$; black diamonds: difference $\bar{n}_{\mathrm{f},\uparrow} - \bar{n}_{\mathrm{f},\downarrow}$. The plateau (black dashed line) indicates superfluid pairing (*12*). Gray solid line: Thomas-Fermi profile of a noninteracting Fermi gas for the fully spin-polarized outer shell prolonged by the partially polarized normal phase (gray dashed line).

Laboratoire Kastler-Brossel, École Normale Supérieure, Collège de France, CNRS and UPMC, 24 rue Lhomond, 75005 Paris, France.
***Corresponding author. E-mail: iferrier@lkb.ens.fr** †Present address: Van Swinderen Institute, University of Groningen, Faculty of Mathematics and Natural Sciences, Zernikelaan 25, 9747 AA Groningen, Netherlands. ‡Present address: Institut für Laserphysik, Universität Hamburg, Luruper Chaussee 149, Building 69, D-22761 Hamburg, Germany.

to $\tilde{\omega}_\mathrm{b} = 2\pi \times 15.00(2)$ Hz. Second, the amplitude of oscillations of the bosonic species displays a beat at a frequency $\simeq(\tilde{\omega}_\mathrm{f} - \tilde{\omega}_\mathrm{b})/(2\pi)$, revealing coherent energy transfer between the two clouds (Fig. 2B). To interpret the frequency shift of the ^{7}Li atoms, we note that $N_\mathrm{b} \ll N_\mathrm{f}$, which allows us to treat the BEC as a mesoscopic impurity immersed in a Fermi superfluid. Similarly to the Fermi polaron case (*22*), the effective potential seen by the bosons is the sum of the trapping potential $V(r)$ and the mean-field interaction $g_\mathrm{bf} n_\mathrm{f}(r)$, where n_f is the total fermion density, $g_\mathrm{bf} = 2\pi\hbar^2 a_{bf}/m_\mathrm{bf}$, and $m_\mathrm{bf} = \frac{m_\mathrm{b} m_\mathrm{f}}{m_\mathrm{b}+m_\mathrm{f}}$ is the ^{6}Li/^{7}Li reduced mass. Neglecting at first the back-action of the bosons on the fermions, we can assume that n_f is given by the local-density-approximation result $n_\mathrm{f}(r) = n_\mathrm{f}^{(0)}(\mu_\mathrm{f}^0 - V(r))$, where $n_\mathrm{f}^{(0)}(\mu)$ is the stationary equation of state (EoS) of the Fermi gas. Because the Bose-Einstein condensate is much smaller than the Fermi cloud (Fig. 2A), $V(r)$ is smaller than μ_f^0 over the BEC volume. We can thus expand $n_\mathrm{f}^{(0)}$, and we get

$$V_\mathrm{eff}(r) = g_\mathrm{bf} n_\mathrm{f}(0) + V(r)\left[1 - g_\mathrm{bf}\left(\frac{dn_\mathrm{f}^{(0)}}{d\mu_\mathrm{f}}\right)_{r=0}\right] \tag{1}$$

We observe that the effective potential is still harmonic and the rescaled frequency is given by

$$\tilde{\omega}_\mathrm{b} \simeq \omega_\mathrm{b}\left(1 - \frac{1}{2} g_\mathrm{bf}\left(\frac{dn_\mathrm{f}^{(0)}}{d\mu_\mathrm{f}}\right)_{r=0}\right) \tag{2}$$

For a unitary Fermi gas, the chemical potential is related to the density by $\mu_\mathrm{f} = \xi\hbar^2(3\pi^2 n_\mathrm{f})^{2/3}/2m_\mathrm{f}$. In the weakly coupled limit, we get $\frac{\delta\omega_\mathrm{b}}{\omega_\mathrm{b}} = \frac{\omega_\mathrm{b} - \tilde{\omega}_\mathrm{b}}{\omega_\mathrm{b}} = \frac{13 k_\mathrm{F} a_{bf}}{7\pi\xi^{5/4}}$, where $\hbar k_\mathrm{F} = \sqrt{2\hbar m_\mathrm{f}\overline{\omega}_\mathrm{f}(3N_\mathrm{f})^{1/3}}$ is the Fermi momentum of a noninteracting harmonically trapped Fermi gas. Using our experimental parameters $k_\mathrm{F} = 4.6 \times 10^6\ \mathrm{m}^{-1}$, we predict a value $\tilde{\omega}_\mathrm{b} \simeq 2\pi \times 14.97$ Hz, in very good agreement with the observed value 15.00(2)Hz.

To understand the amplitude modulation, we now take into account the back-action on the fermions. A fully quantum formalism using a sum-rule approach (*23*–*25*) leads to a coupled oscillator model in which the positions of the two clouds obey the following equations (*10*)

$$M_\mathrm{f}\ddot{z}_\mathrm{f} = -K_\mathrm{f} z_\mathrm{f} - K_\mathrm{bf}(z_\mathrm{f} - z_\mathrm{b}) \tag{3}$$

$$M_\mathrm{b}\ddot{z}_\mathrm{b} = -K_\mathrm{b} z_\mathrm{b} - K_\mathrm{bf}(z_\mathrm{b} - z_\mathrm{f}) \tag{4}$$

where $M_\mathrm{b} = N_\mathrm{b} m_\mathrm{b}$ ($M_\mathrm{f} = N_\mathrm{f} m_\mathrm{f}$) is the total mass of the ^{7}Li (^{6}Li) cloud, $K_\mathrm{b} = M_\mathrm{b}\omega_\mathrm{b}^2$ ($K_\mathrm{f} = M_\mathrm{f}\omega_\mathrm{f}^2$) is the spring constant of the axial magnetic confinement, and K_bf is a phenomenological (weak) coupling constant describing the mean-field interaction between the two isotopes. To recover the correct frequency shift (Eq. 2), we take $K_\mathrm{bf} = 2K_\mathrm{b}\frac{\delta\omega_\mathrm{b}}{\omega_\mathrm{b}}$. Solving these equations with the initial condition $z_\mathrm{f}(0) = z_\mathrm{b}(0) = d$, and defining $\rho = N_\mathrm{b}/N_\mathrm{f}$ and $\varepsilon = \frac{2m_\mathrm{b}}{m_\mathrm{b}-m_\mathrm{f}}\left(\frac{\tilde{\omega}_\mathrm{b} - \omega_\mathrm{b}}{\omega_\mathrm{b}}\right)$, in the limit $\rho, \varepsilon \ll 1$ we get

$$z_\mathrm{f} = d[(1 - \varepsilon\rho)\cos(\tilde{\omega}_\mathrm{f} t) + \varepsilon\rho\cos(\tilde{\omega}_\mathrm{b} t)] \tag{5}$$

$$z_\mathrm{b} = d[-\varepsilon\cos(\tilde{\omega}_\mathrm{f} t) + (1 + \varepsilon)\cos(\tilde{\omega}_\mathrm{b} t)] \tag{6}$$

The predictions of Eqs. 5 and 6 agree well with experiment (Fig. 2B). Interestingly, the peak-to-peak modulation of the amplitude of ^{7}Li is much larger than the relative frequency shift, a consequence of the almost exact tuning of the two oscillators (up to a factor $\sqrt{6/7}$). Thus, the mass prefactor in the expression for ε is large (=14) and leads to $\varepsilon \simeq 0.25$ at unitarity. This results in efficient energy transfer between the two modes despite their weak coupling, as observed.

We now extend our study of the Bose-Fermi superfluid mixture to the BEC-BCS crossover by tuning the magnetic field away from the resonance value $B_\mathrm{f} = 832$ G. We explore a region from 860 G down to 780 G where $1/k_\mathrm{F} a_\mathrm{f}$ spans the interval $[-0.4, +0.8]$. In this whole domain, except in a narrow region between 845 and 850 G where the boson-boson scattering length

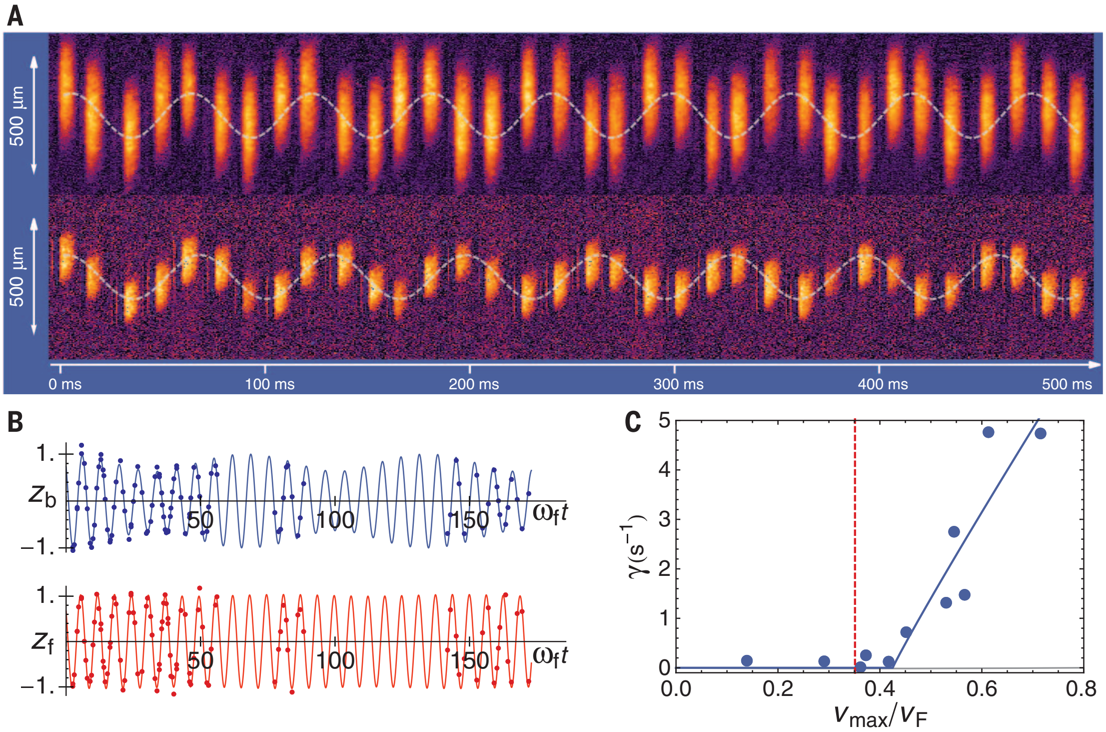

Fig. 2. Coupled oscillations of the superfluid mixture. (**A**) Center-of-mass oscillations. The oscillations are shown over the first 500 ms at a magnetic field of 835 G for a Fermi superfluid (top) and a Bose superfluid (bottom).The oscillation period of ^{6}Li (^{7}Li) is 59.7(1) ms [66.6(1) ms], leading to a dephasing of π near 300 ms. These oscillations persist for more than 4 s with no visible damping. The maximum relative velocity between the two clouds is 1.8 cm/s. (**B**) Coupled oscillations. Symbols: Center-of-mass oscillation of ^{7}Li (top) and ^{6}Li (bottom) displaying coherent energy exchange between both superfluids. Solid lines: Theory for an initial displacement *d* of 100 µm at a magnetic field of 835 G; see text. (**C**) Critical damping. Symbols: Damping rate (blue circles) of the amplitude of the center-of-mass oscillations of the ^{7}Li BEC as a function of the maximal relative velocity between the two superfluids normalized to the Fermi velocity of the ^{6}Li gas. Data taken at 832 G. From these data and using a fit function given in (*10*) (solid line), we extract $v_\mathrm{c} = 0.42^{+0.05}_{-0.11} v_\mathrm{F}$. The red dashed line shows the speed of sound of an elongated unitary Fermi superfluid $v_\mathrm{s}' = \xi^{1/4} v_\mathrm{F}/\sqrt{5} = 0.35 v_\mathrm{F}$ (*20*).

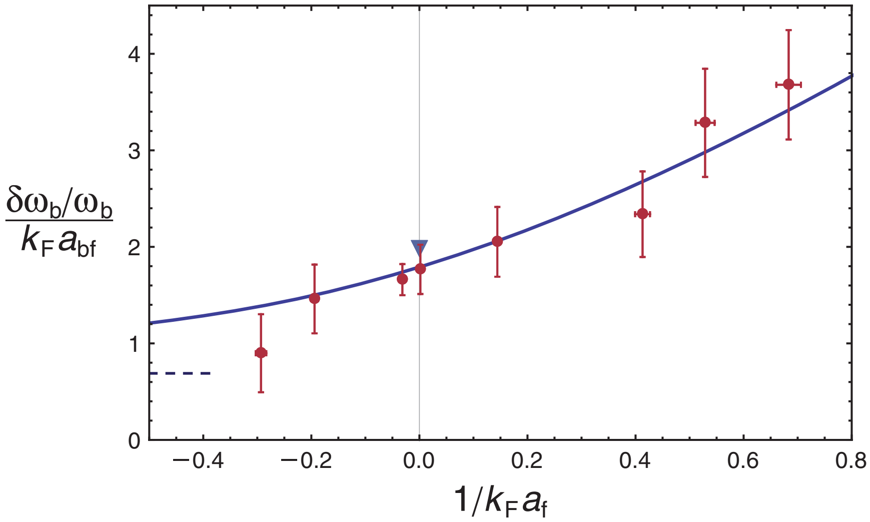

Fig. 3. Dipole mode frequency shift in the BEC-BCS crossover. Red circles: Experiment. Blue line: zero-temperature prediction from the equation of state of (*26*); dashed line: ideal Fermi gas. Blue triangle: prediction from (*13*). Error bars include systematic and statistical errors at 1 SD.

is negative, the mixture is stable and the damping extremely small.

The frequency shift of the BEC (Eq. 2) now probes the derivative of the EoS $n_f(\mu_f)$ in the BEC-BCS crossover. In the zero-temperature limit and under the local density approximation, Eq. 2 obeys the universal scaling $\frac{\delta\omega_b}{\omega_b} = k_F a_{bf} f\left(\frac{1}{k_F a_f}\right)$

In Fig. 3, we compare our measurements to the prediction for the function f obtained from the zero-temperature EoS measured in (*26*). On the BCS side, ($1/k_F a_f < 0$), the frequency shift is reduced and tends to that of a noninteracting Fermi gas. Far on the BEC side ($1/k_F a_f \gg 1$), we can compute the frequency shift using the EoS of a weakly interacting gas of dimers. Within the mean-field approximation, we have $\frac{dn_f}{d\mu_f} = \frac{2m_f}{\pi\hbar^2 a_{dd}}$, where $a_{dd} = 0.6a_f$ is the dimer-dimer scattering length. This expression explains the increase in the frequency shift when a_f is reduced, i.e., moving toward the BEC side [see (*10*) for the effect of Lee-Huang-Yang quantum correction].

The excellent agreement between experiment and our model confirms that precision measurements of collective modes are a sensitive dynamical probe of equilibrium properties of many-body quantum systems (*27*). Our approach can be extended to the study of higher-order excitations. In particular, although there are two first sound modes, one for each atomic species, we expect only one second sound for the superfluid mixture (*28*) if cross-thermalization is fast enough. In addition, the origin of the critical velocity for the relative motion of Bose and Fermi superfluids is an intriguing question that can be further explored in our system. Finally, a richer phase diagram may be revealed when N_b/N_f is increased (*29*) or when the superfluid mixture is loaded in an optical lattice (*30*).

REFERENCES AND NOTES

1. W. Ketterle, *Rev. Mod. Phys.* **74**, 1131–1151 (2002).
2. E. A. Cornell, C. E. Wieman, *Rev. Mod. Phys.* **74**, 875–893 (2002).
3. Z. Hadzibabic, P. Krüger, M. Cheneau, B. Battelier, J. Dalibard, *Nature* **441**, 1118–1121 (2006).
4. M. Greiner, O. Mandel, T. Esslinger, T. W. Hänsch, I. Bloch, *Nature* **415**, 39–44 (2002).
5. W. Zwerger, Ed., *The BCS-BEC Crossover and the Unitary Fermi Gas*, vol. 836 of *Lecture Notes in Physics* (Springer, Berlin, 2012).
6. F. Schreck *et al.*, *Phys. Rev. Lett.* **87**, 080403 (2001).
7. A. G. Truscott, K. E. Strecker, W. I. McAlexander, G. B. Partridge, R. G. Hulet, *Science* **291**, 2570–2572 (2001).
8. J. Rysti, J. Tuoriniemi, A. Salmela, *Phys. Rev. B* **85**, 134529 (2012).
9. J. Tuoriniemi *et al.*, *J. Low Temp. Phys.* **129**, 531–545 (2002).
10. See supplementary materials on *Science* Online.
11. G. Zürn *et al.*, *Phys. Rev. Lett.* **110**, 135301 (2013).
12. T. De Silva, E. Mueller, *Phys. Rev. A* **73**, 051602 (2006).
13. M. J. H. Ku, A. T. Sommer, L. W. Cheuk, M. W. Zwierlein, *Science* **335**, 563–567 (2012).
14. K. Mølmer, *Phys. Rev. Lett.* **80**, 1804–1807 (1998).
15. D. S. Hall, M. R. Matthews, J. R. Ensher, C. E. Wieman, E. A. Cornell, *Phys. Rev. Lett.* **81**, 1539–1542 (1998).
16. P. Maddaloni, M. Modugno, C. Fort, F. Minardi, M. Inguscio, *Phys. Rev. Lett.* **85**, 2413–2417 (2000).
17. F. Ferlaino *et al.*, *J. Opt. B Quantum Semiclassical Opt.* **5**, S3–S8 (2003).
18. A. Sommer, M. Ku, G. Roati, M. W. Zwierlein, *Nature* **472**, 201–204 (2011).
19. T. Kinoshita, T. Wenger, D. S. Weiss, *Nature* **440**, 900–903 (2006).
20. Because of a slight deviation from the Paschen-Back regime for ^{7}Li, this ratio is 1.1 instead of 1.08.
21. Y. Hou, L. Pitaevskii, S. Stringari, *Phys. Rev. A* **88**, 043630 (2013).
22. C. Lobo, A. Recati, S. Giorgini, S. Stringari, *Phys. Rev. Lett.* **97**, 200403 (2006).
23. S. Stringari, *J. Phys. IV France* **116**, 47–66 (2004).
24. T. Miyakawa, T. Suzuki, H. Yabu, *Phys. Rev. A* **62**, 063613 (2000).
25. A. Banerjee, *Phys. Rev. A* **76**, 023611 (2007).
26. N. Navon, S. Nascimbène, F. Chevy, C. Salomon, *Science* **328**, 729–732 (2010).
27. M. K. Tey *et al.*, *Phys. Rev. Lett.* **110**, 055303 (2013).
28. G. Volovik, V. Mineev, I. Khalatnikov, *Sov. Phys. JETP* **69**, 675 (1975).
29. T. Ozawa, A. Recati, S. Stringari, http://arxiv.org/abs/1405.7187 (2014).
30. A. B. Kuklov, B. V. Svistunov, *Phys. Rev. Lett.* **90**, 100401 (2003).

ACKNOWLEDGMENTS

We thank S. Stringari and Y. Castin for fruitful discussions and S. Balibar, J. Dalibard, F. Gerbier, S. Nascimbène, C. Cohen-Tannoudji, and M. Schleier-Smith for critical reading of the manuscript. We acknowledge support from the European Research Council Ferlodim and Thermodynamix, the Ile de France Nano-K (contract Atomix), and Institut de France Louis D. Prize.

SUPPLEMENTARY MATERIALS

www.sciencemag.org/content/345/6200/1035/suppl/DC1
Materials and Methods
Figs. S1 to S4
References (*31–34*)

29 April 2014; accepted 30 June 2014

10.1126/science.1255380

EARTHQUAKE DYNAMICS

Strength of stick-slip and creeping subduction megathrusts from heat flow observations

Xiang Gao[1] and Kelin Wang[2,3]*

Subduction faults, called megathrusts, can generate large and hazardous earthquakes. The mode of slip and seismicity of a megathrust is controlled by the structural complexity of the fault zone. However, the relative strength of a megathrust based on the mode of slip is far from clear. The fault strength affects surface heat flow by frictional heating during slip. We model heat-flow data for a number of subduction zones to determine the fault strength. We find that smooth megathrusts that produce great earthquakes tend to be weaker and therefore dissipate less heat than geometrically rough megathrusts that slip mainly by creeping.

Subduction megathrusts that primarily exhibit stick-slip behavior can produce great earthquakes, but some megathrusts are observed to creep while producing small and moderate-size earthquakes. The relationship between seismogenesis and strength of subduction megathrust is far from clear. Faults that produce great earthquakes are commonly thought of as being stronger than those that creep (*1*). Megathrusts that are presently locked to build up stress for future great earthquakes are thus described as being "strongly coupled." However, some studies have proposed strong creeping megathrusts because of the geometric irregularities of very rugged subducted sea floor (*2*, *3*).

Contrary to a widely held belief, geodetic and seismic evidence shows that very rough subducting sea floor promotes megathrust creep (*2*). All

Momentum distribution of a dilute unitary Bose gas with three-body losses

Sébastien Laurent, Xavier Leyronas, and Frédéric Chevy

Physical Review Letters, **113**, 220601 (2014)

Momentum Distribution of a Dilute Unitary Bose Gas with Three-Body Losses

Sébastien Laurent,[1] Xavier Leyronas,[2] and Frédéric Chevy[1]
[1]*Laboratoire Kastler Brossel, CNRS, UPMC, Ecole Normale Supérieure, 24 rue Lhomond, 75231 Paris, France*
[2]*Laboratoire de Physique Statistique, Ecole Normale Supérieure, UPMC Université Paris 06, Université Paris Diderot, CNRS, 24 rue Lhomond, 75005 Paris, France*

(Received 29 November 2013; published 25 November 2014)

Using a combination of Boltzmann's equation and virial expansion, we study the effect of three-body losses and interactions on the momentum distribution of a homogeneous unitary Bose gas in the dilute limit where quantum correlations are negligible. The comparison of our results to the recent measurement made at JILA on a unitary gas of ^{85}Rb allows us to determine an experimental fugacity $z = 0.5(1)$.

DOI: 10.1103/PhysRevLett.113.220601 PACS numbers: 67.85.-d, 05.20.Dd, 34.50.Cx, 67.10.-j

In the past few years, ultracold gases have become a unique tool for the experimental study of strongly correlated systems. In atomic vapors, strong interactions can be achieved either by trapping the atoms in an optical lattice or by using Feshbach resonances. While the first route has been very successful and has led to ground-breaking discoveries such as the observation of the Mott transition in both Bose [1] and Fermi gases [2,3], Feshbach resonances could only be used to study strongly correlated Fermi gases. Indeed, despite interest in strongly correlated bosonic systems [4–13], the lifetime of the cloud of bosons near a Feshbach resonance is strongly reduced by the onset of three-body recombination towards deeply bound molecular states [14,15]. Recent experimental results suggested new routes to overcome this challenge and that it might be possible to quantitatively study the unitary Bose gas. First, it was demonstrated that at finite temperature the increase of the three-body loss rate scaling as a^4 actually saturates when $a \gg \lambda_{\mathrm{th}}$, where $\lambda_{\mathrm{th}} = h/\sqrt{2\pi m k_B T}$ is the thermal wavelength [16,17]. Moreover, recent experimental results from JILA demonstrated universal local dynamics of the momentum distribution of a unitary Bose gas towards a quasi-equilibrium state [18] and have triggered several theoretical works on the dynamics of strongly correlated Bose gases near Feshbach resonances [19–21].

The stability of the unitary Bose gas hinges on the following argument [11]. First, the three-body losses are characterized by a coefficient L_3 such that $\dot{N} = -L_3 n^2 N$, where N is the total atom number and n is the particle density. This phenomenological law defines a characteristic loss rate $\gamma_3 = L_3 n^2$. For a thermal gas, the cloud is brought back to equilibrium by elastic scattering at a characteristic rate $\gamma_2 \simeq n\sigma v$, where σ is the scattering cross section and v is the characteristic velocity of the atoms. At unitarity, the scattering cross section follows a universal scaling $\sigma = 8\pi/k^2$, where k is the relative wave vector of two scattering particles. In the presence of losses, the system can be kept in a quasiequilibrium state provided that the ratio γ_3/γ_2 stays small. It was shown both theoretically and experimentally [16,17] that at unitarity the three-body loss rate is given by

$$L_3 \simeq 36\sqrt{3}\pi^2 \frac{\hbar^5}{m^3 (k_B T)^2} (1 - e^{-4\eta}), \tag{1}$$

where η is a dimensionless parameter characterizing the probability of forming a deeply bound molecule at a short distance [22]. Plugging Eq. (1) into the expression for γ_3, we see that quasiequilibrium can be achieved as long as $(1 - e^{-4\eta}) n \lambda_{\mathrm{th}}^3$ is small, i.e., when the system is not too deeply in the quantum degenerate regime.

In this Letter, we investigate the effect of three-body losses on the momentum distribution of a unitary Bose gas. Our analysis is based on a semianalytical resolution of Boltzmann's equation. Since Boltzmann's equation neglects all many-body correlations, our work is restricted to a low phase-space density regime where, as aforementioned, three-body losses can be treated perturbatively. We calculate the first correction to the momentum distribution and we compare it to the effect of two-body interactions. We show that in the dilute limit, both effects deplete the center of the momentum distribution proportionally to the phase-space density of the gas. Moreover, for realistic parameters, this depletion is dominated by three-body losses.

Consider a homogeneous Bose gas that we describe by a phase-space density $f(\boldsymbol{p})$. In the presence of losses, f is the solution of Boltzmann's equation that we write formally

$$\partial_t f = I_{\mathrm{coll}}[f] - \mathcal{L}_3[f], \tag{2}$$

where I_{coll} and $\mathcal{L}_3$ are nonlinear operators describing, respectively, the elastic collisions and the three-body losses. At low phase-space density, we can neglect the bosonic stimulation and we have

$$I_{\mathrm{coll}}[f](\boldsymbol{p}_1) = \int d^3\boldsymbol{p}_2 d^2\boldsymbol{\omega}' \frac{d\sigma}{d\omega'} \frac{|\boldsymbol{p}_2 - \boldsymbol{p}_1|}{m}(f_3 f_4 - f_1 f_2). \tag{3}$$

Here, f_α stands for $f(\boldsymbol{p}_\alpha)$, $(\boldsymbol{p}_1, \boldsymbol{p}_2)$ [respectively, $(\boldsymbol{p}_3, \boldsymbol{p}_4)$] are the incoming (outgoing) momenta satisfying energy and momentum conservation and $d\sigma/d\omega' = 8\hbar^2/|\boldsymbol{p}_1 - \boldsymbol{p}_2|^2$ is the differential scattering cross section towards the outgoing solid angle $\boldsymbol{\omega}'$.

From [16], the loss rate operator for a unitary Bose gas can be written as

$$\mathcal{L}_3[f](\boldsymbol{p}_1) = \int d^3\boldsymbol{p}_2 d^3\boldsymbol{p}_3 \frac{\mathcal{A}_3}{E_{123}^2} |\phi(\Omega_3)|^2 f(\boldsymbol{p}_1) f(\boldsymbol{p}_2) f(\boldsymbol{p}_3), \tag{4}$$

where $E_{123} = (p_1^2 + p_2^2 + p_3^2)/2m - (\boldsymbol{p}_1 + \boldsymbol{p}_2 + \boldsymbol{p}_3)^2/6m$ is the energy in the center of mass frame of the three particles of momenta $(\boldsymbol{p}_1, \boldsymbol{p}_2, \boldsymbol{p}_3)$, $\mathcal{A}_3 = 2\pi^3(k_{\mathrm{B}}T)^2 L_3$ and $\phi(\Omega_3)$ is the hyperangular wave function describing the angular structure of the Efimov trimers that we normalize by the condition $\int d^5\Omega_3 |\phi(\Omega_3)|^2 = 1$.

In the absence of losses, the system thermalizes to a distribution G solution of $I_{\mathrm{col}}[G] = 0$. For a classical gas, the solution of this equation is a Gaussian distribution $G(n, E; p) = n\lambda_{\mathrm{th}}^3 e^{-\beta p^2/2m}/h^3$, where $\beta = 1/k_B T$ and $E = \int (G(p) p^2/2m) d^3\boldsymbol{p} = 3nk_B T/2$ is the energy density.

In the quasistatic regime $\gamma_3/\gamma_2 \ll 1$, three-body losses are small and we can use $\mathcal{A}_3$ as an expansion parameter. Since for $\mathcal{A}_3 = 0$ the system can reach a stationary thermal state, we expect the characteristic evolution time in the presence of losses to vary as $\mathcal{A}_3^{-1}$ and thus ∂_t must be considered to scale as $\mathcal{A}_3$. We write then $f = f_0 + f_1 + \cdots$ where $f_j \propto \mathcal{A}_3^j$. The expansion of Eq. (2) to first order in $\mathcal{A}_3$ yields

$$I_{\mathrm{coll}}[f_0] = 0, \tag{5}$$

$$\partial_t f_0 = I'_{\mathrm{coll}}[f_1] - \mathcal{L}_3[f_0], \tag{6}$$

where I'_{coll} is the linearized collisional operator.

According to Eq. (5), f_0 is a Maxwell-Boltzmann distribution. However, since the system loses particles by three-body recombination, its atom number and its energy vary with time. We therefore have $f_0(p, t) = G(n_t, E_t; p)$. We then have in Eq. (6)

$$I'_{\mathrm{coll}}[f_1] = \mathcal{L}_3[f_0] + \dot{E}\partial_E G + \dot{n}\partial_n G. \tag{7}$$

Take $f_1(p, t) = G(n_t, E_t; p)\alpha(p, t)$. Equation (7) then becomes

$$C[\alpha] = \frac{1}{G}\mathcal{L}_3[G] + \dot{E}\partial_E \ln(G) + \dot{n}\partial_n \ln(G), \tag{8}$$

with

$$C[\alpha] = \frac{1}{G} I'_{\mathrm{coll}}[G\alpha] \tag{9}$$

$$= \int d^3\boldsymbol{p}_2 d^2\boldsymbol{\omega}' f_0(\boldsymbol{p}_2) \frac{d\sigma}{d\omega'} \frac{|\boldsymbol{p}_2 - \boldsymbol{p}_1|}{m} \times (\alpha_3 + \alpha_4 - \alpha_1 - \alpha_2), \tag{10}$$

and $\alpha_k = \alpha(\boldsymbol{p}_k)$ for $k = 1, \ldots, 4$. The operator C is symmetric for the scalar product [23]

$$\langle \alpha | \alpha' \rangle = \int d^3\boldsymbol{p} G(p)\alpha(p)\alpha'(p). \tag{11}$$

Because of energy and particle number conservation, the kernel of C is spanned by $\alpha(p) = 1$ and $\alpha(p) = p^2$. Finally, being a symmetric operator, its image is orthogonal to its kernel. To find the time evolution of the energy and the atom number, we project Eq. (8) on 1 and p^2. Using the structure of the kernel of C, the collisional term vanishes and we obtain

$$\dot{n}_t = -\left\langle 1 \middle| \frac{1}{G}\mathcal{L}_3[G] \right\rangle, \tag{12}$$

$$\dot{E}_t = -\left\langle \frac{p^2}{2m} \middle| \frac{1}{G}\mathcal{L}_3[G] \right\rangle. \tag{13}$$

The explicit calculation of the rhs of these equations involves nine-dimensional integrals over the three momenta $(\boldsymbol{p}_1, \boldsymbol{p}_2, \boldsymbol{p}_3)$ in the three-body loss rate operator. This calculation can be performed analytically by introducing the momentum-space Jacobi coordinates [24] and we finally obtain

$$\dot{n}_t = -L_3 n^3, \tag{14}$$

$$\dot{E}_t = -\frac{5}{9} E L_3 n^2, \tag{15}$$

where we recover the usual formula for three-body losses, as well as the recombination heating discussed in [16,17].

To find α, we project Eq. (8) on the range of C [i.e., orthogonally to $\mathrm{Span}(1, p^2)$]. We then have

$$C[\alpha] = P\left[\frac{1}{G}\mathcal{L}_3[G]\right], \tag{16}$$

where P is the orthogonal projector on $\mathrm{Im}(C)$, and where we used the fact that $\ln G$ is a linear combination of 1 and p^2 and thus lies in the kernel of C and P.

Equation (16) is solved numerically by decomposing its solution over a basis of orthogonal polynomials [24]. The results are displayed in Fig. 1, where we observe a

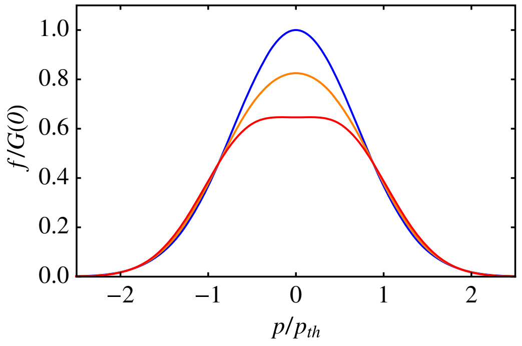

FIG. 1 (color online). Deformation of the momentum distribution of a unitary Bose gas due to three-body losses. From top to bottom: $n\lambda_{\rm th}^3(1-e^{-4\eta})=0$ (blue, Boltzmann gas), $n\lambda_{\rm th}^3(1-e^{-4\eta})=0.05$ (orange), and $n\lambda_{\rm th}^3(1-e^{-4\eta})=0.1$ (red).

flattening of the momentum distribution when the three-body losses strength is increased.

In the experiment described in [18], the cloud is not directly prepared in the quasistatic, strongly interacting state. Rather, the experimental sequence starts with a the weakly interacting Bose-Einstein condensate in a regime where losses can be neglected. The magnetic field is then ramped quickly to unitarity where the system can relax towards the quasiequilibrium described above. To get some insight on the relaxation of the system towards equilibrium, we consider the simpler case of a noncondensed gas for which the momentum distribution before the ramp is Gaussian. We write as before $f=f_0+f_1$ with $f_1=f_{1,{\rm qs}}+\delta f_1$, where $f_{1,{\rm qs}}$ is the quasistatic solution and δf_1 satisfies the initial condition $\delta f_1(p,t=0)=-f_{1,{\rm qs}}(p;t=0)$, since at $t=0$, $f=f_0$. Expanding Boltzmann's equation to first order in f_1 and using the properties of $f_{1,{\rm qs}}$, we obtain for δf_1,

$$\partial_t\delta f_1 = I'_{\rm coll}[\delta f_1]. \tag{17}$$

This equation shows that the relaxation towards the quasistatic regime is solely driven by two-body collisions and occurs at a rate $\sim\gamma_2$. This may seem paradoxical since one would rather expect the three-body characteristic rate $\sim\gamma_3$. However, as far as the phase-space density is concerned, the depletion of f at low momenta is quite small since the relative decrease of the peak momentum density is $\propto n\lambda^3$. Since $1/\gamma_3$ is the time required to lose typically half the initial atom number, the dip should form on a time scale, $\simeq n\lambda^3/\gamma_3\simeq 1/\gamma_2$.

The three-body losses lead to a correction to the momentum distribution proportional to $n\lambda^3$. This scaling is similar to the first virial correction, and one may wonder if the three-body losses might not mask the effects of two-body interactions. To clarify this point, we calculated the leading order corrections to the occupation number $\rho(p)=h^3f(p)$ using the scheme presented in [26]. In the virial expansion, the leading order term corresponds to the ideal Boltzmann gas. In the grand canonical ensemble, this term reads $\rho^{(1)}(p)=ze^{-\beta\epsilon_p}$, where z is the fugacity and $\epsilon_p=p^2/2m$. The next order term is the sum of two contributions. The first one corresponds to Bose's statistics and is simply $\rho^{(2,a)}(p)=z^2e^{-2\beta\epsilon_p}$, while the second one is more involved and is due to interactions. Following [26], it is given by

$$\rho^{(2,b)}(p)=\frac{8\pi z^2}{m}\int_{\mathcal{C}_\gamma}\frac{ds}{2\pi i}\int_0^{+\infty}\frac{dPP^2}{2\pi^2}\frac{e^{-\beta s}}{\sqrt{-ms}}\times\frac{e^{-\beta(P^2/4m)}}{[s+\frac{P^2}{4m}-\frac{p^2}{2m}-\frac{(P-p)^2}{2m}][s+\frac{P^2}{4m}-\frac{p^2}{2m}-\frac{(P+p)^2}{2m}]}, \tag{18}$$

where $\mathcal{C}_\gamma$ is a Bromwich contour [27]. We note that this expression is simply twice that obtained for spin 1/2 fermions [26]. To convert this momentum distribution to the canonical ensemble, we use the virial expansion of the equation of state of the unitary Bose gas, $n\lambda_{\rm th}^3=z+2b_2z^2+\cdots$, with $b_2=9/4\sqrt{2}$ [13]. We thus obtain

$$\rho(p)=n\lambda_{\rm th}^3e^{-\beta\epsilon_p}+(n\lambda_{\rm th}^3)^2[\xi(\lambda_{\rm th}p/\hbar)-2b_2e^{-\beta\epsilon_p}], \tag{19}$$

where we took $\rho^{(2)}(p)=\rho^{(2,a)}(p)+\rho^{(2,b)}(p)=z^2\xi(\lambda_{\rm th}p/\hbar)$.

In Fig. 2, we compare the effect of three-body losses with the virial corrections to the momentum distribution. We observe that for ^{7}Li, for which $\eta=0.2$, the dip in the momentum distribution is dominated by three-body losses.

We now turn to the quantitative comparison of our results with the experimental data presented in [18]. In this experiment an ultracold, weakly interacting Bose-Einstein condensate is ramped abruptly to the Feshbach Resonance and after a 100-μs-long waiting time, the system reaches a quasiequilibrium characterized by the momentum

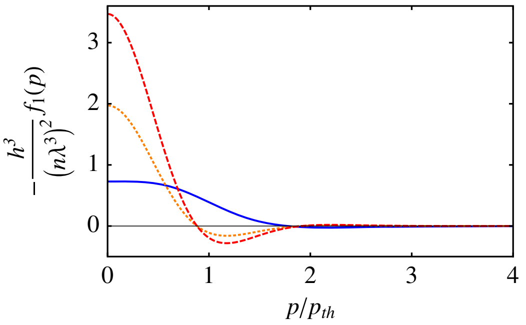

FIG. 2 (color online). Correction to the Boltzmann gas: Three-body losses vs interactions. The correction to Boltzmann's distribution is plotted for maximal three-body losses ($\eta=\infty$, red dashed line), $\eta=0.2$, corresponding to ^{7}Li (orange dotted line). The blue solid line corresponds to the correction, Eq. (19), due to Bose statistics and two-body interactions.

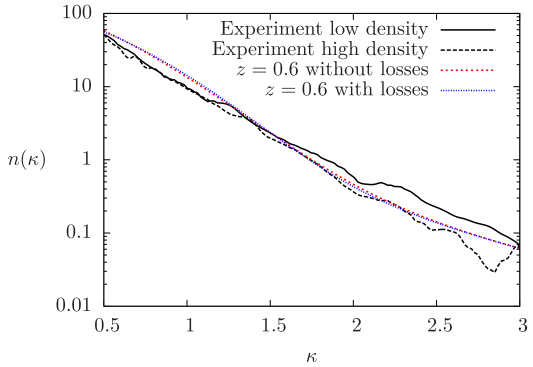

FIG. 3 (color online). The dimensionless momentum occupation number for the unitary Bose gas in a semilog scale. $\kappa = p/\hbar k_n$ with $k_n \equiv (6\pi^2\langle n\rangle)^{1/3}$ and $\langle n\rangle$ the spatially averaged density ($\langle n\rangle = 5.5\times 10^{12}$ cm^{-3} and $\langle n\rangle = 1.6\times 10^{12}$ cm^{-3}). The occupation number is normalized so that $\int n(\kappa)4\pi\kappa d\kappa = 8\pi^3$. The continuous line is the experimental result from Ref. [18] , the dashed line is the result of Eq. (19) averaged over the initial density profile for $z = 0.6$, and the dotted line includes the effect of three-body losses. The fit is restricted to $\kappa > 0.5$ since for lower momenta, the momentum distribution never equilibrates.

distribution of Fig. 3. To compare this experiment with our results, we must first determine the temperature of the cloud and since the dynamics is very fast (in the experiment the trapping frequencies are a few Hz), it is most likely inhomogeneous. We therefore assume a purely local heating and we consider that the thermalization mechanism depends only on elastic processes. Neglecting the initial scattering length, we conclude that the local temperature must scale like $T(\mathbf{r}) = CT_{n(\mathbf{r})}$ where C is a numerical constant and $T_n = \hbar^2(6\pi^2 n)^{2/3}/k_B m$. In other words, the phase-space density (or equivalently the fugacity) is homogeneous over the cloud. Furthermore, the dynamics being too fast for transport phenomena to occur, we can assume that the density profile is not affected by the thermalization. We can therefore average the predicted momentum distribution over the Thomas-Fermi density profile of the initial, weakly interacting Bose-Einstein condensate and we fit the experimental data taking $\eta = 0.06$ and using the uniform fugacity z as the only fitting parameter [24]. In this way, we find a surprisingly good agreement between experiment and theory for $z = 0.6(1)$ (Note that as expected for such a small value of η, the three-body losses play only a small role in the wing of the momentum distribution.) Using the virial expansion, this fugacity corresponds to a temperature of 110 nK at the center of the trap. This temperature is much higher than that of the initial weakly interacting Bose gas and justifies the universal thermalization hypothesis.

In principle, the virial expansion is valid only in the limit of vanishingly small fugacities, and its accuracy is therefore questionable in the present case. Even though there is no reliable way to assess the accuracy of the virial expansion for unitary Bose gases, we note that for the equation of state of the unitary *Fermi* gas, the first-order virial expansion gives the correct result at a $\simeq$10% level at $z = 0.6$ [28,29]. If we assume that the same level of accuracy is achieved in the case of bosons, our calculation should provide a quantitative description of JILA's experiment. To further support our analysis we note that the temperature deduced from the virial expansion yields a three-body loss rate comparable to the one observed in [18].

The approach presented above provides a quantitative way to study unitary Bose gases in the dilute limit. In the case of the results presented in [18], we find that three-body losses are negligible and that the tail of the momentum distribution is well described by a first-order virial expansion at a fugacity $z = 0.6(1)$. This value raises a series of open questions. First, is it possible to derive this value from a purely microscopic model describing the dynamics of a Bose gas projected from a weakly interacting regime to unitarity. Second, is it really universal? In our work, we assumed that, after the ramp, the thermalization was only driven by the two-body scattering length. However, for strongly interacting bosons, we know that three-body Efimov physics cannot be neglected and requires the introduction of the three-body parameter R_t. In this case, the fugacity would be a log-periodic function of the dimensionless parameter $k_F R_t$, as suggested in [20]. This assumption could be tested by reproducing JILA's experiment on different atoms to vary the value of R_t.

We thank A. Grier, C. Salomon, F. Werner, and the ENS cold atom group for careful reading and helpful discussions. We also thank C. Klauss and E. Cornell for comments and for providing us with the data of Fig. 3. The authors acknowledge support from the ERC (Advanced grant Ferlodim and starting grant Thermodynamix), Institut Universitaire de France, and Région Ile de France (IFRAF). F. C. thanks Laure Saint-Raymond for fruitful discussions.

[1] M. Greiner, O. Mandel, T. Esslinger, T. W. Hänsch, and I. Bloch, Nature (London) **415**, 39 (2002).
[2] U. Schneider, L. Hackermuller, S. Will, T. Best, I. Bloch, T. A. Costi, R. W. Helmes, D. Rasch, and A. Rosch, Science **322**, 1520 (2008).
[3] R. Jördens, N. Strohmaier, K. Günter, H. Moritz, and T. Esslinger, Nature (London) **455**, 204 (2008).
[4] S.-J. Jiang, W.-M. Liu, G. W. Semenoff, and F. Zhou, Phys. Rev. A **89**, 033614 (2014).
[5] T. L. Ho, Phys. Rev. Lett. **92**, 090402 (2004).
[6] S. Cowell, H. Heiselberg, I. E. Mazets, J. Morales, V. R. Pandharipande, and C. J. Pethick, Phys. Rev. Lett. **88**, 210403 (2002)
[7] J.-L. Song and F. Zhou, Phys. Rev. Lett. **103**, 025302 (2009).
[8] Y.-L. Lee and Y.-W. Lee, Phys. Rev. A **81**, 063613 (2010).

[9] J. M. Diederix, T. C. F. Van Heijst, and H. T. C. Stoof, Phys. Rev. A **84**, 033618 (2011).

[10] D. Borzov, M. S. Mashayekhi, S. Zhang, J.-L. Song, and F. Zhou, Phys. Rev. A **85**, 023620 (2012).

[11] W. Li and T.-L. Ho, Phys. Rev. Lett. **108**, 195301 (2012).

[12] S. Piatecki and W. Krauth, Nat. Commun. **5**, 3503 (2014).

[13] Y. Castin and F. Werner, Can. J. Phys. **91**, 382 (2013).

[14] J. L. Roberts, N. R. Claussen, S. L. Cornish, and C. E. Wieman, Phys. Rev. Lett. **85**, 728 (2000).

[15] S. Inouye, M. R. Andrews, J. Stenger, H.-J. Miesner, D. M. Stamper-Kurn, and W. Ketterle, Nature (London) **392**, 151 (1998).

[16] B. S. Rem, A. T. Grier, I. Ferrier-Barbut, U. Eismann, T. Langen, N. Navon, L. Khaykovich, F. Werner, D. S. Petrov, F. Chevy, and C. Salomon, Phys. Rev. Lett. **110**, 163202 (2013).

[17] R. J. Fletcher, A. L. Gaunt, N. Navon, R. P. Smith, and Z. Hadzibabic, Phys. Rev. Lett. **111**, 125303 (2013).

[18] P. Makotyn, C. E. Klauss, D. L. Goldberger, E. A. Cornell, and D. S. Jin, Nat. Phys. **10**, 116 (2014).

[19] A. G. Sykes, J. P. Corson, J. P. D'Incao, A. P. Koller, C. H. Greene, A. M. Rey, K. R. A. Hazzard, and J. L. Bohn, Phys. Rev. A **89**, 021601(R) (2014).

[20] D. Hudson Smith, E. Braaten, D. Kang, and L. Platter, Phys. Rev. Lett. **112**, 110402 (2014).

[21] X. Yin and L. Radzihovsky, Phys. Rev. A **88**, 063611 (2013).

[22] E. Braaten, H.-W. Hammer, and M. Kusunoki, Phys. Rev. A **67**, 022505 (2003).

[23] H. Smith and H. Højgaard Jensen, *Transport Phenomena* (Oxford University Press, New York, 1989).

[24] See Supplemental Material at http://link.aps.org/supplemental/10.1103/PhysRevLett.113.220601, which includes Ref. [25], for more details on the calculations.

[25] M. Abramowitz and I. Stegun, *Handbook of Mathematical Functions* (Dover Publishing Inc., New York, 1970).

[26] X. Leyronas, Phys. Rev. A **84**, 053633 (2011).

[27] W. Appel and E. Kowalski, *Mathematics for Physics and Physicists* (Princeton University Press, Princeton, 2007).

[28] S. Nascimbène, N. Navon, K. Jiang, F. Chevy, and C. Salomon, Nature (London) **463**, 1057 (2010).

[29] M. J. H. Ku, A. T. Sommer, L. W. Cheuk, and M. W. Zwierlein, Science **335**, 563 (2012).

Critical velocity and dissipation of an ultracold Bose-Fermi counterflow

Marion Delehaye, Sébastien Laurent, Igor Ferrier-Barbut, Shuwei Jin,
Frédéric Chevy, and Christophe Salomon

Physical Review Letters, **115**, 265303 (2015)

Critical Velocity and Dissipation of an Ultracold Bose-Fermi Counterflow

Marion Delehaye, Sébastien Laurent, Igor Ferrier-Barbut,[*] Shuwei Jin, Frédéric Chevy, and Christophe Salomon
Laboratoire Kastler Brossel, ENS-PSL, CNRS, UPMC-Sorbonne Universités, and Collège de France, 75005 Paris, France

(Received 10 October 2015; revised manuscript received 19 November 2015; published 23 December 2015)

We study the dynamics of counterflowing bosonic and fermionic lithium atoms. First, by tuning the interaction strength we measure the critical velocity v_c of the system in the BEC-BCS crossover in the low temperature regime and we compare it to the recent prediction of Castin *et al.*, C. R. Phys. 16, 241 (2015). Second, raising the temperature of the mixture slightly above the superfluid transitions reveals an unexpected phase locking of the oscillations of the clouds induced by dissipation.

DOI: 10.1103/PhysRevLett.115.265303 PACS numbers: 67.85.-d, 03.75.Kk, 03.75.Ss, 37.10.Gh

Superconductivity and superfluidity are spectacular macroscopic manifestations of quantum physics at low temperature. Besides liquid helium 4 and helium 3, dilute quantum gases have emerged over the years as a versatile tool to probe superfluid properties in diverse and controlled situations. Frictionless flows have been observed with both bosonic and fermionic atomic species, in different geometries and in a large range of interaction parameters from the weakly interacting Bose gas to strongly correlated fermionic systems [1–6]. Several other hallmarks of superfluidity such as quantized vortices or second sound were also observed in cold atoms [7–9].

A peculiar feature of superfluid flows is the existence of a critical velocity above which dissipation arises. In Landau's original argument, this velocity is associated with the threshold for creation of elementary excitations in the superfluid: for a linear dispersion relation, it predicts that the critical velocity is simply given by the sound velocity in the quantum liquid. This critical velocity has been measured both in superfluid helium [10] and ultracold atoms [1,4–6,11]. However, the recent production of a Bose-Fermi double superfluid [12] raised new questions on Bose-Fermi mixtures [13–16] and interrogations on the validity of Landau's argument in the case of superfluid counterflow [17–22].

In this Letter, we study the dynamics of a Bose-Fermi superfluid counterflow in the crossover between the Bose-Einstein condensate (BEC) and Bardeen-Cooper-Schrieffer (BCS) regimes and at finite temperature. We show how friction arises when the relative velocity of the Bose and Fermi clouds increases and we confirm that damping occurs only above a certain critical relative velocity v_c. We compare our measurements to Landau's prediction and its recent generalization $v_c = c_s^F + c_s^B$, where c_s^F and c_s^B are the sound velocities of the fermionic and bosonic components, respectively [18]. Finally, we study finite temperature damping of the counterflow and we show that the system can be mapped onto a Caldeira-Leggett-like model [23] of two quantum harmonic oscillators coupled to a bath of excitations. This problem has been recently studied as a toy model for decoherence in quantum networks [24] or for heat transport in crystals [25] and we show here that the emergence of dissipation between the two clouds leads to a Zeno-like effect which locks their relative motions.

Our Bose and Fermi double-superfluid setup was previously described in [12]. We prepare vapors of bosonic (B) ^{7}Li atoms spin polarized in the second-to-lowest energy state and fermionic (F) ^{6}Li atoms prepared in a balanced mixture of the two lowest spin states noted $|\uparrow\rangle$, $|\downarrow\rangle$. The two species are kept in the same cigar-shaped hybrid magnetic-optical trap in which evaporative cooling is performed in the vicinity of the 832 G ^{6}Li Feshbach resonance [26]. The final number of fermions $N_F = 2.5 \times 10^5$ greatly exceeds that of the bosons $N_B \sim 2.5 \times 10^4$ and the temperature of the sample is adjusted by stopping the evaporation at different trap depths. The thermal pedestal surrounding the ^{7}Li BEC provides a convenient low temperature thermometer for both species after sufficiently long thermalization time (~1 sec). The lowest temperature achieved in this study corresponds to almost entirely superfluid clouds with $T/T_{c,\alpha=B,F} \leq 0.5$, where $T_{c,\alpha}$ is the superfluidity transition temperature of species α.

The magnetic field values used in the experiment (780–880 G) enable us to scan the fermion-fermion interaction within a range $-0.5 \leq 1/k_F a_F \leq 1$. Here, a_F is the s-wave scattering length between $|\uparrow\rangle$ and $|\downarrow\rangle$ fermions and the Fermi momentum k_F is defined by $\hbar^2 k_F^2/2m_F = \hbar\bar{\omega}(3N_F)^{1/3}$ with $\bar{\omega}$ the geometric mean of the trap frequencies, and N_F the total number of fermions of mass m_F. In our shallowest traps, typical trap frequencies for ^{6}Li are $\omega_x = \omega_y = 2\pi \times 550$ Hz and $\omega_z = 2\pi \times 17$ Hz. Since the bosonic and fermionic isotopes experience the same trapping potentials, the oscillation frequencies of the two species are within a ratio $\sqrt{6/7} \simeq 0.9$.

We excite the dipole modes of the system by displacing adiabatically the centers of mass of the clouds from their initial position by a distance z_0 along the weakly confined z direction, and abruptly releasing them in the trap. The two clouds evolve for a variable time t before *in situ* absorption images perpendicular to the z direction are taken. The measurement of their doubly integrated density profiles gives access to axial positions and atom numbers of both species. Typical time evolutions of the centers of mass are shown in Fig. 1 for different parameter values. Since the Bose and Fermi components oscillate at different frequencies, they oscillate in quadrature after a few periods. By changing z_0, we can thus tune the maximum relative velocity between the two clouds and probe the critical superfluid counterflow.

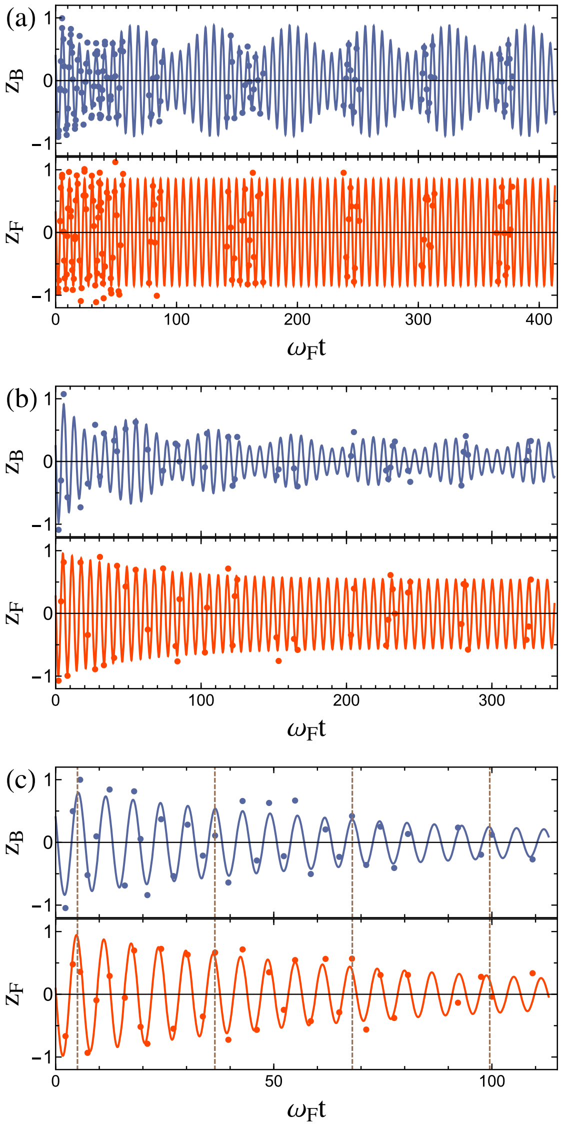

FIG. 1 (color online). Center-of-mass oscillations of bosons (blue, top) and fermions (red, bottom), for different sets of parameters at unitarity. Solid lines: fits using Eq. (1) for the bosons and a similar equation for the fermions. (a) $T/T_F = 0.03$, $T/T_{c,b} \leq 0.5$, $z_0 = 10\ \mu$m. Superfluid regime, no damping is observed and $\omega_B = 2\pi \times 15.41(1)$ Hz $\approx \sqrt{6/7}\omega_F$. The observed beating at $\omega_F - \omega_B$ is due to coherent energy exchange between the clouds. (b) $T/T_F = 0.03$ and $z_0 = 150\ \mu$m. For a larger initial displacement, initial damping ($\gamma_B = 2.4\ \mathrm{s}^{-1}$) is followed by steady-state evolution. $\omega_B = 2\pi \times 14.2(1)$ Hz $\approx \sqrt{6/7}\omega_F$. (c) $T/T_F = 0.4$ and $z_0 = 80\ \mu$m. At higher temperature, phase locking of the two frequencies is observed with $\omega_F \approx \omega_B = 2\pi \times 17.9(3)$ Hz and $\gamma_B = \gamma_F = 1.4(5)\ \mathrm{s}^{-1}$.

As shown in Fig. 1(a), the superfluid counterflow exhibits no visible damping on a $\simeq$5 s time scale for very low temperature and small initial displacement. A striking feature is the beat note on the ^{7}Li oscillation amplitude due to the coherent mean-field coupling to the ^{6}Li cloud [12]. For larger relative velocities, ^{7}Li oscillations are initially damped [Fig. 1(b)] until a steady-state regime as in Fig. 1(a) is reached. We fit the time evolution of the cloud position using the phenomenological law

$$z_B(t) = d(t)[a\cos(\omega_B t) + b\cos(\omega_F t)],$$
$$d(t) = d_1 + d_2\exp(-\gamma_B t). \qquad (1)$$

We measure the damping rate γ_B as a function of relative velocity for six different values of magnetic field, exploring a large region of the crossover going from the BCS ($1/k_F a_F = -0.42$, $B = 880$ G) to the BEC side ($1/k_F a_F = 0.68$, $B = 780$ G), see Fig. 2. For these magnetic field values, the Bose gas remains in the weakly interacting (repulsive) regime and the Bose-Fermi scattering length is $a_{BF} \simeq 41 a_0$, constant in this magnetic field range, and equal for both $|\uparrow\rangle$ and $|\downarrow\rangle$ spin states.

We extract the critical velocity v_c using an *ad hoc* power-law fitting function $\gamma_B = A\Theta(v - v_c)[(v - v_c)/v_F]^\alpha$, where Θ is the Heaviside function and v_F is the Fermi velocity given by $v_F = \hbar k_F/m_F$. For details, see [27]. v_c in the BEC-BCS crossover is displayed in Fig. 3 (red dots) and compared to the predictions of Landau and Castin *et al.* [18]. In this latter work, dissipation arises by the creation of excitation pairs and yields a critical velocity

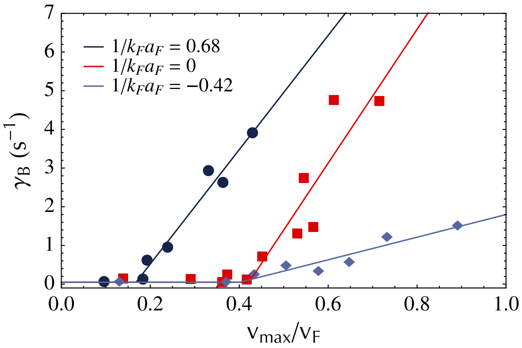

FIG. 2 (color online). Damping rate of the center-of-mass oscillations versus maximal relative velocity in the BEC-BCS crossover in units of the Fermi velocity v_F. Dark blue dots, BEC side (780 G) $1/k_F a_F = 0.68$; red squares, unitarity (832.2 G) $1/k_F a_F = 0$; light blue diamonds, BCS side (880 G) $1/k_F a_F = -0.42$. Power law fits with thresholds provide the critical velocity (solid lines).

$v_c = \underset{\substack{p\\ \sigma=f,b}}{\mathrm{Min}}\{[\epsilon^B(\boldsymbol{p})+\epsilon^F_\sigma(\boldsymbol{p})]/[p]\}$. In this expression, $\epsilon^B(\boldsymbol{p})$ denotes the dispersion relation of excitations in the BEC and $\epsilon^F_\sigma(\boldsymbol{p})$ refers to the two possible branches of the Fermi superfluid, phononlike ($\sigma = b$), and threshold for pair breaking excitations ($\sigma = f$) [28]. For homogeneous gases, at unitarity and on the BEC side of the crossover, this critical relative velocity turns out to be simply the sum of the respective sound velocities of the Bose and Fermi superfluids, $v_c = c_s^F + c_s^B$. We thus plot in Fig. 3 the calculated sound velocities of both superfluids in an elongated geometry obtained by integration over the transverse direction [29–33] (red dashed line c_s^F, blue bars c_s^B). Typically, c_s^B contributes ≃20%–25% to the sum shown as green squares in Fig. 3. Around unitarity and on the BCS side of the resonance, our experimental data are consistent with this interpretation as well as with a critical velocity $v_c = c_s^F$ that one would expect by considering the BEC as a single impurity moving inside the fermionic superfluid. By contrast, we clearly exclude the bosonic sound velocity as a threshold for dissipation.

Our measured critical velocities are significantly higher than those previously reported in pure fermionic systems which, for all interaction strengths, were lower than Landau's criterion [4,6]. The main difference with our study is the use of focused laser beams instead of a BEC as a moving obstacle. In [6], the laser beam is piercing the whole cloud including its nonsuperfluid part where the density is low, and its potential may create a strong density modulation of the superfluid. These effects make a direct comparison to Landau criterion difficult [35]. On the contrary, in our system the size of the BEC (Thomas Fermi radii of 73, 3, 3 μm) is much smaller than the typical size of the Fermi cloud (350, 13, 13 μm around unitarity). For oscillation amplitudes up to ±200 μm the BEC probes only the superfluid core of the fermionic cloud. During its oscillatory motion along z the Bose gas may explore the edges of the Fermi superfluid where the density is smaller. However, it is easy to check that the ratio v/c_s^F is maximum when the centers of the two clouds coincide [27]. Finally, as the mean-field interaction between the two clouds is very small [27] our BEC acts as a weakly interacting local probe of the Fermi superfluid.

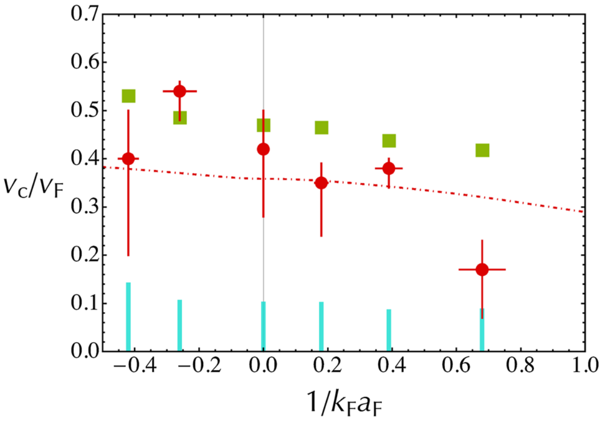

FIG. 3 (color online). Critical velocity of the Bose-Fermi superfluid counterflow in the BEC-BCS crossover normalized to the Fermi velocity v_F. Red dots, measurements. Red dot-dashed line, sound velocity c_s^F of an elongated homogeneous Fermi superfluid calculated from its equation of state [29,30] after integration of the density in the transverse plane, and also measured in [34]. Blue bars, calculated sound velocity c_s^B of the elongated ^{7}Li BEC for each magnetic field (880, 860, 832, 816, 800, 780 G). Green squares indicate the prediction $v_c = c_s^F + c_s^B$. Error bars and c_s^B are discussed in [27].

On the BEC side of the resonance (780 G), however, we observe a strong reduction of the measured critical velocity compared to the predicted values. The effect is strikingly seen in Fig. 2, dark blue dots (see also Supplemental Material [27]). This anomalously small value for positive scattering lengths is consistent with previous measurements [4,6]. Its origin is still unclear but several explanations can be put forward [35]. First, it is well known that vortex shedding can strongly reduce superfluid critical velocity. However, this mechanism requires a strong perturbation. The density of the Bose gas and the mean-field interaction between the two clouds are probably too small for vortex generation through a collective nucleation process. Second, inelastic losses increase on the BEC side of a fermionic Feshbach resonance and heat up the system [36]. This hypothesis is supported by the presence of a clearly visible pedestal in the density profiles of the BEC taken at 780 G. At this value of the magnetic field, we measure a ≃60% condensed fraction, corresponding to a temperature $T/T_{c,B} \simeq 0.5$. Even though the two clouds are still superfluids as demonstrated by the critical behavior around v_c, the increased temperature could be responsible for the decrease of v_c.

We now present results of experiments performed at a higher temperature ($0.03 \lesssim T/T_F \lesssim 0.5$) for $B = 835$ G. For low temperatures ($T/T_F \leq 0.2$), the two clouds remain weakly coupled and, as observed in Fig. 4, the bosonic and fermionic components oscillate at frequencies in the expected ratio $\simeq 0.9 \simeq \sqrt{6/7}$. A new feature emerges for $T \gtrsim T_{c,B} \approx 0.34 T_F > T_{c,F}$ where both gases are in the normal phase. In this "high" temperature regime, the two clouds are locked in phase: ^{7}Li oscillates at ^{6}Li frequency (Fig. 4) and the two components are equally damped [Fig. 1(c)]. This remarkable behavior can be understood as a Zeno effect arising from the increased dissipation between the two components. Indeed, the system can be described as a set of two harmonic oscillators describing, respectively, the macroscopic motion of the global center of mass of the system (Kohn's mode [37]) and the relative motion of the two clouds [27]. These two degrees of freedom are themselves coupled to the "bath" of

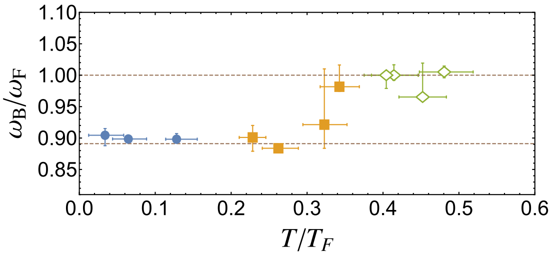

FIG. 4 (color online). Ratio ω_B/ω_F versus temperature of the cloud. Blue circles, the two clouds are superfluids. Yellow squares, only the bosonic component is superfluid. Green open diamonds, the two components are normal. Above $T \approx T_{c,B} \approx 0.34 T_F > T_{c,F}$, oscillations of the Bose and Fermi clouds become locked together at ω_F. Oscillations frequencies are obtained using a Lomb-Scargle algorithm [27]. The lower dashed line is the prediction of a low temperature mean field model [12].

the internal excitations of the two clouds (breathing mode, quadrupole modes, pair breaking excitations…).

In the spirit of the dressed-atom picture, we can represent the state of the two harmonic oscillators by the "radiative" cascade of Fig. 5. Here the states $|N, n\rangle$ are labeled by the quantum numbers associated to Kohn's mode (N) and relative motion (n) of the two clouds and we trace out the degrees of freedom of the bath. On the one hand, Kohn's mode is not an eigenstate of the system for fermions and bosons of different masses; center-of-mass and relative-motion modes are coupled and this coherent coupling is responsible for the dephasing of the oscillations of the two clouds in the weakly interacting regime. On the other hand, interspecies interactions do not act on the center of mass of the whole system, owing to Kohn's theorem, but on the contrary lead to an irreversible "radiative" decay of the *relative* motion at a rate γ.

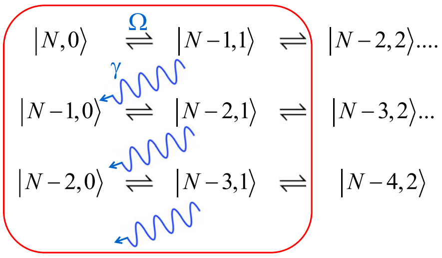

FIG. 5 (color online). Radiative cascade of the center-of-mass motion. In $|N, n\rangle$, N (respectively, n) refers to the center-of-mass (respectively, relative) motion of the two clouds (see text). When the decay rate of the relative motion is larger than the oscillation frequency difference between the two species, the dynamics is restricted to the center-of-mass degree of freedom: in this Zeno-like process, dissipation prevents excitation of the relative motion and the center-of-mass modes of the Bose and Fermi gases do not dephase.

In our experiments, the initial state is a pure center-of-mass excitation $|N, 0\rangle$. If we neglect the interspecies coupling, the system evolves in the subspace spanned by $|N-n, n\rangle_{n=0,\ldots,N}$ of the two coupled oscillators and the system oscillates at a frequency $\delta\omega \simeq \omega_B - \omega_F$ as the centers of mass of the Bose and Fermi clouds dephase. If we now consider the opposite limit where the decay rate γ is larger than the dephasing frequency $\delta\omega$, the strong coupling to the bath prevents the conversion of the center-of-mass excitations into relative motion. As soon as the system is transferred into $|N-1, 1\rangle$ it decays towards state $|N-1, 0\rangle$. Similarly to optical pumping in quantum optics, we can eliminate adiabatically the excited states of the relative motion and restrict the dynamics of the system to the subspace $|N, 0\rangle_{N=0,\ldots,\infty}$ of Kohn's excitations. This situation is reminiscent of the synchronization of two spins immersed in a thermal bath predicted in [38] or to phenomenological classical two-coupled oscillators model.

In this Letter, we have investigated how a Bose-Fermi superfluid flow is destabilized by temperature or relative velocity between the two clouds. In the limit of very low temperature the measured critical velocity for superfluid counterflow slightly exceeds the speed of sound of the elongated Fermi superfluid and decreases sharply towards the BEC side of the BEC-BCS crossover. In a future study, we will investigate the role of temperature, of the confining potential, and of the accelerated motion of the two clouds [35] that should provide a more accurate model for the damping rate versus velocity and more insights on the nature of the excitations. In particular, the *ab initio* calculation of the damping rate will require clarification of the dissipation mechanism at play in a trapped system where the bandwidth of the excitation spectrum is narrow, in contrast to a genuine Caldeira-Leggett model [39].

The authors acknowledge support from Institut Francilien de Recherche sur les Atomes Froids (Atomix Project), ERC (ThermoDynaMix Project), and Institut de France (Louis D. Prize). They thank I. Danaila, N. Proukakis, K. L. Lee, and M. Pierce for insightful comments and discussions, and J. Dalibard, Y. Castin, S. Nascimbène, and T. Yefsah for critical reading of the manuscript.

M. D. and S. L. contributed equally to this work.

---

[*] Present Address: 5. Physikalisches Institut and Center for Integrated Quantum Science and Technology, Universität Stuttgart, Pfaffenwaldring 57, 70550 Stuttgart, Germany.

[1] C. Raman, M. Köhl, R. Onofrio, D. S. Durfee, C. E. Kuklewicz, Z. Hadzibabic, and W. Ketterle, Phys. Rev. Lett. **83**, 2502 (1999).
[2] A. P. Chikkatur, A. Görlitz, D. M. Stamper-Kurn, S. Inouye, S. Gupta, and W. Ketterle, Phys. Rev. Lett. **85**, 483 (2000).

[3] C. Ryu, M. F. Andersen, P. Cladé, V. Natarajan, K. Helmerson, and W. D. Phillips, Phys. Rev. Lett. **99**, 260401 (2007).

[4] D. E. Miller, J. K. Chin, C. A. Stan, Y. Liu, W. Setiawan, C. Sanner, and W. Ketterle, Phys. Rev. Lett. **99**, 070402 (2007).

[5] R. Desbuquois, L. Chomaz, T. Yefsah, J. Léonard, J. Beugnon, C. Weitenberg, and J. Dalibard, Nat. Phys. **8**, 645 (2012).

[6] W. Weimer, K. Morgener, V. P. Singh, J. Siegl, K. Hueck, N. Luick, L. Mathey, and H. Moritz, Phys. Rev. Lett. **114**, 095301 (2015).

[7] K. W. Madison, F. Chevy, W. Wohlleben, and J. Dalibard, Phys. Rev. Lett. **84**, 806 (2000).

[8] M. Zwierlein, J. Abo-Shaeer, A. Schirotzek, C. Schunck, and W. Ketterle, Nature (London) **435**, 1047 (2005).

[9] L. A. Sidorenkov, M. K. Tey, R. Grimm, Y.-H. Hou, L. Pitaevskii, and S. Stringari, Nature (London) **498**, 78 (2013).

[10] J. Wilks and D. Betts, *An Introduction to Liquid Helium* (Oxford Science Publications, Clarendon Press, Oxford, 1987).

[11] D. Dries, S. E. Pollack, J. M. Hitchcock, and R. G. Hulet, Phys. Rev. A **82**, 033603 (2010).

[12] I. Ferrier-Barbut, M. Delehaye, S. Laurent, A. T. Grier, M. Pierce, B. S. Rem, F. Chevy, and C. Salomon, Science **345**, 1035 (2014).

[13] T. Ozawa, A. Recati, M. Delehaye, F. Chevy, and S. Stringari, Phys. Rev. A **90**, 043608 (2014).

[14] R. Zhang, W. Zhang, H. Zhai, and P. Zhang, Phys. Rev. A **90**, 063614 (2014).

[15] X. Cui, Phys. Rev. A **90**, 041603 (2014).

[16] J. J. Kinnunen and G. M. Bruun, Phys. Rev. A **91**, 041605 (2015).

[17] M. Abad, A. Recati, S. Stringari, and F. Chevy, Eur. Phys. J. D **69**, 126 (2015).

[18] Y. Castin, I. Ferrier-Barbut, and C. Salomon, C.R. Phys. **16**, 241 (2015).

[19] W. Zheng and H. Zhai, Phys. Rev. Lett. **113**, 265304 (2014).

[20] L. Wen and J. Li, Phys. Rev. A **90**, 053621 (2014).

[21] F. Chevy, Phys. Rev. A **91**, 063606 (2015).

[22] H. Shen and W. Zheng, Phys. Rev. A **92**, 033620 (2015).

[23] A. O. Caldeira and A. J. Leggett, Physica (Amsterdam) **121A**, 587 (1983).

[24] C.-H. Chou, T. Yu, and B. L. Hu, Phys. Rev. E **77**, 011112 (2008).

[25] U. Zürcher and P. Talkner, Phys. Rev. A **42**, 3267 (1990).

[26] G. Zürn, T. Lompe, A. N. Wenz, S. Jochim, P. S. Julienne, and J. M. Hutson, Phys. Rev. Lett. **110**, 135301 (2013).

[27] See Supplemental Material at http://link.aps.org/supplemental/10.1103/PhysRevLett.115.265303 for extra comments and discussion.

[28] R. Combescot, M. Y. Kagan, and S. Stringari, Phys. Rev. A **74**, 042717 (2006).

[29] N. Navon, S. Nascimbène, F. Chevy, and C. Salomon, Science **328**, 729 (2010).

[30] G. Astrakharchik, Ph.D thesis, University of Trento, 2004, arXiv:1412.4529.

[31] S. Stringari, Phys. Rev. A **58**, 2385 (1998).

[32] P. Capuzzi, P. Vignolo, F. Federici, and M. P. Tosi, Phys. Rev. A **73**, 021603 (2006).

[33] L. Luo, B. Clancy, J. Joseph, J. Kinast, and J. E. Thomas, Phys. Rev. Lett. **98**, 080402 (2007).

[34] J. Joseph, B. Clancy, L. Luo, J. Kinast, A. Turlapov, and J. E. Thomas, Phys. Rev. Lett. **98**, 170401 (2007).

[35] V. P. Singh, W. Weimer, K. Morgener, J. Siegl, K. Hueck, N. Luick, H. Moritz, and L. Mathey, arXiv:1509.02168.

[36] C. A. Regal, M. Greiner, and D. S. Jin, Phys. Rev. Lett. **92**, 083201 (2004).

[37] W. Kohn, Phys. Rev. **123**, 1242 (1961).

[38] P. P. Orth, D. Roosen, W. Hofstetter, and K. Le Hur, Phys. Rev. B **82**, 144423 (2010).

[39] R. Onofrio and B. Sundaram, Phys. Rev. A **92**, 033422 (2015).

Universal loss dynamics in a unitary Bose gas

Ulrich Eismann, Lev Khaykovich, Sébastien Laurent, Igor Ferrier-Barbut,
Benno S. Rem, Andrew T. Grier, Marion Delehaye, Frédéric Chevy,
Christophe Salomon, Li-Chung Ha, and Cheng Chin

Physical Review X, **6**, 021025 (2016)

PHYSICAL REVIEW X **6,** 021025 (2016)

Universal Loss Dynamics in a Unitary Bose Gas

Ulrich Eismann,[1,3,*] Lev Khaykovich,[1,2] Sébastien Laurent,[1] Igor Ferrier-Barbut,[1,†] Benno S. Rem,[1,‡] Andrew T. Grier,[1,§]
Marion Delehaye,[1] Frédéric Chevy,[1] Christophe Salomon,[1] Li-Chung Ha,[3] and Cheng Chin[3]
[1]*Laboratoire Kastler Brossel, ENS-PSL Research University, CNRS, UPMC, Collège de France,*
24 rue Lhomond, 75005, Paris, France
[2]*Department of Physics, Bar-Ilan University, Ramat-Gan 52900, Israel*
[3]*James Franck Institute, Enrico Fermi Institute and Department of Physics, University of Chicago,*
Chicago, Illinois 60637, USA

(Received 29 April 2015; revised manuscript received 5 January 2016; published 20 May 2016)

The low-temperature unitary Bose gas is a fundamental paradigm in few-body and many-body physics, attracting wide theoretical and experimental interest. Here, we present experiments performed with unitary ^{133}Cs and ^{7}Li atoms in two different setups, which enable quantitative comparison of the three-body recombination rate in the low-temperature domain. We develop a theoretical model that describes the dynamic competition between two-body evaporation and three-body recombination in a harmonically trapped unitary atomic gas above the condensation temperature. We identify a universal "magic" trap depth where, within some parameter range, evaporative cooling is balanced by recombination heating and the gas temperature stays constant. Our model is developed for the usual three-dimensional evaporation regime as well as the two-dimensional evaporation case, and it fully supports our experimental findings. Combined ^{133}Cs and ^{7}Li experimental data allow investigations of loss dynamics over 2 orders of magnitude in temperature and 4 orders of magnitude in three-body loss rate. We confirm the $1/T^2$ temperature universality law. In particular, we measure, for the first time, the Efimov inelasticity parameter $\eta_* = 0.098(7)$ for the 47.8-G d-wave Feshbach resonance in ^{133}Cs. Our result supports the universal loss dynamics of trapped unitary Bose gases up to a single parameter η_*.

DOI: 10.1103/PhysRevX.6.021025 Subject Areas: Atomic and Molecular Physics

I. INTRODUCTION

Resonantly interacting Bose systems realized in ultracold atomic gases are attracting growing attention thanks to being among the most fundamental systems in nature and also among the least studied. Recent theoretical studies have included hypothetical BEC-BCS–type transitions [1–5] and, at unitarity, calculations of the universal constant connecting the total energy of the system with the only energy scale left when the scattering length diverges: $E_n = \hbar^2 n^{2/3}/m$ [6–9]. The latter assumption itself remains a hypothesis as the Efimov effect might break the continuous scaling invariance of the unitary Bose gas and introduce another relevant energy scale to the problem. A rich phase diagram of the hypothetical unitary Bose gas at finite temperature has also been predicted [10,11].

In experiments, several advances in the study of the resonantly interacting Bose gas have recently been made using the tunability of the s-wave scattering length a near a Feshbach resonance. The JILA group showed signatures of beyond-mean-field effects in two-photon Bragg spectroscopy performed on a ^{85}Rb BEC [12], and the ENS group quantitatively studied the beyond-mean-field Lee-Huang-Yang corrections to the ground-state energy of the Bose-Einstein condensate [13]. Logarithmic behavior of a strongly interacting two-dimensional (2D) superfluid was also reported by the Chicago group [14]. Experiments have also started to probe the regime of unitarity ($1/a = 0$) directly. Three-body recombination rates in the nondegenerate regime have been measured in two different species, ^{7}Li [15] and ^{39}K [16], and they clarified the temperature dependence of the unitary Bose gas lifetime. In another experiment, fast and nonadiabatic projection of the BEC on the regime of unitarity revealed the establishment of thermal quasiequilibrium on a time scale faster than inelastic losses [17].

---

[*] Corresponding author.
ueismann@gmail.com
Present address: Toptica Photonics AG, Lochhamer Schlag 19, 82166 Gräfelfing, Germany.

[†] Present address: 5. Physikalisches Institut and Center for Integrated Quantum Science and Technology, Universität Stuttgart, Pfaffenwaldring 57, 70550 Stuttgart, Germany.

[‡] Present address: Institut für Laserphysik, Universität Hamburg, Luruper Chaussee 149, Building 69, D-22761 Hamburg, Germany.

[§] Present address: Department of Physics, Columbia University, 538 West 120th Street, New York, NY 10027-5255, USA.

In a three-body recombination process, three atoms collide and form a dimer, the binding energy of which is transferred into kinetic energies of the colliding partners. The binding energy is usually larger than the trap depth and thus leads to the loss of all three atoms. Because three-body recombination occurs more frequently at the center of the trap, this process is associated with “anti-evaporative” heating (loss of atoms with small potential energy) which competes with two-body evaporation and leads to a nontrivial time dependence for the sample temperature.

In this article, we analyze the loss dynamics of ^{133}Cs and ^{7}Li unitary Bose gases prepared at various temperatures and atom numbers. We develop a theoretical model that describes these atom loss dynamics. By simultaneously taking into account two- and three-body losses, we quantitatively determine each of these contributions. Our analysis covers both the case of three-dimensional evaporation, which applies to our ^{133}Cs experimental data, and two-dimensional evaporation, which applies to the ^{7}Li data. In both cases, we find the existence of a “magic” value for the trap-depth-over-temperature ratio, where residual evaporation compensates for three-body loss heating and maintains the gas temperature constant within some range of parameters. Comparing measurements in these two atomic species, we find the dynamics to be universal; i.e., in both systems, the three-body loss rate is found to scale universally with temperature. Excellent agreement between theory and experiment confirms that the dynamic evolution of the unitary Bose gas above the condensation temperature can be well modeled by the combination of two- and three-body interaction processes.

II. EXPERIMENTS

In this section, we present experimental $T(N)$ trajectories of unitary ^{133}Cs and ^{7}Li Bose gases trapped in shallow potentials with non-negligible evaporation, where T is the cloud temperature and N the atom number. We initially prepare the samples at temperature T_{in} and atom number N_{in} in a trap of depth U, as described in Appendix A. We measure the atom numbers and the temperatures from *in situ* absorption images taken after a variable hold time t.

The ^{133}Cs Feshbach resonance at 47.8 Gauss and the ^{7}Li Feshbach resonance at 737.8 Gauss used in the experiments have very similar resonance strength parameters $s_{\mathrm{res}} = 0.67$ and 0.80, respectively [18,19], and are in the intermediate coupling regime (neither in the broad nor narrow resonance regime). We note that in the ^{133}Cs case, the dimer state giving rise to the Feshbach resonance is of d-wave nature. Both the two-body and three-body collisions happen in the s-wave channel; we therefore expect to observe universal Efimov (s-wave) physics.

In Fig. 1(a), we present typical results for the evolution $T(N)$ in the case of ^{133}Cs. We show trajectories for different initial relative trap depths $\eta_{\mathrm{in}} = U/k_{\mathrm{B}}T_{\mathrm{in}}$, where k_{B} is Boltzmann’s constant. We also plot the relative temperature

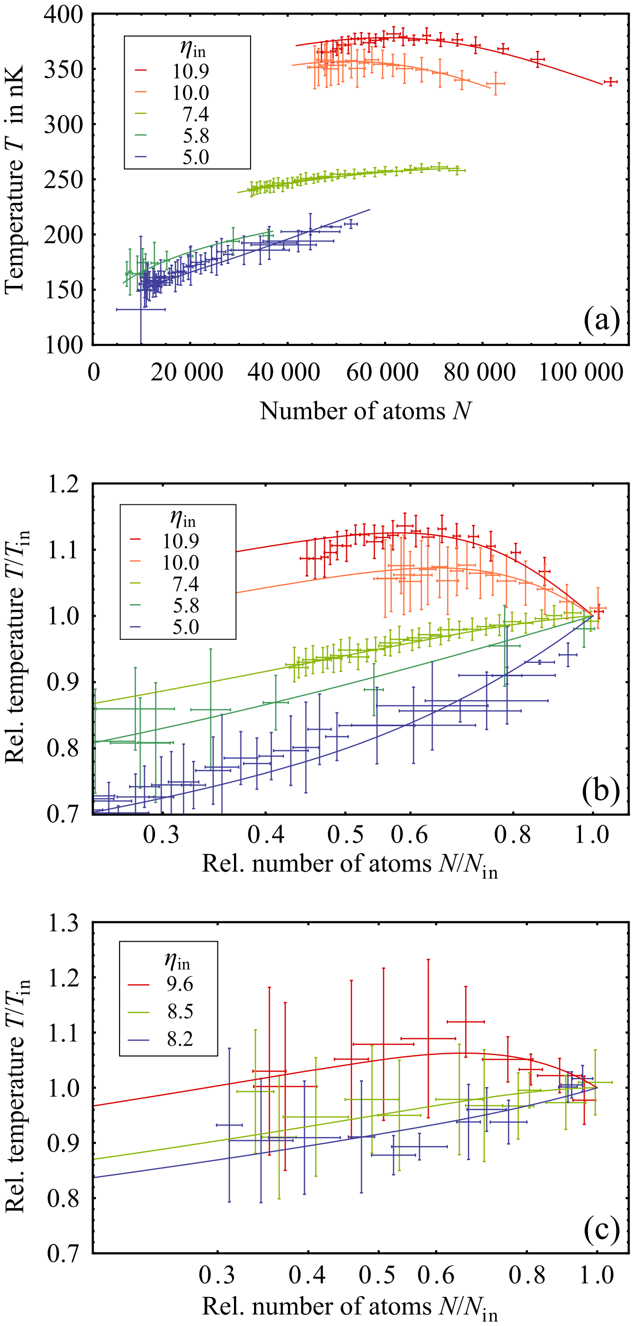

FIG. 1. Evolution of the unitary ^{133}Cs gas in (a) absolute and (b) relative numbers (points). The solid lines are fits of the data using the theory presented in Sec. III, and the fitted initial relative trap depth $\eta_{\mathrm{in}} = U/k_{\mathrm{B}}T_{\mathrm{in}}$ is given in the legend. The condition for $(\mathrm{d}T/\mathrm{d}N)|_{t=0}$ is expected for $\eta_{\mathrm{in}} \approx \eta_{\mathrm{m}} \approx 8.2$, very close to the measured data for $\eta_{\mathrm{in}} = 7.4$ [green lines in (a) and (b)]. (c) Evolution of the unitary ^{7}Li gas. The solid lines are fits of the data using our 2D evaporation model and the fitted initial relative trap depth η_{in} as in (b). In 2D evaporation, $\eta_{\mathrm{in}} \approx \eta_{\mathrm{m}}^{\mathrm{eff}} = \eta_{\mathrm{m}} + 1 = 8.5$ is required to meet the $(\mathrm{d}T/\mathrm{d}N)|_{t=0}$ condition and is found to be in good agreement with the measured value 8.5 [green line in (c)]; see text. All error bars represent 1 standard deviation.

T/T_{in} as a function of the relative atom number N/N_{in} for the same data in Fig. 1(b), and for ^{7}Li in Fig. 1(c). Each data point results from averaging about ten $\{N(t), T(t)\}$ measurements at a given t, and error bars are 1 standard deviation from the mean.

The readily observed maxima in the $T-N$ plots indicate deviation from the usually applied model for three-body recombination loss of atoms and "anti-evaporation" heating associated with it [20]. This model is valid in the limit of deep trapping potentials (trapping depth much larger than the gas temperature) and for temperature-independent losses. We show below that the additional dynamics come from the two-body evaporation due to the finite trap depth. In order to analyze the observed data quantitatively, and to correctly extract the three-body recombination loss rate constant, we now describe our theoretical model which generalizes the study [20] to arbitrary trap depths.

III. THEORETICAL MODEL

A. Rate equation for atom number

The locally defined three-body recombination rate $L_3 n^3(\mathbf{r})/3$ leads, through integration over the whole volume, to the loss rate of atoms:

$$\dot{N} = -3\int \frac{L_3 n^3(\mathbf{r})}{3}\mathrm{d}^3\mathbf{r} = -L_3\langle n^2\rangle N, \tag{1}$$

where the factor of 3 in front of the integral reflects the fact that all 3 atoms are lost per each recombination event. In the following, we neglect single-atom losses due to collisions with the background gas, and we assume that two-body inelastic collisions are forbidden, a condition that is fulfilled for atoms polarized in the absolute ground state.

An expression for the three-body recombination loss coefficient at unitarity for a nondegenerate gas has been developed in Ref. [15]. Averaged over the thermal distribution, it reads

$$L_3 = \frac{72\sqrt{3}\pi^2\hbar(1-e^{-4\eta_*})}{m k_{\text{th}}^6} \times \int_0^\infty \frac{(1-|s_{11}|^2)e^{-k^2/k_{\text{th}}^2}k\mathrm{d}k}{|1+(kR_0)^{-2is_0}e^{-2\eta_*}s_{11}|^2}, \tag{2}$$

where $k_{\text{th}} = \sqrt{mk_B T}/\hbar$, R_0 is the three-body parameter, and the Efimov inelasticity parameter η_* characterizes the strength of the short-range inelastic processes. Here, $\hbar$ is the reduced Planck's constant, and $s_0 = 1.00624$ for three identical bosons [21]. The matrix element s_{11} relates the incoming to outgoing wave amplitudes in the Efimov scattering channel and shows the emerging discrete scaling symmetry in the problem (see, for example, Ref. [22]). Details are given in the supplementary material to Ref. [15] for the calculation of $s_{11}(ka)$, where a is the scattering length and k is the relative wave number of the colliding partners. Because of its numerically small value for three identical bosons at unitarity, we can set $|s_{11}| = 0$, and L_3 is well approximated by

$$L_3 \approx \frac{\hbar^5}{m^3} 36\sqrt{3}\pi^2 \frac{1-e^{-4\eta_*}}{(k_B T)^2} = \frac{\lambda_3}{T^2}, \tag{3}$$

where λ_3 is a temperature-independent constant. Assuming a harmonic trapping potential, we directly express the average square density $\langle n^2\rangle$ through N and T. In combination with Eq. (3), Eq. (1) is represented as

$$\dot{N} = -\gamma_3 \frac{N^3}{T^5}, \tag{4}$$

where

$$\gamma_3 = \lambda_3\left(\frac{m\bar{\omega}^2}{2\sqrt{3}\pi k_B}\right)^3, \tag{5}$$

with $\bar{\omega}$ being the geometric mean of the angular frequencies in the trap.

To model the loss of atoms induced by evaporation, we consider time evolution of the phase-space density distribution of a classical gas:

$$f(\mathbf{r},\mathbf{p}) = \frac{n_0 {\lambda_{\text{dB}}}^3}{(2\pi\hbar)^3} e^{-U(\mathbf{r})/k_B T} e^{-\mathbf{p}^2/2mk_B T}, \tag{6}$$

which obeys the Boltzmann equation. Here, n_0 is the central peak density of atoms, $\lambda_{\text{dB}} = (2\pi\hbar^2/mk_B T)^{1/2}$ is the thermal de Broglie wavelength, and $U(\mathbf{r})$ is the external trapping potential. The normalization constant is fixed by the total number of atoms, such that $\int f(\mathbf{r},\mathbf{p})\mathrm{d}^3\mathbf{p}\mathrm{d}^3\mathbf{r} = N$.

If the gas is trapped in a three-dimensional (3D) trap with a potential depth U, the collision integral in the Boltzmann equation can be evaluated analytically [23]. Indeed, the low-energy collisional cross section

$$\sigma(k) = \frac{8\pi}{k^2 + a^{-2}} \tag{7}$$

reduces at unitarity to a simple dependence on the relative momentum of colliding partners: $\sigma(k) = 8\pi/k^2$. However, not every collision leads to a loss of atoms due to evaporation. Consider

$$\eta = U/k_B T. \tag{8}$$

In the case of $\eta \gg 1$, such loss is associated with a transfer of a large amount of energy to the atom, which ultimately leads to the energy-independent cross section. This can be understood with a simple argument [24]. Assume that two atoms collide with the initial momenta $\mathbf{p}_1$ and $\mathbf{p}_2$. After the collision, they emerge with the momenta $\mathbf{p}_3$ and $\mathbf{p}_4$, and if one of them acquires a momentum $|\mathbf{p}_3| \gtrsim \sqrt{2mU}$, the momentum $|\mathbf{p}_4|$ is necessarily smaller than the most probable momentum of atoms in the gas and $|\mathbf{p}_3| \gg |\mathbf{p}_4|$. In the center-of-mass coordinates, the absolute value of the relative momentum is preserved, so $\frac{1}{2}|\mathbf{p}_1 - \mathbf{p}_2| = \frac{1}{2}|\mathbf{p}_3 - \mathbf{p}_4| \approx \frac{1}{2}|\mathbf{p}_3|$. Assuming $|\mathbf{p}_3| = \sqrt{2mU}$, we get $|\mathbf{p}_1 - \mathbf{p}_2| = \sqrt{2mU}$. Substituting the relative momentum in the center-of-mass coordinate, $\hbar\mathbf{k} = \frac{1}{2}(\mathbf{p}_1 - \mathbf{p}_2)$, into the unitary form of the collisional cross section, we find that the latter is energy independent:

$$\sigma_U = \frac{16\pi\hbar^2}{mU}, \tag{9}$$

and the rate equation for the atom number can be written as

$$\dot{N} = -\Gamma_{\mathrm{ev}} N, \qquad \Gamma_{\mathrm{ev}} = n_0 \sigma_U \bar{v} e^{-\eta} \frac{V_{\mathrm{ev}}}{V_{\mathrm{e}}}. \tag{10}$$

The peak density is $n_0 = N/V_{\mathrm{e}}$, where V_{e} is the effective volume of the sample. In the harmonic trap, V_{e} can be related to $\bar{\omega}$ and the temperature T: $V_{\mathrm{e}} = (2\pi k_{\mathrm{B}} T / m\bar{\omega}^2)^{3/2}$. The ratio of the evaporative and effective volumes is defined by [23]

$$\frac{V_{\mathrm{ev}}}{V_{\mathrm{e}}} = \eta - 4(3,\eta)\,\frac{P(a+1,\eta)}{P(a,\eta)}, \tag{11}$$

where $P(a,\eta)$ is the incomplete Gamma function

$$P(a,\eta) = \frac{\int_0^\eta u^{a-1} e^{-u} \mathrm{d}u}{\int_0^\infty u^{a-1} e^{-u} \mathrm{d}u}.$$

Finally, taking into account both three-body recombination loss [see Eqs. (4) and (5)] and evaporative loss, we can express the total atom number loss rate equation as

$$\dot{N} = -\gamma_3 \frac{N^3}{T^5} - \gamma_2 e^{-\eta} \frac{V_{\mathrm{ev}}}{V_{\mathrm{e}}} \frac{N^2}{T}, \tag{12}$$

where

$$\gamma_2 = \frac{16}{\pi} \frac{\hbar^2 \bar{\omega}^3}{k_{\mathrm{B}} U}. \tag{13}$$

Note that η and the ratio of the evaporative and effective volumes explicitly depend on temperature, and γ_2 is temperature independent.

B. Rate equation for temperature

1. Anti-evaporation and recombination heating

Reference [20] points out that in each three-body recombination event, a loss of an atom is associated with an excess of $k_{\mathrm{B}} T$ of energy that remains in the sample. This mechanism is caused by the fact that recombination events occur mainly at the center of the trap, where the density of atoms is highest, and it is known as anti-evaporation heating. We now show that the unitary limit is more anti-evaporative than the regime of finite scattering lengths considered in Ref. [20], where L_3 is temperature independent. We separate center-of-mass and relative motions of the colliding atoms and express the total loss of energy per three-body recombination event as follows:

$$\dot{E}_{3\mathrm{b}} = -\int \left\{ \frac{L_3 n^3(\mathbf{r})}{3} (\langle E_{\mathrm{cm}} \rangle + 3U(\mathbf{r})) + \frac{n^3(\mathbf{r})}{3} \langle L_3(k) E_k \rangle \right\} \mathrm{d}^3\mathbf{r}. \tag{14}$$

The first two terms in parentheses represent the mean center-of-mass kinetic energy $\langle E_{\mathrm{cm}} \rangle = \langle P_{\mathrm{cm}}^2 \rangle / 2M$ and the local potential energy $3U(\mathbf{r})$ per each recombination triple. $M = 3m$ is the total mass of the three-body system. The last term stands for thermal averaging of the three-body coefficient over the relative kinetic energy $E_k = (\hbar k)^2 / 2\mu$, where μ is the reduced mass.

Averaging the kinetic energy of the center-of-mass motion over the phase-space density distribution [Eq. (6)] gives $\langle E_{\mathrm{cm}} \rangle = (3/2) k_{\mathrm{B}} T$. Then, the integration over this term is straightforward, and using Eq. (1), we have

$$-\int \frac{L_3 n^3(\mathbf{r})}{3} \langle E_{\mathrm{cm}} \rangle \mathrm{d}^3\mathbf{r} = \frac{1}{2} k_{\mathrm{B}} T \dot{N}. \tag{15}$$

The integration over the second term can be easily evaluated as well:

$$-\int \frac{3L_3}{3} n^3(\mathbf{r}) U(\mathbf{r}) \mathrm{d}^3\mathbf{r} = \frac{1}{2} k_{\mathrm{B}} T \dot{N}. \tag{16}$$

To evaluate the third term, we recall the averaged over the thermal distribution expression of the three-body recombination rate in Eq. (2). Now, its integrand has to be supplemented with the loss of the relative kinetic energy per recombination event E_k. Keeping the limit of Eq. (3), this averaging can be easily evaluated to give $\langle L_3(k) E_k \rangle = L_3 k_{\mathrm{B}} T$. Finally, the last term in Eq. (14) gives

$$-\int \frac{n^3(\mathbf{r})}{3} \langle L_3(k) E_k \rangle \mathrm{d}^3\mathbf{r} = \frac{1}{3} k_{\mathrm{B}} T \dot{N}. \tag{17}$$

Finally, getting together all the terms, the lost energy per lost atom in a three-body recombination event becomes

$$\frac{\dot{E}_{3\mathrm{b}}}{\dot{N}} = \frac{4}{3} k_{\mathrm{B}} T. \tag{18}$$

This expression shows that the unitarity limit is more anti-evaporative than the regime of finite scattering length

($k|a| \le 1$). As the mean energy per atom in the harmonic trap is $3k_\mathrm{B}T$, at unitarity each escaped atom leaves behind $(3-4/3)k_\mathrm{B}T = (5/3)k_\mathrm{B}T$ of the excess energy as compared to $1k_\mathrm{B}T$ when L_3 is energy independent. In the latter case, thermal averaging of the relative kinetic energy gives $\langle E_k \rangle = 3k_\mathrm{B}T$, and thus $\dot{E}_{3\mathrm{b}}/\dot{N} = 2k_\mathrm{B}T$.

Equation (18) is readily transformed into the rate equation for the rise of temperature per lost atom using the fact that $E_{3\mathrm{b}} = 3Nk_\mathrm{B}T$ in the harmonic trap and Eq. (4):

$$\dot{T} = \frac{5}{3}\frac{T}{3}\gamma_3\frac{N^2}{T^5}. \tag{19}$$

Another heating mechanism pointed out in Ref. [20] is associated with the creation of weakly bound dimers whose binding energy is smaller than the depth of the potential. In such a case, the three-body recombination products stay in the trap, and the binding energy is converted into heat.

In the unitary limit, this mechanism causes no heating. In fact, in this regime, as shown in the supplementary material to Ref. [15], the atoms and dimers are in chemical equilibrium with each other; e.g., the rate of dimer formation is equal to the dissociation rate. We therefore exclude this mechanism from our considerations.

2. Evaporative cooling

"Anti-evaporative" heating can be compensated by evaporative cooling. The energy loss per evaporated atom is expressed as

$$\dot{E} = \dot{N}(\eta + \tilde{\kappa})k_\mathrm{B}T, \tag{20}$$

where $\tilde{\kappa}$ in a harmonic trap is [23]

$$\tilde{\kappa} = 1 - \frac{P(5,\eta)}{P(3,\eta)}\frac{V_\mathrm{e}}{V_\mathrm{ev}}, \tag{21}$$

with $0 < \tilde{\kappa} < 1$.

In a harmonic trap, the average energy per atom is $3k_\mathrm{B}T = (E/N)$. Taking the derivative of this equation and combining it with Eq. (20), we get

$$3\frac{\dot{T}}{T} = \frac{\dot{N}}{N}(\eta + \tilde{\kappa} - 3). \tag{22}$$

From Eqs. (10) and (22), evaporative cooling is expressed as

$$\dot{T} = -\gamma_2 e^{-\eta}\frac{V_\mathrm{ev}}{V_\mathrm{e}}(\eta + \tilde{\kappa} - 3)\frac{N}{T}\frac{T}{3}, \tag{23}$$

where, as before, the temperature dependence remains in η.

Finally, combining the two processes of recombination heating [Eq. (19)] and evaporative cooling [Eq. (23)], we get

$$\dot{T} = \frac{T}{3}\left(\frac{5}{3}\gamma_3\frac{N^2}{T^5} - \gamma_2 e^{-\eta}\frac{V_\mathrm{ev}}{V_\mathrm{e}}(\eta + \tilde{\kappa} - 3)\frac{N}{T}\right). \tag{24}$$

Equations (12) and (24) form a set of coupled rate equations that describe the atom loss dynamics which we fit to our data.

C. Extension of the model to 2D evaporation

The above model was developed to explain 3D isothermal evaporation in a harmonic trap, and experiments with ^{133}Cs presented below correspond to this situation. Our model can also be extended to 2D isothermal evaporation, as realized in the ^{7}Li gas studied in Ref. [15] and presented in Fig. 1. In this setup, the atoms were trapped in a combined trap consisting of optical confinement in the radial direction and magnetic confinement in the axial direction. Evaporation was performed by lowering the laser beam power, which did not lower the axial (essentially infinite) trap depth due to the magnetic confinement. Such a scenario realizes a 2D evaporation scheme. Here, we explore the consequences of having 2D evaporation. In the experimental section, we show the validity of these results with the evolution of a unitary ^{7}Li gas.

Lower-dimensional evaporation is, in general, less efficient than its 3D counterpart. One-dimensional evaporation can be nearly totally solved analytically, and it has been an intense subject of interest in the context of evaporative cooling of magnetically trapped hydrogen atoms [23,25,26]. In contrast, analytically solving the 2D evaporation scheme is infeasible in practice. It also poses a rather difficult question considering ergodicity of motion in the trap [27]. The only practical way to treat 2D evaporation is by using Monte Carlo simulations, which were performed in Ref. [27] to describe evaporation of an atomic beam. However, as noted in Ref. [27], these simulations follow amazingly well a simple theoretical consideration, which leaves the evaporation dynamics as in 3D but introduces an "effective" η parameter to take into account its 2D character.

This consideration is as follows. In the 3D evaporation model, the cutting energy ϵ_c is introduced in the Heaviside function that is multiplied by the classical phase-space distribution of Eq. (6) [23]. For the 2D scheme, this Heaviside function is $Y(\epsilon_\mathrm{c} - \epsilon_\perp)$, where ϵ_c is the 2D truncation energy and $\epsilon_\perp$ is the radial energy of atoms in the trap, the only direction in which atoms can escape. Now, we simply add and subtract the axial energy of atoms in the trap and introduce an effective 3D truncation energy as follows:

$$Y(\epsilon_\mathrm{c} - \epsilon_\perp) = Y((\epsilon_\mathrm{c} + \epsilon_z) - (\epsilon_\perp + \epsilon_z)) = Y(\epsilon_\mathrm{c}^\mathrm{eff} - \epsilon_\mathrm{tot}), \tag{25}$$

where ϵ_tot is the total energy of atoms in the trap and the effective truncation energy is given as $\epsilon_\mathrm{c}^\mathrm{eff} = \epsilon_\mathrm{c} + \epsilon_z \simeq \epsilon_\mathrm{c} + k_\mathrm{B}T$, where we replaced ϵ_z by its mean value

$k_B T$ in a harmonic trap. The model then suggests that the evaporation dynamics follows the same functional form as the well-established 3D model, but it requires a modification of the evaporation parameter (8):

$$\eta^{\mathrm{eff}} = \eta + 1. \tag{26}$$

Then, the experimentally provided 2D η should be compared with the theoretically found 3D η^{eff} reduced by 1 (i.e., $\eta^{\mathrm{eff}} - 1$).

IV. DATA ANALYSIS

A. *N*-*T* dynamics and the magic η_m

We now perform a coupled least-squares fit of the atom number and temperature trajectories, Eqs. (12) and (24), to the data. We note that with our independent knowledge of the geometric mean of the trapping frequencies, $\bar{\omega}$, the only free fit parameters apart from initial temperature and atom number are the trap depth U and the temperature-independent loss constant λ_3. The solid lines in Fig. 1 are the fits (see Appendix D for details on the fitting) to our theory model that describe the experimental data well for a large variety of initial temperatures, atom numbers, and relative trap depth. We are able to experimentally realize the full predicted behavior of rising, falling, and constant-to-first-order temperatures.

The existence of maxima in the T-N plots indicates the existence of a "magic" relative trap depth η_m, where the first-order time derivative of the sample temperature vanishes.

The theoretical value of $\eta_m(T, N)$ is found by solving the equation $dT/dN = 0$, i.e., when $T(N)$ becomes independent on the atom number up to the first order in N. From the general structure of this equation, we see that η_m is solely a function of the dimensionless parameter:

$$\alpha = N\left(\frac{\hbar\bar{\omega}}{k_B T}\right)^3 (1 - e^{-4\eta_*}). \tag{27}$$

Up to a factor $(1 - e^{-4\eta_*})$, η_m depends only on the phase-space density $N(\hbar\bar{\omega}/k_B T)^3$ of the cloud. We plot in Fig. 2 the dependence of η_m vs α. Since our approach is valid only in the nondegenerate regime where the momentum distribution is a Gaussian, we restricted the plot to small (and experimentally relevant) values of α.

Using the knowledge of η_* for both ^{133}Cs and ^{7}Li, we can compare the observed values of η_m to the theory values of Fig. 2 (note that in the case of ^{7}Li, we plot η_m^{eff}, which enters into the effective 3D evaporation model). We see that for both the 3D evaporation ^{133}Cs data and 2D evaporation ^{7}Li data, the agreement between experiment and theory is remarkable.

Furthermore, in Appendix E, we show that from the three-body loss coefficients and the evaporation model, we can obtain the trap depth, which is found to be in good agreement with the value deduced from the laser power, beam waist, and atomic polarizability. Note that, although the theory is developed for harmonic traps, it can be applied to more complex setups (crossed dipole traps or hybrid magnetic-optical traps), where the average-energy atoms sense the harmonic part of the potential only.

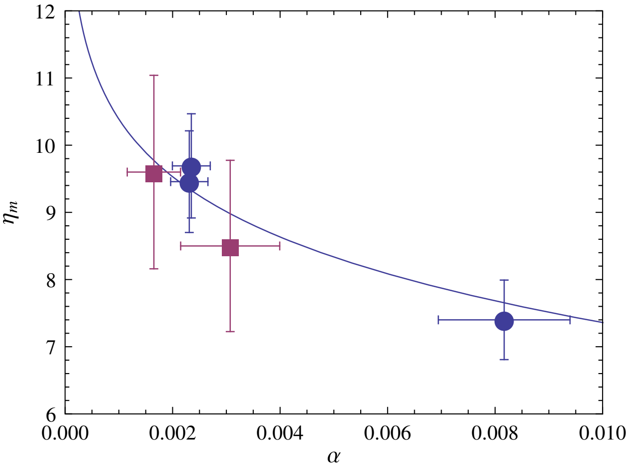

FIG. 2. "Magic" η_m as a function of the dimensionless parameter $\alpha = N(\hbar\bar{\omega}/k_B T)^3(1 - e^{-4\eta_*})$ (solid line). The blue solid circles correspond to the results obtained for ^{133}Cs in Fig. 1(a) with $\eta_* = 0.098$. The red solid squares correspond to the ^{7}Li data of Fig. 1(c) with $\eta_* = 0.21$ [28]. Error bars are statistical.

We furthermore note that in an experimental situation with a finite error bar on temperature δT, and a range of atom number $\Delta N = \max N(t) - \min N(t)$, the $(dT/dN)|_{t=0} = 0$ condition can be of less practical meaning than the weaker expression $|(dT/dN)|_{\text{finite } t}| < \delta T/\Delta N$. If the atom number spread ΔN needs to be maximized at approximately constant temperature, this second condition requires a slightly higher value than η_m given by $(dT/dN)|_{t=0} = 0$. For instance, with $\alpha = 0.002$, $\eta_m = 8.2$ and $\delta T/T_{\mathrm{in}} = 10\%$, $\eta \approx 10$ maximizes the spread in ΔN at nearly constant T.

B. Universality of the three-body loss

We now show the validity of the $L_3 \propto T^{-2}$ law for the three-body loss of unitary ^{7}Li and ^{133}Cs Bose gases. Because both species are situated at the extreme ends of the (stable) alkaline group, they have a large mass ratio of $133/7 = 19$, and the temperature range is varied over 2 orders of magnitude from 0.1 μK to 10 μK. We determine the three-body loss coefficients λ_3 from fits to decay curves such as those shown in Fig. 1. We present in Fig. 3 the results for the rate coefficient L_3, which varies over approximately 2 orders of magnitude for both species. In order to emphasize universality, the loss data are plotted as a function of $(m/m_H)^3 T_{\mathrm{in}}^2$, where m_H is the hydrogen mass. In this representation, the unitary limit for any species collapses to a single universal line [dotted line in Fig. 3, cf. Eq. (3)].

For ^{7}Li, we cover the 1–10 μK temperature range. For the temperature-independent loss coefficient, we find

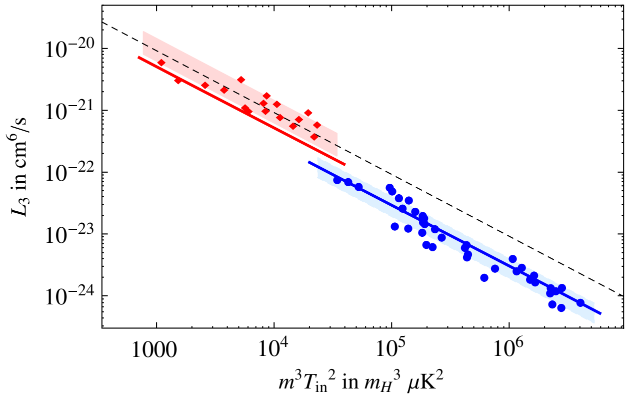

FIG. 3. The magnitude of three-body loss rate at unitarity for ^{7}Li (red) and ^{133}Cs (blue), with the respective standard deviations (shaded areas). On the horizontal axis, masses are scaled to the hydrogen atom mass m_{H}. The dashed line represents the unitary limit [Eq. (3) with $\eta_* \to \infty$]. For comparison, we show predictions of universal theory [15] with $\eta_* = 0.21$ for ^{7}Li [28] and $\eta_* = 0.098(7)$ for ^{133}Cs as solid lines (see text). The data confirm the universality of the $L_3 \propto T^{-2}$ law.

$\lambda_3 = 3.0(3) \times 10^{-20}$ cm$^6\mu$K^{2}s^{-1}, very close to the unitary limit $\lambda_3^{\max} \approx 2.7 \times 10^{-20}$ cm$^6\mu$K^{2}s^{-1}. It is also consistent with the result $\lambda_3 = 2.5(3)_{\mathrm{stat}}(6)_{\mathrm{syst}} \times 10^{-20}$ cm$^6\mu$K^{2}s^{-1} found in Ref. [15] with a restricted set of data, and to the prediction from Eq. (3) with $\eta_* = 0.21$ from Ref. [28] (red solid line in Fig. 3). Because the ^{7}Li data nearly coincide with the unitary limit, the value of η_* cannot be deduced from our measurements.

Furthermore, the quality of the ^{133}Cs temperature and atom number data enables us to directly measure the previously unknown η_* parameter of the 47.8-G Feshbach resonance. The standard technique for obtaining η_* is by measuring the three-body loss rate $L_3(a, T \to 0)$ as a function of scattering length in the zero-temperature limit and subsequently fitting the resulting spectrum to universal theory. However, for a given experimental magnetic field stability, this method is difficult to put into practice for narrow resonances like the 47.8-G resonance in ^{133}Cs. Instead, we use the fits to our theory model in order to obtain η_* from λ_3. We cover the 0.1–1 μK range and find $\lambda_3 = 1.27(7) \times 10^{-24}$ cm$^6\mu$K^{2}s^{-1}. Plugging this number into Eq. (3), we deduce a value for the Efimov inelasticity parameter $\eta_* = 0.098(7)$. The corresponding curve is the blue line in Fig. 3 and is significantly below the unitary line because of the smallness of η_*. This new value is comparable to the Efimov inelasticity parameter found for other resonances in ^{133}Cs, in the range $0.06, \ldots, 0.19$ [29,30].

The plot of the full theoretical expression Eq. (2) for $L_3(m^3 T_{\mathrm{in}}^2)$ in Fig. 3 (solid lines) requires an additional parameter describing three-body scattering around this Feshbach resonance, the so-called three-body parameter. It can be represented by the location of the first Efimov resonance position R_0 [31]. Because of the lack of experimental knowledge for the 47.8-G resonance, we take the quasiuniversal value $R_0 = -9.73(3) r_{\mathrm{vdW}}$, r_{vdW} being the van der Waals radius, for which theoretical explanations have been given recently [31–33]. The theory curve then displays log-periodic oscillations with a temperature period set by the Efimov state energy spacing of $\exp(2\pi/s_0) \approx 515$, where $s_0 = 1.00624$, and with a phase given by R_0. The relative peak-to-peak amplitude is 7% for ^{133}Cs with $\eta_* = 0.098$. As seen in Fig. 3, such oscillations cannot be resolved in the experimental data because of a limited signal-to-noise ratio and the limited range of temperature. Thus, the assumption of the quasiuniversal value of R_0 for the 47.8-G resonance, although strongly suggested by theory and experimental findings [30], remains to be proven. The predicted contrast of these oscillations for ^{7}Li with $\eta_* = 0.21$ is even smaller (about 6%). This is a general property of the system of three identical bosons due to the smallness of $|s_{11}|$ [15].

V. CONCLUSIONS

In this article, we have examined the coupled time dynamics of atom number and temperature of the 3D harmonically trapped unitary Bose gas in the nondegenerate regime. We have presented a set of experiments using lithium and cesium with vastly different mass and temperature ranges.

We have developed a general theoretical model for the dynamics observed, taking full account of evaporative loss and the related cooling mechanism, as well as of the universal three-body loss and heating. It is furthermore extended to the special case of 2D evaporation. We have theoretically obtained and experimentally verified the existence of a "magic" trap depth, where the time derivative of temperature vanishes both in 3D and 2D evaporation, and which only depends on phase-space density and the Efimov inelasticity parameter η_*. Our data illustrate the universal T^{-2} scaling over 2 orders of magnitude in temperature, and we obtained an experimental value of η_* for the 47.8-G resonance in ^{133}Cs. Furthermore, the theory enables an independent determination of the trap depth in the experiment. The agreement we have found here with standard methods shows that it can be used in more complex trap geometries, where the actual trap depth is often not easy to measure.

In future work, it would be very interesting to probe the discrete symmetry of the unitary Bose gas by revealing the 7% log-periodic modulation of the three-body loss coefficient expected over a factor 515 energy range.

ACKNOWLEDGMENTS

We would like to thank the Institut de France, the region Ile de France DIM nanoK/IFRAF (ATOMIX project), and the European Research Council ERC (ThermoDynaMix grant) for support. We acknowledge support from NSF

MRSEC (Grant No. DMR-1420709), NSF Grant No. PHY-1511696, and ARO-MURI Grant No. W911NF-14-1-0003. L. K. acknowledges the United States–Israel Binational Science Foundation (BSF) for support. L.-C. H. is supported by the Grainger Fellowship and the Taiwan Government Scholarship. We also acknowledge support from the France-Chicago Center.

U. E. and L. K. contributed equally to this work.

APPENDIX A: CESIUM SETUP

Our setup is a modified version of the one presented in Ref. [34]. The ^{133}Cs atoms are trapped by means of three intersecting laser beams, and a variable magnetic-field gradient in the vertical direction (partially) compensates gravity. An intrinsic advantage of the scheme is the perfect spin polarization in the lowest hyperfine ground state $|F, m_F\rangle = |3, 3\rangle$ because the dipole trap potential is too weak to hold atoms against gravity if they are in any other ground state. As we will see, the trap frequencies stay almost constant when reducing the trap depth, making evaporation very efficient [34].

1. Trap model

The trap consists of three 1064-nm laser beams and an additional magnetic gradient field [see Fig. 4(a)]. All beams propagate in the horizontal plane. An elliptical light sheet beam [power $P_{\mathrm{LS}} = 520$ mW, waists of $w_{\mathrm{LSv}} = 33.0\ \mu$m (vertical direction) and $w_{\mathrm{LSh}} = 225\ \mu$m (horizontal direction)] creates the vertical confinement, together with the magnetic gradient. Two round beams ($P_{\mathrm{R1,R2}} = 1.1/1.2$ W, waist of $w_{\mathrm{R}} = 300\ \mu$m) stabilize the horizontal confinement. The light sheet center is $z_0 = 6\ \mu$m lower than the center of the trap formed by the round beams only. The potential along the vertical axis can therefore be written as

$$V(z) = -U_{\mathrm{LS}} e^{-[(2z^2)/(w_{\mathrm{LSv}}^2)]} - U_{\mathrm{R}} e^{-[2(z-z_0)^2/(w_{\mathrm{R}}^2)]} + \gamma z, \tag{A1}$$

where the U_{LS} and U_{R} are the contributions from the light sheet and round beams, respectively. The tilt γ has a gravitational and a magnetic contribution,

$$\gamma = mg - \mu B', \tag{A2}$$

where m is the atomic mass, g is the gravitational acceleration, $B' = \partial_z B_z$ is the magnetic field gradient along the z axis, and $\mu = 0.75\,\mu_{\mathrm{B}}$ is the atom's magnetic moment in the $|3, 3\rangle$ state, with μ_{B} being Bohr's magnetic moment. Thus, a gradient of $B'_0 = B'(\gamma = 0) = 31.3$ G/cm is needed for magnetically levitating the cloud. An example potential shape is given in Fig. 4(b).

2. Trap frequency calibration

When we intentionally change the trap depth, we also change the trap frequencies, mostly affecting the vertical direction. The data were taken during two different measurement campaigns in 2012 and 2013. Therefore, the trap had to be recalibrated for each of these campaigns, and the data are presented in a normalized way.

We measure the oscillation frequency ω_z along the z axis as a function of the tilt [see Fig. 4(c)]. This is established by inducing sloshing oscillations to a small, weakly interacting Bose-Einstein condensate (BEC) and performing time-of-flight measurements of its position after a variable hold time.

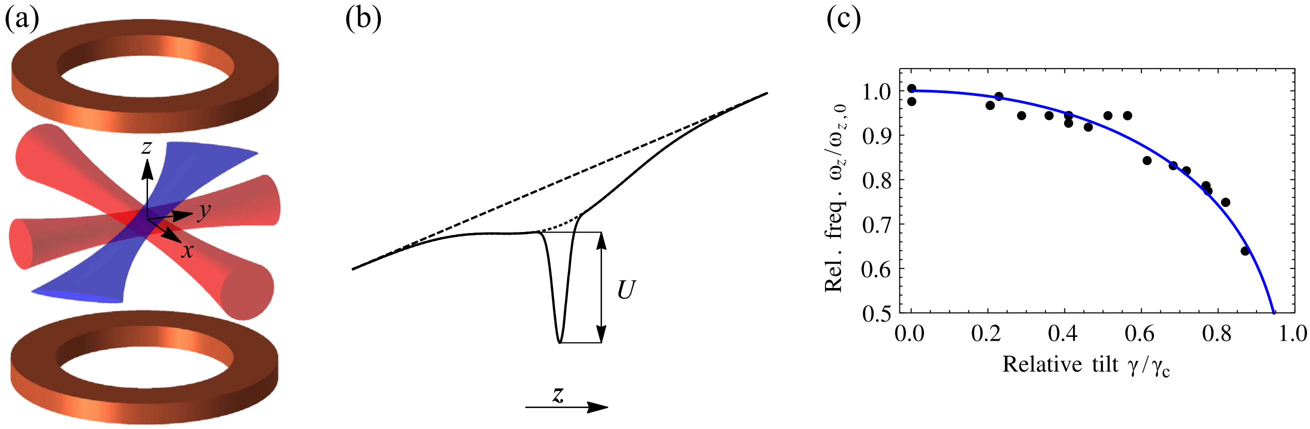

FIG. 4. (a) Schematic drawing of the hybrid trap. It consists of three intersecting lasers, and a magnetic-field gradient in the z direction (vertical) created by a pair of coils. The light sheet beam (blue) confines dominantly along the vertical direction. The additional round beams (red) stabilize the horizontal confinement. (b) Trap shape along the vertical (z) direction. It is composed of two Gaussians and a linear contribution from the tilt [see Eq. (A1)]. Relative dimensions are to scale. Also indicated are the contributions of the tilt only (dashed line) and the round beams (dotted line). (c) Trap frequency measurements (dots) and fits (line) as a function of the tilt of the trap. The frequencies are normalized with respect to the zero-tilt frequency $\omega_{z,0} = 2\pi \times 140$ Hz. We normalize the tilt from our knowledge of the critical γ_{c}, where the trap opens (see text).

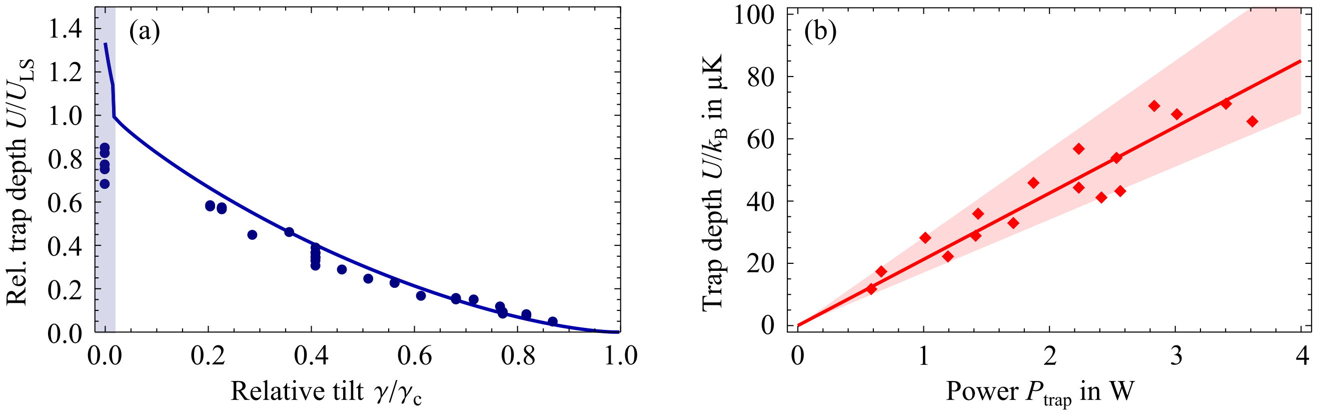

FIG. 5. (a) Relative ^{133}Cs trap-depth results from the fits to our data (dots) and theoretical model [Eqs. (A1) and (A3), line]. The trap depth is normalized with respect to the trap depth $U_{\mathrm{LS}} \approx 11\ \mu$K given by the Gaussian light sheet only. The shaded area corresponds to the region where the horizontal confinement beams significantly contribute to the trap depth. (b) Absolute ^{7}Li trap-depth results from the fits to our data (dots). The solid line indicates theoretical knowledge of our trap [Eqs. (A1) and (A3), line], with $w_R = 38(1)\ \mu$m. The shaded area accounts for the combined uncertainty of w_R and P_{trap}.

We fit the measured z-axis frequencies to a numerical model of the trap potential Eq. (A1). In the model, we insert the aspect ratio of the trap depth contributions from the three beams i,

$$U_i = \frac{2}{\pi}\frac{\alpha P_i}{w_h w_v}, \tag{A3}$$

where $\alpha/k_B = 2.589 \times 10^{-12}\ \mathrm{K cm^2\, mW^{-1}}$ is the atomic polarizability at 1064 nm [35], P_i is the power in beam i, and $w_{h/v}$ are the waists in the horizontal or vertical direction. We are left with two fit parameters: The frequency at zero tilt $\omega_z(\gamma = 0) = \omega_{z,0}$ and the critical tilt $\gamma_c = \gamma(B' = B'_c)$ where the trap opens [local minimum in $V(z)$ disappears] and ω_z goes to zero by construction. We find $\omega_{z,0} = 2\pi \times 139(1)$ Hz and $2\pi \times 140(1)$ Hz for 2012 and 2013, and $B'_c = -0.3(4)$ G/cm and $-4.3(7)$ G/cm for 2012 and 2013. With this calibration, we introduce the normalized tilt γ/γ_c. The values for B'_c coincide well with the gradient values observed when increasing the tilt until a small (< 5000 atoms) weakly interacting BEC drops out of the trap.

The kink in the trap depth theory curve (Fig. 5) near $\gamma/\gamma_c = 0.02$ [shaded area in Fig. 5(a)] corresponds to a situation depicted in Fig. 4(b), where the contribution of the large-waist horizontal beams on the trap depth vanishes. The blue-shaded region of the horizontal beams' contribution extends over the small region from $\gamma/\gamma_c = -0.02$ to 0.02. Therefore, small experimental uncertainties on the applied magnetic gradient, or additional trap imperfections, can explain the fact that we do not find this sudden rise in U. Other than that, we see a remarkable correspondence between theory and experiment.

We note that the data can also be well described by the analytical model of a single Gaussian potential ($U_R = 0$) with tilt, as presented in Ref. [34]. Because of the large mismatch between w_R and w_{LS}, the presence of the round beams mainly affects the horizontal trapping. The critical gradient we find is only 2% larger than the single-Gaussian value $\sqrt{e}\gamma w_{\mathrm{LS}}/2U_{\mathrm{LSv}}$ [34]. Furthermore, the horizontal trapping frequencies $(\omega_x, \omega_y) \approx 2\pi \times (13, 30)$ Hz, measured with a similar method for each data set, remain constant.

3. Imaging system calibration

The high-resolution imaging system is similar to the one presented in Ref. [14]. It is well calibrated using the equation of state of a weakly interacting 2D Bose gas for the absorption-coefficient-to-atomic-density conversion (in good accordance with the method of classical 2D gas atomic shot noise [36]). The imaging magnification is obtained from performing Bragg spectroscopy on a 3D BEC, using the variable retroreflection of the 1064-nm round beams.

4. ^{133}Cs sample preparation

We prepare the ^{133}Cs samples in the trap described before. In brief, after magneto-optical trapping and degenerate Raman sideband cooling, we obtain magnetically levitated ($\gamma = 0$) samples of 10^6 ^{133}Cs atoms at 1 μK [34]. We can cool the samples further by evaporative cooling. In order to achieve this, we adjust the trap depth $U(\gamma)$ by changing the tilt γ of the potential (A1). Thus, the samples can be evaporatively cooled all the way to quantum degeneracy in ≈ 2 s [34] at 20.8 G, yielding a scattering length of 200 a_0, with a_0 being the Bohr radius [29].

We prepare our samples by stopping the evaporation at a given tilt. We then ramp the tilt adiabatically to the desired value. Finally, at a time t_0, we jump the field to the Feshbach resonance at 47.8 G [18] in typically < 1 ms and wait for at least $2\pi/\omega_x$ in order for the samples to reach dynamical equilibrium. We are therefore able to prepare samples of variable initial parameters: Atom number N_{in}, temperature T_{in}, and relative trap depth $\eta_{\mathrm{in}} = U(\gamma)/k_{\mathrm{B}}T_{\mathrm{in}}$, where k_{B} is the Boltzmann constant. After a hold time t, we take an *in situ* absorption image with a vertical imaging setup.

APPENDIX B: LITHIUM SETUP

The ^{7}Li data were taken using the apparatus described in Ref. [15]. This trap consists of a 1073-nm single-beam optical dipole trap providing adjustable radial confinement, and an additional magnetic-field curvature providing essentially infinitely deep harmonic axial confinement along the beam axis. After loading into this trap, the gas is evaporated by lowering the radial trap depth at a magnetic field of 720 G, where the two-body scattering length is 200 a_0. The evaporation in this hybrid trap is then effectively 2D. After the temperature and atom number of the gas have stabilized, the radial trap is adiabatically recompressed by about a factor of 2. Since the axial magnetic confinement is practically unchanged, this recompression causes the temperature of the gas to increase with $\omega_r^{3/2}$, while the trap depth increases as ω^2. Consequently, by varying the amount of recompression, we can vary η_{in}. After this recompression, the magnetic field is ramped to the Feshbach resonance field of 737.8 G in 100–500 ms, and $N(t)$ and $T(t)$ are measured with *in situ* resonant absorption imaging perpendicular to the long axis of the cloud. The trap shape can be described by Eq. (A1) with $U_{\mathrm{LS}} = 0$, $w_{\mathrm{R}} = 37(1)$ μm, and by replacing z by ρ, the radial coordinate. U_{R} is the dipole trap potential with power P_{trap}, and α is the polarizability of the ^{7}Li atoms at 1073 nm. We can neglect the tilt γ because of the small mass of ^{7}Li.

APPENDIX C: TIME SCALE ORDER

In order for the theory to be valid, we make sure the time-scale order is not violated:

$$\tau_{3\mathrm{B}}, \tau_{\mathrm{ev}} \gg \tau_{\mathrm{trap}}, \tau_{2\mathrm{B}}, \tag{C1}$$

where we have the three-body loss time constant [cf. Eq. (19)]

$$\tau_{3\mathrm{B}}^{-1} = \frac{5}{9}\gamma_3 \frac{N^2}{T^5}, \tag{C2}$$

the evaporation time constant [cf. Eq. (24)]

$$\tau_{\mathrm{ev}}^{-1} = \frac{1}{3}\gamma_2 \left(e^{-\eta}\frac{V_{\mathrm{ev}}}{V_{\mathrm{e}}}\right)(\eta + \tilde{\kappa} - 3)\frac{N}{T}, \tag{C3}$$

the two-body scattering time constant

$$\tau_{2\mathrm{B}}^{-1} = n_0 \sigma_U \bar{v}, \tag{C4}$$

and the trapping time constant

$$\tau_{\mathrm{trap}}^{-1} = \omega_{\mathrm{slow}}, \tag{C5}$$

where ω_{slow} is the slowest trapping frequency (along z in the ^{133}Cs case).

APPENDIX D: FITS TO THE MODEL

For each data set, we have decay data for $N(t)$ and $T(t)$ from the mean values of ≈10 individual measurements. The error bars from Figs. 3(a)–3(c) are the 1σ standard deviations of the individual measurements. We fit both temperature and atom number individually with solutions to the coupled differential equation set of Eqs. (12) and (24). For both fits, we use a common three-body loss coefficient λ_3 and a common trap depth U. The fitting is done by minimizing the weighted sum $\alpha\chi_T + \alpha^{-1}\chi_N$ by varying both the weighing factor α and the fit parameters. The quadratic deviations are defined as $\chi_{T,N} = \Sigma\sigma_{T,N}^2$ ($\sigma_{T,N}$ being the deviations of data and the fit). This method also accounts for the different amount of relative signal-to-noise ratio of both data sets.

APPENDIX E: TRAP DEPTH

As an independent test of the theory fits, we compare the fitted trap depth U to its independently known counterpart from experimental parameters. In Fig. 5(a), we plot the ^{133}Cs results as a function of the relative trap tilt $\gamma/\gamma_{\mathrm{c}}$. We also plot the theoretical value for $U(\gamma/\gamma_{\mathrm{c}})$ as a solid line. Except near zero tilt, we find excellent agreement of the fitted values with the values known from experimental parameters. For ^{7}Li [see Fig. 5(b)], we find excellent agreement with our theoretical knowledge of the trap depth, which is given by the dipole laser waist w_{R}, power P_{trap}, and the atom's polarizability. It is indicated by the shaded area in Fig. 5(b). Therefore, we can infer the dipole trap laser's waist in an independent fashion. From the fit to our measured trap depths (solid line) in Fig. 5(b), we obtain $w_{\mathrm{R}} = 38(1)$ μm. This value coincides with independent measurements of w_{R} from fitting the trap frequencies as a function of P_{trap}. These results emphasize the validity of the theory model [Eqs. (12) and (24)].

[1] Y.-W. Lee and Y.-L. Lee, *Quantum Phase Transition in an Atomic Bose Gas near a Feshbach Resonance*, Phys. Rev. B **70**, 224506 (2004).

[2] M. W. J. Romans, R. A. Duine, S. Sashdev, and H. T. C. Stoof, *Quantum Phase Transition in an Atomic Bose Gas with a Feshbach Resonance*, Phys. Rev. Lett. **93**, 020405 (2004).

[3] L. Radzihovsky, P. B. Weichmann, and J. I. Park, *Superfluidity and Phase Transitions in a Resonant Bose Gas*, Ann. Phys. (Amsterdam) **323**, 2376 (2008).

[4] A. Koetsier, P. Massignan, R. A. Duine, and H. T. C. Stoof, *Strongly Interacting Bose Gas: Nosiéres and Schmitt-Rink Theory and Beyond*, Phys. Rev. A **79**, 063609 (2009).

[5] F. Cooper, C.-C. Chien, B. Mihaila, J. F. Dawson, and E. Timmermans, *Non-Perturbative Predictions for Cold Atom Bose Gases with Tunable Interactions*, Phys. Rev. Lett. **105**, 240402 (2010).

[6] S. Cowell, H. Heiselberg, I. E. Mazets, J. Morales, V. R. Pandharipande, and C. J. Pethick, *Cold Bose Gases with Large Scattering Length*, Phys. Rev. Lett. **88**, 210403 (2002).

[7] J. L. Song and F. Zhou, *Ground State Properties of Cold Bosonic Atoms at Large Scattering Lengths*, Phys. Rev. Lett. **103**, 025302 (2009).

[8] Y.-L. Lee and Y.-W. Lee, *Universality and Stability for a Dilute Bose Gas with a Feshbach Resonance*, Phys. Rev. A **81**, 063613 (2010).

[9] J. M. Diederix, T. C. F. van Heijst, and H. T. C. Stoof, *Ground State of a Resonantly Interacting Bose Gas*, Phys. Rev. A **84**, 033618 (2011).

[10] W. Li and T.-L. Ho, *Bose Gases near Unitarity*, Phys. Rev. Lett. **108**, 195301 (2012).

[11] S. Piatecki and W. Krauth, *Efimov-Driven Phase Transitions of the Unitary Bose Gas*, Nat. Commun. **5**, 3503 (2014).

[12] S. B. Papp, J. M. Pino, R. J. Wild, S. Ronen, C. E. Wiemann, D. S. Jin, and E. A. Cornell, *Bragg Spectroscopy of a Strongly Interacting* ^{85}Rb *Bose-Einstein Condensate*, Phys. Rev. Lett. **101**, 135301 (2008).

[13] N. Navon, S. Piatecki, K. Günter, B. Rem, T. C. Nguyen, F. Chevy, W. Krauth, and C. Salomon, *Dynamics and Thermodynamics of the Low-Temperature Strongly Interacting Bose Gas*, Phys. Rev. Lett. **107**, 135301 (2011).

[14] L.-C. Ha, C.-L. Hung, X. Zhang, U. Eismann, S.-K. Tung, and C. Chin, *Strongly Interacting Two-Dimensional Bose Gases*, Phys. Rev. Lett. **110**, 145302 (2013).

[15] B. Rem, A. T. Grier, I. Ferrier-Barbut, U. Eismann, T. Langen, N. Navon, L. Khaykovich, F. Werner, D. S. Petrov, F. Chevy, and C. Salomon, *Lifetime of the Bose Gas with Resonant Interactions*, Phys. Rev. Lett. **110**, 163202 (2013).

[16] R. J. Fletcher, A. L. Gaunt, N. Navon, R. P. Smith, and Z. Hadzibabic, *Stability of a Unitary Bose Gas*, Phys. Rev. Lett. **111**, 125303 (2013).

[17] P. Makotyn, C. E. Klauss, D. L. Goldberg, E. A. Cornell, and D. S. Jin, *Universal Dynamics of a Degenerate Unitary Bose Gas*, Nat. Phys. **10**, 116 (2014).

[18] A. D. Lange, K. Pilch, A. Prantner, F. Ferlaino, B. Engeser, H.-C. Nägerl, R. Grimm, and C. Chin, *Determination of Atomic Scattering Lengths from Measurements of Molecular Binding Energies near Feshbach Resonances*, Phys. Rev. A **79**, 013622 (2009).

[19] C. Chin, R. Grimm, P. Julienne, and E. Tiesinga, Rev. Mod. Phys. **82**, 1225 (2010).

[20] T. Weber, J. Herbig, M. Mark, H.-C. Nägerl, and R. Grimm, *Three-Body Recombination at Large Scattering Lengths in an Ultracold Atomic Gas*, Phys. Rev. Lett. **91**, 123201 (2003).

[21] V. Efimov, *Energy Levels Arising from Resonant Two-Body Forces in a Three-Body System*, Phys. Lett. B **33**, 563 (1970).

[22] S.-K. Tung, K. Jiménez-García, J. Johansen, C. V. Parker, and C. Chin, Phys. Rev. Lett. **113**, 240402 (2014).

[23] O. J. Luiten, M. W. Reynolds, and J. T. M. Walraven, *Kinetic Theory of the Evaporative Cooling of a Trapped Gas*, Phys. Rev. A **53**, 381 (1996).

[24] L. Luo, B. Clancy, J. Joseph, J. Kinast, A. Turlapov, and J. E. Thomas, New J. Phys. **8**, 213 (2006).

[25] E. L. Surkov, J. T. M. Walraven, and G. V. Shlyapnikov, *Collisionless Motion and Evaporative Cooling of Atoms in Magnetic Traps*, Phys. Rev. A **53**, 3403 (1996).

[26] P. W. H. Pinkse, A. Mosk, M. Weidemüller, M. W. Reynolds, T. W. Hijmans, and J. T. M. Walraven, *One-Dimensional Evaporative Cooling of Magnetically Trapped Atomic Hydrogen*, Phys. Rev. A **57**, 4747 (1998).

[27] E. Mandonnet, A. Minguzzi, R. Dum, I. Carusotto, Y. Castin, and J. Dalibard, *Evaporative Cooling of an Atomic Beam*, Eur. Phys. J. D **10**, 9 (2000).

[28] N. Gross, Z. Shotan, S. J. J. M. F. Kokkelmans, and L. Khaykovich, *Nuclear-Spin-Independent Short-Range Three-Body Physics in Ultracold Atoms*, Phys. Rev. Lett. **105**, 103203 (2010).

[29] T. Kraemer, M. Mark, P. Waldburger, J. G. Danzl, C. Chin, B. Engeser, A. D. Lange, K. Pilch, A. Jaakkola, H.-C. Nägerl, and R. Grimm, *Evidence for Efimov Quantum States in an Ultracold Gas of Caesium Atoms*, Nature **440**, 315 (2006).

[30] M. Berninger, A. Zenesini, B. Huang, W. Harm, H.-C. Nägerl, F. Ferlaino, R. Grimm, P. S. Julienne, and J. M. Hutson, *Universality of the Three-Body Parameter for Efimov States in Ultracold Cesium*, Phys. Rev. Lett. **107**, 120401 (2011).

[31] C. Chin, *Universal Scaling of Efimov Resonance Positions in Cold Atom Systems*. arXiv:1111.1484.

[32] J. Wang, J. P. D'Incao, B. D. Esry, and C. H. Greene, *Origin of the Three-Body Parameter Universality in Efimov Physics*, Phys. Rev. Lett. **108**, 263001 (2012).

[33] P. Naidon, S. Endo, and M. Ueda, *Microscopic Origin and Universality Classes of the Efimov Three-Body Parameter*, Phys. Rev. Lett. **112**, 105301 (2014).

[34] C.-L. Hung, X. Zhang, N. Gemelke, and C. Chin, *Accelerating Evaporative Cooling of Atoms into Bose-Einstein Condensation in Optical Traps*, Phys. Rev. A **78**, 011604 (2008).

[35] C.-L. Hung (private communication).

[36] C.-L. Hung, X. Zhang, L.-C. Ha, S.-K. Tung, N. Gemelke, and C. Chin, *Extracting Density–Density Correlations from In Situ Images of Atomic Quantum Gases*, New J. Phys. **13**, 075019 (2011).

Connecting few-body inelastic decay to quantum correlations in a many-body system: a weakly coupled impurity in a resonant Fermi gas

Sébastien Laurent, Matthieu Pierce, Marion Delehaye, Tarik Yefsah,
Frédéric Chevy, and Christophe Salomon

Physical Review Letters, **118**, 103403 (2017)

Connecting Few-Body Inelastic Decay to Quantum Correlations in a Many-Body System: A Weakly Coupled Impurity in a Resonant Fermi Gas

Sébastien Laurent,[*] Matthieu Pierce, Marion Delehaye,[†] Tarik Yefsah, Frédéric Chevy, and Christophe Salomon
Laboratoire Kastler Brossel, ENS-PSL Research University, CNRS, UPMC-Sorbonne Universités,
Collège de France, 24 rue Lhomond, 75005 Paris, France

(Received 22 December 2016; published 10 March 2017)

We study three-body recombination in an ultracold Bose-Fermi mixture. We first show theoretically that, for weak interspecies coupling, the loss rate is proportional to Tan's contact. Second, using a ^{7}Li/^{6}Li mixture we probe the recombination rate in both the thermal and dual superfluid regimes. We find excellent agreement with our model in the BEC-BCS crossover. At unitarity where the fermion-fermion scattering length diverges, we show that the loss rate is proportional to $n_f^{4/3}$, where n_f is the fermionic density. This unusual exponent signals nontrivial two-body correlations in the system. Our results demonstrate that few-body losses can be used as a quantitative probe of quantum correlations in many-body ensembles.

DOI: 10.1103/PhysRevLett.118.103403

Understanding strongly correlated quantum many-body systems is one of the most daunting challenges in modern physics. Thanks to a high degree of control and tunability, quantum gases have emerged as a versatile platform for the exploration of a broad variety of many-body phenomena [1], such as the crossover from Bose-Einstein condensation (BEC) to Bardeen-Cooper-Schrieffer (BCS) superfluidity [2], quantum magnetism [3], or many-body localization [4]. At ultralow temperatures, atomic vapors are metastable systems and are plagued by three-body recombination which represents a severe limitation for the study of some dense interacting systems. A prominent example is the strongly correlated Bose gas [5,6] that bears the prospect of bridging the gap between dilute quantum gases and liquid helium. However, inelastic losses can also be turned into an advantage. For instance, they can be used to control the state of a system through the Zeno effect [7–9], or serve as a probe of nontrivial few-body states, as demonstrated by the observation of Efimov trimers, originally predicted in nuclear physics, but observed for the first time in Bose gases as resonances in three-body loss spectra [10].

In this Letter, we study inelastic losses in a mixture of spinless bosons and spin $1/2$ fermions with tunable interaction. We show that when the Bose-Fermi coupling is weak, the loss rate can be related to the fermionic contact parameter, a universal quantity overarching between microscopic and macroscopic properties of a many-body system with zero-range interactions [11–19]. We first check our prediction on the strongly attractive side of the fermionic Feshbach resonance, where we recover known results on atom-dimer inelastic scattering. We then turn to the unitary limit where the fermion-fermion scattering length is infinite. We demonstrate both theoretically and experimentally—with a ^{6}Li/^{7}Li Fermi-Bose mixture—that the bosons decay at a rate proportional to $n_f^{4/3}$, where n_f is the fermion density. The unusual fractional exponent results from nontrivial quantum correlations in the resonant gas. Our method offers a new way to measure the two-body contact of the homogeneous Fermi gas. More generally, our work shows that the decay of an impurity immersed in a strongly correlated many-body system is a quantitative probe of its quantum correlations.

Inelastic decay of an impurity inside a two-component Fermi gas has been studied previously both in the weakly

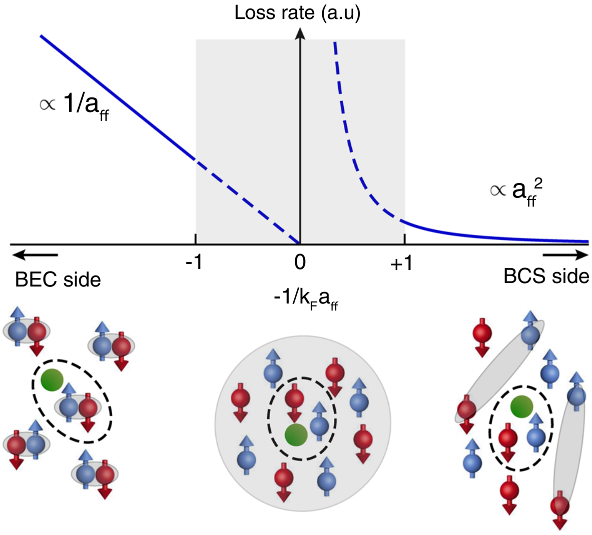

FIG. 1. Sketch of inelastic decay of an impurity immersed in a tunable Fermi gas. On the BEC side, ↑ and ↓ fermions are paired in tightly bound molecules and the decay mechanism is a two-body process involving the impurity (green disk) and a molecule. The loss rate scales as $1/a_{ff}$ [20,24]. On the BCS side, the loss occurs through a three-body process and it scales as a_{ff}^2 in the mean-field limit [20]. The extrapolation of these two asymptotic behaviors towards the strongly correlated regime yields contradictory results (grey area).

TABLE I. Scaling of the boson-fermion mixture loss rate and of Tan's contact [11], C_2, in the BEC-BCS crossover. Both scalings are identical in the weakly and strongly attractive limits. As $k_F = (3\pi^2 n_f)^{1/3}$, at unitarity C_2 scales as $n_f^{4/3}$. ζ is a dimensionless constant, $\zeta = 0.87(3)$ [17,25].

	BEC	Unitary	BCS
$(\dot{n}_b/n_b)$	$\propto (n_m/a_{ff})$ [20]	$\propto n_f^{4/3}$	$\propto a_{ff}^2 n_f^2$ [20]
C_2	$8\pi(n_m/a_{ff})$	$(2\zeta/5\pi)k_F^4$	$4\pi^2 a_{ff}^2 n_f^2$

and strongly attractive limits of the BEC-BCS crossover [20–23], see Fig. 1 and Table I. When the fermion-fermion interaction is weak, the fermions behave almost as isolated particles and the recombination can be described as a three-body process involving one spin-up (↑), one spin-down (↓) fermion and the impurity (a boson in our experiments). In this case, the impurity or boson density n_b follows a rate equation $\dot{n}_b = -L_3 n_f^2 n_b$, with $L_3 \propto a_{ff}^2$, where a_{ff} is the fermion-fermion scattering length [20,22,24]. In contrast, on the strongly attractive side of the Feshbach resonance, the fermions form halo dimers of size $\simeq a_{ff}$ and the relaxation occurs through two-body processes between one such molecule and one boson. In this case the rate equation for bosons reads $\dot{n}_b = -L_2 n_m n_b$, where $n_m = n_f/2$ is the molecule density. Far from the Feshbach resonance, the two-body loss rate scales as $1/a_{ff}$ as a consequence of the enhanced overlap of the halo dimer wave function with the deeply bound product molecules [20,24]. However, these two scalings give rise to a paradox in the central region of the BEC-BCS crossover. Indeed, as depicted in Fig. 1, the extrapolation towards unitarity leads to contradictory results depending on whether we approach the resonance from the BEC or the BCS side. In the former case, one would predict an increasingly long lifetime at unitarity while it tends to a vanishingly small value in the latter case. This paradox has a fundamental origin: these two scalings are obtained in the dilute limit where the recombination can be described by a well-defined few-body process, whereas this hypothesis fails in the strongly correlated regime where $n_f|a_{ff}|^3 \gg 1$. There, it is not possible to single out two fermions from the whole many-body system. Instead, the inelastic loss involving a boson and two fermions is tied to the correlations of the whole ensemble. A first hint towards reconciling these two behaviors near unitarity is to assume that they saturate for $a_{ff} \simeq n_f^{-1/3}$, yielding the same scaling $\dot{n}_b \propto n_f^{4/3} n_b$.

The three asymptotic regimes—BEC, BCS, and unitary—were obtained using different theoretical approaches and we now show that, using Tan's contact, they can be unified within the same framework. The recombination rate is proportional to the probability of having the three particles within a distance b from each other, where b is the typical size of the deeply bound molecule formed during the collision [26–28]. Take $\rho_3(\boldsymbol{r}_\uparrow, \boldsymbol{r}_\downarrow, \boldsymbol{r}_b)$ the three-body probability distribution of the system. When the bosons are weakly coupled to the fermions, we can factor it as $\rho_3(\boldsymbol{r}_\uparrow, \boldsymbol{r}_\downarrow, \boldsymbol{r}_b) = \rho_f(\boldsymbol{r}_\uparrow, \boldsymbol{r}_\downarrow)\rho_b(\boldsymbol{r}_b)$. Integrating over the positions of the three atoms we readily see that the three-body loss rate is proportional to Tan's contact parameter C_2 of the fermions that gives the probability of having two fermions close to each other [11]. C_2 is calculated using the equation of state of the system thanks to the adiabatic-sweep theorem

$$C_2 = -\frac{4\pi m_f}{\hbar^2}\frac{\partial F}{\partial(1/a_{ff})}, \tag{1}$$

where m_f is the fermion mass and F is the free-energy of the fermionic gas per unit-volume [12,13]. The asymptotic expressions of C_2 in the BEC, BCS and unitary regimes are listed in Table I. In the deep BEC limit, the free energy is dominated by the binding energy of the molecules $\hbar^2/m_f a_{ff}^2$; in the BCS regime C_2 is derived using the mean-field approximation [11]. At unitary, the expression of the contact stems from the absence of any length scale other than the interparticle distance. The dimensionless parameter $\zeta = 0.87(3)$ was determined both theoretically [29] and experimentally [14–19]. Expressions listed in Table I confirm that the contact parameter and the bosonic loss rate follow the same scalings with density and scattering length.

We support this relationship between inelastic losses and Tan's contact by considering a microscopic model where the recombination is described by a three-body Hamiltonian

$$\begin{aligned}\hat{H}_3 = \int & d^3\boldsymbol{r}_b d^3\boldsymbol{r}_\uparrow d^3\boldsymbol{r}_\downarrow g(\boldsymbol{r}_b, \boldsymbol{r}_\uparrow, \boldsymbol{r}_\downarrow) \\ & \times \hat{\Psi}_m^\dagger\left(\frac{\boldsymbol{r}_\uparrow + \boldsymbol{r}_\downarrow}{2}\right)\hat{\Psi}_b^\dagger(\boldsymbol{r}_b)\hat{\Psi}_b(\boldsymbol{r}_b)\hat{\Psi}_\uparrow(\boldsymbol{r}_\uparrow)\hat{\Psi}_\downarrow(\boldsymbol{r}_\downarrow) \\ & + \mathrm{H.c.},\end{aligned} \tag{2}$$

where $\hat{\Psi}_\alpha$ is the field operator for the species α and the coupling g takes significant values only when the three particles are within a distance b [30]. Assuming that b is the smallest distance scale in the problem and that this Hamiltonian can be treated within Born's approximation we find that (see Ref. [31])

$$\dot{n}_b = -\gamma C_2 n_b. \tag{3}$$

The constant γ depends on the coupling g and describes the coupling to deeply bound nonresonant states; hence, γ has essentially no variation with the magnetic field across the fermionic Feshbach resonance.

Equation (3) is the main prediction of this Letter and we explore the consequences of this equation by measuring the lifetime of an ultracold Fermi-Bose mixture of ^{6}Li and ^{7}Li atoms. Our experimental setup is described in Ref. [37].

The ^{6}Li atoms are prepared in a spin mixture ↑, ↓ of $|F = 1/2, m_F = \pm 1/2\rangle$ for which there is a broad Feshbach resonance at 832 G [33]. The ^{7}Li atoms are transferred into the $|F = 1, m_F = 0\rangle$ featuring two Feshbach resonances, a narrow one at 845.5 G and a broad one at 893.7 G [31]. The scattering length between bosons and fermions is $a_{\rm bf} = 40.8a_0$ and is equal for the ↑, ↓ states. It can be considered constant in the magnetic field range that we explored, 680–832 G. The atoms are confined in a hybrid magnetic-optical trap and are evaporated at the ^{6}Li Feshbach resonance until we reach dual superfluidity or any target temperature. We ramp the magnetic field to an adjustable value in 200 ms and wait for a variable time t. We then measure the atom numbers of the two species by *in situ* imaging or after time of flight.

We first show that the dominant boson loss mechanism on the BEC side of the resonance involves one boson, one fermion ↑, and one fermion ↓. This is easily done by comparing the boson losses for spin-balanced and spin-polarized fermionic samples. Figure 2 displays the remaining fraction of bosons and fermions after a waiting time of 1 s for balanced fermions and 1.5 s for spin-polarized fermions with 90% polarization. We observe that the losses for high spin polarization are strongly suppressed indicating that fermions of both spin components are required to eliminate one boson.

Second we show that the losses in the weakly interacting regime $na_{ff}^3 \ll 1$ (deep BEC side of the resonance, 720 G) are proportional to the fraction of molecules in the sample, $\eta = 2N_m/(N_f + 2N_m)$. This fraction is varied by changing the temperature from 1 μK to 4 μK and ^{6}Li densities from 2×10^{12} cm^{-3} to 1.0×10^{13} cm^{-3}. In these temperature and density ranges, both gases are well described by Maxwell-Boltzmann position and velocity distributions. The molecular fraction is calculated using the law of mass action [31,36] and is assumed to be time independent owing to the high formation rate of halo dimers $(\simeq \hbar a_{ff}^4/m_f)$[38]. We extract the interspecies decay rate by fitting the time evolution of the bosonic population

$$\dot{N}_b = -L_{\rm bf}\langle n_f\rangle N_b - \Gamma_v N_b, \tag{4}$$

where $\langle \cdots \rangle$ represents the trap average, and Γ_v is the one-body residual gas loss rate (0.015 s^{-1}).

The data in Fig. 3(a) show that the boson loss rate is proportional to the molecule fraction of the fermionic cloud. Introducing the boson-fermion dimer molecule loss rate $L_{\rm bm}$ defined by $L_{\rm bm}\langle n_m\rangle = L_{\rm bf}\langle n_f\rangle$, we check the proportionality of $L_{\rm bm}$ with $1/a_{ff}$ predicted in Table I by

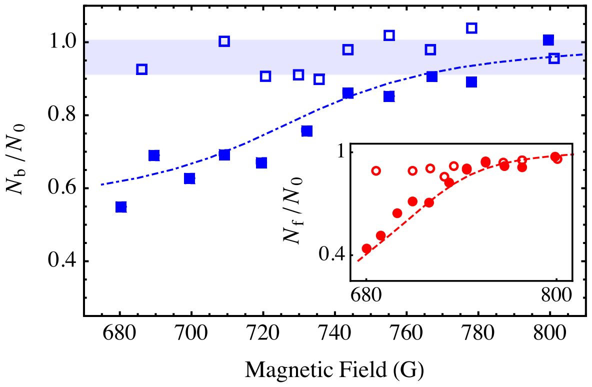

FIG. 2. Remaining fraction of bosons (blue symbols) and fermions (red symbols, inset) after a 1 s and 1.5 s waiting time for spin-balanced (filled symbols), resp. 90% polarized (open symbols) fermions. The blue dash-dotted (red dashed, inset) curve is a coupled loss model describing the competition between boson fermion-dimer decay ($\propto 1/a_{ff}$) and dimer-dimer decay ($\propto 1/a_{ff}^{2.55}$) [27,31]. The blue-shaded area represents the 1σ fluctuations for the remaining fraction of bosons with spin-polarized fermions. The initial atom numbers are 3×10^5 for ^{6}Li and 1.5×10^5 for ^{7}Li at a temperature $T \simeq 1.6$ μK with trap frequencies $\nu_z = 26$ Hz and $\nu_r = 2.0$ kHz.

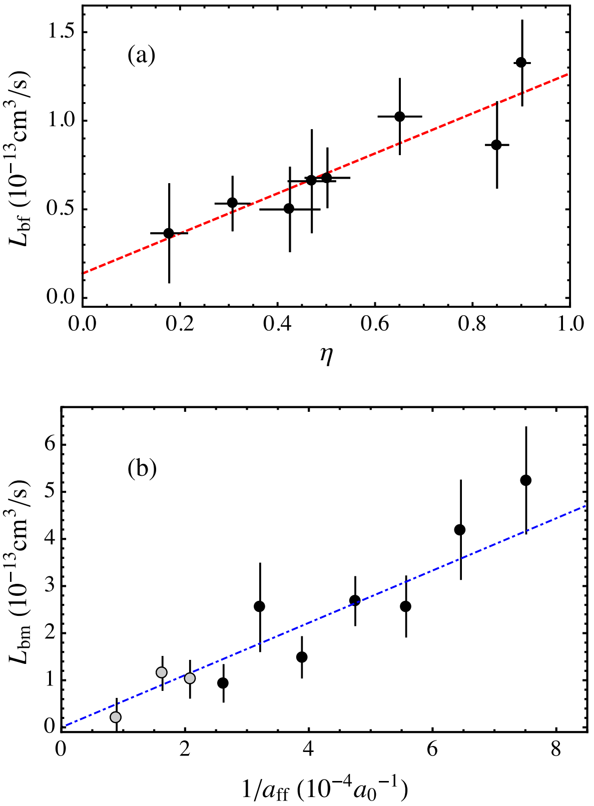

FIG. 3. (a) Boson-fermion loss rate vs molecule fraction. Circles: Experimental data. The vertical error bars represent the statistical errors for $L_{\rm bf}$ from fitting the loss curves. The horizontal error bars represent the statistical errors on the molecule fraction due to ^{6}Li number fluctuations. The red dashed line is a linear fit to the data. (b) Boson-dimer loss rate vs inverse scattering length. The blue dot-dashed line is a linear fit to the data with $n_f a_{ff}^3 \le 0.025$ (black circles), providing $\gamma = 1.17(11) \times 10^{-27}$ m$^4 \cdot$s^{-1}, see Eq. (3).

repeating the loss measurements for different magnetic fields in the interval 690–800 G, see Fig. 3(b). From a linear fit to the data where interaction effects are negligible ($n_f a_{ff}^3 \leq 0.025$), we extract the slope $\gamma = 1.17(11) \times 10^{-27}\ \mathrm{m}^4 \cdot \mathrm{s}^{-1}$ entering in Eq. (3).

Since γ doesn't depend on the magnetic field, we can now predict the loss rate anywhere in the BEC-BCS crossover using Eq. (3). The strongly interacting unitary regime ($1/a_{ff} = 0$) is particularly interesting and we measure the boson decay rate at 832 G in the low temperature dual superfluid regime [37]. The mixture is initially composed of about 40×10^3 fully condensed ^{7}Li bosons and 150×10^3 ^{6}Li spin-balanced fermions at a temperature $\mathrm{T} \simeq 100$ nK which corresponds to $T/T_\mathrm{F} \simeq 0.1$ where T_F is the Fermi temperature. At this magnetic field value, the atoms are now closer to the boson Feshbach resonance located at 845.5 G and bosonic three-body losses are no longer negligible. The time dependence of the boson number is then given by

$$\dot{N}_b = -L_b \langle n_b^2 \rangle N_b - \Gamma_{\mathrm{bf}} N_b - \Gamma_v N_b. \qquad (5)$$

To extract Γ_{bf} we measure independently L_b with a BEC without fermions in the same trap and inject it in Eq. (5), see Ref. [31]. We typically have $L_b \langle n_b^2 \rangle = 0.1\text{–}0.4\ \mathrm{s}^{-1}$, and $L_b = 0.11(1) \times 10^{26}\ \mathrm{cm}^6 \cdot \mathrm{s}^{-1}$ consistent with the model of Ref. [35]. Repeating such measurements for different fermion numbers and trap confinement, we now test the expected $n_f^{4/3}$ dependence of the Bose-Fermi loss rate at unitarity (central column in Table I). In this dual superfluid regime, the size of the BEC is much smaller than that of the fermionic superfluid and the BEC will mainly probe the central density region $n_f(r = 0)$. However, it is not truly a pointlike probe, and introducing the ratio ρ of the Thomas-Fermi radii for bosons and fermions, we obtain the finite size correction for Eq. (3) [31]:

$$\Gamma_{\mathrm{bf}} = \gamma C_2(0) \left(1 - \frac{6}{7}\rho^2\right), \qquad (6)$$

where $C_2(0) = (2\zeta/5\pi)(3\pi^2 n_f(0))^{4/3}$, and the last factor in parenthesis amounts to 0.9. The prediction of Eq. (6) is plotted as a red line in Fig. 4 and is in excellent agreement with our measurements without any adjustable parameter. Alternatively, a power-law fit An^p to the data yields an exponent $p = 1.36(15)$ which confirms the $n_f^{4/3}$ predicted scaling at unitarity. Finally, fixing p to 4/3 provides the coefficient A and a value of the homogeneous contact $\zeta = 0.82(9)$ in excellent agreement with previous measurements, $\zeta = 0.87(3)$ [17,25]. This demonstrates that impurity losses act as a microscopic probe of quantum correlations in a many-body system.

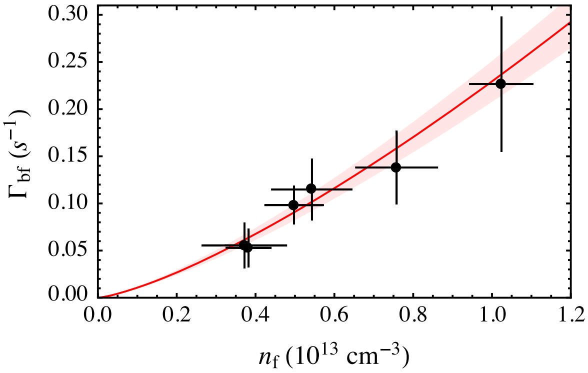

FIG. 4. Boson loss rate versus fermion central density at unitarity, $n_f = n_f(0)$. Circles: Experimental data. The red line is the $n_f^{4/3}$ prediction of Eq. (6) without any adjustable parameter. The red shaded area represents the 1σ uncertainty resulting from the error on γ.

The bosonic or fermionic nature of the probe is of no importance. Provided the coupling between the impurity and the resonant gas is weak, our method can also be applied to other mixtures. It gives a framework to interpret the experimental data on ^{6}Li/^{40}K [22] and, in particular, to test our prediction on the BCS side of the Feshbach resonance. It can also be applied to the recently observed ^{6}Li/^{174}Yb [39], ^{6}Li/^{41}K [40], and ^{6}Li/^{7}Li [41] dual-superfluid Bose-Fermi mixtures and even to the case where one of the collision partners is a photon as in photo-association experiments [42,43]. Our observation of a loss rate scaling $\propto n_f^{4/3}$ at unitarity is in stark contrast with the generic case n^p, where the integer p is the number of particles involved in the recombination process. A fractional exponent is also predicted to occur for the resonant Bose gas [5,6] and Fermi gas [27,44].

A first extension of this work is to investigate regimes where $a_{\mathrm{bf}} \simeq a_{ff} \gg n^{-1/3}$ and the Born approximation breaks down. In this case Efimovian features are expected to occur [45,46]. Second, our method provides a unique microscopic way to measure the contact quasilocally in a harmonic trap. An important perspective is to determine the homogeneous contact of the unitary Fermi gas at finite temperature, whose behavior is largely debated near the normal-superfluid transition [18].

The authors thank G. Shlyapnikov, B. Svistunov, and F. Werner for helpful discussions. They acknowledge support from Région Ile de France (DIM IFRAF/NanoK), ANR (Grant SpiFBox), and European Union (ERC Grant ThermoDynaMix).

---

[*] slaurent@lkb.ens.fr

[†] Present address: FEMTO-ST UMR CNRS 6174—UFC/ENSMM/UTBM, 26 chemin de l'Epitaphe, 25030 Besançon, France.

[1] I. Bloch, J. Dalibard, and W. Zwerger, Many-body physics with ultracold gases, Rev. Mod. Phys. **80**, 885 (2008).

[2] *The BCS-BEC Crossover and the Unitary Fermi Gas*, edited by W. Zwerger, Lecture Notes in Physics Vol. 836 (Springer, Berlin, 2012).

[3] Quantum Matter at Ultralow Temperatures, edited by M. Inguscio, W. Ketterle, S. Stringari, and G. Roati, *Proceedings of the International School of Physics "Enrico Fermi"*, Vol. 191 (IOS Press, Varenna, 2016).

[4] J.-y. Choi, S. Hild, J. Zeiher, P. Schauß, A. Rubio-Abadal, T. Yefsah, V. Khemani, D. A. Huse, I. Bloch, and C. Gross, Exploring the many-body localization transition in two dimensions, Science **352**, 1547 (2016).

[5] P. Makotyn, C. E. Klauss, D. L. Goldberger, E. A. Cornell, and D. S. Jin, Universal dynamics of a degenerate unitary Bose gas, Nat. Phys. **10**, 116 (2014).

[6] F. Chevy and C. Salomon, Strongly correlated Bose gases, J. Phys. B **49**, 192001 (2016).

[7] N. Syassen, D. M. Bauer, M. Lettner, T. Volz, D. Dietze, J. J. Garcia-Ripoll, J Ignacio Cirac, G. Rempe, and S. Dürr, Strong dissipation inhibits losses and induces correlations in cold molecular gases, Science **320**, 1329 (2008).

[8] A. J. Daley, J. M. Taylor, S. Diehl, M. Baranov, and P. Zoller, Atomic Three-Body Loss as a Dynamical Three-Body Interaction, Phys. Rev. Lett. **102**, 040402 (2009).

[9] B. Zhu *et al.* Suppressing the Loss of Ultracold Molecules via the Continuous Quantum Zeno Effect, Phys. Rev. Lett. **112**, 070404 (2014).

[10] T. Kraemer *et al.*, Evidence for Efimov quantum states in an ultracold gas of caesium atoms, Nature (London) **440**, 315 (2006).

[11] S. Tan, Energetics of a strongly correlated Fermi gas, Ann. Phys. (Amsterdam) **323**, 2952 (2008).

[12] S. Tan, Large momentum part of a strongly correlated Fermi gas, Ann. Phys. (Amsterdam) **323**, 2971 (2008).

[13] M. Olshanii and V. Dunjko, Short-Distance Correlation Properties of the Lieb-Liniger System and Momentum Distributions of Trapped One-Dimensional Atomic Gases, Phys. Rev. Lett. **91**, 090401 (2003).

[14] J. T. Stewart, J. P. Gaebler, T. E. Drake, and D. S. Jin, Verification of Universal Relations in a Strongly Interacting Fermi Gas, Phys. Rev. Lett. **104**, 235301 (2010).

[15] E. D. Kuhnle, H. Hu, X.-J. Liu, P. Dyke, M. Mark, P. D. Drummond, P. Hannaford, and C. J. Vale, Universal Behavior of Pair Correlations in a Strongly Interacting Fermi Gas, Phys. Rev. Lett. **105**, 070402 (2010).

[16] R. J. Wild, P Makotyn, J. M. Pino, E. A. Cornell, and D. S. Jin, Measurements of tans contact in an atomic Bose-Einstein condensate, Phys. Rev. Lett. **108**, 145305 (2012).

[17] N. Navon, S. Nascimbène, F. Chevy, and C. Salomon, The equation of state of a low-temperature fermi gas with tunable interactions, Science **328**, 729 (2010).

[18] Y. Sagi, T. E. Drake, R. Paudel, and D. S. Jin, Measurement of the Homogeneous Contact of a Unitary Fermi Gas, Phys. Rev. Lett. **109**, 220402 (2012).

[19] E. D. Kuhnle, S. Hoinka, P. Dyke, H. Hu, P. Hannaford, and C. J. Vale, Temperature Dependence of the Universal Contact Parameter in a Unitary Fermi Gas, Phys. Rev. Lett. **106**, 170402 (2011).

[20] J. P. DIncao and B. D. Esry, Suppression of Molecular Decay in Ultracold Gases without Fermi Statistics, Phys. Rev. Lett. **100**, 163201 (2008).

[21] J. P. D'Incao, C. H. Greene, and B. D Esry, The short-range three-body phase and other issues impacting the observation of efimov physics in ultracold quantum gases, J. Phys. B **42**, 044016 (2009).

[22] F. M. Spiegelhalder, A. Trenkwalder, D. Naik, G. Hendl, F. Schreck, and R. Grimm, Collisional Stability of ^{40}K Immersed in a Strongly Interacting Fermi Gas of ^{6}Li, Phys. Rev. Lett. **103**, 223203 (2009).

[23] A. Y. Khramov, A. H. Hansen, A. O. Jamison, W. H. Dowd, and S. Gupta, Dynamics of feshbach molecules in an ultracold three-component mixture, Phys. Rev. A **86**, 032705 (2012).

[24] J. J. Zirbel, K.-K. Ni, S. Ospelkaus, J. P. DIncao, C. E. Wieman, J. Ye, and D. S. Jin, Collisional Stability of Fermionic Feshbach Molecules, Phys. Rev. Lett. **100**, 143201 (2008).

[25] S. Hoinka, M. Lingham, K. Fenech, H. Hu, C. J. Vale, J. E. Drut, and S. Gandolfi, Precise Determination of the Structure Factor and Contact in a Unitary Fermi Gas, Phys. Rev. Lett. **110**, 055305 (2013).

[26] Y. Kagan, B. V. Svistunov, and G. V. Shlyapnikov, Effect of Bose condensation on inelastic processes in gases, JETP Lett. **42**, 209 (1985).

[27] D. S. Petrov, C. Salomon, and G. V. Shlyapnikov, Weakly Bound Dimers of Fermionic Atoms, Phys. Rev. Lett. **93**, 090404 (2004).

[28] E. Braaten and H.-W. Hammer, Universal relation for the inelastic two-body loss rate, J. Phys. B **46**, 215203 (2013).

[29] G. E. Astrakharchik, J. Boronat, J. Casulleras, and S. Giorgini, Equation of State of a Fermi Gas in the BEC-BCS Crossover: A Quantum Monte Carlo Study, Phys. Rev. Lett. **93**, 200404 (2004).

[30] This Hamiltonian describes the formation of deeply bound fermion-fermion molecules but Eq. (3) is also valid for boson-fermion molecules.

[31] See Supplemental Material at http://link.aps.org/supplemental/10.1103/PhysRevLett.118.103403 for a microscopic three-body loss model, Feshbach resonance data, and methods for loss coefficient extraction, which includes Refs. [32–36].

[32] F. Werner and Y. Castin, General relations for quantum gases in two and three dimensions: Two-component fermions, Phys. Rev. A **86**, 013626 (2012).

[33] G. Zürn, T. Lompe, A. N. Wenz, S. Jochim, P. S. Julienne, and J. M. Hutson, Precise Characterization of ^{6}Li Feshbach Resonances Using Trap-Sideband-Resolved RF Spectroscopy of Weakly Bound Molecules, Phys. Rev. Lett. **110**, 135301 (2013).

[34] N. Gross, Z. Shotan, O. Machtey, S. J. J. M. F Kokkelmans, and L. Khaykovich, Study of Efimov Physics in two nuclear-spin sublevels of 7 Li, C.R. Phys. **12**, 4 (2011).

[35] Z. Shotan, O. Machtey, S. Kokkelmans, and L. Khaykovich, Three-Body Recombination at Vanishing Scattering Lengths in an Ultracold Bose Gas, Phys. Rev. Lett. **113**, 053202 (2014).

[36] C. Chin and R. Grimm, Thermal equilibrium and efficient evaporation of an ultracold atom-molecule mixture, Phys. Rev. A **69**, 033612 (2004).

[37] I. Ferrier-Barbut, M. Delehaye, S. Laurent, A. T. Grier, M. Pierce, B. S. Rem, F. Chevy, and C. Salomon, A mixture of Bose and Fermi superfluids, Science **345**, 1035 (2014).

[38] P. O. Fedichev, M. W. Reynolds, and G. V. Shlyapnikov, Three-body Recombination of Ultracold Atoms to a Weakly Bound *s* Level, Phys. Rev. Lett. **77**, 2921 (1996).

[39] R. Roy, A. Green, R. Bowler, and S. Gupta, Two-element Mixture of Bose and Fermi Superfluids, Phys. Rev. Lett., **118**, 055301 (2017).

[40] X.-C. Yao, H.-Z. Chen, Y.-P. Wu, X.-P. Liu, X.-Q. Wang, X. Jiang, Y. Deng, Y.-A. Chen, and J.-W. Pan, Observation of Two-Species Vortex Lattices in a Mixture of Mass-Imbalance Bose and Fermi Superfluids, Phys. Rev. Lett. **117**, 145301 (2016).

[41] T. Ikemachi, A. Ito, Y. Aratake, Y. Chen, M. Koashi, M. Kuwata-Gonomaki, and M. Horikoshi, All-optical production of a superfluid bose-fermi mixture of ^{6}Li and ^{7}Li, arXiv:1606.09404.

[42] G. B. Partridge, K. E. Strecker, R. I. Kamar, M. W. Jack, and R. G. Hulet, Molecular Probe of Pairing in the BEC-BCS Crossover, Phys. Rev. Lett. **95**, 020404 (2005).

[43] F. Werner, L. Tarruell, and Y. Castin, Number of closed-channel molecules in the bec-bcs crossover, Eur. Phys. J. B **68**, 401 (2009).

[44] X. Du, Y. Zhang, and J. E. Thomas, Inelastic Collisions of a Fermi Gas in the BEC-BCS Crossover, Phys. Rev. Lett. **102**, 250402 (2009).

[45] E. Braaten, H.-W. Hammer, D. Kang, and L. Platter, Three-Body Recombination of ^{6}Li Atoms with Large Negative Scattering Lengths, Phys. Rev. Lett. **103**, 073202 (2009).

[46] T. B. Ottenstein, T. Lompe, M. Kohnen, A. N. Wenz, and S. Jochim, Collisional Stability of a Three-Component Degenerate Fermi Gas, Phys. Rev. Lett. **101**, 203202 (2008).

Bibliography

[1] Heike Kamerlingh Onnes. Investigations into the properties of substances at low temperatures, which have led, amongst other things, to the preparation of liquid helium. *Nobel lecture*, 4, 1913.

[2] P Kapitza. Viscosity of Liquid Helium below the λ-Point. *Nature*, 141(3):74, January 1938.

[3] J F Allen and A D Misener. Flow of Liquid Helium II. *Nature*, 141(3):75, January 1938.

[4] D. C. Tsui, H. L. Stormer, and A. C. Gossard. Two-dimensional magnetotransport in the extreme quantum limit. *Phys. Rev. Lett.*, 48:1559–1562, May 1982.

[5] R. B. Laughlin. Anomalous quantum hall effect: An incompressible quantum fluid with fractionally charged excitations. *Phys. Rev. Lett.*, 50:1395–1398, May 1983.

[6] J. Bardeen, L.N. Cooper, and J.R. Schrieffer. Theory of superconductivity. *Phys. Rev.*, 108(5):1175–1204, 1957.

[7] J George Bednorz and K Alex Müller. Possible hightc superconductivity in the bala- cu- o system. *Zeitschrift für Physik B Condensed Matter*, 64(2):189–193, 1986.

[8] Alfred Kastler. Quelques suggestions concernant la production optique et la détection optique d'une inégalité de population des niveaux de quantifigation spatiale des atomes. application à l'expérience de stern et gerlach et à la résonance magnétique. *J. phys. radium*, 11(6):255–265, 1950.

[9] William D Phillips, John V Prodan, and Harold J Metcalf. Laser cooling and electromagnetic trapping of neutral atoms. *JOSA B*, 2(11):1751–1767, 1985.

[10] M H Anderson, J R Ensher, M R Matthews, C E Wieman, and Eric A Cornell. Observation of Bose-Einstein Condensation in a Dilute Atomic Vapor. *Science*, 269(5221):198–201, July 1995.

[11] K Davis, M Mewes, M Andrews, N van Druten, D Durfee, D Kurn, and W Ketterle. Bose-Einstein Condensation in a Gas of Sodium Atoms. *Phys. Rev. Lett.*, 75(22):3969–3973, November 1995.

[12] B. DeMarco and D.S. Jin. Onset of Fermi degeneracy in a trapped atomic gas. *Science*, 285(5434):1703, 1999.

[13] I. Bloch, J. Dalibard, and W. Zwerger. Many-body physics with ultracold gases. *Rev. Mod. Phys.*, 80(3):885–964, 2008.

[14] E Flowers, M Ruderman, and P Sutherland. Neutrino pair emission from finite-temperature neutron superfluid and the cooling of young neutron stars. *The Astrophysical Journal*, 205:541–544, 1976.

[15] A. Gezerlis and J. Carlson. Strongly paired fermions: Cold atoms and neutron matter. *Phys. Rev. C*, 77(3):32801, 2008.

[16] Nicola Cabibbo and Giorgio Parisi. Exponential hadronic spectrum and quark liberation. *Physics Letters B*, 59(1):67–69, 1975.

[17] K. Maeda, G. Baym, and T. Hatsuda. Simulating dense QCD matter with ultracold atomic boson-fermion mixtures. *Phys. Rev. Lett.*, 103(8):85301, 2009.

[18] John Hubbard. Electron correlations in narrow energy bands. In *Proceedings of the royal society of london a: mathematical, physical and engineering sciences*, volume 276, pages 238–257. The Royal Society, 1963.

[19] N F Mott and R Peierls. Discussion of the paper by de boer and verwey. *Proceedings of the Physical Society*, 49(4S):72, 1937.

[20] M. Greiner, O. Mandel, T. Esslinger, T.W. Hänsch, and I. Bloch. Quantum phase transition from a superfluid to a Mott insulator in a gas of ultracold atoms. *Nature*, 415(6867):39–44, 2002.

[21] R. Jördens, N. Strohmaier, K. Günter, H. Moritz, and T. Esslinger. A Mott insulator of fermionic atoms in an optical lattice. *Nature*, 455(7210):204–207, 2008.

[22] U. Schneider, L. Hackermuller, S. Will, T. Best, I. Bloch, T. A. Costi, R. W. Helmes, D. Rasch, and A. Rosch. Metallic and insulating phases of repuslsively interacting fermions in a 3D optical lattice. *Science*, 322(5907):1520, 2008.

[23] Waseem S Bakr, Jonathon I Gillen, Amy Peng, Simon Folling, and Markus Greiner. A quantum gas microscope for detecting single atoms in a hubbard-regime optical lattice. *Nature*, 462(7269):74–77, 2009.

[24] Jacob F. Sherson, Christof Weitenberg, Manuel Endres, Marc Cheneau, Immanuel Bloch, and Stefan Kuhr. Single-atom-resolved fluorescence imaging of an atomic mott insulator. *Nature*, 467(7311):68–72, 09 2010.

[25] Elmar Haller, James Hudson, Andrew Kelly, Dylan A Cotta, Bruno Peaudecerf, Graham D Bruce, and Stefan Kuhr. Single-atom imaging of fermions in a quantum-gas microscope. *Nature Physics*, 11(9):738, 2015.

[26] Ahmed Omran, Martin Boll, Timon A Hilker, Katharina Kleinlein, Guillaume Salomon, Immanuel Bloch, and Christian Gross. Microscopic observation of pauli blocking in degenerate fermionic lattice gases. *Physical review letters*, 115(26):263001, 2015.

[27] GJA Edge, R Anderson, D Jervis, DC McKay, R Day, S Trotzky, and JH Thywissen. Imaging and addressing of individual fermionic atoms in an optical lattice. *Physical Review A*, 92(6):063406, 2015.

[28] Lawrence W Cheuk, Matthew A Nichols, Katherine R Lawrence, Melih Okan, Hao Zhang, and Martin W Zwierlein. Observation of 2d fermionic mott insulators of k 40 with single-site resolution. *Physical review letters*, 116(23):235301, 2016.

[29] Walter Hofstetter, J Ignacio Cirac, Peter Zoller, Eugene Demler, and MD Lukin. High-temperature superfluidity of fermionic atoms in optical lattices. *Physical review letters*, 89(22):220407, 2002.

[30] Masatoshi Sato, Yoshiro Takahashi, and Satoshi Fujimoto. Non-abelian topological order in s-wave superfluids of ultracold fermionic atoms. *Phys. Rev. Lett.*, 103:020401, Jul 2009.

[31] Jay D. Sau, Rajdeep Sensarma, Stephen Powell, I. B. Spielman, and S. Das Sarma. Chiral rashba spin textures in ultracold fermi gases. *Phys. Rev. B*, 83:140510, Apr 2011.

[32] Shi-Liang Zhu, L.-B. Shao, Z. D. Wang, and L.-M. Duan. Probing non-abelian statistics of majorana fermions in ultracold atomic superfluid. *Phys. Rev. Lett.*, 106:100404, Mar 2011.

[33] Xia-Ji Liu, Lei Jiang, Han Pu, and Hui Hu. Probing majorana fermions in spin-orbit-coupled atomic fermi gases. *Phys. Rev. A*, 85:021603, Feb 2012.

[34] W. Zwerger, editor. *The BCS-BEC Crossover and the Unitary Fermi Gas*, volume 836 of *Lecture Notes in Physics*. Springer, Berlin, 2012.

[35] Richard J Fletcher, Alexander L Gaunt, Nir Navon, Robert P Smith, and Zoran Hadzibabic. Stability of a unitary Bose gas. *Physical review letters*, 111(12):125303, 2013.

[36] BS Rem, AT Grier, I Ferrier-Barbut, U Eismann, T Langen, N Navon, L Khaykovich, F Werner, DS Petrov, F Chevy, et al. Lifetime of the Bose gas with resonant interactions. *Physical review letters*, 110(16):163202, 2013.

[37] Philip Makotyn, Catherine E Klauss, David L Goldberger, EA Cornell, and Deborah S Jin. Universal dynamics of a degenerate unitary Bose gas. *Nature Physics*, 10(2):116–119, 2014.

[38] Vitaly Efimov. Energy levels arising from resonant two-body forces in a three-body system. *Physics Letters B*, 33(8):563–564, 1970.

[39] Alexander L. Gaunt, Tobias F. Schmidutz, Igor Gotlibovych, Robert P. Smith, and Zoran Hadzibabic. Bose-einstein condensation of atoms in a uniform potential. *Phys. Rev. Lett.*, 110:200406, May 2013.

[40] Biswaroop Mukherjee, Zhenjie Yan, Parth B. Patel, Zoran Hadzibabic, Tarik Yefsah, Julian Struck, and Martin W. Zwierlein. Homogeneous atomic fermi gases. *Phys. Rev. Lett.*, 118:123401, Mar 2017.

[41] P. Fulde and R.A. Ferrell. Superconductivity in a strong spin-exchange field. *Phys. Rev*, 135:A550, 1964.

[42] A.I. Larkin and Y.N. Ovchinnikov. Nonuniform state of superconductors. *Zh. Eksp. Teor. Fiz*, 47:1136, 1964.

[43] MR Andrews, CG Townsend, H-J Miesner, DS Durfee, DM Kurn, and W Ketterle. Observation of interference between two bose condensates. *Science*, 275(5300):637–641, 1997.

[44] E. A. Burt, R. W. Ghrist, C. J. Myatt, M. J. Holland, E. A. Cornell, and C. E. Wieman. Coherence, correlations, and collisions: What one learns about bose-einstein condensates from their decay. *Phys. Rev. Lett.*, 79:337–340, Jul 1997.

[45] I Bloch, TW Hansch, and T Esslinger. Measurement of the spatial coherence of a trapped bose gas at the phase transition. *Nature*, 403(6766):166, 2000.

[46] Destruction of long-range order in one-dimensional and two-dimensional systems having a continuous symmetry group i. classical systems. *Sov. Phys. JETP*, 32(3):493–500, 1971.

[47] John Michael Kosterlitz and David James Thouless. Ordering, metastability and phase transitions in two-dimensional systems. *Journal of Physics C: Solid State Physics*, 6(7):1181, 1973.

[48] Z. Hadzibabic, P. Krüger, M. Cheneau, B. Battelier, and J. Dalibard. Berezinskii–Kosterlitz–Thouless crossover in a trapped atomic gas. *Nature*, 441(7097):1118–1121, 2006.

[49] P. A. Murthy, I. Boettcher, L. Bayha, M. Holzmann, D. Kedar, M. Neidig, M. G. Ries, A. N. Wenz, G. Zürn, and S. Jochim. Observation of the berezinskii-kosterlitz-thouless phase transition in an ultracold fermi gas. *Phys. Rev. Lett.*, 115:010401, Jun 2015.

[50] Juliette Billy, Vincent Josse, Zhanchun Zuo, Alain Bernard, Ben Hambrecht, Pierre Lugan, David Clément, Laurent Sanchez-palencia, Philippe Bouyer, and Alain Aspect. Direct observation of anderson localization of matter waves in a controlled disorder. *Nature*, 453(7197):891–894, 2008.

[51] Giacomo Roati, Chiara DÕErrico, Leonardo Fallani, Marco Fattori, Chiara Fort, Matteo Zaccanti, Giovanni Modugno, Michele Modugno, and Massimo Inguscio. Anderson localization of a non-interacting bose–einstein condensate. *Nature*, 453(7197):895–898, 2008.

[52] G. B. Hess and W. M. Fairbank. Measurements of angular momentum in superfluid helium. *Phys. Rev. Lett.*, 19:216–218, Jul 1967.

[53] S. Riedl, E.R.S. Guajardo, C. Kohstall, J.H. Denschlag, and R. Grimm. Superfluid Quenching of the Moment of Inertia in a Strongly Interacting Fermi Gas. *arXiv:0907.3814*, 2009.

[54] AA Abrikosov. The magnetic properties of superconducting alloys. *Journal of Physics and Chemistry of Solids*, 2(3):199–208, 1957.

[55] Michael Robin Matthews, Brian P Anderson, PC Haljan, DS Hall, CE Wieman, and EA Cornell. Vortices in a Bose-Einstein condensate. *Physical Review Letters*, 83(13):2498, 1999.

[56] KW Madison, F Chevy, W Wohlleben, and J Dalibard. Vortex formation in a stirred Bose-Einstein condensate. *Physical Review Letters*, 84(5):806, 2000.

[57] JR Abo-Shaeer, C Raman, JM Vogels, and Wolfgang Ketterle. Observation of vortex lattices in Bose-Einstein condensates. *Science*, 292(5516):476–479, 2001.

[58] M.W. Zwierlein, J.R. Abo-Shaeer, A. Schirotzek, C.H. Schunck, and W. Ketterle. Vortices and superfluidity in a strongly interacting Fermi gas. *Nature*, 435(7045):1047–1051, 2005.

[59] M.W. Zwierlein, A. Schirotzek, C.H. Schunck, and W. Ketterle. Fermionic superfluidity with imbalanced spin populations. *Science*, 311(5760):492–496, 2006.

[60] C Ryu, M Andersen, P Cladé, Vasant Natarajan, K Helmerson, and W Phillips. Observation of Persistent Flow of a Bose-Einstein Condensate in a Toroidal Trap. *Phys. Rev. Lett.*, 99(26):260401, December 2007.

[61] Scott Beattie, Stuart Moulder, Richard J Fletcher, and Zoran Hadzibabic. Persistent currents in spinor condensates. *Phys. Rev. Lett.*, 110(2):025301, 2013.

[62] L Landau. The Theory of Superfluid Helium II. *J. Phys. USSR*, 5:70, August 1941.

[63] C Raman, M Köhl, R Onofrio, DS Durfee, CE Kuklewicz, Z Hadzibabic, and W Ketterle. Evidence for a critical velocity in a Bose-Einstein condensed gas. *Physical Review Letters*, 83(13):2502, 1999.

[64] R Onofrio, C Raman, JM Vogels, JR Abo-Shaeer, AP Chikkatur, and W Ketterle. Observation of superfluid flow in a Bose-Einstein condensed gas. *Physical Review Letters*, 85(11):2228, 2000.

[65] Rémi Desbuquois, Lauriane Chomaz, Tarik Yefsah, Julian Léonard, Jérôme Beugnon, Christof Weitenberg, and Jean Dalibard. Superfluid behaviour of a two-dimensional Bose gas. *Nature Physics*, 8(9):645–648, 2012.

[66] D. Miller, J. Chin, C. Stan, Y. Liu, W. Setiawan, C. Sanner, and W. Ketterle. Critical Velocity for Superfluid Flow across the BEC-BCS Crossover. *Phys. Rev. Lett.*, 99(7):070402, August 2007.

[67] Wolf Weimer, Kai Morgener, Vijay Pal Singh, Jonas Siegl, Klaus Hueck, Niclas Luick, Ludwig Mathey, and Henning Moritz. Critical velocity in the BEC-BCS crossover. *Phys. Rev. Lett.*, 114:095301, Mar 2015.

[68] Leonid A. Sidorenkov, Meng Khoon Tey, Rudolf Grimm, Yan-Hua Hou, Lev Pitaevskii, and Sandro Stringari. Second sound and the superfluid fraction in a fermi gas with resonant interactions. *Nature*, 498(7452):78–81, 06 2013.

[69] D. S. Hall, M. R. Matthews, J. R. Ensher, C. E. Wieman, and E. A. Cornell. Dynamics of Component Separation in a Binary Mixture of Bose-Einstein Condensates. *Phys. Rev. Lett.*, 81:1539–1542, Aug 1998.

[70] C Hamner, JJ Chang, P Engels, and MA Hoefer. Generation of dark-bright soliton trains in superfluid-superfluid counterflow. *Physical review letters*, 106(6):065302, 2011.

[71] J Stenger, S Inouye, DM Stamper-Kurn, H-J Miesner, AP Chikkatur, and W Ketterle. Spin domains in ground-state bose-einstein condensates. *Nature*, 396(6709):345–348, 1998.

[72] Tetsuo Ohmi and Kazushige Machida. Bose-einstein condensation with internal degrees of freedom in alkali atom gases. *Journal of the Physical Society of Japan*, 67(6):1822–1825, 1998.

[73] T. Kraemer, M. Mark, P. Waldburger, JG Danzl, C. Chin, B. Engeser, AD Lange, K. Pilch, A. Jaakkola, H.C. Nägerl, et al. Evidence for Efimov quantum states in an ultracold gas of caesium atoms. *Nature*, 440(7082):315–318, 2006.

[74] N. Gross, Z. Shotan, O. Machtey, S.J.J.M.F Kokkelmans, and L. Khaykovich. Study of Efimov Physics in two nuclear-spin sublevels of 7 Li. *Comptes Rendus Physique*, 12(1):4–12, 2011.

[75] Scott E Pollack, Daniel Dries, and Randall G Hulet. Universality in three-and four-body bound states of ultracold atoms. *Science*, 326(5960):1683–1685, 2009.

[76] Matteo Zaccanti, Benjamin Deissler, Chiara DErrico, Marco Fattori, Mattia Jona-Lasinio, Stefan Müller, Giacomo Roati, Massimo Inguscio, and Giovanni Modugno. Observation of an efimov spectrum in an atomic system. *Nature Physics*, 5(8):586–591, 2009.

[77] D.S. Petrov, C. Salomon, and G.V. Shlyapnikov. Weakly bound dimers of fermionic atoms. *Phys. Rev. Lett.*, 93(9):090404, 2004.

[78] T. Bourdel, L. Khaykovich, J. Cubizolles, J. Zhang, F. Chevy, M. Teichmann, L. Tarruell, S.J.J.M.F. Kokkelmans, and C. Salomon. Experimental Study of the BEC-BCS Crossover Region in Lithium 6. *Phys. Rev. Lett.*, 93(5):050401, 2004.

[79] C. A. Regal, M. Greiner, and D. S. Jin. Lifetime of Molecule-Atom Mixtures near a Feshbach Resonance in^{40} K. *Phys. Rev. Lett.*, 92(8):83201, 2004.

[80] X. Du, Y. Zhang, and J. E. Thomas. Inelastic collisions of a fermi gas in the bec-bcs crossover. *Phys. Rev. Lett.*, 102:250402, Jun 2009.

[81] V. Efimov. Energy levels of three resonantly interacting particles. *Nuclear Physics A*, 210(1):157 – 188, 1973.

[82] Yvan Castin, Christophe Mora, and Ludovic Pricoupenko. Four-body efimov effect for three fermions and a lighter particle. *Phys. Rev. Lett.*, 105:223201, Nov 2010.

[83] Betzalel Bazak and Dmitry S Petrov. Five-body efimov effect and universal pentamer in fermionic mixtures. *Physical Review Letters*, 118(8):083002, 2017.

[84] Y. Kagan, B. V. Svistunov, and G. V. Shlyapnikov. Effect of Bose condensation on inelastic processes in gases. *Soviet Journal of Experimental and Theoretical Physics Letters*, 42:209, August 1985.

[85] Catherine E Klauss, Xin Xie, Carlos Lopez-Abadia, José P D'Incao, Zoran Hadzibabic, Deborah S Jin, and Eric A Cornell. Observation of efimov molecules created from a resonantly interacting bose gas. *arXiv preprint arXiv:1704.01206*, 2017.

[86] Yvan Castin, Igor Ferrier-Barbut, and Christophe Salomon. The landau critical velocity for a particle in a fermi superfluid. *Comptes Rendus Physique*, 16(2):241–253, 2015.

[87] G. F. Gribakin and V. V. Flambaum. Calculation of the scattering length in atomic collisions using the semiclassical approximation. *Phys. Rev. A*, 48:546–553, Jul 1993.

[88] J. Walraven. *Quantum Gases - Collisions and Statistics.*

[89] V. V. Flambaum, G. F. Gribakin, and C. Harabati. Analytical calculation of cold-atom scattering. *Phys. Rev. A*, 59:1998–2005, Mar 1999.

[90] Cheng Chin, Rudolf Grimm, Paul Julienne, and Eite Tiesinga. Feshbach resonances in ultracold gases. *Reviews of Modern Physics*, 82(2):1225, 2010.

[91] G. B. Partridge, K. E. Strecker, R. I. Kamar, M. W. Jack, and R. G. Hulet. Molecular probe of pairing in the bec-bcs crossover. *Phys. Rev. Lett.*, 95(2):020404, Jul 2005.

[92] Eric Braaten and H-W Hammer. Universality in few-body systems with large scattering length. *Physics Reports*, 428(5):259–390, 2006.

[93] Félix Werner. *Trapped cold atoms with resonant interactions: unitary gas and three-body problem.* Theses, Université Pierre et Marie Curie - Paris VI, July 2008.

[94] V Efimov. Weakly-bound states of three resonantly-interacting particles. *Sov. J. Nucl. Phys*, 12(589):101, 1971.

[95] GS Danilov. On the three-body problem with short-range forces. *Sov. Phys. JETP*, 13(349):3, 1961.

[96] F. Ferlaino, A. Zenesini, M. Berninger, B. Huang, H. C. Nägerl, and R. Grimm. Efimov resonances in ultracold quantum gases. *Few-Body Systems*, 51(2):113, 2011.

[97] L. H. Thomas. The interaction between a neutron and a proton and the structure of h^3. *Phys. Rev.*, 47:903–909, Jun 1935.

[98] R. D. Amado and F. C. Greenwood. There is no efimov effect for four or more particles. *Phys. Rev. D*, 7:2517–2519, Apr 1973.

[99] Dmitry K. Gridnev. Why there is no efimov effect for four bosons and related results on the finiteness of the discrete spectrum. *Journal of Mathematical Physics*, 54(4):042105, 2013.

[100] J. von Stecher, J. P. D/'Incao, and Chris H. Greene. Signatures of universal four-body phenomena and their relation to the efimov effect. *Nat Phys*, 5(6):417–421, 06 2009.

[101] Félix Werner and Yvan Castin. General relations for quantum gases in two and three dimensions. ii. bosons and mixtures. *Physical Review A*, 86(5):053633, 2012.

[102] Mark Edwards and K Burnett. Numerical solution of the nonlinear schrödinger equation for small samples of trapped neutral atoms. *Phys. Rev. A*, 51(2):1382, 1995.

[103] F. Dalfovo and S. Stringari. Bosons in anisotropic traps: Ground state and vortices. *Phys. Rev. A*, 53(4):2477–2485, Apr 1996.

[104] T. D. Lee, Kerson Huang, and C. N. Yang. Eigenvalues and eigenfunctions of a bose system of hard spheres and its low-temperature properties. *Phys. Rev.*, 106:1135–1145, Jun 1957.

[105] N. M. Hugenholtz and D. Pines. Ground-state energy and excitation spectrum of a system of interacting bosons. *Phys. Rev.*, 116:489–506, Nov 1959.

[106] F. Chevy, S. Nascimbène, N. Navon, J. Kaijun, C. Lobo, and S. Salomon. Thermodynamics of the unitary fermi gas. *J. Phys.: Conf. Ser.*, 264:012012, 2011.

[107] Nir Navon, Sylvain Nascimbène, Frédéric Chevy, and Christophe Salomon. The equation of state of a low-temperature fermi gas with tunable interactions. *Science*, 328(5979):729–732, 2010.

[108] A. Altmeyer, S. Riedl, C. Kohstall, M. J. Wright, R. Geursen, M. Bartenstein, C. Chin, J. Hecker Denschlag, and R. Grimm. Precision measurements of collective oscillations in the bec-bcs crossover. *Phys. Rev. Lett.*, 98:040401, Jan 2007.

[109] Shao-Jian Jiang and Fei Zhou. Stability and anomalous compressibility of bose gases near resonance: The scale-dependent interactions and thermal effects. *Phys. Rev. A*, 92:013619, Jul 2015.

[110] Tommaso Comparin and Werner Krauth. Momentum distribution in the unitary bose gas from first principles. *Phys. Rev. Lett.*, 117:225301, Nov 2016.

[111] Marcus Barth and Johannes Hofmann. Efimov correlations in strongly interacting bose gases. *Phys. Rev. A*, 92:062716, Dec 2015.

[112] Shao-Jian Jiang, Jeff Maki, and Fei Zhou. Long-lived universal resonant bose gases. *Phys. Rev. A*, 93:043605, Apr 2016.

[113] Yu-Li Lee and Yu-Wen Lee. Universality and stability for a dilute Bose gas with a feshbach resonance. *Phys. Rev. A*, 81:063613, Jun 2010.

[114] J.-L. Song and F. Zhou. Ground state properties of cold bosonic atoms at large scattering lengths. *Phys. Rev. Lett.*, 103:025302, Jul 2009.

[115] A. J. Leggett. Cooper pairing in spin-polarized Fermi systems. *J. Phys. Colloques*, 41(C7):19–26, 1980.

[116] P. Nozières and S. Schmitt-Rink. Bose condensation in an attractive fermion gas: From weak to strong coupling superconductivity. *J. Low Temp. Phys.*, 59(3):195–211, 1985.

[117] G.E. Astrakharchik, J. Boronat, J. Casulleras, and S. Giorgini. Equation of state of a Fermi gas in the BEC-BCS crossover: A quantum Monte Carlo study. *Phys. Rev. Lett.*, 93(20):200404, 2004.

[118] Nir Navon. PhD Thesis: Thermodynamics of ultracold Bose and Fermi gases. *CCSD Repository tel-01081100*, 2011.

[119] Munekazu Horikoshi, Masato Koashi, Hiroyuki Tajima, Yoji Ohashi, and Makoto Kuwata-Gonokami. Ground-state thermodynamic quantities of homogeneous spin-$1/2$ fermions from the bcs region to the unitarity limit. *arXiv preprint arXiv:1612.04026*, 2016.

[120] S. Nascimbène, N. Navon, F. Chevy, and C. Salomon. The equation of state of ultracold Bose and Fermi gases: a few examples. *New J. Phys.*, 12:103206, 2010.

[121] M. J. H. Ku, A. T. Sommer, L. W. Cheuk, and M. W. Zwierlein. Revealing the superfluid lambda transition in the universal thermodynamics of a unitary fermi gas. *Science*, 335(6068):563–567, 2012.

[122] V. Galitskii. The energy spectrum of a non-ideal fermi gas. *Sov. Phys. JETP*, 7:104, 1958.

[123] T. D. Lee and C. N. Yang. Many-body problem in quantum mechanics and quantum statistical mechanics. *Phys. Rev.*, 105(3):1119–1120, 1957.

[124] R.B. Diener, R. Sensarma, and M. Randeria. Quantum fluctuations in the superfluid state of the BCS-BEC crossover. *Phys. Rev. A*, 77(2):23626, 2008.

[125] X. Leyronas and R. Combescot. Superfluid equation of state of dilute composite bosons. *Phys. Rev. Lett.*, 99(17):170402, 2007.

[126] Sascha Hoinka, Marcus Lingham, Kristian Fenech, Hui Hu, Chris J. Vale, Joaquín E. Drut, and Stefano Gandolfi. Precise determination of the structure factor and contact in a unitary fermi gas. *Phys. Rev. Lett.*, 110:055305, Jan 2013.

[127] Gabriele Ferrari. *Simultaneous trapping of the bosonic and fermionic isotopes of lithium, theoretical study of the collisional relaxation in a degenerate Fermi gas.* PhD thesis, Université Pierre et Marie Curie-Paris VI, 2000.

[128] Florian Schreck. *Mixtures of ultracold gases: Fermi sea and Bose-Einstein condesnate of lithium isotopes.* PhD thesis, Université Pierre et Marie Curie-Paris VI, 2000.

[129] Leticia Tarruell. *Superfluidité dans un gaz de fermions ultrafroids.* PhD thesis, Université Pierre et Marie Curie-Paris VI, 2008.

[130] Sylvain Nascimbène. *Thermodynamique des gaz de fermions ultrafroids.* PhD thesis, Ecole Normale Supérieure, 2010.

[131] Igor Ferrier-Barbut. *Mixtures of Bose and Fermi Superfluids.* Theses, Ecole normale supérieure - ENS PARIS, October 2014.

[132] G. Zürn, T. Lompe, A. N. Wenz, S. Jochim, P. S. Julienne, and J. M. Hutson. Precise Characterization of ^{6}Li Feshbach Resonances Using Trap-Sideband-Resolved RF Spectroscopy of Weakly Bound Molecules. *Phys. Rev. Lett.*, 110(13):135301, 2013.

[133] David E. Pritchard. Cooling neutral atoms in a magnetic trap for precision spectroscopy. *Phys. Rev. Lett.*, 51:1336–1339, Oct 1983.

[134] Harold J Metcalf and Peter Van der Straten. *Laser cooling and trapping*. Springer Science & Business Media, 2012.

[135] O. J. Luiten, M. W. Reynolds, and J. T. M. Walraven. Kinetic theory of the evaporative cooling of a trapped gas. *Phys. Rev. A*, 53:381–389, Jan 1996.

[136] Rudolf Grimm, Matthias Weidemüller, and Yurii B Ovchinnikov. Optical dipole traps for neutral atoms. *Advances in atomic, molecular, and optical physics*, 42:95–170, 2000.

[137] J. M. Gerton, C. A. Sackett, B. J. Frew, and R. G. Hulet. Dipolar relaxation collisions in magnetically trapped ^{7}Li. *Phys. Rev. A*, 59:1514–1516, Feb 1999.

[138] Y. Castin and R. Dum. Bose-einstein condensates in time dependent traps. *Phys. Rev. Lett.*, 77:5315–5319, Dec 1996.

[139] S. Nascimbène, N. Navon, K. Jiang, F. Chevy, and C. Salomon. Exploring the Thermodynamics of a Universal Fermi Gas. *Nature*, 463:1057–1060, 2010.

[140] A.M. Clogston. Upper limit for the critical field in hard superconductors. *Phys. Rev. Lett.*, 9(6):266–267, 1962.

[141] B.S. Chandrasekhar. A note on the maximum critical field of high-field superconductors. *App. Phys. Lett.*, 1(1):7–8, 1962.

[142] Y. Shin, C.H. Schunck, A. Schirotzek, and W. Ketterle. Phase diagram of a two-component Fermi gas with resonant interactions. *Nature*, 451(4):689–693, 2008.

[143] F. London. On the bose-einstein condensation. *Phys. Rev.*, 54:947–954, Dec 1938.

[144] Laszlo Tisza. Transport phenomena in helium ii. *Nature*, 141(3577):913, 1938.

[145] D Osheroff, R Richardson, and D Lee. Evidence for a New Phase of Solid ^{3}He. *Phys. Rev. Lett.*, 28(14):885–888, April 1972.

[146] L.N. Cooper. Bound electron pairs in a degenerate Fermi gas. *Phys. Rev.*, 104(4):1189–1190, 1956.

[147] G.E. Volovik, V.P. Mineev, and I.M. Khalatnikov. Theory of solutions of a superfluid Fermi liquid in a superfluid Bose liquid. *Sov. Phys. JETP*, 69(2):675–687, 1975.

[148] AF Andreev and EP Bashkin. Three-velocity hydrodynamics of superfluid solutions. *Soviet Journal of Experimental and Theoretical Physics*, 42:164, 1976.

[149] J. Rysti, J. Tuoriniemi, and A. Salmela. Effective ^{3}He interactions in dilute ^{3}He-^{4}He mixtures. *Phys. Rev. B*, 85:134529, Apr 2012.

[150] J. Tuoriniemi, J. Martikainen, E. Pentti, A. Sebedash, S. Boldarev, and G. Pickett. Towards Superfluidity of ^{3}He Diluted by ^{4}He. *Journal of Low Temperature Physics*, 129(5-6):531–545, 2002.

[151] C. A. Regal, M. Greiner, and D. S. Jin. Observation of resonance condensation of fermionic atom pairs. *Phys. Rev. Lett.*, 92:040403, 2004.

[152] M. W. Zwierlein, C. A. Stan, C. H. Schunck, S. M. F. Raupach, A. J. Kerman, and W. Ketterle. Condensation of pairs of fermionic atoms near a feshbach resonance. *Phys. Rev. Lett.*, 92:120403, 2004.

[153] C. J. Myatt, E. A. Burt, R. W. Ghrist, E. A. Cornell, and C. E. Wieman. Production of two overlapping bose-einstein condensates by sympathetic cooling. *Phys. Rev. Lett.*, 78:586–589, Jan 1997.

[154] L. Landau. Theory of the superfluidity of helium ii. *Phys. Rev.*, 60:356–358, Aug 1941.

[155] Marion Delehaye. *Mixtures of superfluids*. Theses, PSL Research University, April 2016.

[156] P. Maddaloni, M. Modugno, C. Fort, F. Minardi, and M. Inguscio. Collective oscillations of two colliding Bose-Einstein condensates. *Phys. Rev. Lett.*, 85(12):2413, 2000.

[157] F. Ferlaino, R.J. Brecha, P. Hannaford, F. Riboli, G. Roati, G. Modugno, and M. Inguscio. Dipolar oscillations in a quantum degenerate Fermi–Bose atomic mixture. *Journal of Optics B: Quantum and Semiclassical Optics*, 5(2):S3, 2003.

[158] A. Sommer, M. Ku, G. Roati, and M. W. Zwierlein. Universal spin transport in a strongly interacting fermi gas. *Nature*, 472:201–204, 2011.

[159] T. Kinoshita, T. Wenger, and D. S Weiss. A quantum Newton's cradle. *Nature*, 440(7086):900–903, April 2006.

[160] S. Stringari. Sum rules and the collective oscillations of a quantum gas. *J. Phys. IV (Proceedings)*, 116:47–66, 2004.

[161] T. Miyakawa, T. Suzuki, and H. Yabu. Sum-rule approach to collective oscillations of a boson-fermion mixed condensate of alkali-metal atoms. *Phys. Rev. A*, 62:063613, Nov 2000.

[162] A. Banerjee. Collective oscillations of a Bose-Fermi mixture: Effect of unequal masses of Bose and Fermi particles. *Physical Review A*, 76(2):023611, 2007.

[163] Ren Zhang, Wei Zhang, Hui Zhai, and Peng Zhang. Calibration of the interaction energy between bose and fermi superfluids. *Phys. Rev. A*, 90:063614, Dec 2014.

[164] L. Landau. Theory of the superfluidity of helium ii. *Phys. Rev.*, 60:356–358, Aug 1941.

[165] R. Combescot, M. Kagan, and S. Stringari. Collective mode of homogeneous superfluid Fermi gases in the BEC-BCS crossover. *Phys. Rev. A*, 74(4):042717, October 2006.

[166] Abad, Marta, Recati, Alessio, Stringari, Sandro, and Chevy, Frédéric. Counter-flow instability of a quantum mixture of two superfluids. *Eur. Phys. J. D*, 69(5):126, 2015.

[167] F Chevy. Counterflow in a doubly superfluid mixture of bosons and fermions. *Phys. Rev. A*, 91(6):063606, 2015.

[168] GE Astrakharchik. Quantum monte carlo study of ultracold gases (phd thesis). *arXiv preprint arXiv:1412.4529*, 2014.

[169] S Stringari. Dynamics of Bose-Einstein condensed gases in highly deformed traps. *Phys. Rev. A*, 58(3):2385, 1998.

[170] P. Capuzzi, P. Vignolo, F. Federici, and M. P. Tosi. Sound propagation in elongated superfluid fermionic clouds. *Phys. Rev. A*, 73:021603, Feb 2006.

[171] D. E. Miller, J. K. Chin, C. A. Stan, Y. Liu, W. Setiawan, C. Sanner, and W. Ketterle. Critical velocity for superfluid flow across the bec-bcs crossover. *Phys. Rev. Lett.*, 99(7):070402, Aug 2007.

[172] Vijay Pal Singh, Wolf Weimer, Kai Morgener, Jonas Siegl, Klaus Hueck, Niclas Luick, Henning Moritz, and Ludwig Mathey. Probing superfluidity of bose-einstein condensates via laser stirring. *Phys. Rev. A*, 93:023634, Feb 2016.

[173] P. O. Fedichev and G. V. Shlyapnikov. Critical velocity in cylindrical bose-einstein condensates. *Phys. Rev. A*, 63:045601, Mar 2001.

[174] Pierre-Philippe Crépin, Xavier Leyronas, and Frédéric Chevy. Hydrodynamic spectrum of a superfluid in an elongated trap. *EPL (Europhysics Letters)*, 114(6):60005, 2016.

[175] Pavel A Cherenkov. Visible emission of clean liquids by action of γ radiation. *Doklady Akademii Nauk SSSR*, 2:451, 1934.

[176] W. Thomson. On ship waves. *Institution of Mechanical Engineers, Proceedings*, 38:409–434, 1887.

[177] E. Raphaël and P.-G. de Gennes. Capillary gravity waves caused by a moving disturbance: Wave resistance. *Phys. Rev. E*, 53:3448–3455, Apr 1996.

[178] R.P. Feynman. Chapter {II} application of quantum mechanics to liquid helium. volume 1 of *Progress in Low Temperature Physics*, pages 17 – 53. Elsevier, 1955.

[179] Th Frisch, Yves Pomeau, and Sergio Rica. Transition to dissipation in a model of superflow. *Physical review letters*, 69(11):1644, 1992.

[180] B. Jackson, J. F. McCann, and C. S. Adams. Dissipation and vortex creation in bose-einstein condensed gases. *Phys. Rev. A*, 61:051603, Apr 2000.

[181] C. Nore, C. Huepe, and M. E. Brachet. Subcritical dissipation in three-dimensional superflows. *Phys. Rev. Lett.*, 84:2191–2194, Mar 2000.

[182] Woo Jin Kwon, Geol Moon, Sang Won Seo, and Y. Shin. Critical velocity for vortex shedding in a bose-einstein condensate. *Phys. Rev. A*, 91:053615, May 2015.

[183] Andrew G. Sykes, Matthew J. Davis, and David C. Roberts. Drag force on an impurity below the superfluid critical velocity in a quasi-one-dimensional bose-einstein condensate. *Phys. Rev. Lett.*, 103:085302, Aug 2009.

[184] Guillaume Lang, Frank Hekking, and Anna Minguzzi. Dynamic structure factor and drag force in a one-dimensional strongly interacting bose gas at finite temperature. *Phys. Rev. A*, 91:063619, Jun 2015.

[185] AD Chepelianskii, Frédéric Chevy, and Elie Raphael. Capillary-gravity waves generated by a slow moving object. *Physical review letters*, 100(7):074504, 2008.

[186] John David Jackson. *Classical electrodynamics*. Wiley, 1999.

[187] Romain Dubessy, Camilla De Rossi, Thomas Badr, Laurent Longchambon, and Hélène Perrin. Imaging the collective excitations of an ultracold gas using statistical correlations. *New Journal of Physics*, 16(12):122001, 2014.

[188] Weizhu Bao and Yongyong Cai. Mathematical theory and numerical methods for bose-einstein condensation. *arXiv preprint arXiv:1212.5341*, 2012.

[189] Gilbert Strang. On the construction and comparison of difference schemes. *SIAM Journal on Numerical Analysis*, 5(3):506–517, 1968.

[190] Shuwei Jin. Internship report, 2015.

[191] E Zaremba. Sound propagation in a cylindrical Bose-condensed gas. *Physical Review A*, 57(1):518, 1998.

[192] Tin-Lun Ho and Michael Ma. Quasi 1 and 2d dilute bose gas in magnetic traps: Existence of off-diagonal order and anomalous quantum fluctuations. *Journal of Low Temperature Physics*, 115(1):61–70, 1999.

[193] Chiara Menotti and Sandro Stringari. Collective oscillations of a one-dimensional trapped bose-einstein gas. *Phys. Rev. A*, 66:043610, Oct 2002.

[194] M. J. Edmonds, K. L. Lee, and N. P. Proukakis. Kinetic model of trapped finite-temperature binary condensates. *Phys. Rev. A*, 91:011602, Jan 2015.

[195] Kean Loon Lee, Nils B. Jørgensen, I-Kang Liu, Lars Wacker, Jan J. Arlt, and Nick P. Proukakis. Phase separation and dynamics of two-component bose-einstein condensates. *Phys. Rev. A*, 94:013602, Jul 2016.

[196] Nir Navon, Alexander L Gaunt, Robert P Smith, and Zoran Hadzibabic. Emergence of a turbulent cascade in a quantum gas. *Nature*, 539(7627):72–75, 2016.

[197] Shina Tan. Energetics of a strongly correlated fermi gas. *Annals of Physics*, 323(12):2952 – 2970, 2008.

[198] S. Tan. Large momentum part of a strongly correlated Fermi gas. *Ann. Phys.*, 323(12):2971–2986, 2008.

[199] Maxim Olshanii and Vanja Dunjko. Short-distance correlation properties of the lieb-liniger system and momentum distributions of trapped one-dimensional atomic gases. *Phys. Rev. Lett.*, 91:090401, Aug 2003.

[200] Eric Braaten, Daekyoung Kang, and Lucas Platter. Universal relations for identical bosons from three-body physics. *Physical review letters*, 106(15):153005, 2011.

[201] Félix Werner and Yvan Castin. General relations for quantum gases in two and three dimensions: Two-component fermions. *Physical Review A*, 86(1):013626, 2012.

[202] J.T. Stewart, J.P. Gaebler, and D.S. Jin. Using photoemission spectroscopy to probe a strongly interacting Fermi gas. *Nature*, 454(7205):744–747, 2008.

[203] Eric Braaten, Daekyoung Kang, and Lucas Platter. Short-time operator product expansion for rf spectroscopy of a strongly interacting fermi gas. *Phys. Rev. Lett.*, 104:223004, Jun 2010.

[204] J. T. Stewart, J. P. Gaebler, T. E. Drake, and D. S. Jin. Verification of universal relations in a strongly interacting fermi gas. *Phys. Rev. Lett.*, 104(23):235301, Jun 2010.

[205] Richard J. Fletcher, Raphael Lopes, Jay Man, Nir Navon, Robert P. Smith, Martin W. Zwierlein, and Zoran Hadzibabic. Two- and three-body contacts in the unitary bose gas. *Science*, 355(6323):377–380, 2017.

[206] F. Werner, L. Tarruell, and Y. Castin. Number of closed-channel molecules in the BEC-BCS crossover. *Eur. Phys. J. B*, 68(3):401–415, 2009.

[207] H. Hu, X.-J. Liu, and P. D. Drummond. Static structure factor of a strongly correlated fermi gas at large momenta. *EPL (Europhysics Letters)*, 91(2):20005, 2010.

[208] Dam T. Son and Ethan G. Thompson. Short-distance and short-time structure of a unitary fermi gas. *Phys. Rev. A*, 81:063634, Jun 2010.

[209] E. D. Kuhnle, H. Hu, X.-J. Liu, P. Dyke, M. Mark, P. D. Drummond, P. Hannaford, and C. J. Vale. Universal behavior of pair correlations in a strongly interacting fermi gas. *Phys. Rev. Lett.*, 105(7):070402, Aug 2010.

[210] Eric Braaten and H-W Hammer. Universal relation for the inelastic two-body loss rate. *Journal of Physics B: Atomic, Molecular and Optical Physics*, 46(21):215203, 2013.

[211] Sébastien Laurent, Matthieu Pierce, Marion Delehaye, Tarik Yefsah, Frédéric Chevy, and Christophe Salomon. Connecting few-body inelastic decay to quantum correlations in a many-body system: A weakly coupled impurity in a resonant fermi gas. *Phys. Rev. Lett.*, 118:103403, Mar 2017.

[212] Eric Braaten, H.-W. Hammer, Daekyoung Kang, and Lucas Platter. Three-body recombination of identical bosons with a large positive scattering length at nonzero temperature. *Phys. Rev. A*, 78:043605, Oct 2008.

[213] D. S. Petrov and F. Werner. Three-body recombination in heteronuclear mixtures at finite temperature. *Phys. Rev. A*, 92:022704, Aug 2015.

[214] P. O. Fedichev, M. W. Reynolds, and G. V. Shlyapnikov. Three-body recombination of ultracold atoms to a weakly bound s level. *Phys. Rev. Lett.*, 77:2921–2924, Sep 1996.

[215] B. D. Esry, Chris H. Greene, and James P. Burke. Recombination of three atoms in the ultracold limit. *Phys. Rev. Lett.*, 83:1751–1754, Aug 1999.

[216] P. F. Bedaque, Eric Braaten, and H.-W. Hammer. Three-body recombination in bose gases with large scattering length. *Phys. Rev. Lett.*, 85:908–911, Jul 2000.

[217] Eric Braaten and H.-W. Hammer. Three-body recombination into deep bound states in a bose gas with large scattering length. *Phys. Rev. Lett.*, 87:160407, Oct 2001.

[218] D. S. Petrov. Three-boson problem near a narrow feshbach resonance. *Phys. Rev. Lett.*, 93:143201, Sep 2004.

[219] Eric Braaten, H.-W. Hammer, and M. Kusunoki. Universal equation for efimov states. *Phys. Rev. A*, 67:022505, Feb 2003.

[220] Ulrich Eismann, Lev Khaykovich, Sébastien Laurent, Igor Ferrier-Barbut, Benno S. Rem, Andrew T. Grier, Marion Delehaye, Frédéric Chevy, Christophe Salomon, Li-Chung Ha, and Cheng Chin. Universal loss dynamics in a unitary Bose gas. *Phys. Rev. X*, 6:021025, May 2016.

[221] Xiao Yin and Leo Radzihovsky. Quench dynamics of a strongly interacting resonant bose gas. *Phys. Rev. A*, 88:063611, Dec 2013.

[222] Swann Piatecki and Werner Krauth. Efimov-driven phase transitions of the unitary Bose gas. *Nature communications*, 5, 2014.

[223] AG Sykes, JP Corson, JP D'Incao, AP Koller, CH Greene, AM Rey, KRA Hazzard, and JL Bohn. Quenching to unitarity: Quantum dynamics in a three-dimensional Bose gas. *Physical Review A*, 89(2):021601, 2014.

[224] D Hudson Smith, Eric Braaten, Daekyoung Kang, and Lucas Platter. Two-body and three-body contacts for identical bosons near unitarity. *Physical review letters*, 112(11):110402, 2014.

[225] L Luo, B Clancy, J Joseph, J Kinast, A Turlapov, and J E Thomas. Evaporative cooling of unitary fermi gas mixtures in optical traps. *New Journal of Physics*, 8(9):213, 2006.

[226] Mandonnet, E., Minguzzi, A., Dum, R., Carusotto, I., Castin, Y., and Dalibard, J. Evaporative cooling of an atomic beam. *Eur. Phys. J. D*, 10(1):9–18, 2000.

[227] Chen-Lung Hung, Xibo Zhang, Nathan Gemelke, and Cheng Chin. Accelerating evaporative cooling of atoms into bose-einstein condensation in optical traps. *Phys. Rev. A*, 78:011604, Jul 2008.

[228] A. D. Lange, K. Pilch, A. Prantner, F. Ferlaino, B. Engeser, H.-C. Nägerl, R. Grimm, and C. Chin. Determination of atomic scattering lengths from measurements of molecular binding energies near feshbach resonances. *Phys. Rev. A*, 79:013622, Jan 2009.

[229] Noam Gross, Zav Shotan, Servaas Kokkelmans, and Lev Khaykovich. Nuclear-spin-independent short-range three-body physics in ultracold atoms. *Phys. Rev. Lett.*, 105:103203, Sep 2010.

[230] M. Berninger, A. Zenesini, B. Huang, W. Harm, H.-C. Nägerl, F. Ferlaino, R. Grimm, P. S. Julienne, and J. M. Hutson. Universality of the three-body parameter for efimov states in ultracold cesium. *Phys. Rev. Lett.*, 107:120401, Sep 2011.

[231] Cheng Chin. Universal scaling of efimov resonance positions in cold atom systems. *arXiv preprint arXiv:1111.1484*, 2011.

[232] Sébastien Laurent, Xavier Leyronas, and Frédéric Chevy. Momentum distribution of a dilute unitary bose gas with three-body losses. *Phys. Rev. Lett.*, 113:220601, Nov 2014.

[233] Henrik Smith and Henning Højgaard Jensen. *Transport phenomena*. Oxford University Press, USA, 1989.

[234] Xavier Leyronas. Virial expansion with feynman diagrams. *Phys. Rev. A*, 84(5):053633, 2011.

[235] Walter Appel and Emmanuel Kowalski. *Mathematics for physics and physicists*. Princeton University Press, 2007.

[236] Yvan Castin and Félix Werner. Third virial coefficient of the unitary Bose gas. *Canadian Journal of Physics*, 91:382, 2013.

[237] AB Bardon, S Beattie, C Luciuk, W Cairncross, D Fine, NS Cheng, GJA Edge, E Taylor, S Zhang, S Trotzky, et al. Transverse demagnetization dynamics of a unitary fermi gas. *Science*, 344(6185):722–724, 2014.

[238] B. Fröhlich, M. Feld, E. Vogt, M. Koschorreck, M. Köhl, C. Berthod, and T. Giamarchi. Two-dimensional fermi liquid with attractive interactions. *Phys. Rev. Lett.*, 109:130403, Sep 2012.

[239] Yoav Sagi, Tara E Drake, Rabin Paudel, and Deborah S Jin. Measurement of the homogeneous contact of a unitary fermi gas. *Physical review letters*, 109(22):220402, 2012.

[240] E.D. Kuhnle, S. Hoinka, P. Dyke, H. Hu, P. Hannaford, and C.J. Vale. Temperature dependence of the universal contact parameter in a unitary Fermi gas. *Phys. Rev. Lett.*, 106(17):170402, 2011.

[241] Igor Boettcher, Luca Bayha, Dhruv Kedar, PA Murthy, Mathias Neidig, MG Ries, AN Wenz, Gerhard Zuern, Selim Jochim, and Tilman Enss. Equation of state of ultracold fermions in the 2d bec-bcs crossover region. *Physical review letters*, 116(4):045303, 2016.

[242] K. Fenech, P. Dyke, T. Peppler, M. G. Lingham, S. Hoinka, H. Hu, and C. J. Vale. Thermodynamics of an attractive 2d fermi gas. *Phys. Rev. Lett.*, 116:045302, Jan 2016.

[243] J.P. D'Incao and B.D. Esry. Suppression of molecular decay in ultracold gases without Fermi statistics. *Phys. Rev. Lett.*, 100(16):163201, 2008.

[244] J.J. Zirbel, K.-K. Ni, S. Ospelkaus, J.P. D'Incao, C.E. Wieman, J. Ye, and D.S. Jin. Collisional stability of fermionic Feshbach molecules. *Phys. Rev. Lett.*, 100(14):143201, 2008.

[245] F. M. Spiegelhalder, A. Trenkwalder, D. Naik, G. Hendl, F. Schreck, and R. Grimm. Collisional Stability of ^{40}K Immersed in a Strongly Interacting Fermi Gas of ^{6}Li. *Phys. Rev. Lett.*, 103(22):223203, Nov 2009.

[246] Alexander Y. Khramov, Anders H. Hansen, Alan O. Jamison, William H. Dowd, and Subhadeep Gupta. Dynamics of feshbach molecules in an ultracold three-component mixture. *Phys. Rev. A*, 86:032705, Sep 2012.

[247] T. B. Ottenstein, T. Lompe, M. Kohnen, A. N. Wenz, and S. Jochim. Collisional stability of a three-component degenerate fermi gas. *Phys. Rev. Lett.*, 101:203202, Nov 2008.

[248] J. H. Huckans, J. R. Williams, E. L. Hazlett, R. W. Stites, and K. M. O'Hara. Three-body recombination in a three-state fermi gas with widely tunable interactions. *Phys. Rev. Lett.*, 102:165302, Apr 2009.

[249] Eric Braaten, H.-W. Hammer, Daekyoung Kang, and Lucas Platter. Three-body recombination of ^{6}Li atoms with large negative scattering lengths. *Phys. Rev. Lett.*, 103:073202, Aug 2009.

[250] R. Combescot, S. Giorgini, and S. Stringari. Molecular signatures in the structure factor of an interacting fermi gas. *EPL (Europhysics Letters)*, 75(5):695, 2006.

[251] C. Lobo, A. Recati, S. Giorgini, and S. Stringari. Normal state of a polarized Fermi gas at unitarity. *Phys. Rev. Lett.*, 97(20):200403, 2006.

[252] R. Haussmann, M. Punk, and W. Zwerger. Spectral functions and rf response of ultracold fermionic atoms. *Phys. Rev. A*, 80:063612, Dec 2009.

[253] Hui Hu, Xia-Ji Liu, and Peter D Drummond. Universal contact of strongly interacting fermions at finite temperatures. *New Journal of Physics*, 13(3):035007, 2011.

[254] F. Palestini, A. Perali, P. Pieri, and G. C. Strinati. Temperature and coupling dependence of the universal contact intensity for an ultracold fermi gas. *Phys. Rev. A*, 82:021605, Aug 2010.

[255] Cheng Chin and Rudolf Grimm. Thermal equilibrium and efficient evaporation of an ultracold atom-molecule mixture. *Phys. Rev. A*, 69:033612, Mar 2004.

[256] J Söding, D Guéry-Odelin, P Desbiolles, F Chevy, H Inamori, and J Dalibard. Three-body decay of a rubidium bose–einstein condensate. *Applied Physics B: Lasers and Optics*, 69(4):257–261, 1999.

[257] Zav Shotan, Olga Machtey, Servaas Kokkelmans, and Lev Khaykovich. Three-body recombination at vanishing scattering lengths in an ultracold bose gas. *Phys. Rev. Lett.*, 113:053202, Jul 2014.

[258] Yoav Sagi, Tara E. Drake, Rabin Paudel, and Deborah S. Jin. Measurement of the homogeneous contact of a unitary fermi gas. *Phys. Rev. Lett.*, 109:220402, Nov 2012.

[259] B. Svistunov, F. Werner, private communication.

[260] M. F. Andersen, C. Ryu, Pierre Cladé, Vasant Natarajan, A. Vaziri, K. Helmerson, and W. D. Phillips. Quantized rotation of atoms from photons with orbital angular momentum. *Phys. Rev. Lett.*, 97:170406, Oct 2006.

[261] Stuart Moulder, Scott Beattie, Robert P. Smith, Naaman Tammuz, and Zoran Hadzibabic. Quantized supercurrent decay in an annular bose-einstein condensate. *Phys. Rev. A*, 86:013629, Jul 2012.

[262] Stephen P Eckel, Jeffrey Lee, Fred Jendrzejewski, Noel Murray, Charles W Clark, Christopher J Lobb, William D Phillips, Edwards Mark, and Gretchen K Campbell. Hysteresis in quantized superfluid atomtronic circuit. *Nature*, 506, 2014.

[263] Hélène Perrin and Barry M Garraway. Chapter four-trapping atoms with radio frequency adiabatic potentials. *Advances In Atomic, Molecular, and Optical Physics*, 66:181–262, 2017.

[264] Xing-Can Yao, Hao-Ze Chen, Yu-Ping Wu, Xiang-Pei Liu, Xiao-Qiong Wang, Xiao Jiang, Youjin Deng, Yu-Ao Chen, and Jian-Wei Pan. Observation of coupled vortex lattices in a mass-imbalance bose and fermi superfluid mixture. *Phys. Rev. Lett.*, 117:145301, Sep 2016.

[265] J.P. D'Incao and B.D. Esry. Scattering length scaling laws for ultracold three-body collisions. *Physical review letters*, 94(21):213201, 2005.

[266] V. S. Babichenko and Yu. Kagan. Influence of cooper pairing on the inelastic processes in a gas of fermi atoms. *Phys. Rev. A*, 85:033604, Mar 2012.

[267] B. D. Esry, Chris H. Greene, and H. Suno. Threshold laws for three-body recombination. *Phys. Rev. A*, 65:010705, Dec 2001.

[268] Hans-Werner Hammer, Andreas Nogga, and Achim Schwenk. Colloquium: Three-body forces: From cold atoms to nuclei. *Reviews of modern physics*, 85(1):197, 2013.

[269] I Ferrier-Barbut, M. Delehaye, S. Laurent, A.T. Grier, M. Pierce, B.S Rem, F. Chevy, and C. Salomon. A mixture of Bose and Fermi superfluids. *Science*, 345:1035–1038, 2014.

[270] Milton Abramowitz and Irene A Stegun. *Handbook of mathematical functions: with formulas, graphs, and mathematical tables*, volume 55. Courier Corporation, 1964.

Remerciements

J'ai rejoins le laboratoire Kastler Brossel en janvier 2013 afin d'y effectuer mon stage de master 2 pour ne le quitter qu'en octobre 2017 une fois ma thèse de doctorat terminée. Ces quelques années passées dans cet univers si particulier furent riches en découvertes, rencontres, émotions, et je souhaite ici remercier toutes les personnes qui auront fait de cette étape de ma vie une si belle aventure.

Tout d'abord, je remercie chaleureusement mes deux directeurs de thèse Christophe Salomon et Frédéric Chevy qui m'ont pris sous leurs ailes en stage et ont su me renouveler leur confiance pour quelques années supplémentaires en thèse. C'est une chance immense d'avoir pu travailler tout au long de cette thèse avec eux et d'avoir pu bénéficier de leurs grandes qualités de physicien.

It was also a great honor to have Amandine Aftalion, Nikolaos Proukakis, Vincent Josse, Eric Cornell, and Ionut Danaila in my PhD comitee and I thank them for their careful reading, remarks and more generally for their interest in this work.

La plupart des résultats expérimentaux présentés dans cette thèse ont été obtenus sur l'expérience lithium. Une machine à l'aspect organique et aux rouages si complexes et si nombreux que seul l'effort acharné de toute une équipe peut faire fonctionner à bien. L'équipe a beaucoup changé au cours du temps et j'en remercie ses membres passés et présents. Mon premier contact avec cette manip fut auprès de deux géants Andrew Grier et Benno Rem qui semblaient incroyablement à l'aise dans leurs tâches malgré l'étroitesse de la salle d'expérience. C'est Igor Ferrier-Barbut qui m'a transmis les arcanes de l'expérience ainsi qu'un certain goût pour la ténacité et la débrouillardise. Enfin, c'est avec Marion Delehaye puis Matthieu Pierce que nous avons affronté vents et marées avec cette machine[1]. Il ne restera cependant de ces moments parfois difficiles que de bons souvenirs. Je souhaite à Matthieu ainsi qu'aux nouveaux membres de l'équipe Lianghui Hang et Gentle Dash une bonne continuation pour les années à venir sur une expérience qui sait malgré tout se montrer généreuse en temps voulus !

Une autre partie des travaux présentés dans ce manuscrit sont le résultat de collaborations avec plusieurs chercheurs que je remercie également. J'ai tout d'abord eu la chance de pouvoir travailler avec Xavier Leyronas d'une part et Lev Khaykovich et Ulrich Eismann d'autre part sur la thématique des pertes dans un gaz de Bose unitaire. Je garde un très bon souvenirs des nombreuses réunions et discussions captivantes que nous avons

---

[1] Pour la postérité en voici une liste non-exhaustive: les diverses fuites d'eau au niveau des bobines et des plaques de refroidissement pour IGBTs et les nombreux seaux d'eau associés qu'il fallait vider quotidiennement, l'opération chirurgicale de remplacement d'une des bobines de Feshbach, la surchauffe du ralentisseur Zeeman, les coupures d'électricité inopinées, les travaux CPER, ...

eus à ce sujet. Plus tard, avec Ionut Danaila, Phillipe Parnaudeau et Atsushi Suzuki nous nous sommes attaqués à la simulation numérique d'un contre-flot de condensats. J'ai découvert grâce à eux l'univers des maths appliqués et des super-calculateurs (ainsi que la fameuse bouillabaisse du CIRM). Malgré le nombre de téraoctets de données à traiter et à comprendre, travailler ensemble fut stimulant et un réel plaisir.

L'équipe gaz de Fermi ultrafroids a été comme une grande famille et je remercie tous ses membres pour les discussions, coups de mains, et nombreux moments forts[2] que j'ai pu partager avec eux durant toute ma thèse. Il me faut remercier en particulier Tarik Yefsah pour sa contribution dans l'obtention et la compréhension de nos derniers résultats sur l'expérience lithium, Félix Werner avec qui j'ai eu de nombreuses discussions éclairantes, les Fermix, Franz Sievers, Diogo Rio Fernandes, Norman Kretzschmar, Daniel Suchet, Mihail Rabinovic, Thomas Reimann, Cedric Enesa et Markus Bohlen, ainsi que les membres de la nouvelle équipe Lithium III, Shuwei Jin, Ragheed Alhyder, et Darby Bates.

Un superbe projet fut l'organisation de la conférence Young Atomic Opticians en juillet 2017. Je suis fier d'avoir pu prendre part à cette aventure pleine de rebondissements et de bons souvenirs de quasiment deux ans en compagnie de Chayma Bouazza, Eva-Katherina Dietsche et Pierre Dussarrat. Évidemment, rien n'aurait pu se faire sans la bonne humeur ni l'aide cruciale des fameux “local helpers”, Frédéric Assemat, Manel Bosch, Jean-Loup Ville et Raphael Bouganne, merci à eux !

Je tiens aussi à remercier les différents services du laboratoire et du département de physique que j'ai pu solliciter durant ma thèse. Merci au secrétariat du laboratoire, Audrey Gholke, Thierry Tardieu, Delphine Charbonneau et Nora Aissous pour leur efficacité administrative ainsi que pour leur assistance et conseils dans l'organisation de YAO. Merci aux services électrique et maintenance, notamment pour avoir su gérer efficacement les différents sinistres du bâtiment qui ont affecté notre expérience lors des travaux CPER, à l'atelier mécanique pour toutes les fabrications de pièces de l'expérience, et à Lionel Pérenès et Toufik El Atmani pour les nombreuses réparations de notre matériel électronique.

Enfin, je remercie affectueusement mes amis, ma famille et Julie pour leur soutien et encouragements tout au long de ce grand périple.

---

[2] En particulier la mémorable nuit du 8 mars 2016 qui fut enflammée en bien des aspects.

Résumé

La compréhension des effets des interactions dans un ensemble de particules quantiques représente un enjeu majeur de la physique moderne. Les atomes ultra-froids sont rapidement devenus un outil incomparable pour étudier ces systèmes quantiques fortement corrélés. Dans cette thèse, nous présentons plusieurs travaux portant sur les propriétés d'un mélange de superfluides de Bose et de Fermi créé à l'aide de vapeurs ultra-froides de ^{7}Li et de ^{6}Li.

Nous étudions tout d'abord les propriétés hydrodynamiques du mélange en créant un contre-courant entre les superfluides. L'écoulement est dissipatif uniquement au dessus d'une vitesse critique que nous mesurons dans le crossover BEC-BCS. Une simulation numérique d'un contre-courant de deux condensats permet de mieux comprendre les mécanismes sous-jacents mis en jeu dans la dynamique. En particulier, l'étude numérique fournit des preuves supplémentaires que l'origine de la dissipation dans nos expériences est liée à l'émission d'excitation élémentaires dans chaque superfluide.

Finalement, nous nous intéressons aux pertes inélastiques par recombinaison à trois corps qui peuvent limiter la stabilité de nos nuages. Ces pertes sont intimement liées aux corrélations à courte distance présentes dans le système et sont ainsi connectées aux propriétés universelles du gaz quantique. Cela se manifeste notamment par l'apparition de dépendances en densité ou en température inusuelles du taux de perte lorsque le système devient fortement corrélé. Nous démontrons cet effet dans deux exemples où les interactions sont résonantes, le cas du gaz de Bose unitaire et celui de notre mélange de superfluides Bose-Fermi. Plus généralement, nos travaux montrent que ces pertes inélastiques peuvent être utilisées pour sonder les corrélations quantiques dans un système en fortes interactions.

Abstract

Understanding the effect of interactions in quantum many-body systems presents some of the most compelling challenges in modern physics. Ultracold atoms have emerged as a versatile platform to engineer and investigate these strongly correlated systems. In this thesis, we study the properties of a mixture of Bose and Fermi superfluids with tunable interactions produced using ultracold vapors of ^{7}Li and ^{6}Li.

We first study the hydrodynamic properties of the mixture by creating a counterflow between the superfluids. The relative motion only exhibit dissipation above a critical velocity that we measure in the BEC-BCS crossover. A numerical simulation of counterflowing condensates allows for a better understanding of the underlying mechanisms at play in the dynamics. In particular, this numerical study provides additional evidence that the onset of friction in our experiment is due to the simultaneous generation of elementary excitations in both superfluids.

Finally, we consider the inelastic losses that occur via three-body recombination in our cold gases. This few-body process is intimately related to short-distance correlations and is thereby connected to the universal properties of the many-body system. This manifests as the apparition of an unusual dependence on density or temperature in the loss rate when increasing the interactions. We demonstrate this effect in two examples where interactions are resonant: the case of a dilute unitary Bose gas and the one of impurities weakly coupled to a unitary Fermi gas. More generally, our work shows that inelastic losses can be used to probe quantum correlations in a many-body system.

Mots Clés

Gaz quantiques, mélange de superfluides, vitesse critique, simulation de Gross-Pitaevskii, gaz de Fermi fortement corrélé, gaz de Bose unitaire, pertes inélastiques, contact de Tan, corrélations quantiques

Keywords

Quantum gases, mixture of superfluids, critical velocity, Gross-Pitaevskii simulation, strongly interacting Fermi gas, unitary Bose gas, inelastic losses, Tan's contact, quantum correlations

Numéro national de thèse:
2017PSLEE023